

Utah State University

DigitalCommons@USU

---

All Graduate Theses and Dissertations

Graduate Studies

---

8-2017

## 29-Day Analysis of Scale Heights and the Inference of the Topside Ionosphere over Millstone Hill during the 2002 Incoherent Scatter Radar Campaign

Jennifer L. Meehan  
*Utah State University*

Follow this and additional works at: <https://digitalcommons.usu.edu/etd>



Part of the [Physics Commons](#)

---

### Recommended Citation

Meehan, Jennifer L., "29-Day Analysis of Scale Heights and the Inference of the Topside Ionosphere over Millstone Hill during the 2002 Incoherent Scatter Radar Campaign" (2017). *All Graduate Theses and Dissertations*. 6528.

<https://digitalcommons.usu.edu/etd/6528>

This Dissertation is brought to you for free and open access by the Graduate Studies at DigitalCommons@USU. It has been accepted for inclusion in All Graduate Theses and Dissertations by an authorized administrator of DigitalCommons@USU. For more information, please contact [digitalcommons@usu.edu](mailto:digitalcommons@usu.edu).



29-DAY ANALYSIS OF SCALE HEIGHTS AND THE INFERENCE OF THE  
TOPSIDE IONOSPHERE OVER MILLSTONE HILL DURING THE 2002  
INCOHERENT SCATTER RADAR CAMPAIGN

by

Jennifer L. Meehan

A dissertation submitted in partial fulfillment  
of the requirements for the degree

of

DOCTOR OF PHILOSOPHY

in

Physics

Approved:

---

Jan J. Sojka, Ph.D.  
Major Professor

---

Michael Taylor, Ph.D.  
Committee Member

---

Jeong-Young Ji, Ph.D.  
Committee Member

---

Vincent Wickwar, Ph.D.  
Committee Member

---

Rees Fullmer, Ph.D.  
Committee Member

---

Mark R. McLellan, Ph.D.  
Vice President for Research and  
Dean of the School of Graduate Studies

UTAH STATE UNIVERSITY  
Logan, Utah

2017

Copyright © Jennifer L. Meehan 2017

All Rights Reserved

## ABSTRACT

29-Day Analysis of Scale Heights and the Inference of the Topside Ionosphere  
Over Millstone Hill During the 2002 Incoherent Scatter Radar Campaign

by

Jennifer L. Meehan, Doctor of Philosophy

Utah State University, 2017

Major Professor: Dr. Jan J. Sojka  
Department: Physics

Ionospheric scale height is a measure of the topside altitude dependence of electron density and is a key ionospheric parameter due to its intrinsic connection to ionospheric dynamics, plasma temperature, and composition. A longtime problem has been that information on the bottomside ionospheric profile is readily available, but the observation of the topside ionosphere is still challenging. Despite numerous data techniques to characterize the topside ionosphere, the knowledge of the behavior of the topside ionosphere and its subsequent scale heights remains insufficient. The goal of this study is to evaluate whether or not we can characterize the topside ionospheric density and temperature profiles in the event that neither temperature nor electron density are measured by using a cost-effective method.

In a simple model, the electron density in the F-region topside decreases exponentially with height. This exponential decay is mainly driven by thermal diffusive equilibrium, but also dependent on the dominant ion species, as well as other drivers during

nondiffusive conditions. A scale height based on observations of the temperature can generate topside electron density profiles. While a measure of the electron density profile enables a scale height to be inferred, hence yielding temperature information.

We found a new way to represent how much total electron content (TEC) is allotted for the topside ionosphere. We then used this information to successfully determine TEC using ionosonde data containing only bottomside electron density information. For the first time, slab thickness, which is directly proportional to scale height, was found to be correlated to the peak density height and introduced as a new index,  $\kappa$ . Ultimately,  $\kappa$  relates electron density parameters and can be a very useful tool for describing the topside ionosphere shape and subsequently, scale height. The methodology of using cost-effective, readily available ionosonde bottomside electron density data combined with GPS TEC was discovered to be capable of inferring the topside ionosphere. This was verified by incoherent scatter radar (ISR) data, though major issues surrounding the availability of ionogram data during nighttime hours greatly limited our study, especially during diffusive equilibrium conditions. Also, significant differences were found between ISR and ionosonde-determined peak density parameters,  $N_mF_2$  and  $h_mF_2$ , and raised concerns in how the instruments were calibrated.

(225 pages)

## PUBLIC ABSTRACT

29-Day Analysis of Scale Heights and the Inference of the Topside Ionosphere  
Over Millstone Hill During the 2002 Incoherent Scatter Radar Campaign

Jennifer Meehan

This study aims to characterize the topside ionospheric density and temperature profiles using readily available Global Positioning System (GPS) total electron content (TEC) and ionosonde bottomside profile of electron density. The aim of this study is to find a technique that can be applied globally rather than specific locations where a wealth of data exists. Knowledge of the distribution of electron density and its altitude dependence, known as scale height, is important for ionospheric empirical modeling and ionospheric studies, and for practical applications, such as time delay correction of radio-wave propagation through the ionosphere.

Over the years, researchers have gathered information and developed several different methods to analyze the topside ionosphere, including: coherent scatter radar observations of underdense electron density irregularities, incoherent scatter radar (ISR) probing, topside sounders onboard satellites, in situ rocket and satellite observations, such as Global Positioning System (GPS), and occultation measurements.

We were able to obtain topside information by an analysis of GPS TEC in combination with bottomside electron density profiles observed by ionosondes. This was verified by a study using one month's worth of data from Millstone Hill ISR observations.

In memory of my grandfather, William J. Meehan, who taught me stubbornness is a virtue.

## ACKNOWLEDGMENTS

I must first thank the two individuals who gave me my first opportunity in the field of space weather and have been with me every step of the way since, supporting me in any way they could, Genene Fisher and William Murtagh. I am indebted to both of you for your endless encouragement to see me succeed as a scientist and for your friendship. To Jan Sojka, your mentorship and enthusiastic personality helped push me to believe in myself and reach my full capabilities as a researcher. I am so very grateful to have worked with you over the years. Thank you to my committee members, Jeong-Young Ji, Michael Taylor, Vincent Wickwar, and Rees Fullmer for providing insight and feedback throughout the dissertation process. Also, thank you for the endless motivation, Shane Larson, and for breakfast conversations at Herms about life and career paths.

I gratefully acknowledge the genuine guidance, support and advice I have received over the years from the USU Physics Department staff; namely, Karalee Ransom and Sharon Pappas. Thank you for all that you have done for me and for always being so kind. You both are diligent, hard workers, that do so much for us graduate students, and deserve more credit than we give. I am also grateful to have received summer funding support from the Gene Adams, Howard L. Blood, and Keith Taylor scholarships.

I do not know where I would be without the support from and conversations with fellow graduate students both at Hampton University and Utah State University, especially Sydney Lewis, Jasper Lewis, Ciara Mason, Chris Spells, David Gomez, Nicole Pothier, Kevin Leavor, David Hansen, Jared Fulgham, Leda Sox, Ivana Molina, Neal Criddle, Kausik Chatterjee, and Mubarack Ukashat. We have all learned together that a big part of



graduate school is overcoming the ups and downs, but always continuing to move forward. I am inspired by every single one of you and wish you well in your future endeavors. I need to also credit the individuals I have been lucky to bond with over the years from the American Meteorological Society's 2009 Summer Policy Colloquium, 2010 Boston CISM Summer School, and 2012 Heliophysics Summer School.

Most importantly, words cannot begin to express the gratitude I have for my family. I dedicate all of my work to you. To my brother for sparking my initial interest in science and teaching me about the weather. My favorite childhood memories are watching storms on the patio with you, as well as watching the weather channel, back when it used to just be the weather forecast. You will always be able to predict the weather better than I can. To my mother, you are everything I aspire to be. Whatever I wanted to be, whatever I wanted to do, you were behind me 100%. Thank you for being my biggest cheerleader. To my father, thank you for teaching me to always go left when everyone else goes right. You have taught me to always be my own person and have set the perfect example. To Jodie and Steve, I am so lucky to call you family and have your love and support over all these years. To my hubby, the love of my life, thank you for wanting to go on this journey with me and standing by me every step of the way; and to Charlotte, giving purpose to everything that I do. I love you.

Jennifer Meehan

## CONTENTS

	Page
ABSTRACT .....	iii
PUBLIC ABSTRACT .....	v
DEDICATION .....	vi
ACKNOWLEDGMENTS .....	vii
LIST OF TABLES .....	xii
LIST OF FIGURES .....	xiii
LIST OF ACRONYMS .....	xxi
CHAPTER	
1. INTRODUCTION .....	1
1.1. The Ionosphere .....	1
1.2. Motivation .....	4
1.3. This Study .....	6
2. TOPSIDE IONOSPHERE BACKGROUND .....	8
2.1. Introduction .....	8
2.2. Diffusive States .....	9
2.3. Chapman Layer .....	11
2.4. Scale Height .....	12
2.5. Slab Thickness .....	14
2.6. Discussion .....	16
3. TOPSIDE IONOSPHERE .....	19
3.1. Plasma Temperature .....	19
3.1.1. Diurnal and Solar Variations .....	21
3.2. Ionic Composition .....	24
3.2.1. Diurnal Variations .....	25
3.3. Electron Density .....	27
3.3.1. Diurnal Variations .....	29
3.4. Discussion .....	33
4. MILLSTONE HILL STUDY .....	36
4.1. Introduction .....	36
4.2. Previous Millstone Hill Statistical Studies .....	37
4.2.1. Zhang et al., 2005 .....	37

4.2.2. Lei et al., 2005 .....	39
4.2.3. Liu et al., 2007 .....	41
4.3. Campaign Observations .....	43
4.3.1. Solar Conditions .....	43
4.3.2. $N_mF_2$ and $h_mF_2$ .....	45
4.3.3. Electron Temperature and Density Profiles .....	47
4.4. Discussion .....	49
5. TOPSIDE SCALE HEIGHT COMPARISONS .....	51
5.1. Introduction .....	51
5.2. ISR Methodology .....	52
5.3. Scale Height Results during Quiet Solar and Geomagnetic Conditions .....	53
5.3.1. Scale Height Comparisons during Nighttime Hours .....	57
5.3.2. Inference of $T_e$ during Nighttime Hours .....	61
5.3.3. Scale Height Comparisons during Daytime Hours .....	67
5.4. Discussion .....	69
6. TOPSIDE RECONSTRUCTION .....	72
6.1. Introduction .....	72
6.2. TEC Methodology .....	73
6.3. Ionosonde Methodology .....	80
6.4. Our Unique Methodology .....	90
6.4.1. TEC Topside Percentage.....	90
6.4.2. Determining Topside TEC from Ionosondes .....	94
6.4.3. Correlation between $h_mF_2$ and $\tau$ .....	96
6.5. Discussion .....	102
7. RECONSTRUCTED TOPSIDE ELECTRON DENSITY PROFILE .....	104
7.1. Introduction .....	104
7.2. Ionosonde Scaling .....	105
7.3. $\alpha$ -Chapman Profile .....	107
7.3.1. $\alpha$ -Chapman Pseudo-Temperature .....	109
7.3.2. $\alpha$ -Chapman Profile Scale Height .....	114
7.3.3. $\alpha$ -Chapman Profile-determined $T_e + T_i$ .....	118
7.3.4. $\alpha$ -Chapman Profile-determined $T_e + T_i$ and the Relationship to $\kappa$ ....	121
7.4. Discussion .....	124
8. CONCLUSIONS AND FUTURE WORK .....	126
8.1. Conclusions .....	126
8.2. Future Work .....	131
REFERENCES .....	135
APPENDICES .....	142

APPENDIX A. SOLAR AND GEOMAGNETIC INDICES .....	143
APPENDIX B. SCALE HEIGHT DERIVATIONS .....	146
APPENDIX C. ISR ERRORS .....	153
APPENDIX D. ISR SCALED TO IONOSONDE RESULTS .....	161
APPENDIX E. IONOSPHERE TOPSIDE RECONSTRUCTION RESULTS .....	165
APPENDIX F. COPYRIGHT PERMISSIONS .....	182
CURRICULUM VITAE .....	195

## LIST OF TABLES

Table	Page
7.1 Day 294 Absolute Difference Between Ionosonde and ISR Data .....	108
7.2 Day 297 Absolute Difference Between Ionosonde and ISR Data .....	108
7.3 Day 294 Chapman Temperature and TECt % Error .....	113
7.4 Day 297 Chapman Temperature and TECt % Error .....	113

## LIST OF FIGURES

Figure	Page
1.1 Layer formation in terms of optical depth .....	1
1.2 Vertical electron density profile .....	3
3.1 Energy sources for the electrons, ions, and neutral particles within the ionosphere .....	20
3.2 Observed electron temperatures (+) during low solar activity (a) and high solar activity (b) .....	22
3.3 Observed seasonal midday average electron temperatures during low solar activity (a) and high solar activity (b) from ISR data at Arecibo .....	22
3.4 $T_i$ (blue circles) and $T_e$ (red dots) altitude profiles taken at the French Saint Santin ISR .....	23
3.5 Ionic composition of the daytime ionosphere during solar minimum .....	25
3.6 Daytime (top row) and nighttime (bottom row) averages of the major and minor ions in the topside ionosphere measured during different seasons .....	26
3.7 Nine daytime comparisons between the two Abel inversions of the occultation data and the Arecibo-determined density profiles .....	30
3.8 Three nighttime comparisons between the two Abel inversions of the occultation data and the Arecibo-determined density profiles .....	31
3.9 Solid lines show COSMIC electron density profiles compared to those measured at Millstone Hill incoherent scatter radar .....	32
4.1 Data from Millstone Hill's 4 October - 4 November 2002 data campaign .....	39
4.2 Variations of scale height according to season, time of day, and solar activity .....	40
4.3 Campaign results of observed ionospheric parameters .....	42
4.4 Solar geophysical conditions between 5 October and 2 November, 2002 .....	44
4.5 The ISR-derived variation of the peak electron height, $h_m F_2$ (km), for days (a) 278-284, (b) 285-291, (c) 292-298, and (d) 299-306 .....	46

4.6	The ISR-derived variation of the log scale peak electron density, $N_m F_2$ ( $\text{cm}^{-3}$ ), for days (a) 278-284, (b) 285-291, (c) 292-298, and (d) 299-306 .....	46
4.7	The ISR-derived diurnal variation for days 278 – 306 .....	47
4.8	The ISR-derived diurnal variation for days 278 – 306 for electron density ( $\text{cm}^{-3}$ ) using log scale, at local midnight (a) and local noon (b) .....	48
5.1	Scale height calculations for quiet days 294 – 296 .....	55
5.2	Hourly ISR electron density profiles for day 295 from 16 – 20 UT .....	57
5.3a	Plasma scale height, $H_p$ , plotted against density-driven vertical scale height, VSH, for quiet days where $K_p < 4$ including nondiffusive shaped profiles during nighttime hours 0 – 10 UT at the topside upper altitude of 520 km .....	59
5.3b	Plasma scale height, $H_p$ , plotted against density-driven vertical scale height, VSH, for quiet days where $K_p < 4$ excluding nondiffusive shaped profiles during nighttime hours 0 – 10 UT at the topside upper altitude of 520 km .....	59
5.4a	Plasma scale height, $H_p$ , plotted against density-driven vertical scale height, VSH, for quiet days where $K_p < 4$ including nondiffusive shaped profiles during nighttime hours 0 – 10 UT at the topside lower altitude of 428 km .....	60
5.4b	Plasma scale height, $H_p$ , plotted against density-driven vertical scale height, VSH, for quiet days where $K_p < 4$ excluding nondiffusive shaped profiles during nighttime hours 0 – 10 UT at the topside lower altitude of 428 km .....	60
5.5a	Comparison between $T_e$ values taken from ISR data and by solving for $T_e$ using VSH for the solution of $H_p$ in equation 5.3 for reference quiet day 294 at the lower altitude of 428 km .....	63
5.5b	Comparison between $T_e$ values taken from ISR data and by solving for $T_e$ using VSH for the solution of $H_p$ in equation 5.3 for reference quiet day 294 at the upper altitude of 520 km .....	63
5.6a	Comparison between $T_e$ values taken from ISR data and by solving for $T_e$ using VSH for the solution of $H_p$ in equation 5.3 for quiet day 295 at the lower altitude of 428 km .....	64
5.6b	Comparison between $T_e$ values taken from ISR data and by solving for $T_e$	

using VSH for the solution of $H_p$ in equation 5.3 for quiet day 295 at the upper altitude of 520 km .....	64
5.7a Comparison between $T_e$ values taken from ISR data and by solving for $T_e$ using VSH for the solution of $H_p$ in equation 5.3 for quiet day 296 at the lower altitude of 428 km .....	65
5.7b Comparison between $T_e$ values taken from ISR data and by solving for $T_e$ using VSH for the solution of $H_p$ in equation 5.3 for quiet day 296 at the upper altitude of 520 km .....	65
5.8 C values and associated daily standard deviation are shown for nighttime hours 0 – 10 UT on quiet days 294 – 296 .....	66
5.9 Plasma scale height, $H_p$ , plotted against density driven, VSH, for days where $K_p < 4$ during daytime hours 12 – 22 UT at the topside upper altitude of 520 km .....	68
5.10 Plasma scale height, $H_p$ , plotted against density driven, VSH, for days where $K_p < 4$ during daytime hours 12 – 22 UT at the topside lower altitude of 428 km .....	68
6.1 ISR TEC compared to GPS STEC for quiet day 294 .....	75
6.2 ISR TEC compared to GPS STEC for active day 297 .....	75
6.3 Inclination angle, $\phi$ .....	77
6.4 STEC versus VTEC .....	78
6.5 ISR TEC results compared to STEC and VTEC from GPS for quiet day 294 .....	81
6.6 ISR TEC results compared to STEC and VTEC from GPS for active day 297 .....	81
6.7 ISR TEC results compared to STEC and VTEC from GPS for quiet day 294 during nighttime hours 0 - 10 UT .....	82
6.8 ISR TEC results compared to STEC and VTEC from GPS for active day 297 during nighttime hours 0 - 10 UT .....	82
6.9 Ionogram from LGDC, Principal Investigator, Prof. B. W. Reinisch, of the University of Massachusetts Lowell .....	84



6.10	Quiet day 294 ionogram-derived bottomside TECU versus ISR TECU bottomside .....	86
6.11	Active day 297 ionogram-derived bottomside TECU versus ISR TECU bottomside .....	86
6.12	$h_m F_2$ for quiet day 294 and active day 297 .....	88
6.13	Electron density profiles for day 297, hours 05 – 10 UT in consecutive order from top left to bottom right .....	89
6.14	Daily average percentages of topside TEC and associated daily standard deviation for days 278 – 306 .....	91
6.15	Daily average percentages of topside TEC for noontime hours 13 – 18 UT and associated daily noontime hours standard deviation for days 278 – 306 .....	92
6.16	Daily average percentages of topside TEC for midnight hours 01 - 06 UT and associated daily midnight hours standard deviation for days 278 – 306 .....	92
6.17	Quiet day 294 ionogram-derived TECU versus ISR TECU .....	95
6.18	Active day 297 ionogram-derived TECU versus ISR TECU .....	95
6.19	Quiet day 294 ISR relationship between $h_m F_2$ and slab thickness .....	97
6.20	Active day 297 ISR relationship between $h_m F_2$ and slab thickness .....	97
6.21	Daily average $h_m F_2 / \tau$ ratio and associated daily standard deviation for days 278 – 306 .....	98
6.22	Daily average ratios of $h_m F_2 / \text{Slab Thickness}$ for noontime hours 13 – 18 UT and associated daily noontime hours standard deviation for days 278 – 306 .....	100
6.23	Daily average ratios of $h_m F_2 / \text{Slab Thickness}$ for midnight hours 01 – 06 UT and associated daily midnight hours standard deviation for days 278 – 306 .....	100
7.1	Quiet day 294, 20 UT density profile ISR versus ionosonde .....	106
7.2	Active day 297, 12 UT density profile ISR versus ionosonde .....	106

7.3	Quiet day 294, 20 UT density profile ISR versus ionosonde .....	112
7.4	Active day 297, 12 UT density profile ISR versus ionosonde .....	112
7.5	Scale height calculations for quiet day 294 at two altitudes above the peak density height .....	116
7.6	Scale height calculations for active day 297 at two altitudes above the peak density height .....	117
7.7	Chapman determined $T_e + T_i$ compared to observed ISR measurements of $T_e + T_i$ during quiet day 294 .....	120
7.8	Chapman determined $T_e + T_i$ compared to observed ISR measurements of $T_e + T_i$ during active day 297 .....	120
7.9	Chapman determined $T_e + T_i$ with $\kappa$ relationship factor compared to observed ISR measurements of $T_e + T_i$ during quiet day 294 .....	123
7.10	Chapman determined $T_e + T_i$ with $\kappa$ relationship factor compared to observed ISR measurements of $T_e + T_i$ during active day 297 .....	123
8.1	TEC topside comparison between ISR, ionosonde, and GPS STEC for quiet day 294 .....	130
8.2	TEC topside comparison between ISR, ionosonde, and GPS STEC for active day 297 .....	130
A.1	NOAA Space Weather Prediction Center's Space Weather Scales .....	145
C.1	$N_e$ results with errors for nighttime hour 02 UT on quiet day 294 .....	155
C.2	$N_e$ results with errors for daytime hour 15 UT on quiet day 294 .....	155
C.3	$N_e$ results with an example error of 10% for daytime hour 11 UT for quiet day 294 .....	156
C.4	$N_e$ results with an example error of 10% for daytime hour 18 UT for quiet day 294 .....	156
C.5	$N_e$ results with errors for nighttime hour 02 UT on active day 297 .....	157
C.6	$N_e$ results with errors for daytime hour 15 UT on active day 297 .....	157
C.7	$T_e$ and $T_i$ results with associated errors for nighttime hour 02 UT on	

quiet day 294 .....	158
C.8 $T_e$ and $T_i$ results with associated errors for daytime hour 12 UT on quiet day 294 .....	159
C.9 $T_e$ and $T_i$ results with associated errors for nighttime hour 02 UT on active day 297 .....	159
C.10 $T_e$ and $T_i$ results with associated errors for daytime hour 12 UT on active day 297 .....	160
C.11 $T_e$ and $T_i$ results with an example error of 10% for daytime hour 18 UT on active day 294 .....	160
D.1 Adjusted ISR to fit ionosonde bottomside Ne data versus GPS TEC results on quiet day 294 .....	163
D.2 Adjusted ISR to fit ionosonde bottomside Ne data versus GPS TEC results on active day 297 .....	163
D.3 TEC topside comparison between ISR, adjusted ISR to ionosonde, GPS STEC, and GPS VTEC for quiet day 294 .....	164
D.4 TEC topside comparison between ISR, adjusted ISR to ionosonde, GPS STEC, and GPS VTEC for active day 297 .....	164
E.1 Quiet day 294, 00 UT density profile ISR versus ionosonde .....	165
E.2 Quiet day 294, 02 UT density profile ISR versus ionosonde .....	166
E.3 Quiet day 294, 12 UT density profile ISR versus ionosonde .....	166
E.4 Quiet day 294, 13 UT density profile ISR versus ionosonde .....	167
E.5 Quiet day 294, 14 UT density profile ISR versus ionosonde .....	167
E.6 Quiet day 294, 15 UT density profile ISR versus ionosonde .....	168
E.7 Quiet day 294, 16 UT density profile ISR versus ionosonde .....	168
E.8 Quiet day 294, 17 UT density profile ISR versus ionosonde .....	169
E.9 Quiet day 294, 18 UT density profile ISR versus ionosonde .....	169

E.10	Quiet day 294, 19 UT density profile ISR versus ionosonde .....	170
E.11	Quiet day 294, 20 UT density profile ISR versus ionosonde .....	170
E.12	Quiet day 294, 21 UT density profile ISR versus ionosonde .....	171
E.13	Quiet day 294, 22 UT density profile ISR versus ionosonde .....	171
E.14	Quiet day 294, 23 UT density profile ISR versus ionosonde .....	172
E.15	Active day 297, 00 UT density profile ISR versus ionosonde .....	173
E.16	Active day 297, 01 UT density profile ISR versus ionosonde .....	173
E.17	Active day 297, 02 UT density profile ISR versus ionosonde .....	174
E.18	Active day 297, 03 UT density profile ISR versus ionosonde .....	174
E.19	Active day 297, 04 UT density profile ISR versus ionosonde .....	175
E.20	Active day 297, 12 UT density profile ISR versus ionosonde .....	175
E.21	Active day 297, 13 UT density profile ISR versus ionosonde .....	176
E.22	Active day 297, 14 UT density profile ISR versus ionosonde .....	176
E.23	Active day 297, 15 UT density profile ISR versus ionosonde .....	177
E.24	Active day 297, 16 UT density profile ISR versus ionosonde .....	177
E.25	Active day 297, 17 UT density profile ISR versus ionosonde .....	178
E.26	Active day 297, 18 UT density profile ISR versus ionosonde .....	178
E.27	Active day 297, 19 UT density profile ISR versus ionosonde .....	179
E.28	Active day 297, 20 UT density profile ISR versus ionosonde .....	179
E.29	Active day 297, 21 UT density profile ISR versus ionosonde .....	180
E.30	Active day 297, 22 UT density profile ISR versus ionosonde .....	180
E.31	Active day 297, 23 UT density profile ISR versus ionosonde .....	181

F.1	Copyright permission received for [ <i>Whitten and Poppoff</i> , 1971] .....	183
F.2	Copyright permission received for <i>Stankov and Warnant</i> [2009] .....	185
F.3	Copyright permission received for <i>Banks and Kockarts</i> [1973] .....	186
F.4	Copyright permission received for <i>Sethi et al.</i> [2003] .....	187
F.5	Copyright permission received for <i>Zhang et al.</i> [2004] .....	188
F.6	Copyright permission received for <i>Johnson</i> [1966] .....	189
F.7	Copyright permission received for <i>Gonzalez et al.</i> [1992] .....	190
F.8	Copyright permission received for <i>Kelley et al.</i> [2009] .....	191
F.9	Copyright permission received for <i>Lei et al.</i> [2007] .....	192
F.10	Copyright permission received for <i>Zhang et al.</i> [2005] .....	193
F.11	Copyright permission received for <i>Lei et al.</i> [2005] .....	194

## LIST OF ACRONYMS

$N_mF_2$	F-region electron density peak value.
$h_mF_2$	F-region height of $N_mF_2$ .
$f_oF_2$	F-region critical frequency measurement equivalent to $N_mF_2$ .
TEC	Total Electron Content.
ISR	Incoherent Scatter Radar.
GPS	Global Positioning System.
$T_e$	Electron Temperature.
$T_i$	Ion Temperature.
$T_n$	Neutral Temperature.

# CHAPTER 1

## INTRODUCTION

### 1.1. The Ionosphere

Several layers of atmosphere surround the Earth, extending from the surface to space. Radiation emitted by the sun is attenuated exponentially in Earth's atmosphere by an absorbing medium. Due to forces of gravity, the density of the atmosphere decreases exponentially with altitude. As you decrease in altitude, the density increases and so does the absorption of solar radiation as shown in Figure 1.1 [Whitten and Poppoff, 1971]. At the outer fringes of the Earth's atmosphere, the density is low and radiation is only slightly absorbed. If the absorption is caused by ionization processes, an ionized layer will result. Solar radiation produces an ionized layer within the Earth's atmosphere known as the ionosphere, forming at about 80 km above the Earth's surface and extending up to 1000 km.

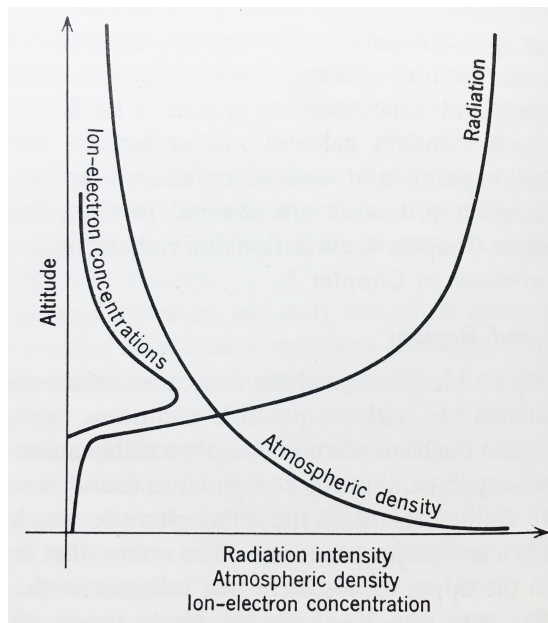


**Figure 1.1.** Layer formation in terms of optical depth, [Whitten and Poppoff, 1971].

Formation of the ionosphere also requires a neutral atmosphere. The neutral atmosphere is very thin in the ionosphere with about 99% of the Earth's atmosphere below 50 km. In the ionosphere, shortwave solar (EM) radiation in the form of both solar extreme ultraviolet (EUV, wavelength = 175 – 17 nm) and X-ray (X, wavelength = 17 – 0.1 nm) ionizes both molecules and atoms separating electrons from their parent particles creating free electrons and positive ions. These free electrons and positive ions are what create several weak ionized layers of plasma that constitute the ionosphere. Unlike other gases, the ionosphere can conduct an electric charge and is affected by magnetic fields. The ionosphere undergoes a diurnal cycle of solar radiation, with ionization being more extensive in the daytime.

The ionosphere acts as a communication medium allowing for radio wave propagation, an idea postulated in 1902 and confirmed in 1925 [*Kivelson and Russell, 1995*]. Telecommunication satellites orbiting Earth transmit signals down from space by using radio waves that interact with free electrons in the ionosphere. An increase in solar radiative energy (EUV) energizes matter in the atmosphere and causes an ionization increase, better known as photoionization. This rapid increase can cause instabilities in the ionosphere and can have major effects on satellite signals [*Kunches, 2007*]. Because of this, electron density distribution in the ionosphere and how it decreases with an increase in altitude, better known as scale height, needs to be understood.

The ionosphere is separated into D, E, F<sub>1</sub>, and F<sub>2</sub> regions, which are based solely on composition and dynamics of the atmosphere and solar radiation. The ionospheric region discussed in this study is the F<sub>2</sub> region, which includes the electron density peak,



formed by competition between chemical and transport processes, and the topside ionosphere, which begins just above the  $F_2$  density peak. Figure 1.2 shows a schematic of the ionospheric vertical electron density profile as a function of altitude. The electron density peak,  $N_mF_2$ , occurs at height,  $h_mF_2$ . The ionospheric topside extends from  $h_mF_2$  and up to a transition height (UTL) where the plasmasphere begins, signifying a change in ion dominance from  $O^+$  to  $H^+$ , and  $He^+$ .  $H_{sc}$  is the scale height and measures the increase in altitude needed to decrease density by a factor of  $e$  above  $h_mF_2$ . *Sydney Chapman* introduced scale height in 1931 and since then, scale height has been found to be the most important parameter used to describe the vertical density structure and regions of the atmosphere, as well as the temperature trends that reflect numerous physical and chemical processes in the ionosphere [*Huang and Reinisch, 2001; Stankov et al., 2003; Tulası Ram et al., 2009*]. Slab thickness is related to the shape of the density profile and is equal to the ratio of total electron content (TEC) to  $N_mF_2$ .

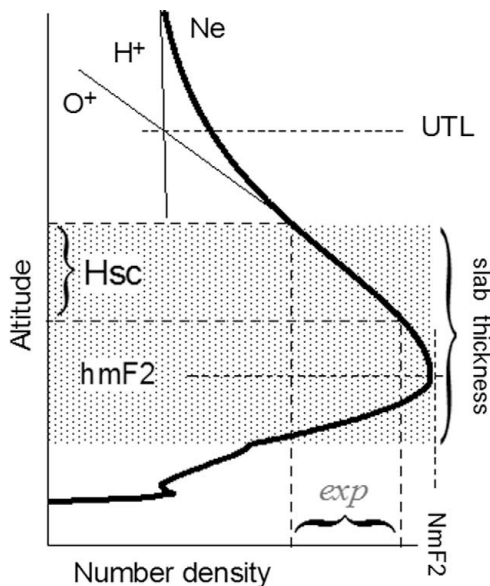


**Figure 1.2.** Vertical electron density profile [*Stankov and Warnant, 2009*].

## 1.2. Motivation

Ground-based ionosondes can measure the vertical electron density profile up to  $h_mF_2$ , leaving no direct information on the topside ionosphere [Huang and Reinisch, 2001]; however, the topside ionosphere can be approximated using a Chapman function with a constant scale height,  $H_c$  [Chapman, 1931; Rishbeth and Garriott, 1969; Stankov and Warnant, 2009]. The ratio of TEC to  $N_mF_2$  provides the slab thickness parameter, which contains information on the shape of the electron density profile and may provide the neutral and ionospheric temperatures and gradients, the ionospheric composition and dynamics [Stankov and Warnant, 2009]. Note: TEC may contain a plasmaspheric component if measured from a GPS satellite orbiting at 20,200 km; however, TEC measured from ISR will likely not contain a plasmaspheric component because the electron density measurement range is between 100 km and 784 km. In general, slab thickness depends upon the plasma scale height, but is not a good indicator of either electron or ion temperature; however, direct proportionality was found between slab thickness and scale height [Furman and Prasad, 1973].

There are several different instruments that researchers use to probe and gather information to analyze the topside ionosphere, including: coherent scatter radar, incoherent scatter radar (ISR) probing, topside sounders onboard satellites, in situ rocket and satellite observations such as Global Positioning System (GPS) and occultation measurements. Numerous techniques have been developed over several decades of study, yet knowledge of the topside ionosphere behavior in terms of scale height, remains insufficient [Stankov and Warnant, 2009]. ISRs measure the electron density profile from top to bottom in the

range of about 100 - 800 km, but are expensive to run and are limited to their geographical locations. Topside sounders and satellite data can provide homogeneous global coverage of electron density measurements from their respected satellite orbit altitude down to the Earth's surface; however, this approach is an integral quantity providing no details of the topside profile shape, and  $N_mF_2$  and  $h_mF_2$  cannot be evaluated unless combined with ionosonde bottomside measurements.

One of the most critical elements in ionospheric modeling-related applications is knowing the electron density profile of the topside ionosphere and its response to geophysical phenomena in terms of basic physical principles. Ionospheric models are critical for forecasting any instabilities in the ionosphere caused by space weather events, and in my interest, to ensure smooth operations of the GPS. Owned and operated by the United States Air Force, 31 operational GPS satellites fly at an altitude of approximately 20,200 km above the surface of the Earth in six equally spaced orbital planes [*National Coordination Office for Space-Based Positioning, Navigation, and Timing*, 2016].

The goal of this study is to better characterize the electron density profile of the topside ionosphere by providing new insights into the ambiguity that still exists for interpreting the physical meaning behind the behaviors of the topside ionosphere, which can improve said forecast models and contribute to alleviating space weather effects on GPS. Space weather is created by electromagnetic energy streaming radially from the sun, emitting rivers of photons and charged particles that sweep through space and threaten our space-based technological infrastructure; namely, GPS. Society is heavily reliant on GPS for positioning, navigation, and timing with critical applications, such as precision

agriculture, emergency response, commercial aviation, and marine navigation [Meehan *et al.*, 2010]. GPS receivers calculate their locations by analyzing signals from a constellation of satellites, but the propagation of those signals can be disrupted by instabilities in the ionosphere caused by space weather events. During large geomagnetic storms caused by space weather events, density gradients in the ionosphere can result in errors of up to 50 meters [Meehan *et al.*, 2010].

### **1.3. This Study**

In 2002, a wealth of data capturing the ionosphere in its entirety was collected from incoherent scatter radars located at Millstone Hill Observatory in Westford, Massachusetts (42.6°N, 288.5°E) and Svalbard, Norway (78.2°N, 16.0°E) from 4 October – 4 November. This 30-day consecutive run of ISRs enables a very thorough, statistical study of a very dynamic ionosphere and is the only one of its kind from the Millstone Hill, mid-latitude location. Running an ISR is very expensive and not practical for day-to-day monitoring of the ionosphere in order to study the electron density profile of the topside ionosphere. For this, we use 29 out of 30 days' of ISR data collected from Millstone Hill in an attempt to find other means of monitoring the topside ionosphere; namely, readily available ionosonde data and GPS TEC measurements, and what physical interpretations we can conclude by a scale heights analysis.

The document is divided into eight chapters. Chapters 2 and 3 give the literature review needed to describe the topside ionosphere in terms of scale height, slab thickness and the Chapman layer and addresses the ionosphere's thermal structure, ionic composition, and electron density formation necessary to conduct this study.

The analysis of ISR data collected from Millstone Hill begins in Chapter 4 by a brief description of why the Millstone Hill location was selected for this study and what exactly comprised the dataset. It continues by highlighting the conclusions and shortfalls of previous statistical studies on the same data campaign, as well as our interpretation of the campaign observations and the methodology adapted moving forward. The dissertation results begin in Chapter 5 by studying how scale height methods differ from day to day. ISR methodology consisted of separating data into nighttime hours, 0 – 10 UT, and daytime hours, 11 - 23 UT, then grouped into active and quiet days by an analysis of corresponding solar indices. New physical parameter correlations and relationships, as well as our unique methodology of characterizing the topside ionosphere, is found in Chapter 6 and applied in Chapter 7.

Finally, Chapter 8 gives the most important results found in this dissertation and outlines future work to thoroughly investigate what these new relationships mean between plasma temperature trends and density parameters.

## CHAPTER 2

### TOPSIDE IONOSPHERE BACKGROUND

#### 2.1. Introduction

The electron density profile is one of the most critical elements in the ionospheric modeling-related applications today. Ionosphere parameters of the F<sub>2</sub> layer:  $f_0F_2$ , the highest frequency of radio signal reflected vertically from the F<sub>2</sub> layer peak (usually converted into a peak density numerical value known as  $N_mF_2$ ), and  $h_mF_2$ , the height of the peak density layer, are generally obtained simply from any global sounding observation network and are easily incorporated into models, theoretical or empirical, as numerical representations. The ionospheric profile shape, however, requires knowledge of several ionospheric parameters: electron, ion and neutral temperatures, ion composition, electric fields, and neutral winds, and is dependent upon seasons, local time, location, and the level of solar and geomagnetic activity [Fox *et al.*, 1991]. Modeling efforts show the effects on the profile shape when varying each of the parameters, but there is a problem with the physical interpretation.

The topside ionosphere is the region just above  $h_mF_2$ , and in a simple model, the density of this region decreases exponentially with height, known as the scale height,  $H$ . Satellite and rocket measurements over the past half century have shown that the important topside ionosphere ions are  $H^+$ ,  $O^+$ , and  $He^+$ . At progressively greater distances from Earth, the equations governing the distributions of ions under the effect of gravity predict that the mean ionic mass should continually decrease, with the particles of smallest mass being predominant in the further regions [Banks and Kockarts, 1973b]. The topside ionosphere

extends upward to a transition height where  $O^+$  ions are less dominant than  $H^+$  and  $He^+$  ions. The transition height can vary anywhere from 500 km at night or 800 km during the day and can reach 1100 km [Knipp, 2011]. The transition height has a major effect on the electron density profile due to dramatic differences in individual scale heights that create vertical distribution gradients and also marks the beginning of the plasmasphere [Stankov *et al.*, 2003].

Over the years, researchers have gathered information and developed several different methods to analyze the topside ionosphere, including: coherent scatter radar observations of underdense electron density irregularities, ISR probing, topside sounders onboard satellites, in situ rocket and satellite observations such as GPS, and occultation measurements [Booker, 1956; Greenwald, 1996; Bowles, 1958; Huang and Reinisch, 1996; Leitinger, 1996; Stankov and Jakowksi, 2006a, b]. The tools to conduct such an analysis are readily available: accumulated databases of ISR [Zhang *et al.*, 2004, 2005; Tepley, 1997; Isham *et al.*, 2000], topside sounders [Bilitza *et al.*, 2006], and radio occultation; however, a thorough analysis investigating the characteristics of the ionospheric scale heights is yet to be completed.

## **2.2. Diffusive States**

Dynamical properties within the topside ionosphere are complex. The state of diffusive equilibrium in the topside ionosphere between different ion species provides a convenient theoretical understanding, though the upper atmosphere is never in a true state of thermal, mechanical, or chemical equilibrium [Whitten and Poppoff, 1971]. Diffusive equilibrium is generally found above 100 km where all atoms and molecules move about

as independent particles and are subject to the effects of gravity. The distribution of ionization in the topside ionosphere is strongly controlled by the geomagnetic field and the perpendicular plasma convection motions resulting from the electric fields of magnetospheric origin [*Banks and Kockarts, 1973*]. Distribution of thermal plasma in the topside ionosphere are driven by electric fields of magnetospheric origin at high and mid-latitudes, while the atmospheric dynamics generate electric fields at midequatorial latitudes, so dynamical processes, such as plasma convection motion of ions, serve as a particular importance for diffusive states in the topside ionosphere. It is widely accepted to describe the vertical distribution in and above the F<sub>2</sub> region by the effect of diffusion with ion-neutral particle collisions relatively unimportant due to a thin neutral atmosphere in the topside ionosphere.

In 1973, *Banks and Kockarts* introduced three basic diffusive states for the plasma in the topside ionosphere: diffusive equilibrium, which corresponds to (1) no net transport of ionization along the tubes of magnetic force; (2) inward diffusive flow, which is a result of excess plasma pressure at high altitudes somewhere along a magnetic field tube; and, (3) outward diffusive flow, which results from a deficit of plasma pressure at some point along a magnetic field tube. Because of the frequent occurrence of plasma disturbances and large time constants associated with ion flow parameters, only the topside ionosphere at low latitudes ever has the opportunity to reach the state of diffusive equilibrium, while mid to high latitudes experiences prolonged periods of plasma outflow or inflow.

Diffusive equilibrium can be a useful concept when dealing with the topside ionosphere because it may appear to fit the observed plasma density profiles. *Bauer*



[1969] notes such an idealized situation is not advised because it is not a true physical representation of observed physical parameters; however, it can be a powerful analytical model of the topside ionosphere by representing general features. Therefore, we follow this model moving forward in our study.

### 2.3. Chapman Layer

In the 1920s, Sydney Chapman was the first person to introduce a theory for ionospheric layers. The Sun's ionizing photons produce more and more ions as they penetrate deeper into the Earth's atmosphere with rapidly increasing density. Up until the launch of an ionospheric topside sounder satellite known as Alouette I on 29 September 1962, knowledge of the topside ionosphere was based on theory, a few incoherent scatter radar facilities and sporadic high-altitude rocket flights [Jursa, 1985]. Ground-based ionosondes were thought to be only sufficient for a precise determination of the bottomside electron density profile up until  $h_mF_2$ , leading to no information of the topside ionosphere. A global picture of the ionosphere in its entirety was lacking in the scientific community.

A typical fix to this problem was to use a  $\alpha$  – Chapman layer [Banks and Kockarts, 1973b], which only needs  $N_mF_2$ ,  $h_mF_2$ , and scale height values to calculate the topside distribution; see equations 2.1, 2.2, and 2.3. This approach demonstrated some disadvantages associated with the use of a constant plasma scale height and is not tied to any additional measurements [Stankov et al., 2003]. The  $\alpha$  – Chapman layer [Chapman, 1931; Rishbeth and Garriott, 1969; Reinisch and Huang, 2001] adapted for this study (derived in Appendix B) is as follows:

$$N(h)_T = N_m F_2 \exp \left[ \frac{1}{2} (1 - z - e^{-z}) \right], \quad (2.1)$$

where

$$z = \frac{h - h_m F_2}{H(h)_C}, \quad (2.2)$$

and

$$H(h)_C = \frac{k_B T_C}{m g_h}. \quad (2.3)$$

Equation 2.1 is dependent on  $N_m F_2$ ,  $h_m F_2$ , and  $H(h)_C$ , with  $H(h)_C$  dependent on gravity due to height,  $h$ . Gravity at  $h$  above the Earth's surface is calculated by:  $g_h = G m_E / (r_E + h)^2$ , where  $G$  is the universal gravitational constant,  $m_E$  the mass of the Earth, and  $r_E$  the radius of the Earth.  $T_C$ , referred to as the Chapman temperature and  $H(h)_C$ , the Chapman scale height, with scale height discussed in the next section. Lastly,  $m$  is the ionic mass and  $k_B$ , the Boltzmann constant.

*Stankov et al.* [2003], tested topside profilers and found no single method can properly represent the entire spectrum of spatial and temporal variations of the topside ionosphere; however, it was found for nighttime conditions that the Chapman layer gave better results compared to three other methods not discussed here.

#### 2.4. Scale Height

The most important parameter used to describe the vertical structure and regions of the neutral atmosphere is the behavior of temperature with altitude, because this trend reflects the numerous physical and chemical processes at play [*Huang and Reinisch*, 2001; *Stankov et al.*, 2003; *Tulasi Ram et al.*, 2009]. Likewise, electron density is the parameter used to describe the vertical structure of the ionosphere. The way to describe the vertical

structure of electron density in the topside ionosphere is by the scale height. Scale height measures the increase in altitude needed to decrease electron density by a factor of  $e$ . The behavior of electron density in the topside ionosphere was first approximated by a Chapman layer (equation 2.1) and described by a monotonic decreasing function (equation 2.3) [Zolesi and Cander, 2014].

In 1931, Sydney Chapman introduced the scale height parameter, equation 2.3, which has since been adopted in all aeronomic problems relating to the logarithmic gradient of pressure. The density of a constituent in the upper (neutral) atmosphere obeys the hydrostatic equation:

$$N_n m_n g = \frac{dp}{dh} = -\frac{d}{dh} (N_n k_B T_n), \quad (2.4)$$

where there is a balance between vertical gravitational force and thermal-pressure-gradient force on the atmospheric gas. Chapman postulated over a range of altitude considered, the density of the atmosphere varied exponentially, with the first order solution derived in Appendix B and given by:

$$N_e(h_2) = N_e(h_1) \exp \frac{-(h_2 - h_1)}{H}, \quad (2.5)$$

where  $N$  is the electron density at some reference level and  $H$  was a slowly varying function of height known throughout the rest of this dissertation as the vertical scale height (VSH). *Chapman*, [1931], suggested constancy of  $H$  would result if the atmosphere was of uniform composition and temperature, but these conditions are only sufficient and not necessary. According to the different layers composing the atmosphere it was convenient to measure heights in terms of  $H$  as a unit; however, it was acknowledged that the actual values and

variations as a function of height and time at high levels in the atmosphere was uncertain at the time.

Electron density above the peak decreases due to the exponential increase of the diffusion coefficient with a scale height equal to that of atomic oxygen. The variation of electron density with height was found to depend on plasma scale height ( $H_p$ ), which is proportional to the mean plasma temperature  $T_p$ , the average of the electron and ion temperatures  $(T_e + T_i)/2$  [Titheridge, 1973] as shown below and derived in Appendix B:

$$H_p = \frac{2kT_p}{m_i g_h}. \quad (2.6)$$

For the topside ionosphere,  $m_i$  is the mass of atomic oxygen.

## 2.5. Slab Thickness

The ratio of total electron content (TEC) to peak density  $N_m F_2$ , provides the slab thickness parameter:

$$\tau = \frac{TEC}{N_m F_2}, \quad (2.7)$$

where

$$TEC = \int N_e(h) dh. \quad (2.8)$$

TEC is the number of electrons in a column stretching from the receiver at the Earth's surface to a satellite with a cross-sectional area of one square meter [Coster and Komjathy, 2008]. The limits of integration for equation 2.8 is dependent on the signal ray path which ranges from 0 - 20,200 km for GPS and 100 – 784 km for ISR. Subsequent chapters will discuss TEC in more detail.

The slab thickness parameter, which is a convenient one-parameter summary of the electron density profile, can relate a variety of elements of interest that effect the overall electron profile shape, such as the neutral and ionospheric temperatures and gradients, the ionospheric composition, and dynamics [Fox *et al.*, 1991; Stankov and Warnant, 2009]. Because ionospheric slab thickness is related to the shape of the density profile equal to the ratio of TEC to  $N_m F_2$ , it can address many ionospheric phenomena, which has been studied over the last six decades [Bhonsle *et al.*, 1965; Kersley and Hosseinieh, 1976; Huang, 1983; Davies and Liu, 1991; Jayachandran *et al.*, 2004]; however, the physical meaning of this parameter remains unclear. Various studies have proposed relations between  $\tau$  and both neutral temperature and  $O^+/H^+$  transition height [Titheridge, 1973], the scale height of atomic oxygen [Furman and Prasad, 1973], and the mean gradient of electron temperature [Amayenc *et al.*, 1971]; however,  $\tau$  is operationally a very useful parameter that allows a simple conversion between  $f_0 F_2$  and TEC [Fox *et al.*, 1991].

It is well known that the slab thickness relates the shape of the electron density profile; the smaller  $\tau$  is, the sharper the profile [Amayenc *et al.*, 1971]. The plasma temperature,  $T_p$ , affects the overall rate of diffusion which plays a part to which height the peak forms, but the thickness of the ionosphere depends primarily on the temperature of the neutral gas,  $T_n$ , and corresponds to a Chapman layer at a temperature of  $0.87T_n$  [Titheridge, 1973]. A rapid increase in  $\tau$  occurs when there is a rapid decrease in electron density at lower heights. This is described in part to occur near sunrise during the equinox months due to the departure from diffusive equilibrium and the downward movement of the ionosphere when the neutral winds decrease or reverse [Titheridge, 1973].

It has been found that, in general,  $\tau$  depends upon the  $H_p$ , but is not a good indicator of either  $T_e$  or  $T_i$  [Furman and Prasad, 1973]; however, direct proportionality was found between slab thickness and scale height [Amayenc et al., 1971; Huang and Reinisch, 2001].  $T_e$  varies with altitude making it difficult to link strong variations of  $\tau$  with ionospheric temperature variations. Amayenc et al. [1971] used an empirical model and found  $\tau$  and plasma temperature does not have great physical significance, especially during the day; however, it is pointed out that if one knows the electron density from an ionogram below the  $h_mF_2$  and a theoretical model for  $T_i$  is assumed, one can deduce the variation of  $T_e$  in a specified altitude region. While  $\tau$  may not be easily interpreted in terms of neutral or plasma temperatures, neutral wind, or ion composition changes, it has been found that the variations it provides are a good indication of how the broad structure of the electron density profile changes as a function of season, time of day and solar activity [Fox et al., 1991].

## 2.6. Discussion

Previous studies have shown further work is still needed to understand the physical processes behind the behavior of the topside ionosphere. There is insufficient understanding in day-to-day, storm-time variability using the well-known methods for extrapolating topside vertical profiles. For example, 18 March 1990 experienced high geomagnetic activity and ionosondes and ISR simultaneously measured TEC with a significant difference of 30% [Reinisch et al., 2004, Stankov and Warnant, 2009].

It is evident that scale height is a key parameter for a realistic topside representation incorporated into every topside model and used for various practical applications; however,

the fundamental question of the electron density altitude dependence and its intrinsic connection to ionospheric dynamics is yet to be determined. Scale height is derived around the F2 peak region and is assumed to remain constant at all altitudes above the F2 peak; however, the real scale height varies with altitude; so, the assumption of the scale height remaining constant with respect to altitude is possibly only valid within a limited altitude range [Liu *et al.*, 2014]. When the topside profile is modeled using a Chapman function with constant scale height, such a model has no theoretical foundation and is simply a hypothesis and only empirical evidence can be shown to reflect how well the model compares to the actual topside profile [Reinisch *et al.*, 2004]. In fact, the accurate reconstruction of the topside ionospheric electron density profile from ground-based sounders depends purely on the topside profiler model that is applied [Stankov *et al.*, 2003].

Operational slab thickness monitoring could be used to characterize or even predict ionospheric density parameters by a simple conversion between  $N_mF_2$  and TEC; however, these capabilities remain largely unexplored [Stankov and Warnant, 2009]. Presently, scientifically sound validation of the profile extrapolation technique for the topside ionosphere is still missing and may be due to the limited database of measured topside profiles and simultaneously measured bottomside profiles [Reinisch *et al.*, 2004].

Ground-based ionosondes can measure the vertical electron density profile up to  $h_mF_2$ , leaving no direct information on the topside ionosphere [Huang and Reinisch, 2001]; however, the topside ionosphere can be approximated using a Chapman function with a constant scale height,  $H_c$  [Chapman, 1931; Rishbeth and Garriott, 1969; Liu *et al.*, 2007]. It is suggested that the scale heights routinely produced by a global network of digital

ionosondes be statistically analyzed and used for input in the construction of a topside electron density model [*Reinisch et al.*, 2004].

It is clear a study is needed to evaluate day-to-day variations in the ionosphere and how the topside can best be inferred by building off of current theory and instrumentation, as well as some sort of physical interpretations by a scale heights analysis. The two scale height techniques adapted for this study were introduced in section 4 of this chapter. Electron density information allows equation 2.5 to be solved, giving vertical scale height (VSH), terminology adapted from *Lei et al.* [2005], and knowing electron and ion temperatures, equation 2.6 can solve for plasma scale height,  $H_p$ .

Moving forward, the literature review continues in the next chapter by discussing the ionosphere's thermal structure, ionic composition, and electron density formation of the topside ionosphere, which will be the main drivers of our scale height calculations.



## CHAPTER 3

### TOPSIDE IONOSPHERE

#### 3.1. Plasma Temperature

Extensive studies of ionospheric thermal structure began in 1960 at a time when it was common to assume thermal equilibrium ( $T_e = T_e = T_n$ ) was present since the various modes of energy exchange between the neutral and ionized gases were sufficiently rapid [Gerson, 1951]. In 1961, a theory by *Hanson and Johnson* predicted electron temperatures ( $T_e$ ) were hotter than the neutral atmosphere was presented and later confirmed by rocket experiments with plasma probes, as well as incoherent scatter radar (ISR) measurements, which showed disequilibrium between electrons and ions [Banks and Kockarts, 1973]. ISRs have been shown to directly monitor the thermal status of the F region in the upper atmosphere, where plasma temperatures and densities can be used to derive neutral temperature and composition [Oliver, 1979].

Previous studies have found the temperature of the electrons ( $T_e$ ) is higher than that of the ions ( $T_i$ ) and neutrals ( $T_n$ ) in the topside ionosphere under most circumstances. The solar extreme ultraviolet (EUV) flux produces photoelectrons. These photoelectrons act to raise  $T_e$  above  $T_i$  and  $T_n$  with  $T_i$  elevated above  $T_n$  due to the very efficient heat transfer by Coulomb collisions between ions and electrons [Bilitza, 1991]. The initial photoelectron energy and subsequent rise in  $T_e$  is dependent, in part, on the composition and density distribution of the neutral atmosphere [Bauer, 1973].

Photoionization in the topside ionosphere is described by interactions between the neutral O atom and an EUV or X-ray photon (of energy  $hf$ ), which has sufficient energy to detach an electron with the result of a positive ion,  $O^+$ :



Ions and electrons receive thermal energy during this photoionization process and lose thermal energy through collisions, see Figure 3.1 [Banks and Kockarts, 1973b]. Since recombination lifetimes are smaller than timescales required to lose excess thermal energy,  $T_i$  and  $T_e$  are both larger than  $T_n$  above about 300 km.

Photoionization is the principal plasma heat source for the topside ionosphere [Bauer, 1973]; therefore, other sources of heating that may be significant, such as fast

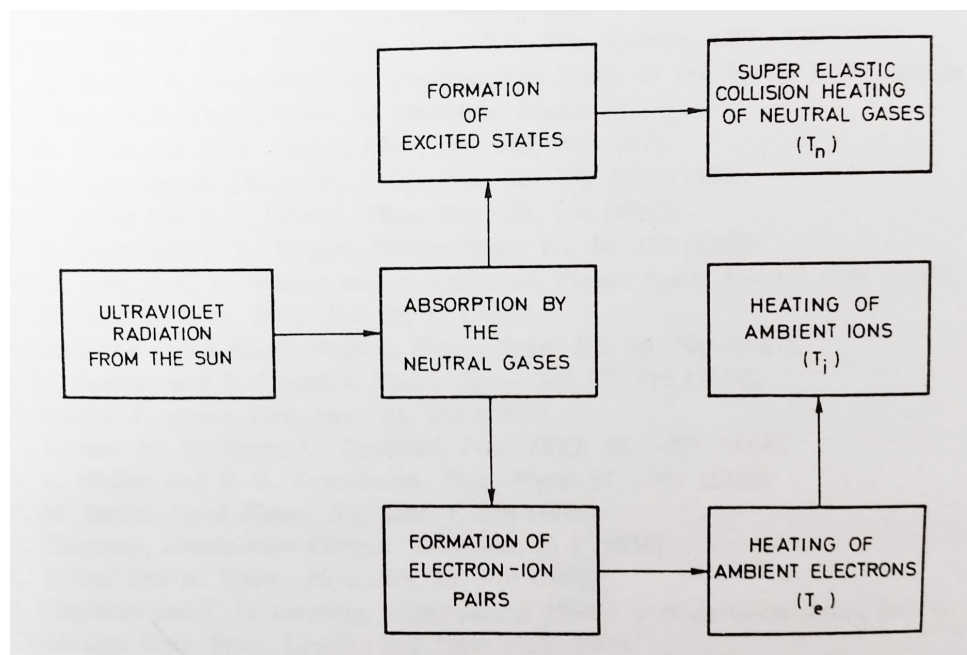


**Figure 3.1.** Energy sources for the electrons, ions, and neutral particles within the ionosphere [Banks and Kockarts, 1973].

streams of electrons in the magnetosphere, Joule heating, and solar wind heating will not be discussed in this study.

### 3.1.1. Diurnal and Solar Variations

Sources of diurnal variations are rapid heat, and at sunrise, ion and electron temperatures increase rapidly, while  $O^+$  is produced by photoionization. After sunset, the ionosphere loses its main source of heating and  $O^+$  decays mostly by reactions with molecular gases. *Sethi et al.* [2003], found large day-to-day seasonal variations in ISR Arecibo  $T_e$  profiles by a study that used 1800  $T_e$  profiles during high solar activity (resolution of 1 minute) and 160  $T_e$  profiles during low solar activity (resolution of 15 minutes). The solar and seasonal effects identified are shown in Figure 3.2 and Figure 3.3, respectively, by using average  $T_e$  profiles.

The profiles used were between local times of 10 - 14 LT for low solar activity and 11 - 13 LT for high solar activity. Due to instrument sensitivity, altitude profiles for low solar activity reach 500 km and for high solar activity, 650 km. This instrument sensitivity can be described by ISR's return signal and its strong dependence on density levels and during solar minimum the ionosphere has less density at equivalent heights compared to solar maximum. In Figure 3.2 it appears that in the topside ionosphere, at 500 km, the average  $T_e$  values seem to be the same for both high solar activity and low solar activity, but the spread of  $T_e$  during high solar activity reaches hotter temperatures by about 300 K. Further, around the F-region peak  $h_mF_2$ , average  $T_e$  varies from 1500K at 250 km and 1400K at 300 km for low solar activity, whereas for high solar activity, 2000K is measured

at 250 km and 1800K at 300 km. This result proves  $T_e$  is highly variable due to solar activity and is altitude dependent.

Interestingly, a noticeable trend is apparent in Figure 3.3: winter  $T_e$  values are hotter during noontime hours, above 200 km for low solar activity and above 350 km for high

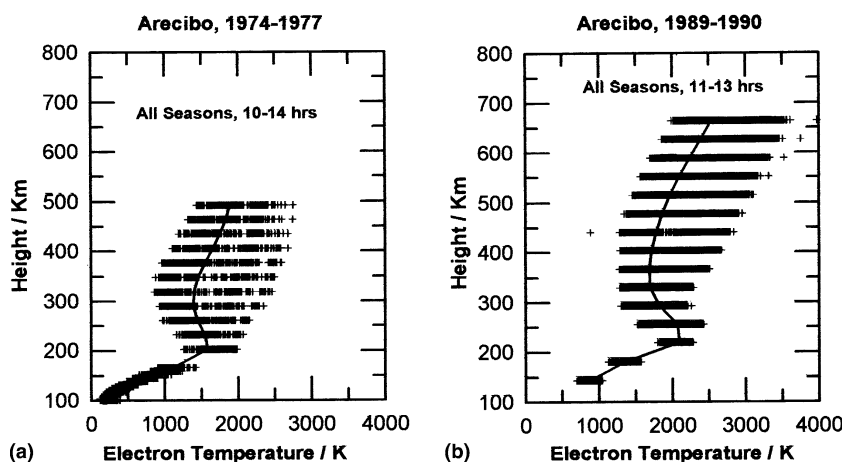


**Figure 3.2.** Observed electron temperatures (+) during low solar activity (a) and high solar activity (b). The solid line the average electron temperature profiles from ISR data at Arecibo [Sethi et al., 2003].

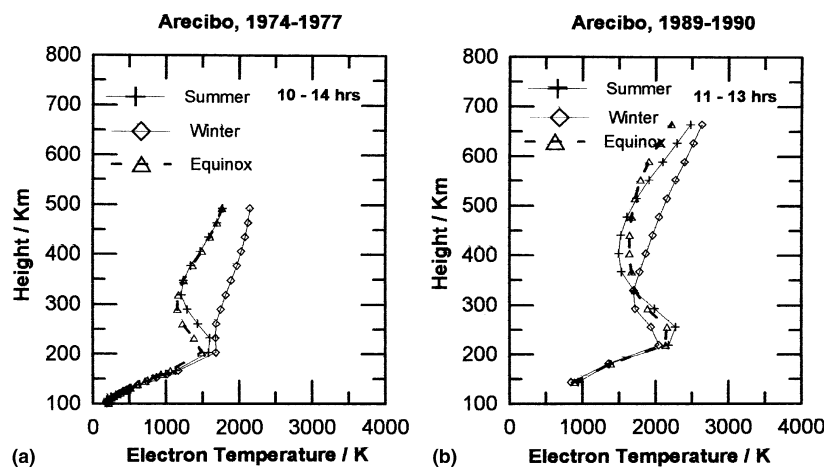


**Figure 3.3.** Observed seasonal midday average electron temperatures during low solar activity (a) and high solar activity (b) from ISR data at Arecibo [Sethi et al., 2003].

solar activity, compared to summer and equinox  $T_e$  values. *Bauer* [1973] points out a lower  $N_e$  concentration at higher altitudes, as seen during winter months, will result in less cooling of electrons because of a net decrease in Coulomb collisions.

*Sethi et al.* [2003] concluded that because  $T_e$  is a complex function of altitude, latitude, season, local time, and solar EUV flux, it is very difficult to accurately separate out the mixed response of  $T_e$ . Their analysis overall showed an increased solar EUV flux is, in part, due to a large increase in solar activity and consequently, sees an increase in  $T_e$  below 350 km, which is not season dependent.

A study conducted by *Zhang et al.* [2004] using French Saint Santin ISR (44.6°N, 2.2°E) observations show diurnal variations in Figure 3.4 for  $T_e$  and  $T_i$  during high and low solar activity. During daytime hours, Figure 3.4 shows there is a large separation of  $T_e$  and  $T_i$  due to the increase in photoelectrons and after sunset, when nocturnal heating dies out, thermal balance between ions and electrons is resumed. Electron cooling effects become

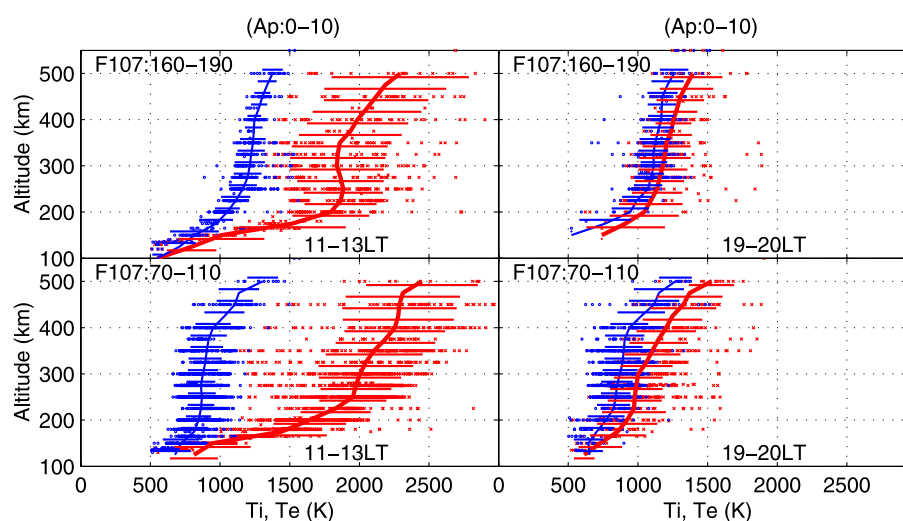


**Figure 3.4.**  $T_i$  (blue circles) and  $T_e$  (red dots) altitude profiles taken at the French Saint Santin ISR. The two local time spans are for high solar activity (top row) and low solar activity (bottom row) levels from 1966 to 1987 [*Zhang et al.*, 2004].

significant at high solar activity due to the enhanced electron density ( $N_e$ ), which is shown by the electron temperature differences in the left, top, and bottom panels of Figure 3.4. *Zhang et al.* [2004] concluded the actual response of  $T_e$  is dependent on background  $N_e$  and to a change in solar EUV, as well as the effects of heat conduction at high altitudes.

### 3.2. Ionic Composition

As introduced, ionospheric plasma is composed of electrons and ions, freed from each other by ultraviolet energy from the sun. In the ionosphere, there are seven major ion species: hydrogen,  $H^+$ ; helium,  $He^+$ ; nitrogen,  $N^+$ ; oxygen,  $O^+$ ; molecular nitrogen,  $N_2^+$ ; nitric oxide,  $NO^+$ ; and molecular oxygen,  $O_2^+$  [*Johnson*, 1966]. Ample amounts of N and O atoms are produced by the photo dissociation of  $N_2$  and  $O_2$  molecules with heavy molecular constituents dominating at low altitudes and the atomic neutrals dominating at higher altitudes [*Schunk and Nagy*, 2009]. Oxygen is second to nitrogen by mass throughout most of Earth's atmosphere; however, the double bonds in molecular oxygen are more easily broken than the triple bonds of molecular nitrogen. Because of this, photoionization of neutral molecules provides the bulk of plasma for the ionosphere and it is well known that atomic oxygen,  $O^+$ , is the dominant species for the F region and the topside ionosphere up until the transition height where the lighter atomic ions, helium and hydrogen dominate, as shown in Figure 3.5 [*Johnson*, 1966].

A generalized daytime ionosphere during solar minimum shown in Figure 3.5, shows ions  $N^+$ ,  $N_2^+$ , and  $He^+$  to play a minor role in ionic composition of the topside ionosphere. As you increase in altitude from the bottomside ionosphere up to the F-region

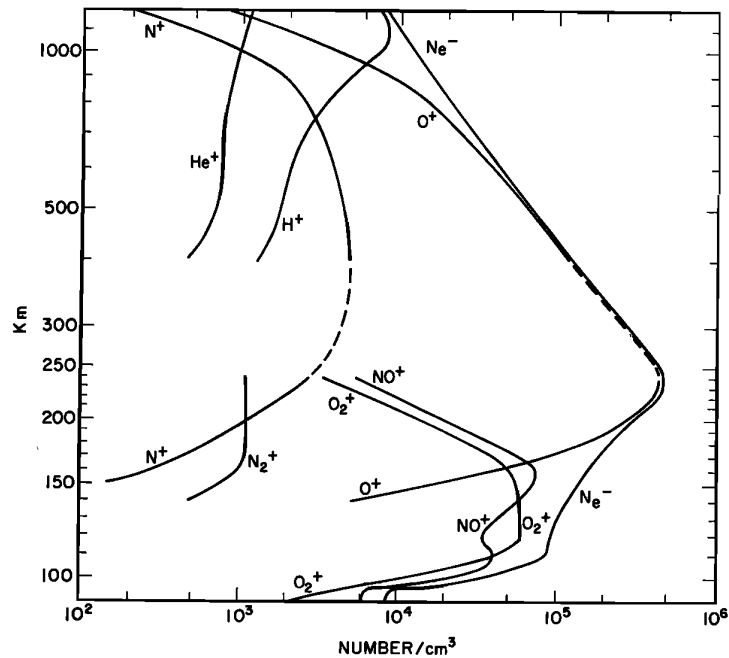


**Figure 3.5.** Ionic composition of the daytime ionosphere during solar minimum. Measurements are from mass spectrometer experiments: Aerobee 150 in 1963 and Electron 2 in 1964 [Johnson, 1966].

peak,  $h_m F_2$ , the ion composition transitions from a combination of several molecules to  $O^+$  atoms at around 180 km. Atomic  $O^+$  continues to dominate until the altitude of 900 km is reached and the dominant ion transitions to  $H^+$ . This transition height between  $O^+$  and  $H^+$  is latitude, season, and solar cycle dependent. According to Figure 3.5, it is safe to assume  $O^+$  as the dominant ion species in the topside ionosphere beginning at 300 km  $\pm$  50 km up to about 800 km, which is the range of altitude focused upon in this research.

### 3.2.1. Diurnal Variations

Measurements from the Atmosphere Explorer E (AE-E) satellite were used by Gonzalez *et al.* [1992] to determine seasonal average behavior of ion concentrations,  $O^+$ ,  $He^+$ , and  $H^+$  and their diurnal behavior near Millstone Hill, shown in Figure 3.6. Because

these observations were made at Millstone Hill, the results are highly relevant to our study. The  $O^+/H^+$  transition altitude was found between 750 and 825 km during the day and between 550 and 600 km at night with  $He^+$  being a minor species at all altitudes and  $H^+$  varying little in concentration with season. This is especially important to consider when calculating scale heights for the topside ionosphere, considering the ion mass is a major contributing factor.  $O^+$  is widely recognized as the controlling ion species for the topside ionosphere up until approximately 800-1000 km, so if the transition altitude of  $O^+/H^+$  dips below 800 km, one can expect to see contamination in scale height calculations. For this reason, scale height calculations using  $O^+$  as the controlling ion species should choose the altitude range slightly above the F2 peak up until 550 km.

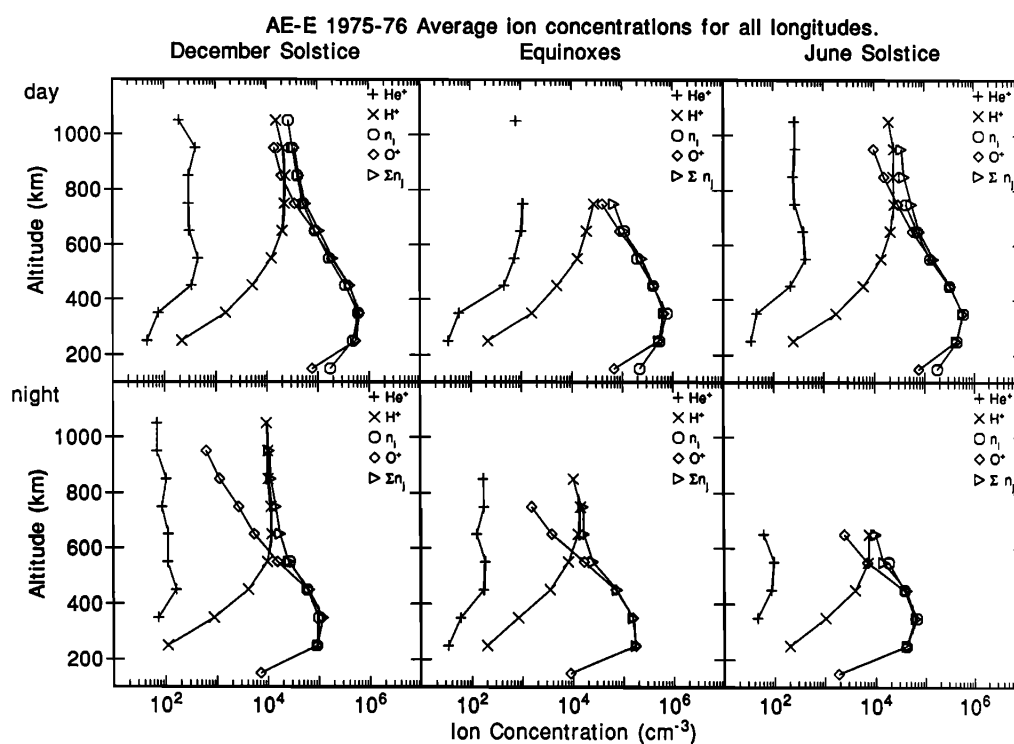


**Figure 3.6.** Daytime (top row) and nighttime (bottom row) averages of the major and minor ions in the topside ionosphere measured during different seasons [Gonzalez *et al.*, 1992]. Helium is represented by (+), hydrogen by (x), ion density,  $n_i$  by (o), and oxygen by ( $\diamond$ ).



### 3.3. Electron Density

High-energy ultraviolet radiation from the sun removes electrons from some of the atoms and molecules in the ionosphere with the density of the electrons ranging from about 10,000 to 1,000,000 per cubic centimeter [Haystack, 2016]. A large electron density is often associated with a large rate of ionization, resulting in the generation of more photoelectrons, which lose their energy to ambient electrons through elastic collisions and to neutrals through inelastic collisions [Zhang *et al.*, 2004]. The electron density is highest in the F region at the peak height of  $h_m F_2$  and peak value of  $N_m F_2$  with the F region existing during both daytime and nighttime.

ISRs are proven instruments for measuring electron content in the ionosphere since the scattering efficiency of high-frequency radio waves scattered from an electron is well known. An ISR measures the number of electrons in the scattering volume by the strength of the radar echo received from the ionosphere [Haystack, 2016]. There is a caveat using an ISR to produce ionospheric density profiles, though, due to the calibration needed with local ionosonde measurements. ISRs use a calibration factor into the radar equation that relates radar signal temperature to electron density. For Millstone Hill, this calibration constant is determined by direct comparison of high-elevation measurements of signal temperature from the F-region peak with University of Massachusetts Lowell ionosonde measurements of peak electron density [Madrigal, 2017].

GPS dual-frequency measurements were discovered early on as a way to measure the ionospheric TEC at multiple locations [MacDoran, 1979]. TEC was introduced in Chapter 2 as an integrated column level of ionospheric density over a specific location and

is often summarized by a TECU ( $10^{16}$  electrons/m<sup>2</sup>). In the Earth's ionosphere, TEC can range from 5-120 TECU and is dependent on local time and geomagnetic activity [Knipp, 2011].

ISR and the ionospheric radio occultation method using navigation satellites, such as GPS, are well established as being powerful sensing methods to obtain key information about the topside ionosphere [Schreiner *et al.*, 1999]. Radio occultation methods were developed in the early 1960s by science teams from Stanford University and the Jet Propulsion Laboratory (JPL) to probe the atmosphere and other properties of Mars using data from the NASA Mariner 3 and 4 spacecraft [Fjeldbo, 1964]. It was not until the 1980s when techniques were devised for geodesy and submitted by JPL for the first GPS occultation proposal to NASA in 1988, but the GPS Geoscience Instrument was cut from NASA's budget in 1993 and did not fly [Yunck *et al.*, 2000]. The concept was established; however, and the University Corporation for Atmospheric Research (UCAR) saw the promise of GPS occultation and conceived the GPS/MET experiment, sponsored by the US National Science Foundation and was launched by a Pegasus rocket into low-Earth orbit aboard NASA's MicroLab I spacecraft in 1995 [Ware *et al.*, 1996]. Because of the substantial success of GPS/MET, COSMIC was launched in 2006 as a joint effort by UCAR and Taiwan's National Space Organization, and was the first operational GPS occultation constellation that refined the systems and techniques of GPS sounding [Yunck *et al.*, 2000]. Due to the pioneering science teams at JPL, Stanford, and UCAR, we now have the capabilities to generate profiles of Earth's electron density profiles using GPS occultation data.

ISR is a small volume measurement, while GPS is a line integral between the receiver and transmitter of the electron density. In the context of the ionosphere, the Abel transform method is a radio occultation inversion technique that allows retrieving electron densities as a function of height from STEC (Slant Total Electron Content) [Aragon-Angel *et al.*, 2009]. These measurements are derived from carrier-phase observations based on precise carrier dual-frequency phase measurements (L-band) of a GPS receiver onboard a low-Earth orbit satellite tracking a rising or setting GPS satellite behind the limb of the Earth [Schreiner *et al.*, 1999]. One can obtain information about the vertical refraction index by means of inversion techniques, which can then be converted into ionospheric vertical electron density profiles and/or neutral atmospheric profiles [Aragon-Angel *et al.*, 2009]. This is one technique to retrieve electron density profiles; however, the global Abel retrieval error has not been quantified due to lacking comparisons between ionosondes and ISR observations [Yue *et al.*, 2010], hence justifying why we do not chose this method to generate electron density profiles.

### **3.3.1. Diurnal Variations**

Typical nighttime and daytime variation in electron density profiles are shown in a study by Kelley *et al.*, [2009]. An ISR located at Arecibo Observatory ran continuous for 160 hours, known as a World Day period, which allowed radar data to be compared with occultation measurements GPS signals received by the COSMIC/Formosat receivers. The results are shown in Figures 3.7 and 3.8. ISR data was normalized using a local ionosonde and GPS occultation-based profiles using the Abel transform method developed independently at UCAR and JPL [Kelley *et al.*, 2009]. The results shown correspond to

two consecutive passes of the COSMIC constellation on 30 June 2006 during the development of an ionospheric storm.

Figure 3.7 shows F-region profiles during daytime hours while Figure 3.8 shows profiles during nighttime hours. Both Figure 3.7 and 3.8 show differences between the JPL and UCAR products when deducing F-region profiles from occultations, which show that data processing methods are not totally straightforward. *Kelley et al.*, [2009] found daytime hours appear in better agreement between the two methods and with the ground

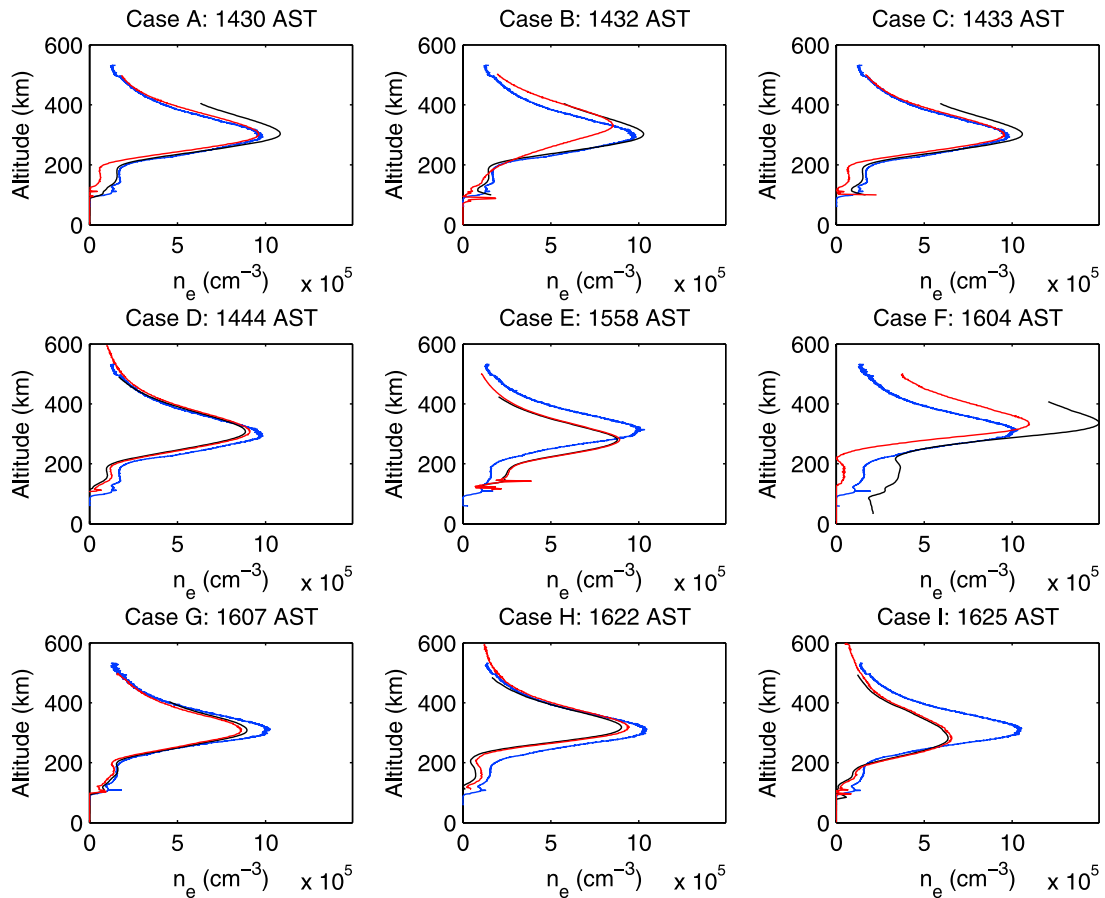


**Figure 3.7.** Nine daytime comparisons between the two Abel inversions of the occultation data (red is UCAR, black is JPL) and the Arecibo-determined density profiles (blue). AST stands for Atlantic Standard Time for which  $\text{UT} = \text{AST} + 4$ . [*Kelley et al.*, 2009].

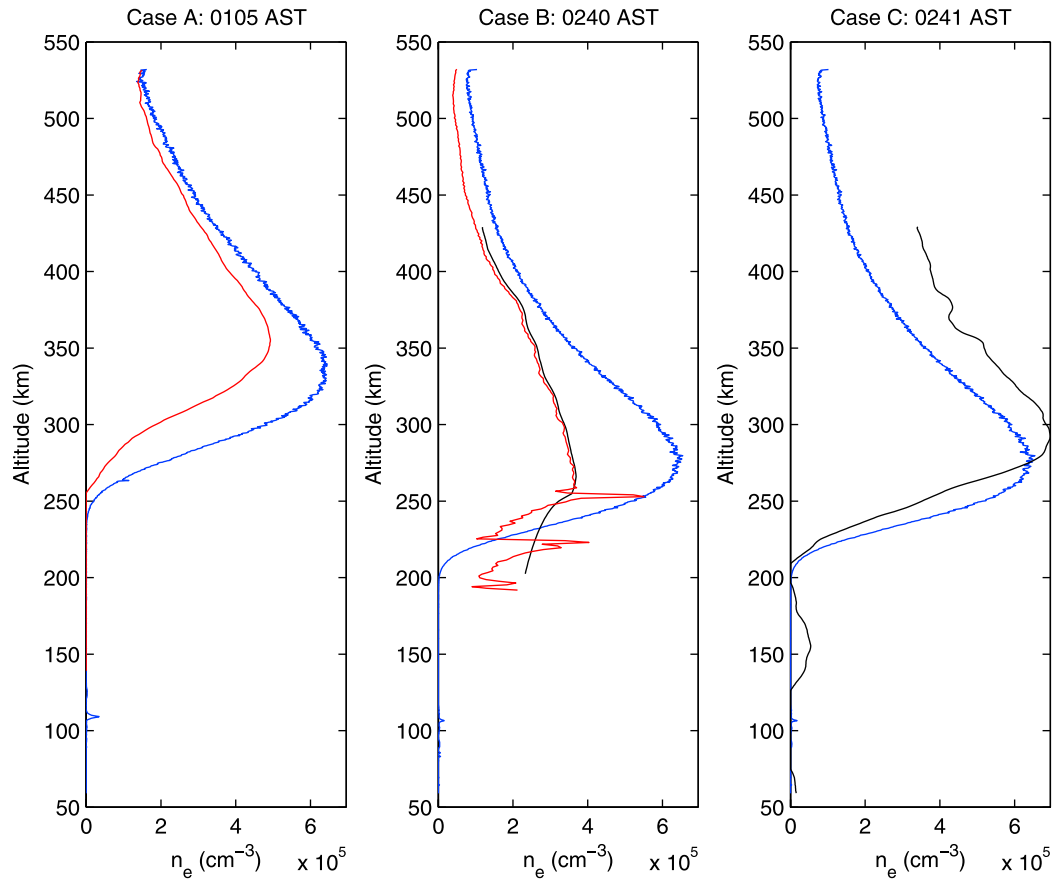


**Figure 3.8.** Three nighttime comparisons between the two Abel inversions of the occultation data (red is UCAR, black is JPL) and the Arecibo-determined density profiles (blue). AST stands for Atlantic Standard Time for which  $UT = AST + 4$ . [Kelley *et al.*, 2009].

truth at Arecibo compared to nighttime hours. It is also suggested these profiles are reasonably accurate, given the distances from Arecibo and the long horizontal tracks involved from GPS to receiver. In terms of geomagnetic variations, Kelley *et al.*, [2009] found the mid-latitude ionosphere to react strongly to a moderate magnetic storm, Kp value equal to four, with the daytime density decreased by a factor of two.

Another study showing electron density profile variations throughout the day was conducted by Lei *et al.* [2007]. Figure 3.9 shows the results using COSMIC satellite data

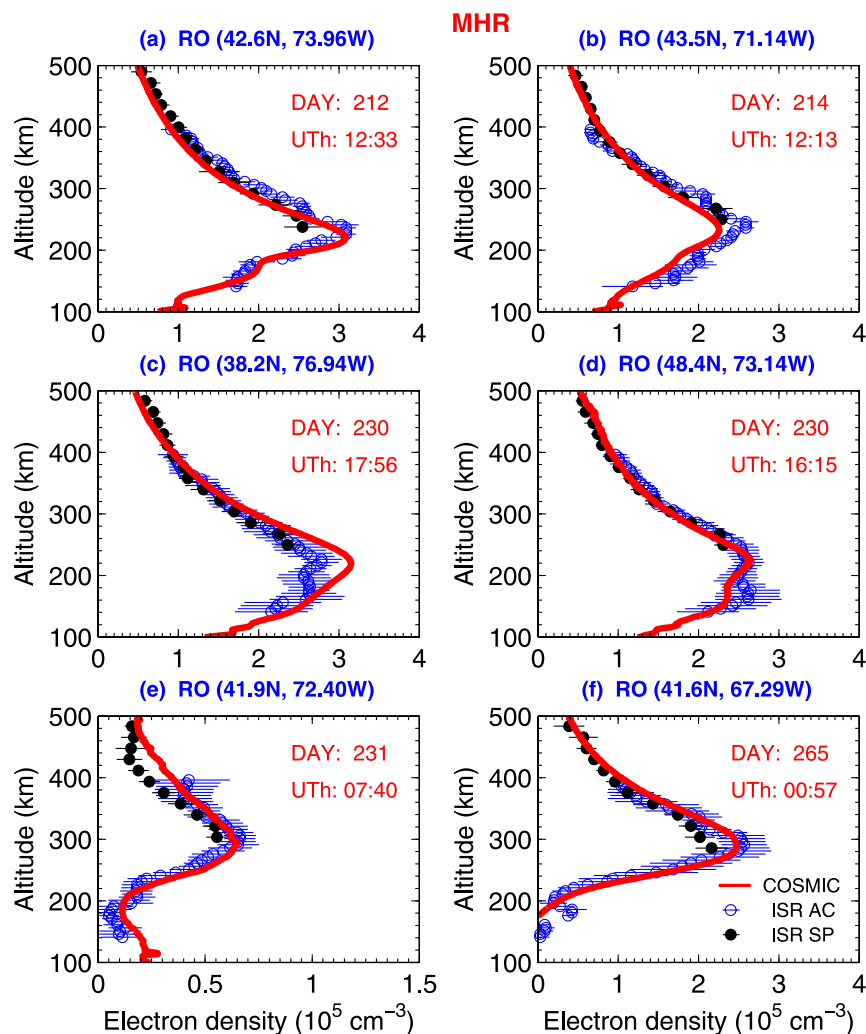


**Figure 3.9.** (a-f) Solid lines show COSMIC electron density profiles compared to those measured at Millstone Hill incoherent scatter radar. Days include July (212), August (214, 230, 231), and September (265) 2006. ISR AC stands for alternate code data, and ISR SP stands for single-pulse data [Lei *et al.*, 2007].

and ISR data at Millstone Hill over a handful of summer days. The top row (a and b) of Figure 3.9 shows the hours just after sunrise with  $h_m F_2$  at about 230 km, the middle row (c and d) around noon with  $h_m F_2$  around 230 km, but a wider peak and signatures of the E-layer bump, the bottom row (f) just after sunset,  $h_m F_2$  is around 280 km, and (e) well into nighttime hours,  $h_m F_2$  is at 300 km. The physical interpretation of this is well understood

[Titheridge, 1968]. At nighttime, the F-region loses its source of radiation and sees a change in electron flux balance between the plasmasphere above and recombination below, which subsequently results in upward movement of the F-region peak,  $h_mF_2$ .

### 3.4. Discussion

This chapter discussed the thermal structure, ionic composition, and electron density profiles found in the topside ionosphere, as well as their respective diurnal variations, which we expect to see reflected in our study. We also expect to see the proven anti-correlation of said characteristics between plasma temperature and electron density in the topside ionosphere [Bauer, 1973; Knipp, 2011], which may be useful to consider in terms of solar variance. This anti-correlation can be described by an increase in topside  $N_e$  will lead to an enhanced electron cooling rate by Coulomb collisions, proportional to  $N_e^2$ , which may lead to a lower  $T_e$  [Zhang *et al.*, 2004; Sharma *et al.*, 2008]. Also, as the solar activity increases, temperature of the ions increases at low altitudes following the corresponding  $T_n$  changes, and at high altitudes, due to increased energy transport from electrons [Zhang *et al.*, 2004].

Understanding the complexities between the thermal structure, ionic composition, and electron density found in the topside ionosphere is important for a simple model to represent how the electron density of the topside ionosphere decreases exponentially with height [Jursa, 1985]. Chapter 2 named the exponential decrease in electron density as the scale height. Thermal energy ( $k_B T$ ) is the dominating variable when calculating plasma scale height,  $H_p$ , and density is the dominating variable when calculating vertical scale height, VSH. As discussed in this chapter, the temperatures and densities of plasma depend

on several contributing factors; neutral atmosphere, ionization, recombination, local heating, transport processes, diffusion, conduction, electric field, neutral winds, and geophysical conditions.

The combination of in situ observations from satellites (GPS) with ground-based experiments (ISR and ionosondes) can provide a wealth of information for temperature and density measurements and consequently, extensive studies highlighted by *Sethi et al.* [2003], have been carried out to understand the physics of the low and mid-latitude ionosphere over the last several years. The issue with the instrumentation used to characterize the topside ionosphere is ground-based ionosondes can probe only up to the F-layer peak height giving only information about  $h_mF_2$  and  $N_mF_2$ , therefore, observational data of the topside ionosphere is lacking since topside sounders and ISR are very sparse. ISR provide full ionospheric profiles, but are expensive and not feasible for extensive, day-to-day monitoring. Bottomside ionosphere physics and chemistry is very different from topside physics and chemistry so moving forward, this study addresses the question of whether or not one can deduce topside physics and chemistry by obtaining bottomside ionosonde data and TEC by GPS satellite data. The history and methodology in regards to the combined use of ionosondes, a Chapman layer and *in situ* observations from satellites to profile the ionosphere is given in detail by *Liu et al.* [2014] and our adaption and contributions to this technique are described in subsequent chapters.

Moving forward, the analysis of ISR data collected from Millstone Hill begins in Chapter 4. The expected key trends in the subsequent topside ionosphere analysis over Millstone Hill Observatory found in this chapter are as follows:



- During daytime hours, there is a large separation of  $T_e$  and  $T_i$  due to the increase in photoelectrons. During nighttime hours, when nocturnal heating dies out, thermal balance between ions and electrons is resumed; therefore,  $T_e$  is expected to be the largest driver for plasma scale height calculations during the daytime.
- Atomic oxygen,  $O^+$ , is the dominant species for the F<sub>2</sub> region, 300 km +/- 50km up until the transition height where  $He^+$  and  $H^+$  dominate; therefore, scale height calculations using  $O^+$  as the controlling ion species will use an altitude range slightly above the F2 peak up to 550 km to avoid any data contamination caused by a lower transition height.
- The electron density profile is highly variable in terms of solar activity and time of day, driven by photoelectrons produced by solar EUV radiation.
- Changes in plasma temperature will dominate plasma scale height calculations (equation 2.6) and changes in electron density structures will dominating vertical scale height calculations (equation 2.5). Both temperature and density are dependent on several contributing factors in the topside ionosphere.

## CHAPTER 4

### MILLSTONE HILL STUDY

#### 4.1. Introduction

This chapter begins the analysis of ISR data collected from Millstone Hill Observatory (42.6°N, 288.5°E), a subauroral, mid-latitude site in North America. The location selected for this study was chosen due to the readily available data from Millstone Hill's ISR, and local ionosonde and GPS receiver data. The ionosonde and GPS data gathered for this study will be discussed in Chapter 6.

In 2002, Millstone Hill collected continuous data for 32 days with a 68 m zenith antenna, a data integration time of four minutes, and an altitude resolution of 4 km. This experiment used a single pulse mode with a pulse length of  $4.80 \times 10^{-4}$  seconds interleaved with an alternating code to measure ionospheric parameters [Zhang *et al.*, 2005]. Data collected from 4 October to 4 November provides a unique opportunity to study ionospheric variability during a time of solar variation covering both geomagnetically active and quiet periods [Zhang *et al.*, 2005, Lei *et al.*, 2005]. ISR data is collected by the Thomson backscatter technique [Thomson, 1906] using ionospheric electrons to deduce height and time resolved plasma drift velocities, electron, ion and neutral temperatures ( $T_e$ ,  $T_i$  and  $T_n$ ), electron densities ( $N_e$ ), ion composition, and ion-neutral collision frequencies.

For this study, an ISR dataset of approximately 696 hourly altitudinal profiles of  $T_e$ ,  $T_i$ ,  $T_n$ , and  $N_e$  across 29 days, was collected from a continuous observation data campaign conducted in October 2002, and subsequently analyzed. We acknowledge the assistance of Dr. John Foster, principal research scientist at the Massachusetts Institute of

Technology, for data provided to Michael David, a USU Center for Atmospheric and Space Sciences (CASS) Research Technician in a convenient format. Millstone Hill data used in this study are available to the public through the URL [<http://madrigan.haystack.mit.edu/madrigan/>]. The Madrigal-distributed database system is operated by MIT Haystack Observatory under support of NSF grant AGS-1242204. Observations at Millstone Hill in 2002 were supported by NSF Cooperative Agreement ATM-9714593 with the Massachusetts Institute of Technology. We would also like to acknowledge Dr. Phil Erickson, Assistant Director of Massachusetts Institute of Technology's Haystack Observatory for providing the above proper citation in regards to using this dataset.

This chapter is separated into two parts: previous Millstone Hill statistical studies and our interpretation of the campaign observations over Millstone Hill.

## **4.2. Previous Millstone Hill Statistical Studies**

This chapter begins by highlighting the conclusions and shortfalls of previous statistical studies using the same Millstone Hill data campaign, as well as the methodology adapted moving forward in this study.

### **4.2.1. Zhang et al., 2005**

One of the first papers to assess data from Millstone Hill's campaign and its potential for long-term theoretical validation and testing was completed by *Zhang et al.* in 2005. The paper mainly focused on day-to-day variations in the ionosphere, shown in Figure 4.1, and a quick overview of the associated dynamics.

The top three rows of Figure 4.1 show the corresponding solar and geomagnetic indices for the entire data campaign. Those indices include the daily solar 10.7 cm flux (F10.7), hourly Dst index, and three-hourly Ap index. Three separate magnetic disturbances are identified on days 280, 287, and 297 with sharp drops in Dst, a rise in F10.7 and Ap and associated recovery periods lasting 12 hours and up to one day. A geomagnetically quiet reference day 294 was identified due to stable F10.7 values over a three-day period and corresponding low magnetic activity values of Dst and Ap. This quiet reference day was also adopted in our study.

The bottom portion of Figure 4.1 shows the ionospheric parameters of ion velocity ( $V_o$ ),  $T_e$ ,  $T_i$ , and  $N_e$ . The day-to-day variability is clearly seen, even under quiet magnetic conditions for  $N_e$ ,  $T_i$ , and  $T_e$ , with changes occurring during local time and in height. The largest variability is seen in  $N_e$  and the smallest in  $T_i$ . Also, variability increases with height in  $N_e$  and  $T_i$ ; however,  $T_e$  variability was relatively large slightly above the F peak. Finally, it appears the daytime hours offered the largest variability in the ionosphere. Because the same days are used in our analysis we can expect to see the same behavior in the ionospheric parameters.

The study done by *Zhang et al.* [2005] also offered to describe the ionospheric variability as a result of long-period ionospheric oscillations and continued to examine such oscillations by using a statistical approach with 24-hour averages. TIMED satellite flyovers at Millstone Hill correlated some of these oscillations with changes in the neutral composition originating from geomagnetic activity, which may have altered the global atmospheric circulation as a result of high-latitude heating processes. It is suggested the

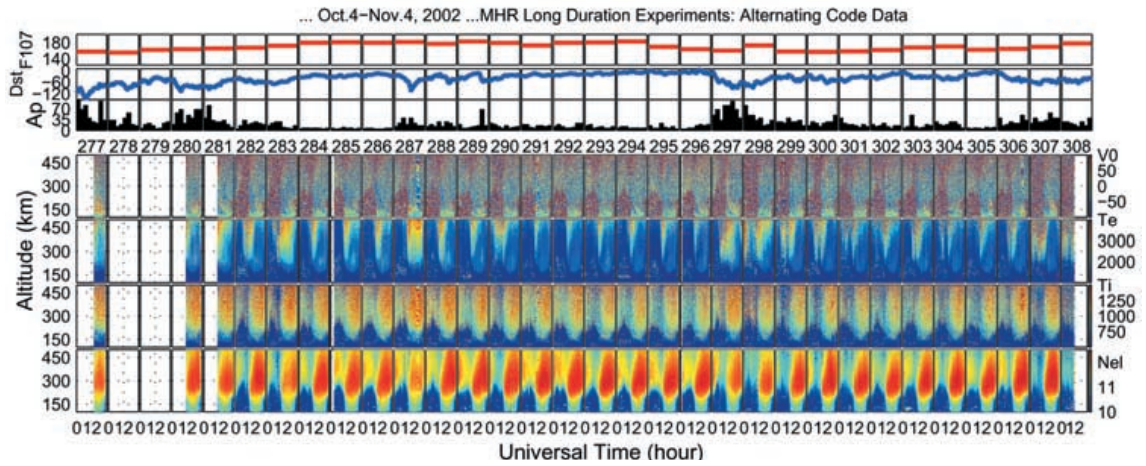


**Figure 4.1.** Data from Millstone Hill's 4 October - 4 November 2022 data campaign. Solar geophysics indices shown: daily solar 10.7 cm flux F107, the hourly Dst index, and the three-hourly ap index. Ionospheric indices shown from the alternating code: electron density, Ne ( $\log_{10} \text{ m}^{-3}$ ), Ion and electron temperatures, Ti and Te (K), and vertical ion velocity, Vo (m/s) [Zhang *et al.*, 2005].

appearance of high  $T_i$  over Millstone Hill could be caused by the precipitating particles enhancing the localized electric fields, such as the Sub-Auroral Polarization Stream associated fields, which were studied by Foster and Vo [2002].

#### 4.2.2. Lei *et al.*, 2005

Lei *et al.* [2005] conducted an extensive study at Millstone Hill covering two solar cycles, including this data campaign, investigating temporal variations in electron density. Electron density profiles were fit to a simple Chapman layer where photoionization is assumed to be a one-species neutral gas ( $\text{O}^+$ ) and transportation processes are ignored. Peak parameters,  $h_m F_2$  and  $N_m F_2$  are derived from the ISR profiles and local ionosonde measurements, as well as the scale height, H. It is noted in this study that a Chapman layer used to fit the ISR profiles and subsequent scale height values do not represent the actual physics of the F layer.

The results of the scale height analysis by *Lei et al.* [2005] is shown in Figure 4.2. There is an apparent effect on scale heights due to seasons, solar activity, and time of day. All seasons, except for summer, see a diurnal variation with a significant dip in scale height values around sunrise followed by a steady increase in values throughout the day. For purposes of our study, we are only concerned about the dashed Autumn line and can expect to see similar patterns in scale height. Values of scale height appear to have a factor of two increase during high solar activity when compared to low solar activity.

This paper speculates that the topside effective scale height (calculated with electron density) is a good measure of the plasma temperatures and that it should be somehow related to the plasma scale height because the topside profile shape is dependent on plasma diffusion; however, this relationship is not explored leaving the question of whether or not you can infer one or the other from temperature or density profiles. We expect to address this question in our analysis.

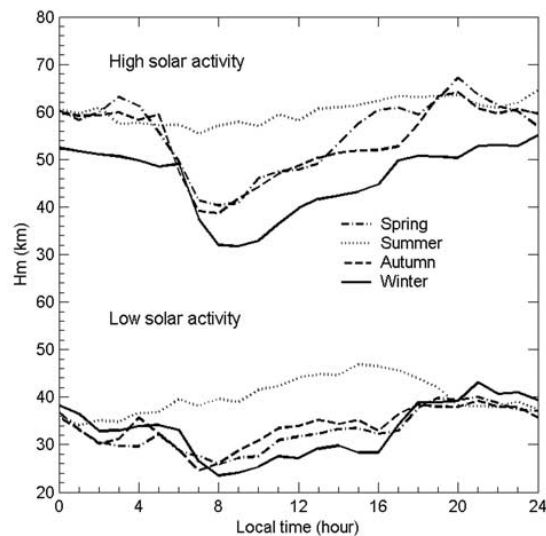


**Figure 4.2.** Variations of scale height according to season, time of day, and solar activity [*Lei et al.*, 2005].

### 4.2.3. Liu et al., 2007

A statistical study using data from the 2002 Millstone Hill data campaign was conducted by *Liu et al.* [2007]. Three techniques for calculating scale height are used, but only two will be given an overview for the purpose of our study; vertical scale height (VSH) calculated by gradients in electron density, and plasma scale height ( $H_p$ ) calculated using plasma temperature,  $(T_e + T_i)/2$  information. Both VSH and  $H_p$  equations were introduced in Chapter 2 of this dissertation as equation 2.5 and 2.6, respectively. The median values for 30-days served as the reference level for this study and is shown in Figure 4.3 with the corresponding upper and lower quartiles during the ISR experiment *Liu et al.* [2007].

There is a clear average pattern of ionospheric scale heights shown in the right side, middle two panels of Figure 4.3 for VSH and  $H_p$ ; however, the diurnal behaviors of the median values in both VSH and  $H_p$  are not tightly correlated, suggesting a disconnect between density scale heights and plasma temperatures. The largest variations between VSH and  $H_p$  occur during predawn local hours (2 – 6 LT) where VSH values approach 200 km and  $H_p$  values fluctuates around 150 km then climb to 200 km by 7 UT. Perhaps the most interesting part of Figure 4.3 is the ratio of VSH and  $H_p$  (right side), which differ diurnally. VSH values are shown to be larger during nighttime hours and  $H_p$  values larger during daytime hours.

This study produced interesting results, but with several limitations. It is explicitly stated that profiles not fitting their least-squares procedure for median topside ionospheric electron density profiles were discarded even though they may have represented actual situations. Also, the altitude ranges used to determine  $H_p$  and VSH differed; ( $h_mF_2$  to  $h_mF_2$

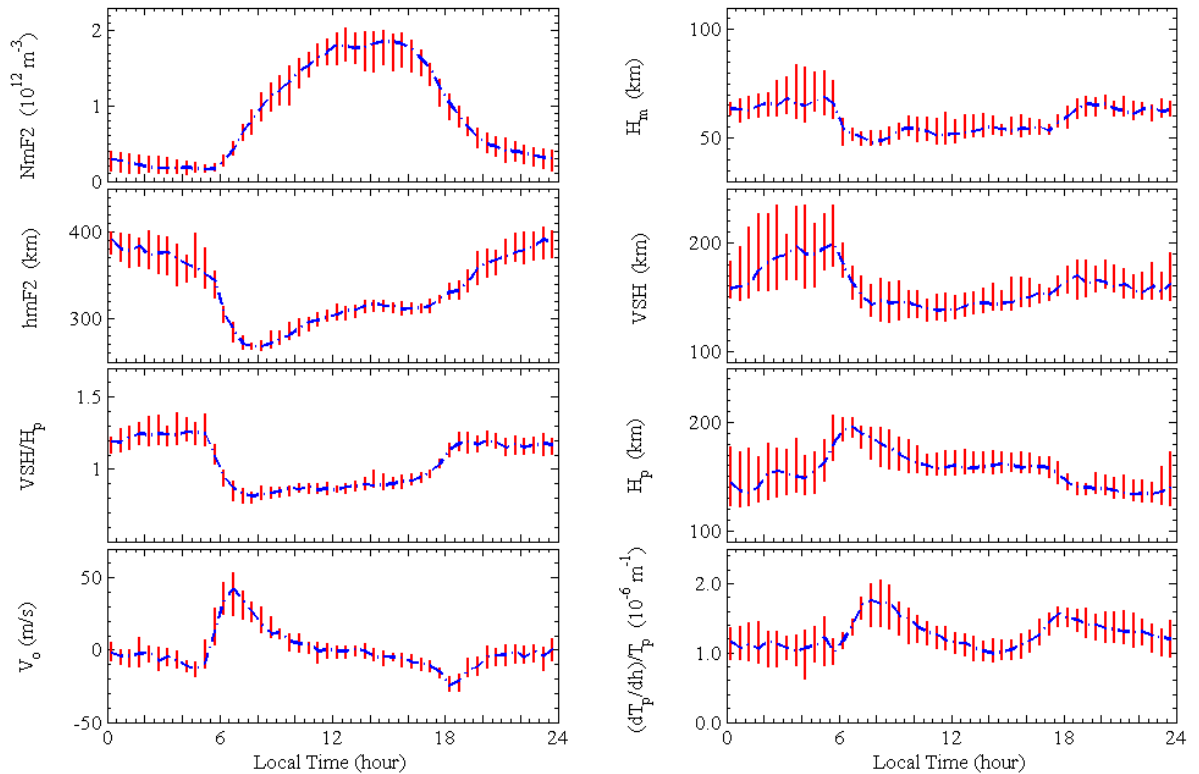


**Figure 4.3.** Campaign results of observed ionospheric parameters. Results include observed  $N_mF_2$ ,  $h_mF_2$ , ratio of vertical scale height (VSH) to plasma scale height ( $H_p$ ), line-of-sight velocity  $V_o$  (around 500 km), Chapman scale height ( $H_m$ ), VSH,  $H_p$ , and plasma temperature relative gradient  $(dT_p/dh)/T_p$ . The blue dashed lines represent half-hourly median values and the corresponding upper and lower quartiles are shown in the vertical red lines. This Figure is by *Liu et al.* [2007] and is licensed under [CC BY 3.0](https://creativecommons.org/licenses/by/3.0/), which does not require permission for reuse.

+200 km) for  $H_p$  and ( $h_mF_2 + 25$  km to  $h_mF_2 + 250$  km) for VSH, which may cause significant issues in comparisons.

*Liu et al.* [2007] found evidence suggesting that both contributions from the temperature structure and diffusion processes can greatly control the shape of electron density profiles in the topside ionosphere over Millstone Hill. It is concluded that despite several decades of study, the knowledge of the behavior of the ionospheric scale heights



remains insufficient and recommends further studies are needed to better understand the complexity of the major impact geomagnetic activity can have on the behavior of topside ionospheric scale heights [Liu *et al.*, 2007].

### **4.3. Campaign Observations**

This section begins the second half of Chapter 4. A discussion of our interpretation in regards to the campaign observations over Millstone Hill during the 2002 data campaign will be given.

#### **4.3.1. Solar Conditions**

As pointed out by *Zhang et al.* [2005], the 2002 data campaign at Millstone Hill offers a unique opportunity to study the ionosphere under solar variations, because the period of observation saw both geomagnetically quiet and active periods. Solar indices, solar radio flux F10.7 (daily averages), planetary K-index, Kp\*10 (three-hour averages) and Dst (hourly averages) are shown in Figure 4.4 and defined in Appendix A. Data for Figure 4.4 was extracted from NASA/GSFC's OMNI data set through OMNIWeb [<https://omniweb.gsfc.nasa.gov/>]. Figure 4.4 shows Kp\*10 ranged from 7 to 63 units with three obvious peaks circled in orange around days 281, 287, and 297. Sharp drops in Dst followed by a recovery period correlated with spikes in Kp\*10 are apparent signatures of solar storms and substorms, respectively. The variations between F10.7 were 155.1 to 181.4 units with a 29-day average of 168.4 units. A severe geomagnetic storm was initiated on day 297 as mentioned by *Zhang et al.* [2005], highlighted in Figure 4.4 by the red oval, and will be considered as the reference active day in this study. The ionosphere was disturbed for about 30 hours.

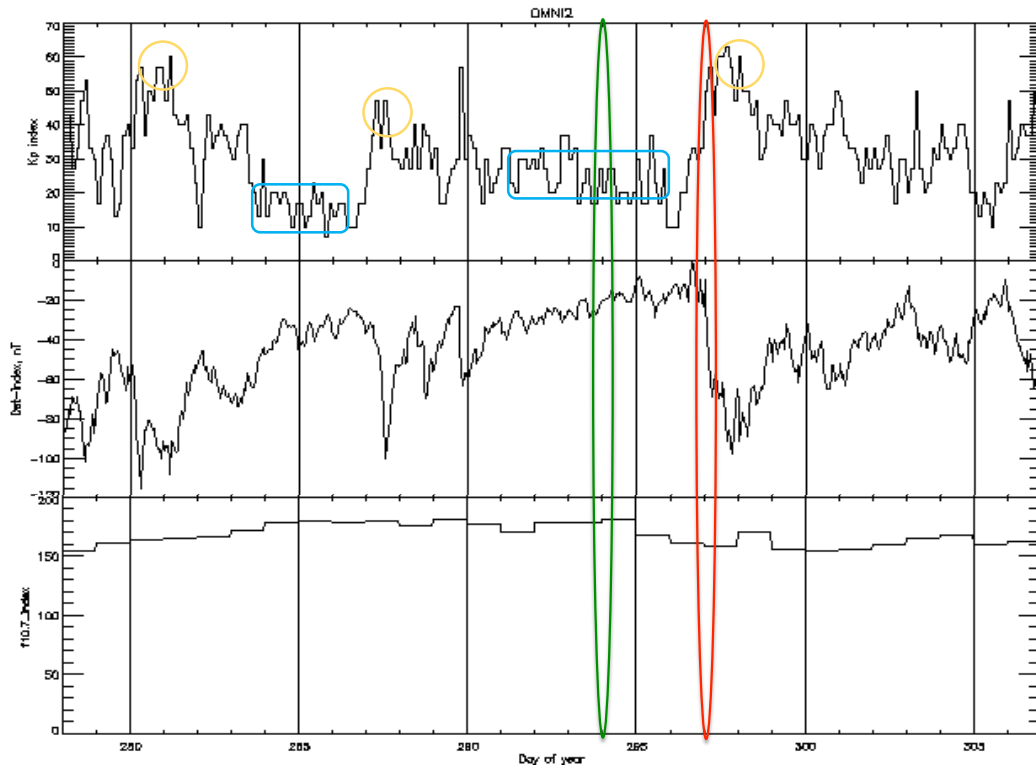


**Figure 4.4.** Solar geophysical conditions between 5 October (day 278) and 2 November (day 306), 2002. Results were extracted from NASA/GSFC's OMNI data set through OMNIWeb. Solar indices are the three-hourly Kp\*10 index and daily solar 10.7 cm radio flux F10.7 from NOAA's National Geophysical Data Center, and the hourly Dst index computed at and obtained from the World Data Center for Geomagnetism, operated by the Data Analysis Center for Geomagnetism and Space Magnetism at Kyoto University, Japan. Quiet reference day 294 is highlighted in green and the severe ionospheric storm, day 297, by red. The orange circles represent the Kp\*10 peaks and the blue boxes represent the quiet Kp\*10 periods.

There are two noticeable quiet periods over the 29 days, day 286 and day 294 shown in Figure 4.4 by the blue boxes. A quiet period is considered when Kp\*10 values are consistently low for two to three days, there are no sharp drops in Dst, and steady F10.7 values. Day 294 is chosen to be a good reference day for quiet geophysical conditions, since the quiet period surrounding day 294 is a day longer compared to the quiet period

around day 286. It also keeps consistent with the previous analysis by *Zhang et al.* [2005]. Day 294 is highlighted by the green oval in Figure 4.4.

#### 4.3.2. $N_mF_2$ and $h_mF_2$

Using collected ISR data over the 29-day data campaign conducted at Millstone Hill, the peak electron height,  $h_mF_2$ , is shown in Figure 4.5 and peak electron density,  $N_mF_2$ , shown in Figure 4.6. Both Figures 4.5 and 4.6 are separated into four panels, which consist of about seven days each for simplicity. Local daytime hours range from 10 - 22 UT and nighttime hours from 22 – 10 UT. It must be noted that the first few days; namely, 278 - 280, of the dataset had several data gaps in the early morning hours and may not display actual ionospheric conditions.

The overall diurnal variations in both Figures 4.5 and 4.6 are apparent. For local daytime hours, there is a broad  $N_mF_2$  peak beginning at 11 UT with a corresponding drop in  $h_mF_2$ ; however,  $h_mF_2$  peaks around 5 UT with a decrease in height through sunrise 10 - 11 UT. A minima peak in  $N_mF_2$  is apparent between predawn hours 5 – 10 UT, that increases sharply at sunrise and tapers slowly with sunset, 21 – 22 UT.  $h_mF_2$  has an average peak height around 350 – 400 km and an average minimal height around 250 – 300 km.  $N_mF_2$  peak values are tightly coupled throughout each day (on log scale) around  $6.25 \text{ cm}^{-3}$ ; however, minima values seem to have the largest day-to-day variation from  $4.5$  to  $5.5 \text{ cm}^{-3}$ .

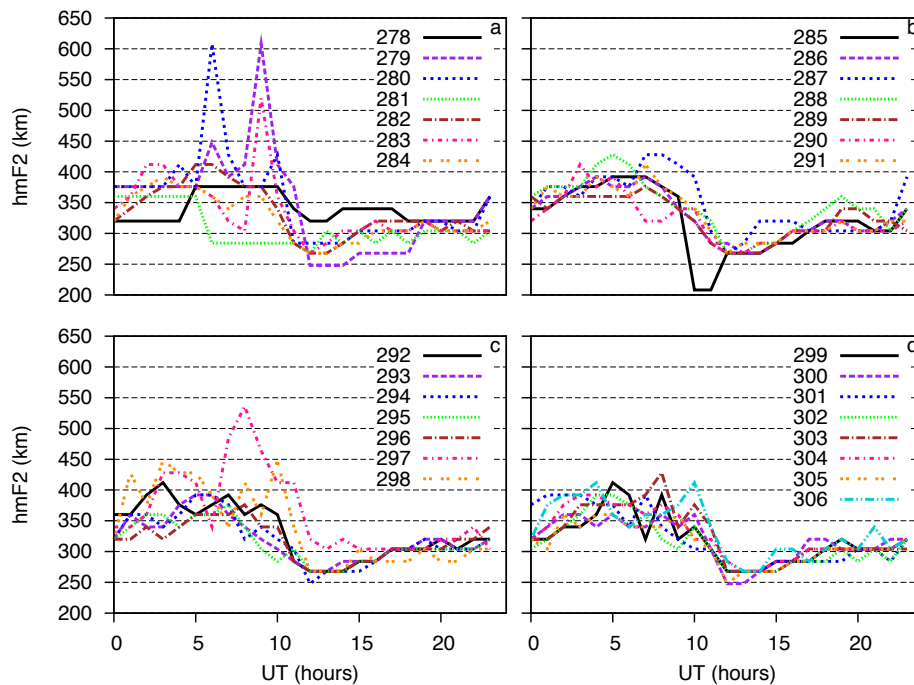


**Figure 4.5.** The ISR-derived variation of the peak electron height,  $h_m F_2$  (km), for days (a) 278-284, (b) 285-291, (c) 292-298, and (d) 299-306.

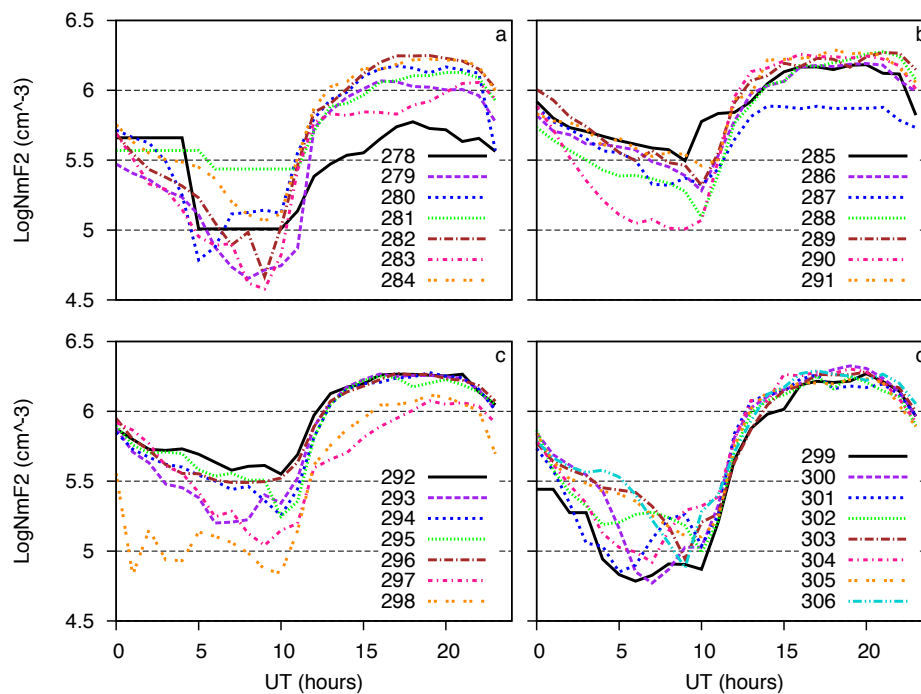


**Figure 4.6.** The ISR-derived variation of the log scale peak electron density,  $N_m F_2$  ( $\text{cm}^{-3}$ ), for days (a) 278-284, (b) 285-291, (c) 292-298, and (d) 299-306.

### 4.3.3. Electron Temperature and Density Profiles

Using the collected ISR data, daily electron temperature ( $T_e$ ) and density ( $N_e$ ) profiles at local midnight and noon for days 278 - 306 are derived and shown in Figure 4.7. The gray shaded area is the altitude range from 428 km – 556 km used to represent the topside ionosphere in this study. The green line represents the reference quiet day 294, the red line, active day 297 and the blue line post-active day 298 to show the continued response in a disturbed ionosphere.

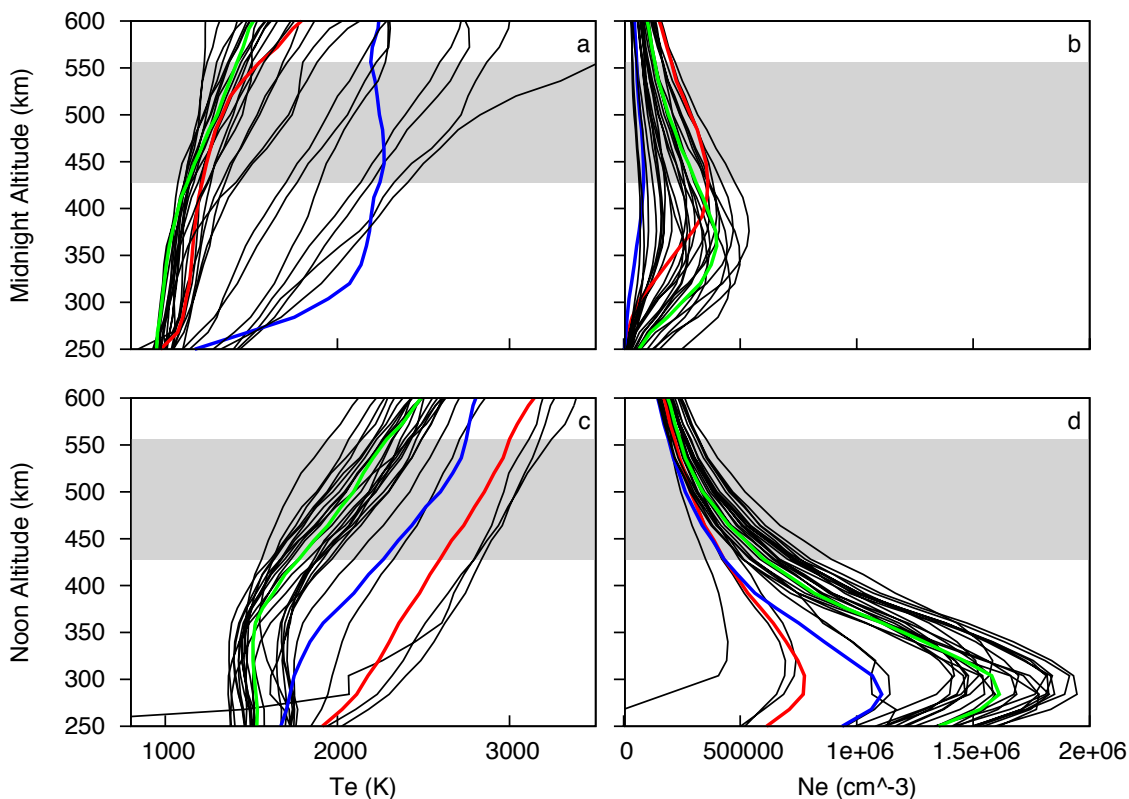


**Figure 4.7.** The ISR-derived diurnal variation for days 278 – 306. Results include electron temperature,  $T_e$  (K), at local midnight (a), local noon (c), and linear plot for electron density,  $N_e$  ( $\text{cm}^{-3}$ ), at local midnight (b), and local noon (d). The green line represents the reference quiet day 294, the red line, active day 297, the blue line, post active day 298, and the gray shaded area, the topside ionosphere used in this study.

Figure 4.7 shows a large diurnal variation from day to day in both  $T_e$  and  $N_e$ . In terms of the topside ionosphere, large variations occur in day-to-day  $T_e$  and  $N_e$  profiles with  $T_e$  seeing more variations overall compared to  $N_e$ . A majority of midnight  $T_e$  profiles average between 1000 – 1500 K. At local noon, average  $T_e$  is higher, between 1750 and 2250 K, as expected due to daytime heating. There are a handful of days whose  $T_e$  profiles are well above the average range between 2500 - 3000 K for both noon and midnight.

At noon,  $N_e$  sees very large variations in the peak values, but the peak height is consistent day to day at about 300 km. For midnight, the peak  $N_e$  values remain below  $500000 \text{ cm}^{-3}$ ; however, the peak height is not as well defined, and sees more variations in the peak height ranging from 325 km to 425 km. Electron density panels b and d in Figure 4.7 is replotted on a log scale in Figure 4.8 to examine the rate of change (slope) in  $N_e$ .

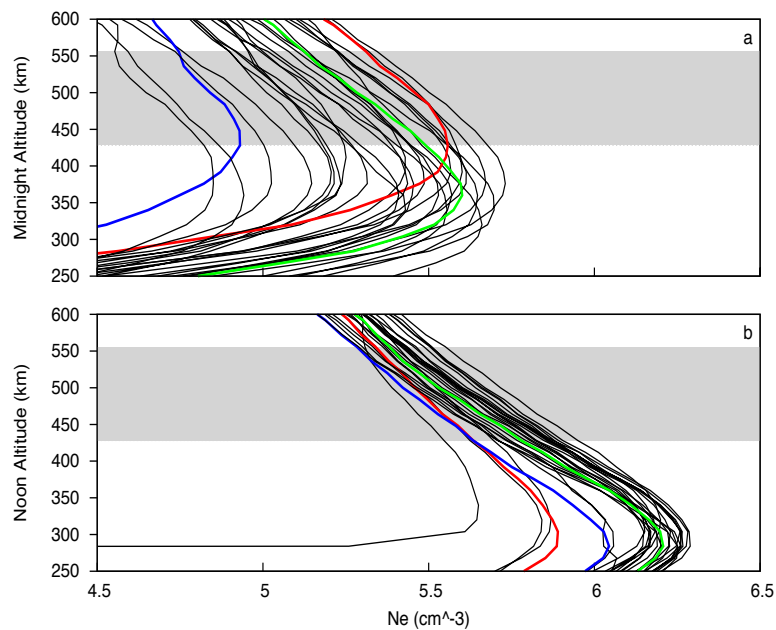


**Figure 4.8.** The ISR-derived diurnal variation for days 278 – 306 for electron density ( $\text{cm}^{-3}$ ) using log scale, at local midnight (a) and local noon (b). The green line represents the reference quiet day 294, the red line, active day 297, the blue line, post active day 298, and the gray shaded area, the topside ionosphere used in this study.

#### 4.4. Discussion

This first part of this chapter began with a discussion of previous statistical studies, which assessed the same Millstone Hill data campaign used in this study. *Zhang et al.* [2005] showed what we can expect in terms of ionospheric variability in electron density, and ion and electron temperatures due to time of day and solar geophysical indices. *Lei et al.* [2005] found an apparent effect on scale heights due to seasons, solar activity and time of day. *Lei et al.* [2005] also suggested the topside profile shape of electron density is dependent on plasma diffusion; however, whether or not scale height can be inferred knowing either plasma temperature or density information was inconclusive. *Liu et al.* [2007] found diurnal differences in the two scale height techniques adapted for this study, VSH and  $H_p$ . Large VSH values during nighttime and small values during daytime hours compared to  $H_p$  values were found by *Liu et al.* [2007] and we expect to see the same trend in our analysis. The study by *Liu et al.* [2007] concluded further studies are needed to understand the behavior of the ionospheric scale heights. A combination of the three presented statistical studies over Millstone Hill set the path forward for our study.

The second part of this chapter discussed our interpretation of the campaign observations over Millstone Hill during the 2002 data campaign. Daily solar variations in the period of study, as introduced by *Zhang et al.* [2005], were discussed in section 4.3.1 and reference days for quiet conditions and active conditions were identified as day 294 and 297, respectively. *Zhang et al.* [2005] suggested this variability will offer a good opportunity for this study to address several ionospheric behavior questions. Sections 4.3.2 and 4.3.3 showed diurnal variations in F-region peak parameters  $N_mF_2$  and  $h_mF_2$  and

electron density and temperature trends we can expect to see in our forthcoming analysis of scale heights in Chapter 5.

The scale height analysis is expected to see a trend in the variation of plasma temperature, driven by rapid changes in  $T_e$ , using both  $H_p$  and VSH techniques as shown by *Lie et al.* [2007]. Topside variations in electron temperature and density are apparent which will be studied in terms of the effect it may have on scale height values.



## CHAPTER 5

### TOPSIDE SCALE HEIGHT COMPARISONS

#### 5.1. Introduction

In the previous chapter, it was discussed what topside ionospheric conditions we expect to see at Millstone Hill by reviewing earlier studies and the campaign observations over Millstone Hill during the 2002 data campaign. To reconstruct the topside ionosphere is the ultimate goal of this study, which depends on a measure of the exponential decrease in electron density; namely, scale height. Previous chapters have shown this exponential decay is mainly driven by thermal diffusive equilibrium, but also dependent on the dominant ion species, as well as other drivers during nondiffusive conditions. A scale height based on observations of the temperature, the plasma scale height ( $H_p$ ), can generate topside electron density profiles. While a measure of the electron density profile enables a scale height to be inferred, the vertical scale height (VSH), hence, yielding temperature information.

This chapter begins the scale height analysis needed for the topside reconstruction technique by using data collected from Millstone Hill Observatory's ISR as described in Chapter 4. We will study how the scale height methods differ and for the first time, offer an explanation of the day-to-day variability in dynamics at mid-latitudes. This chapter will begin to address the fundamental question set out by this study: how the topside electron density over Millstone Hill during the 2002 ISR Campaign is dependent on altitude, its intrinsic connection to ionospheric dynamics, and how to infer the topside ionosphere by a determination of scale heights.

## 5.2. ISR Methodology

The ISR data were smoothed to account for the ISR altitude stepping by a Gaussian type method and separated into nighttime hours, 0 – 10 UT, and daytime hours, 11 - 23 UT. Daytime hours include both sunrise and sunset with local noon at 16 UT (EDT) for days 278 - 300 and 17 UT (EST) for days 301 – 306. Solar noon ranges from 15:32 UT on day 278 to 15:27 UT on day 306. During nighttime hours, local midnight occurs at 04 UT (EDT) for days 278 - 300 and 05 UT (EST) for days 301-306. Solar midnight ranges from 03:32 UT on day 278 to 03:27 UT on day 306.

The errors included in the Madrigal data files for  $N_e$ ,  $T_e$ , and  $T_i$  are very minimal, usually less than 0.1%. This is discussed and shown in Appendix C, as we do not fully understand how the errors can be so small. For this reason, we do not include error bars on Figures 5.1 – 5.8 and 5.10 – 5.11.

The dataset was also separated into active and quiet days by an analysis of corresponding geomagnetic indices. The indices used were the planetary K index ( $K_p$ ) and the northern polar cap index (PCN), and are described in Appendix A. Days with a  $K_p$  value greater than four and/or a PCN value greater than two are considered active days.  $K_p$  values under four and PCN values under two are considered quiet days [*Stauning, 2013; NOAA Space Weather Scales, Appendix A*].

The scale height analysis uses both the electron density-driven vertical scale height (VSH) method given by equation 2.5 and the plasma temperature-determined scale height ( $H_p$ ) method given by equation 2.6. Both equations 2.5 and 2.6 are reproduced below as 5.1 and 5.2 respectively:

$$VSH = \frac{-(h_2 - h_1)}{\ln \left( \frac{N_e(h_2)}{N_e(h_1)} \right)}, \quad (5.1)$$

$$H_p = \frac{2kT_p}{m_i g_h}. \quad (5.2)$$

In both scale height techniques, there are two altitude comparisons located above the F-layer peak height,  $h_m F_2$ . The lower altitude in  $H_p$  calculations is 428 km and upper altitude at 520 km. For VSH calculations the lower altitude range is 448 km – 500 km and the upper, 500 – 556 km. The lower altitude range for VSH was adjusted up from 400 – 448 km to keep peak contamination at minimum.

If the topside F2 region of the ionosphere is controlled by plasma diffusion as postulated in the literature and discussed in Chapter 2, *Whitten and Poppoff* [1971] suggest including a diffusion coefficient,  $(C + 1)$ , in the scale height calculation:

$$H = \frac{(C + 1)k_b T_n}{m_i g_h}, \quad (5.3)$$

where an isothermal atmosphere,  $T_i = T_n$ , is assumed and  $C = (T_e/T_n)$ . This equation is expected to hold true for diffusive conditions.

Ultimately, we will assess the degree to which diffusive equilibrium exists during quiet solar and geomagnetic conditions, revisiting active conditions in subsequent chapters. We expect to confirm the topside ionosphere is not in diffusive equilibrium for daytime hours.

### 5.3. Scale Height Results during Quiet Solar and Geomagnetic Conditions

In this section, we describe the initial results during quiet solar and geomagnetic

conditions between the two methods for calculating scale heights in the topside ionosphere. Consecutive days 294 - 296 (October 21 - 23) are deemed the quietest days contained in the dataset in regards to geomagnetic activity. Because of this, results from these three days will be referred to throughout this section. Also, we are interested in the shape and associated dynamics of the topside ionosphere; therefore, we examine nighttime and daytime hours separately in more detail.

Figure 5.1 shows the initial comparison of the two scale height techniques for consecutive quiet days 294 - 296. Hours 0 – 23 UT represent day 294, 24 – 47 UT, day 295, and 48 – 71 UT, day 296. This figure shows an hourly comparison between scale heights:  $H_p$ , using plasma temperature measurements (black lines); neutral scale heights,  $H_n$ , using neutral temperatures in equation 5.2 (blue lines), and VSH, using density measurements (red lines). For each scale height parameter, the two altitude comparisons are represented by circles for the lower altitude and triangles for the upper altitude.

For nighttime hours, VSH and  $H_p$  seem to be in reasonable agreement. After sunset at about 22 UT, there is a steady decrease in  $H_p$  from 22 – 30 UT at both altitudes as the topside ionosphere loses photoionization, the main source of heating. A decrease in  $H_p$  occurs during nighttime hours until the sun begins to rise and photoionization begins to pick back up at about 32 UT. In VSH, this aforementioned nighttime trend is not so clear; however, the scale height values tend to closely resemble the values produced by the  $H_p$  method just after sunset.

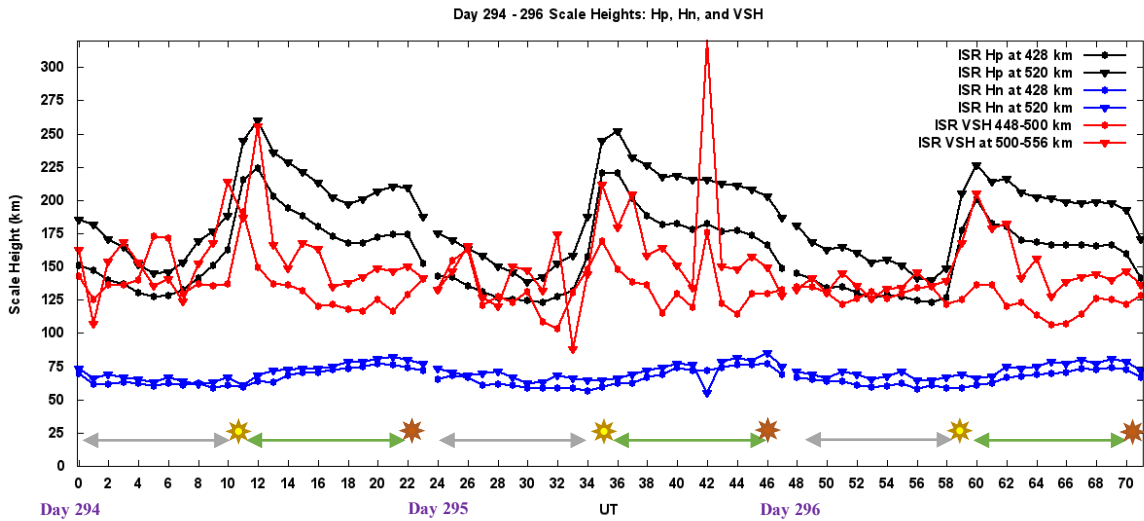


**Figure 5.1.** Scale height calculations for quiet days 294 - 296. Hours 0 – 23 UT represent day 294, 24 – 47 UT, day 295, and 48 – 71 UT, day 296. The black lines show the plasma scale height,  $H_p$  for the two altitudes above the density peak, the red lines show the density-driven vertical scale height and the blue lines, the neutral temperature scale height,  $H_n$ . The lower altitude is represented by circles and the upper altitude is represented by triangles. The grey arrows represent nighttime hours, 0 – 10 UT, each day, and green arrows represent daytime hours, 12 – 22 UT. The yellow sun marks when sunrise occurred each day (11 UT, 35 UT, and 59 UT) and the dark orange sun marks when sunset occurred (22 UT, 46 UT, and 70 UT).

A strong peak in scale heights is seen both for  $H_p$  and VSH at both upper and lower altitudes just after sunrise, beginning around 10 UT and peaking at 12 UT; however, the lower boundary for VSH indicated a weaker peak earlier at 11 UT. Nighttime scale height for day 294 is roughly described by  $150 \pm 30$  km, but on dayside, the  $H_p$  value exceeds its corresponding VSH by about 80 km. The sunrise rapid increase in scale heights is more difficult to describe.

During daytime hours, there is a very gradual decrease in  $H_p$  as the day progresses until sunset. In VSH, this trend is not so obvious. A major discrepancy between the two methods is seen in the diurnal variation, which is very noticeable in  $H_p$ ; but, for VSH,

daytime heating effects in the topside is not apparent with a much lower scale height compared to the  $H_p$  method.

The topside ionosphere during daytime hours is subjected to ionospheric transport processes. Just after sunrise, rapid changes in boundary pressures and temperatures cause an upward flow of plasma into the magnetosphere, increasing the plasma scale height of the F2 region, and therefore, the ion density distribution cannot be in diffusive equilibrium [Banks and Kockarts, 1973]. This may explain why there is such a large discrepancy between the two methods (shown in black and red) during daytime hours. Finally,  $H_n$  is as expected. The neutral temperature does not show much variation as the day progresses so a diurnal fluctuation should not be present with the magnitude shown in Figure 5.1 for  $H_p$  and VSH. The  $H_n$  spread is about 15 km throughout the day with a 5 km difference between the upper and lower altitudes of the topside ionosphere.

Consecutive days 295 and 296 are shown beginning at 24 UT and 48 UT, respectively, in Figure 5.1. The same trends present for day 294 are also present for days 295 and 296; however, a very unusual VSH spike due to an electron density profile change occurs on day 295 at 42 UT (or 18 UT).

Figure 5.2 shows five electron density profiles for day 295 during hours 16, 17, 18, 19, and 20 UT. The anomalous 18 UT profile above 460 km is quite different from the adjacent dayside profiles. This may reflect difficulty in the ISR data or topside plasma dynamics. It is because of this abnormality in the data that we get the large spike at 18 UT in the VSH scale height calculation. We will disregard this VSH calculation since the density profile is not self consistent with prior or later profiles.

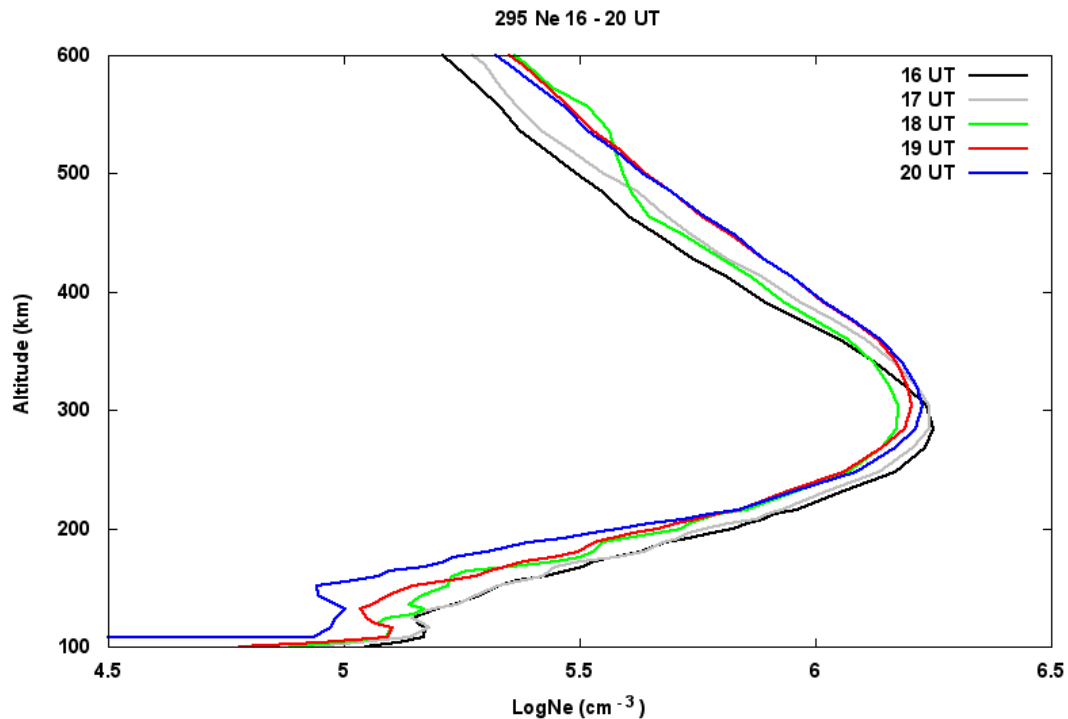


**Figure 5.2.** Hourly ISR electron density profiles for day 295 from 16 – 20 UT.

This indicates that not all profiles have topside smooth slopes. The 18 hour UT profile is not consistent with a diffusive environment; hence, our analysis technique should not be applied to this data. Because of this, we carried out a profile-by-profile review to identify such outliers, which will be discussed in section 5.3.1.

### 5.3.1. Scale Height Comparisons during Nighttime Hours

This section discusses the results of scale height calculations in the previous section only for nighttime hours. It appears nighttime hours have the best agreement between the two separate methods for calculating topside scale heights. As a result, we conclude that the Millstone Hill nighttime topside ionosphere is well described as being in diffusive equilibrium. As previous chapters suggest, the major ion over the range 450 - 550 km is

assumed to be  $O^+$  and the nighttime temperature variations are smaller from one night to the next when compared to daytime hours. The right side of Figure 3.4 from Chapter 3, section 1.1 confirms this, showing  $T_e$  is approximately equal to  $T_i$  and not altitude dependent from 300 km upwards.

The strong correlation between the two scale height analysis techniques is shown in Figure 5.3a for the upper altitude, Figure 5.4a for the lower altitude, and include the density profiles not consistent with a diffusive profile shape, an issue introduced in the previous section and shown in Figure 5.2. In review, a total of 33 out of 110 profiles (~30%) were flagged as not consistent with a diffusive profile shape. 78.8% of these flagged profiles occurred between the nighttime hours of 05 – 10 UT. Figures 5.3a and 5.4a were replotted as Figures 5.3b and 5.4b to exclude these flagged profiles as the nondiffusive shape profiles are not included in the correlation analysis. Both Figures 5.3b and 5.4b contain quiet solar activity days: 284 – 286, 291 – 296, and 305.

In Figure 5.3b, the upper altitude distribution is centered on the line of equality between VSH and  $H_p$  near 160 km with an approximate 34 km spread in both the x and y directions. Overall, the two methods appear to be in good agreement as expected under diffusive, like conditions.

In Figure 5.4b, the lower altitude distribution is centered just above the line of equality between VSH and  $H_p$  near 142 km with an approximate 16 km spread in the x direction and 155 km with a 32 km spread in the y direction. There is a noticeable outlier from day 295 that cannot be explained with the criteria used to flag nondiffusive, like profile shapes. In general, the altitude chosen for the lower boundary region of the topside



Hp vs VSH at 520km from 0UT - 10UT for quiet geomag activity, including non-diffusive shape

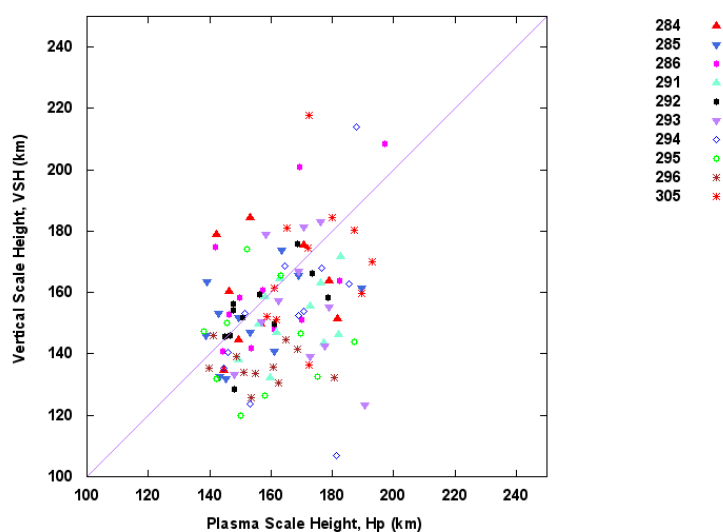


**Figure 5.3a.** Plasma scale height,  $H_p$ , plotted against density-driven vertical scale height, VSH, for quiet days where  $K_p < 4$  including nondiffusive shaped profiles during nighttime hours 0 – 10 UT at the topside upper altitude of 520 km. These days are 284 – 286, 291 – 296, and 305. The purple line represents the line of equality between VSH and  $H_p$ .

Hp vs VSH at 520km from 0UT - 10UT for quiet geomag activity

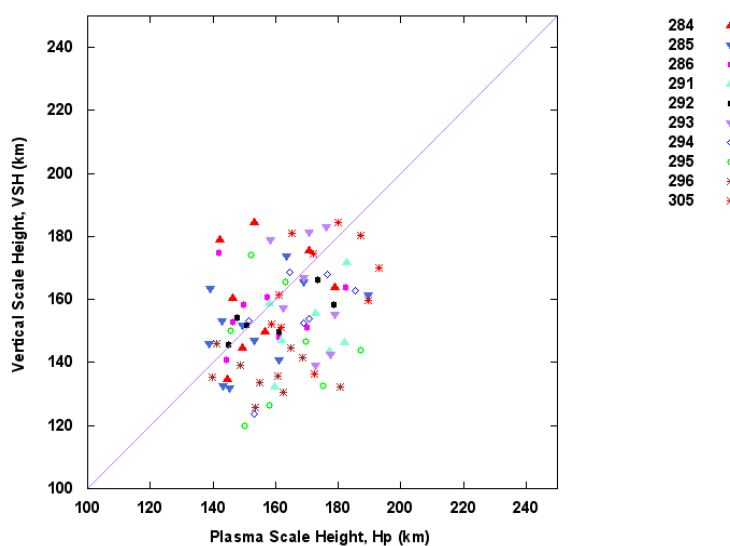


**Figure 5.3b.** Plasma scale height,  $H_p$ , plotted against density-driven vertical scale height, VSH, for quiet days where  $K_p < 4$  excluding nondiffusive shaped profiles during nighttime hours 0 – 10 UT at the topside upper altitude of 520 km. These days are 284 – 286, 291 – 296, and 305. The purple line represents the line of equality between VSH and  $H_p$ .

Hp vs VSH at 428km from 0UT - 10UT for quiet geomag activity, including non-diffusive shape

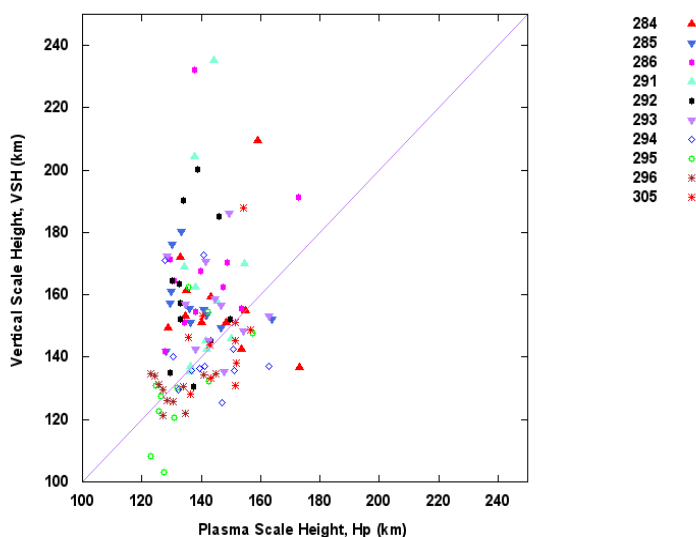


**Figure 5.4a.** Plasma scale height,  $H_p$ , plotted against density-driven vertical scale height, VSH, for quiet days where  $K_p < 4$  including nondiffusive shaped profiles during nighttime hours 0 – 10 UT at the topside lower altitude of 428 km. These days are 284 – 286, 291 – 296, and 305. The purple line represents the line of equality between VSH and  $H_p$ .

Hp vs VSH at 428km from 0UT - 10UT for quiet geomag activity

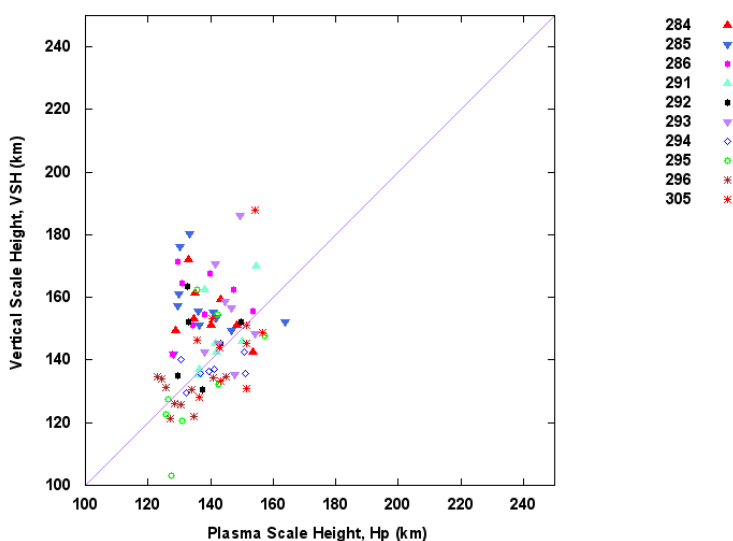


**Figure 5.4b.** Plasma scale height,  $H_p$ , plotted against density-driven vertical scale height, VSH, for quiet days where  $K_p < 4$  excluding nondiffusive shaped profiles during nighttime hours 0 – 10 UT at the topside lower altitude of 428 km. These days are 284 – 286, 291 – 296, and 305. The purple line represents the line of equality between VSH and  $H_p$ .

ionosphere is well above the peak layer; however, the peak may still contaminate our electron density data because it is well known that the peak rises in altitude during nighttime. Again, the two methods appear to be in good agreement as expected under diffusive, like conditions.

### 5.3.2. Inference of $T_e$ during Nighttime Hours

Section 5.3.1 showed a strong correlation between VSH and  $H_p$  during nighttime hours. Because of this, we can assume VSH is approximately equal to  $H_p$  at night. This assumption allows us to infer  $T_e$  values by solving for VSH by using just electron density values and setting VSH equal to  $H_p$  in equation 5.3. This allows us to solve for  $C$  using the neutral temperatures. Results are shown for consecutive quiet solar activity days 294 – 296, keeping consistent with the days shown in the previous section. This method works quite well for nighttime hours when compared to  $T_e$  values obtained by data from Millstone Hill's ISR as shown in Figures 5.5 – 5.7. The hourly results are separated by day and split by upper (5.5a, 5.6a, 5.7a) and lower (5.5b, 5.6b, 5.7b) boundaries to inspect when the method works best. For example, we define a significant spread as a difference of 500 K or larger between the inferred  $T_e$  value and the ISR observed value, which equates to a 30% error when compared to the average nighttime  $T_e$  value of approximately 1500 K. Also, if the points are touching or overlapping, they are considered to be in complete agreement. If a significant spread exists, the method of inferring  $T_e$  from equation 5.3 suggests nondiffusive equilibrium conditions.

Quiet reference day 294 is shown in Figure 5.5a. A significant spread (i.e. > 500 K) in  $T_e$  occurs between hours 05 and 06 UT, but for hours 02, 03, 07, and 08 UT,  $T_e$

inferred is in complete agreement with the observed ISR values. For the upper altitude shown in Figure 5.5b, a significant spread occurs at 01 and 10 UT with hours 05, 06, and 09 UT in complete agreement with the observed ISR values.

Lower altitude for day 295 is shown in Figure 5.6a. There is one significant spread at 02 UT compared to three significant spreads at 08, 09, and 10 UT in the upper altitude shown in Figure 5.6b. There are no hours where  $T_e$  inferred is in complete agreement with the observed ISR values for the upper boundary during day 295; however, for the lower boundary, hours 04, 05, and 09 UT are in complete agreement. The significant spreads shown in Figure 5.6b may suggest the nondiffusive conditions.

Day 296 had the most favorable agreement out of the three consecutive days between Figures 5.7a and 5.7b. There are no significant spreads (i.e.  $> 500$  K) between the inferred  $T_e$  and the observed ISR  $T_e$  values for the lower altitude with hours 02, 06, and 07 UT in complete agreement and hours 01, 04, 05, and 10 UT within 100 K of the observed ISR values. For the upper altitude, there is one significant  $T_e$  difference at 00 UT, one in complete agreement at 09 UT, and a close 100 K difference between  $T_e$  inferred and the observed  $T_e$  at 10 UT.

Overall, observed  $T_e$  values from ISR were higher than the inferred  $T_e$  values 66.7% of the time. For quiet days 294, 295, and 296, the lower altitude produced better results compared to the upper altitude; however, there were no significant trends observed for specific hours when inferred  $T_e$  was in close agreement with observed  $T_e$ .

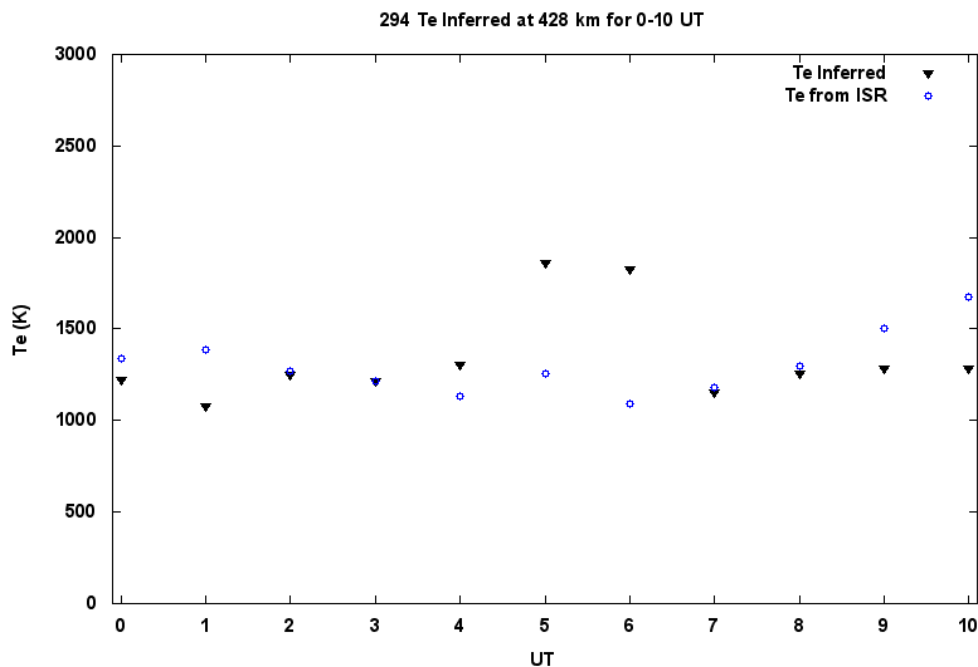


**Figure 5.5a.** Comparison between  $T_e$  values taken from ISR data and by solving for  $T_e$  using VSH for the solution of  $H_p$  in equation 5.3 for reference quiet day 294 at the lower altitude of 428 km.

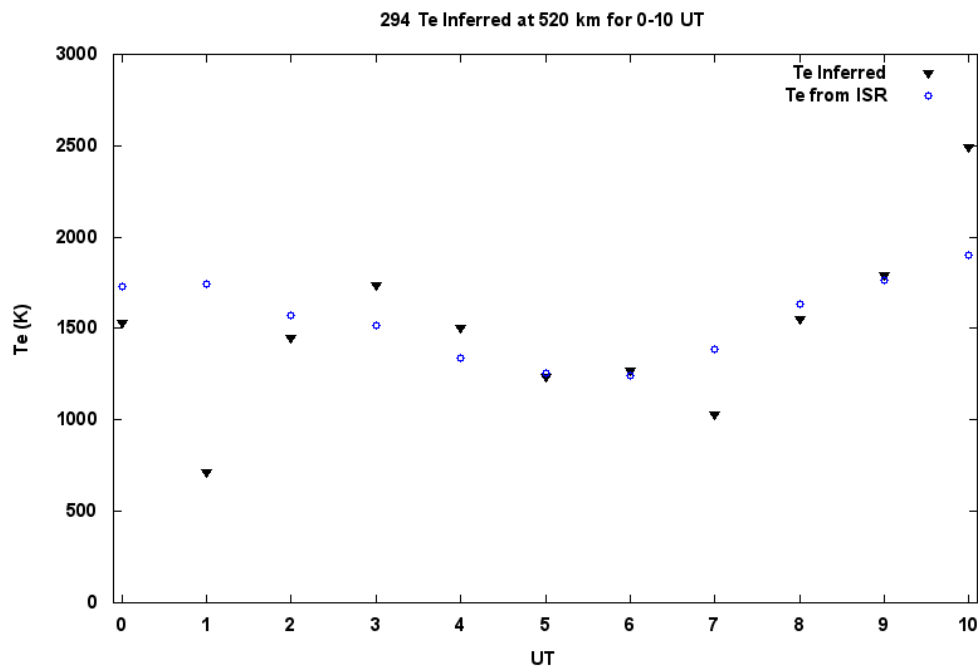


**Figure 5.5b.** Comparison between  $T_e$  values taken from ISR data and by solving for  $T_e$  using VSH for the solution of  $H_p$  in equation 5.3 for reference quiet day 294 at the upper altitude of 520 km.

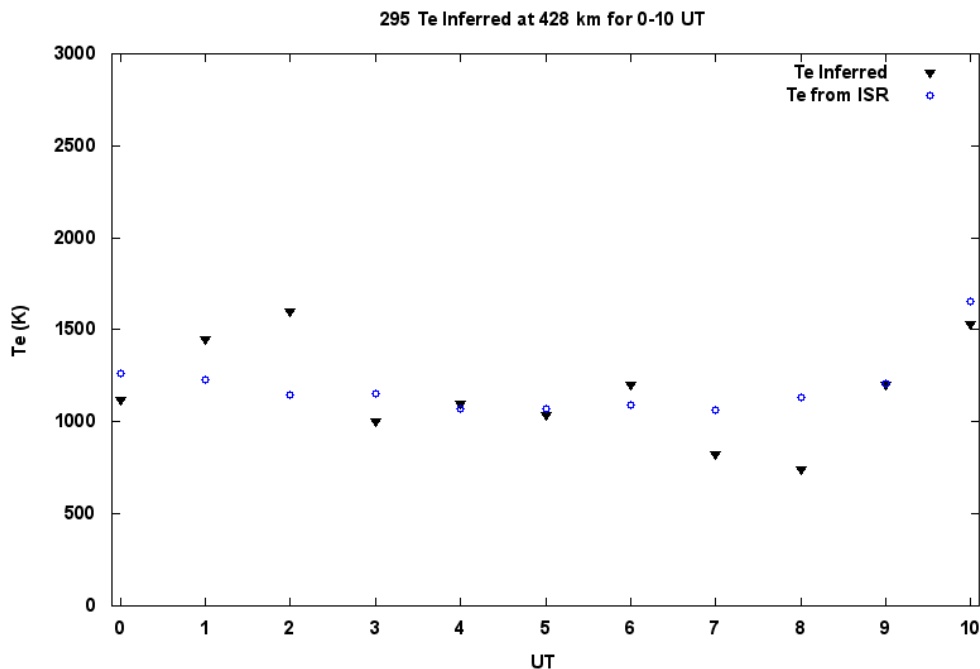


**Figure 5.6a.** Comparison between  $T_e$  values taken from ISR data and by solving for  $T_e$  using VSH for the solution of  $H_p$  in equation 5.3 for quiet day 295 at the lower altitude of 428 km.

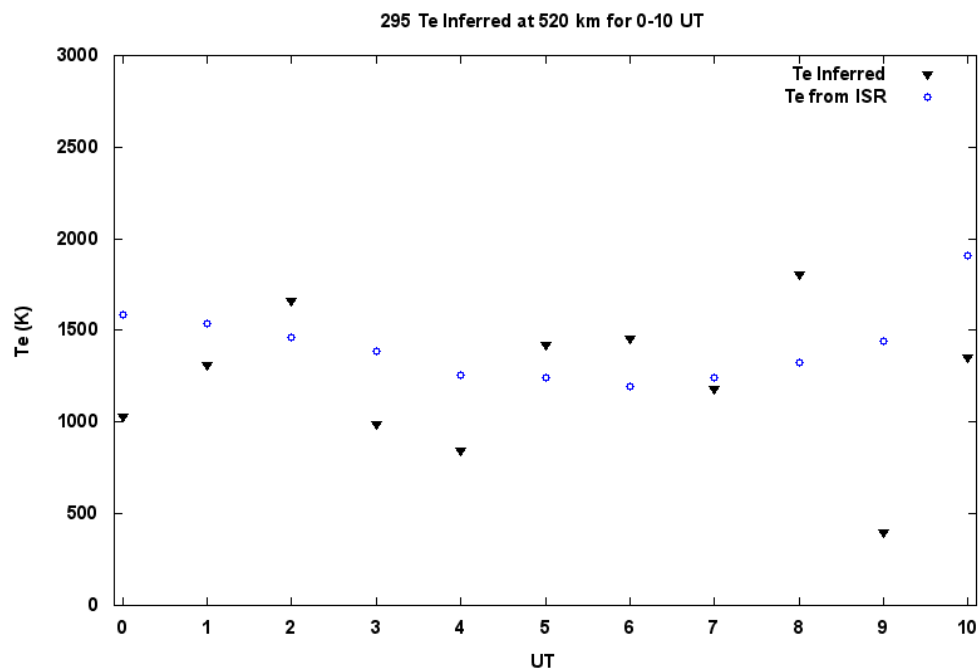


**Figure 5.6b.** Comparison between  $T_e$  values taken from ISR data and by solving for  $T_e$  using VSH for the solution of  $H_p$  in equation 5.3 for quiet day 295 at the upper altitude of 520 km.

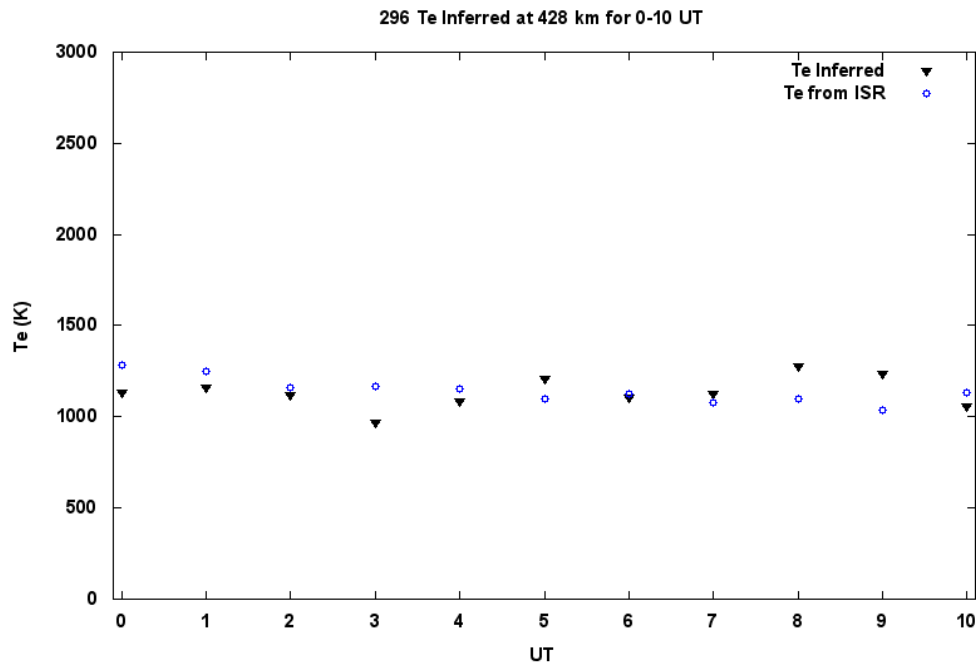


**Figure 5.7a.** Comparison between  $T_e$  values taken from ISR data and by solving for  $T_e$  using VSH for the solution of  $H_p$  in equation 5.3 for quiet day 296 at the lower altitude of 428 km.

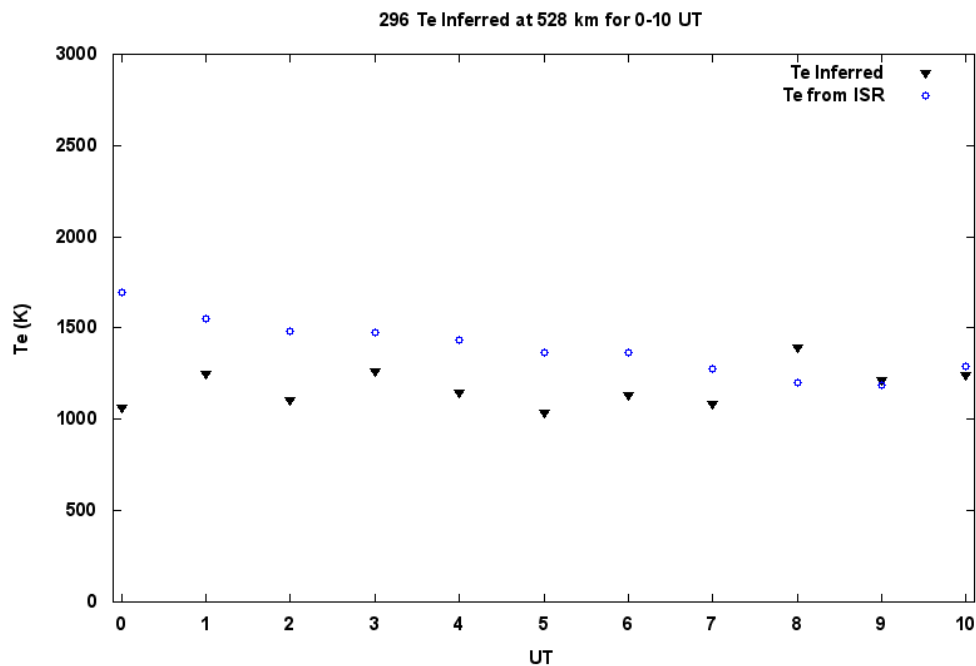


**Figure 5.7b.** Comparison between  $T_e$  values taken from ISR data and by solving for  $T_e$  using VSH for the solution of  $H_p$  in equation 5.3 for quiet day 296 at the upper altitude of 520 km.

Now that the upper and lower altitudes for the inference of  $T_e$  have been examined, it is of interest to look at the distribution of  $C$ , initially calculated in equation 5.3. The  $C$  value spread for quiet days, 294, 295, and 296 during nighttime hours are shown in Figure 5.8. The lower altitude  $C$  values are represented by black dots and the upper altitudes values by green crosshairs. For each  $C$  value, the vertical lines extend to plus/minus one standard deviation. The black line is the overall lower altitude  $C$  average for the three mentioned days and the green line, the overall average for the upper altitude.

Both the upper and lower altitude  $C$  value averages are just above 1, at 1.19 and 1.18, respectively. Days 294 and 295 show a larger spread in both the upper and lower altitudes compared to day 296, which has daily values that appear to be clustered closer to 1 (suggesting thermal equilibrium,  $T_e \approx T_i \approx T_n$ ) with the smallest standard deviation out of

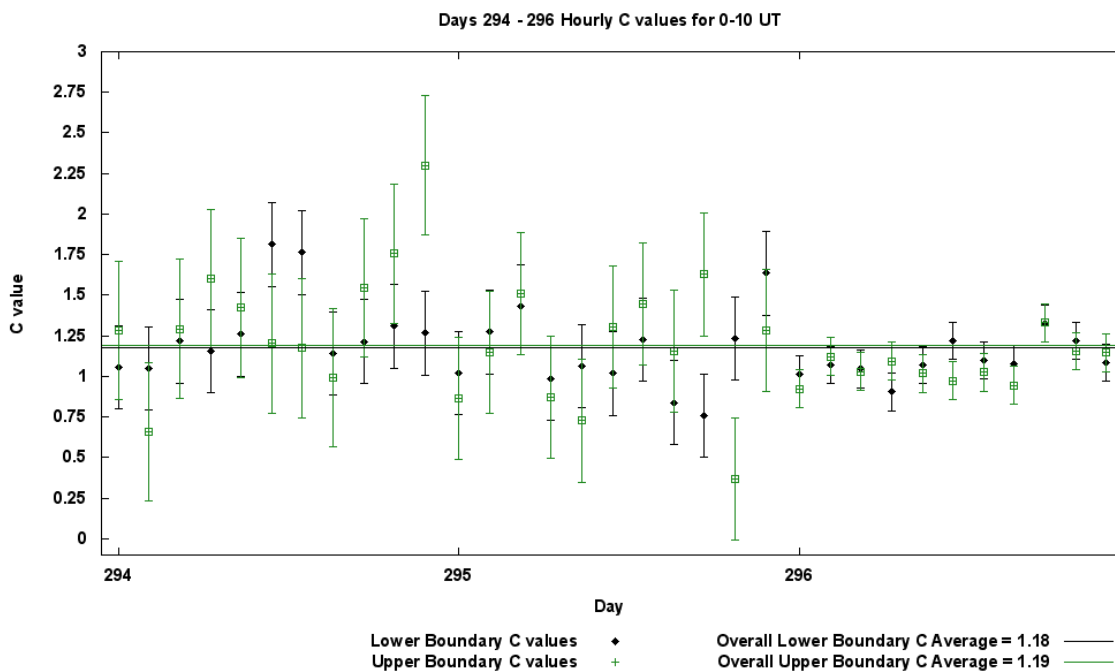


**Figure 5.8.**  $C$  values and associated daily standard deviation are shown for nighttime hours 0 – 10 UT on quiet days 294 – 296.



the three days. This would make the diffusive equilibrium factor in our scale height calculations  $(C + 1)$  from equation 5.3 roughly equal to 2. Note the smaller standard deviations found on day 296 may be associated with better diffusive equilibrium conditions compared to days 294 and 295. About 33% of the hours had either an upper or lower altitude value that did not fall within one standard deviation of the overall mean.

### **5.3.3. Scale Height Comparisons during Daytime Hours**

This section discusses the results of scale height calculations for daytime hours. Because the two methods for determining scale heights during daytime hours has a large discrepancy visible in Figure 5.1, we conclude the Millstone Hill daytime topside ionosphere cannot be described by diffusive equilibrium.

Temperature variations during daytime hours are large and are not consistent from day to day compared to nighttime hours, which shows very little change from one night to the next as described in section 5.2.1. Figures 5.9 and 5.10 show the two scale height analysis techniques for the upper and lower altitudes, respectively, during quiet solar activity days 284 – 286, 291 – 296, and 305, keeping consistent with the previous sections.

In Figure 5.9, the upper altitude distribution is centered around 225 km in the x direction ( $H_p$ ) and 150 km in the y direction (VSH), significantly offset from the line of equality between VSH and  $H_p$  by about 50 km. A similar magnitude offset is shown in the lower altitude distribution, Figure 5.10, centered around 187 km in the x direction ( $H_p$ ) and 125 km in the y direction (VSH). The offset from the line of equality is larger compared to the upper altitude distribution by about 10 km at 60 km.

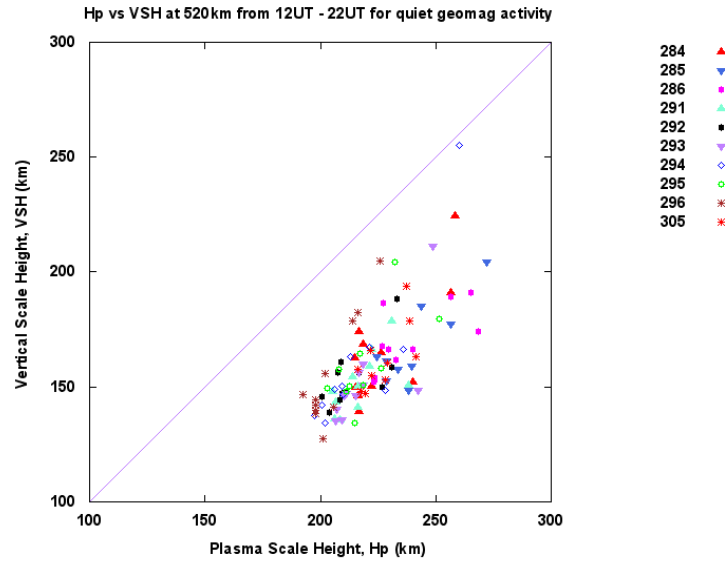


**Figure 5.9.** Plasma scale height,  $H_p$ , plotted against density driven, VSH, for days where  $K_p < 4$  during daytime hours 12 – 22 UT at the topside upper altitude of 520 km. These days are 284 – 286, 291 – 296, and 305. The purple line represents the line of equality between VSH and  $H_p$ .

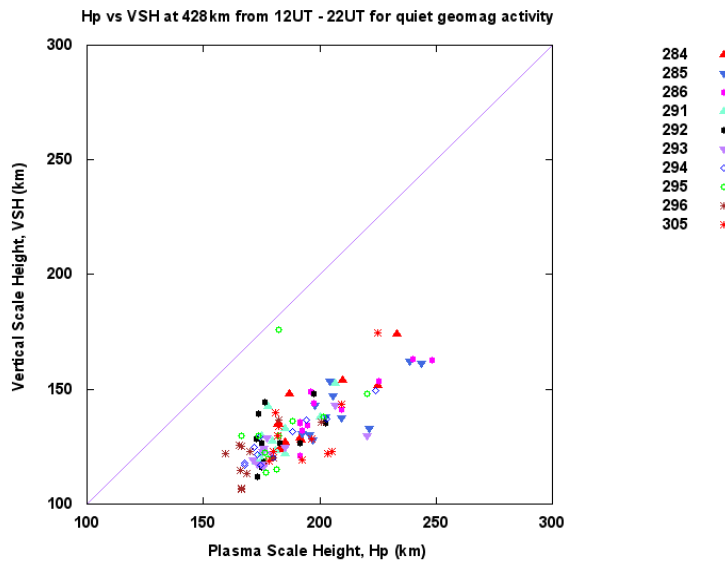


**Figure 5.10.** Plasma scale height,  $H_p$ , plotted against density driven, VSH, for days where  $K_p < 4$  during daytime hours 12 – 22 UT at the topside lower altitude of 428 km. These days are 284 – 286, 291 – 296, and 305. The purple line represents the line of equality between VSH and  $H_p$ .

$H_p$  has a larger scale height than VSH in both Figures 5.9 and 5.10 for all daytime hours. We expected to see a discrepancy between the two methods because daytime hours cannot be described by diffusive equilibrium as mentioned earlier. Our analysis suggests the possibility of a consistent offset that can be quantified for daytime hours since the cluster is more elongated than for the nighttime hours and tracks the slope, which suggests the offset may be real. This finding will be revisited in Chapter 7.

#### **5.4. Discussion**

This chapter was a scale height analysis of the data collected from Millstone Hill Observatory's ISR as described in Chapter 4 for quiet geomagnetic activity. Active conditions will be discussed in subsequent chapters. The two different scale height methods using both plasma temperatures ( $H_p$ ) and electron density (VSH) were quantified and compared. Scale height being the exponential decay is mainly driven by thermal diffusive equilibrium; however, it is also dependent on the dominate ion species, as well as other drivers during nondiffusive conditions.

The results in section 5.3 show that during quiet geomagnetic activity, the two methods of calculating scale heights are nearly always in good agreement during nighttime hours. Also during nighttime hours, the variation in both the x and y directions is within 34 km from the line of equality between the two scale height methods shown in Figures 5.3b and 5.4b, so it is reasonable to conclude the variations in topside  $T_e$ ,  $T_i$  and electron density have minimal effects over the altitude range 428 km – 520 km used to investigate scale height.

We observed signatures in our scale height analysis of contributions from temperature structures and diffusion processes that greatly control the shape of the electron density profile (see Figure 5.2) as suggested by *Liu et al.*, [2007] in section 4.2.3. We conducted a data profile review to separate hours that did not represent diffusive, like conditions. Our review found that nighttime hours between 00 – 04 UT more than likely gave a diffusive profile shape in contrast to hours 05 – 10 UT where 78.8% of the flagged profiles occurred.

Section 5.3.2 proved the topside F2 region of the ionosphere is, indeed, controlled by plasma diffusion during quiet solar and geomagnetic activity for nighttime hours as postulated in the literature and discussed in Chapter 2. We found equation 5.3, given by *Whitten and Poppoff* [1971], is a good method to infer  $T_e$  when only electron density values are available. It is possible to even take it a step further and assume a multiplier of two instead of  $(C + 1)$  in equation 5.3 that will give a good approximation during nighttime diffusive conditions. We can conclude that during said conditions, a measure of the electron density profile enables a scale height to be inferred, yielding temperature information about 66.7% of the time; however, more seasonal data is needed to study this result further.

Concluding, we have assessed the degree to which diffusive equilibrium exists for quiet solar and geomagnetic conditions. Our data analysis shows during nighttime hours, it is reasonable to assume diffusive equilibrium; however, because of such a large discrepancy between the two scale height methods, diffusive equilibrium is not a good representation of the topside ionosphere during daytime hours. This is consistent with what the literature suggests.

In Chapter 6, TEC data collected from a GNSS receiver located in Westford, Massachusetts will be analyzed to determine topside electron density contributions followed by bottomside ionosonde data collected and used to determine bottom TEC. This will lead into the investigation of different topside reconstruction techniques and compare the results.

## CHAPTER 6

### TOPSIDE RECONSTRUCTION

#### 6.1. Introduction

Now that we have explored scale height trends in the topside ionosphere for quiet conditions, this chapter outlines our topside reconstruction technique. Our results from Chapter 5 show little variation between the two scale height calculation techniques during nighttime hours and quiet geomagnetic activity, suggesting diffusive equilibrium conditions. This means we can calculate an appropriate scale height to show the exponential decrease of electron density in the topside ionosphere, whether it be from data containing only density information or only temperature information.

Now we can begin our investigation into the different topside reconstruction techniques and compare the results. This chapter starts with the total electron content (TEC) data collected from a GNSS receiver located in Westford, Massachusetts, five miles from the location of the ISR used in this study. We will determine topside density contributions and compare it to topside contributions calculated using Millstone Hill ISR data as outlined in Chapter 4. Next, bottomside ionosonde data collected from Lowell Global Ionospheric Radio Observatory (GIRO) Data Center [*Reinisch and Galkin, 2011*] for Millstone Hill is used to calculate TEC for the bottomside ionosphere.

Once we know the ionosphere's total TEC and the bottomside contribution to TEC we can then determine the topside contribution to TEC. Our study will, for the first time, address whether or not topside information can be gained by an analysis of GPS TEC and

bottomside electron density profiles observed by ionosonde in the event that neither plasma temperature nor topside electron density are measured.

## **6.2. TEC Methodology**

TEC was first mentioned in Chapter 2, section 5 and Chapter 3, section 3, as the number of electrons in a column stretching over some distance, vertically, with a cross-sectional area of one square meter and can be integrated to give ionospheric electron density over a specific location. In this case, our specific location is that of the Millstone Hill ISR as used in this study. For this chapter, we computed TEC from both the GPS data and from ISR data and compared the results.

It is common to represent TEC in units of TECU, which is equal to  $10^{16}$  electrons/m<sup>2</sup>. TEC can range from 5-120 TECU depending on local time and geomagnetic activity, which previous literature revealed. We can expect to see said variations in our data. Also, the raw GPS data obtained for this study is in the form of slant TEC (STEC) meaning it is not always equal to the TEC directly above Millstone Hill. The GPS satellites could be piercing through the ionosphere at a perceived horizon, which is at an angle from the relative local zenith of the receiver, which we refer to as the inclination angle, and is described in more detail in the following pages.

Absolute GPS TEC was obtained from Dr. Gary S. Bust at Johns Hopkins Applied Physics Laboratory and with the help of Dr. Leda Sox, the NetCDF ECS TEC files were converted to plain text files. The location of the receiver is that of the Millstone Hill ISR, located in Westford, MA. There is a single receiver bias of a residual error of 2-3 TECU

[private email communication with Dr. Gary Bust, confirmed by Dr. Anthea Coster, Millstone Hill Observatory].

STEC was then compared to ISR TEC from Millstone Hill. ISR TEC was calculated each hour by summing electron density values, vertically from 100 km to 784 km. The results are shown in Figure 6.1 for reference quiet day 294 and Figure 6.2 for reference active day 297. ISR determined TECU is represented by the black solid lines, GPS STECU by the black triangles, ISR topside contribution to total TECU by the squares, and the ISR bottomside contribution to total TECU by asterisks. It should be noted that the topside ionosphere is considered to be the altitude just above the peak density height,  $h_mF_2$ , up to 784 km, and the bottomside, directly below the topside down to 100 km, including  $h_mF_2$ .

Both Figures 6.1 and 6.2 show diurnal variations, with higher TECU values during daytime hours 12 - 22 UT and less TECU during nighttime hours 0 – 10 UT. This is true for both ISR TECU and GPS STECU. This change in TECU is due to the loss of photoionization after sunset until sunrise the next day. Figure 6.1 shows the reference quiet day 294 having higher TECU values throughout the day than during active day 297 shown in Figure 6.2, with a daytime peak TECU value of 46 for day 294 and 36 for day 297. The nighttime TECU values seem to be analogous from day 294 to day 297. Both Figures 6.1 and 6.2 show topside ISR TECU contributing more to total TECU than the bottomside, with a larger separation between the two during daytime hours.

Overall, GPS STECU is noticeably higher than ISR TECU throughout the day for both days 294 and 297, Figures 6.1 and 6.2, respectively. The difference between GPS STECU and ISR TECU changes throughout the day: during nighttime hours, the minimum



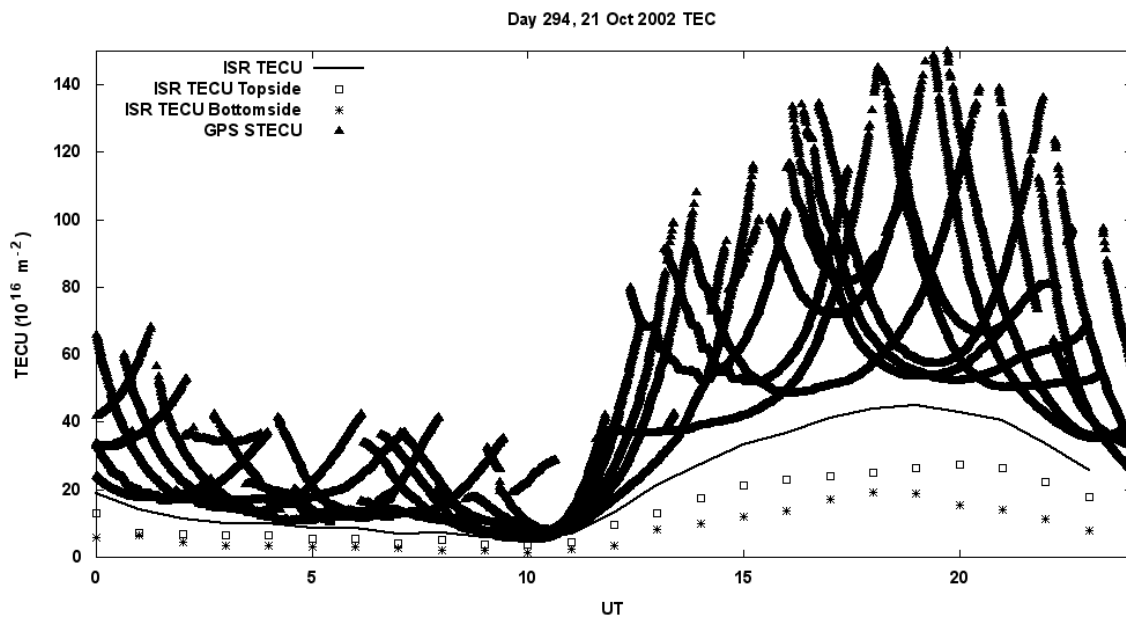


**Figure 6.1.** ISR TEC compared to GPS STEC for quiet day 294.

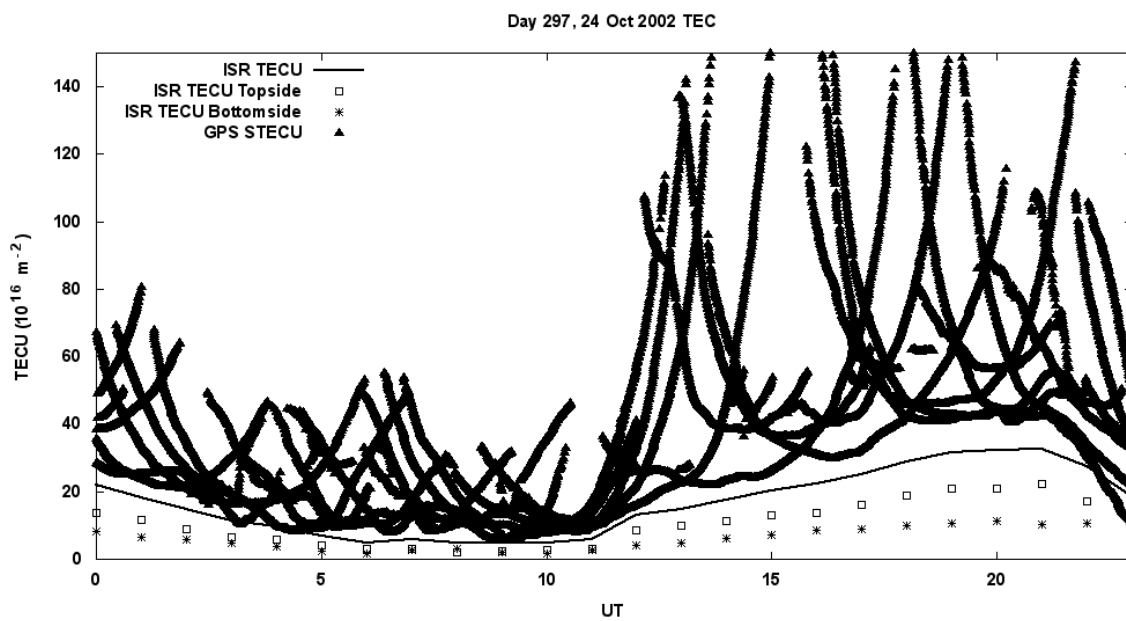


**Figure 6.2.** ISR TEC compared to GPS STEC for active day 297.

difference is about 5 TECU on average, and during daytime hours the minimum difference is about 10 TECU. There are a few explanations as to why there are differences in GPS STECU and ISR TECU. GPS satellites fly in medium Earth orbit (MEO) at an altitude of approximately 20,200 km above Earth's surface [*National Coordination Office for Space-Based Positioning, Navigation, and Timing*, 2016] so a plasmaspheric contribution to TECU is possible, which will be discussed in Chapter 8.

Another reason can be explained by the difference in measurement techniques, discussed in Chapter 3, section 3. ISR is a small volume measurement while GPS is a line integral between the receiver and transmitter of the electron density. Because GPS data is left in STEC, the line integral between receiver and transmitter can be at an angle and not directly above the Westford, MA receiver. This means the GPS signal can be piercing through more ionosphere than the ISR, which we refer to as the inclination angle,  $\phi$ . This is shown in both Figures 6.1 and 6.2 by the triangles, which represent the receiver tracking a rising or setting GPS satellite behind the limb of the Earth. The ISR data are collected directly above the instrument, with an inclination angle of  $0^\circ$ , so it is beneficial to know when the GPS satellite flies directly above the receiver itself. We can determine this by solving for the inclination angle,  $\phi$ , shown in Figure 6.3.

We are given the Cartesian coordinates for both the receiver and satellite in the NetCDF ECS TEC files, so we can then use the dot product to solve for  $\theta_1$  shown in Figure 6.3:

$$\theta_1 = \cos^{-1} \left( \frac{\vec{R} \cdot \vec{S}}{RS} \right), \quad (6.1)$$

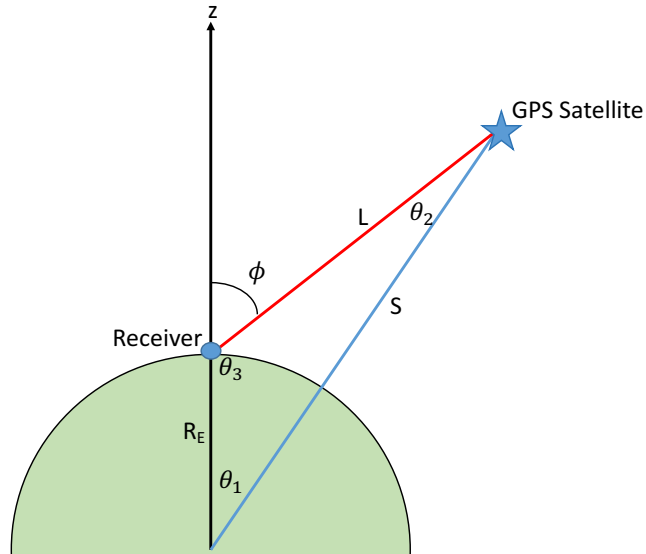


**Figure 6.3.** Inclination angle,  $\phi$ .

where  $R$  represents the unit length from the center of the Earth to the location of the receiver, approximately equal to radius of the Earth ( $R_E$ ), and  $S$ , the length from the center of the Earth to the location of the satellite. Next, we can use the law of cosines to solve for the length of the vector pointing from the location of the receiver to the satellite designated by the red line labeled  $L$  in Figure 6.3:

$$L^2 = R_E^2 + S^2 - 2R_E S \cos\theta_1. \quad (6.2)$$

Law of sines gives us  $\theta_2$ :

$$\frac{L}{\sin\theta_1} = \frac{R_E}{\sin\theta_2}, \quad (6.3)$$

then,

$$\theta_3 = 180 - (\theta_2 + \theta_1), \quad (6.4)$$

and finally,

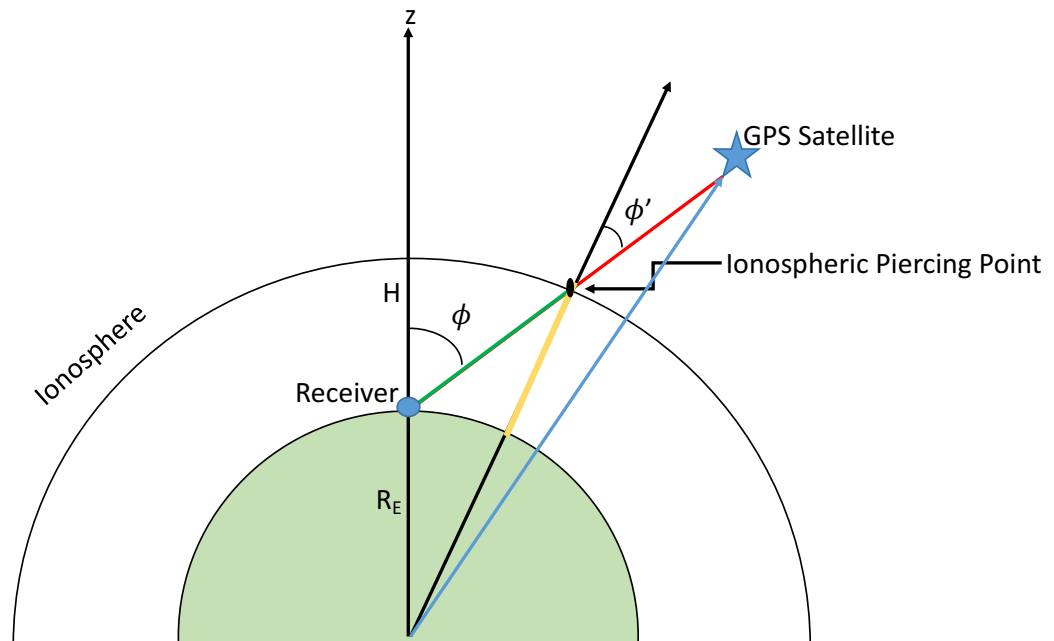
$$\phi = 180 - \theta_3 \quad \text{OR} \quad \phi = \theta_2 + \theta_1. \quad (6.5)$$

Figure 6.4 shows the conversion from slant STEC, green line, to vertical TEC (VTEC), yellow line, by using a mapping function (MF), equation 6.6, adopted from the 2014 research group at the Royal Observatory of Belgium [2014], which uses the technique described by [Schaer, 1999]. VTEC is very useful for the valuable space weather information it can provide, but the conversion is challenging and may not be the best representation of the space and time variations in electron content, especially during ionospheric storms [Hernández-Pajares *et al.*, 2008]. The mapping function equation is defined as:

$$MF(z) = VTEC = STEC \times \cos(\phi') , \quad (6.6)$$

where,

$$\sin(\phi') = \frac{R_E}{R_E + H} \sin(\phi). \quad (6.7)$$



**Figure 6.4.** STEC (green line) versus VTEC (yellow line).

In equation 6.7,  $H$  is the assumed altitude of 350 km above the Earth's surface where the ionosphere is considered a thin layer containing the bulk of all free electrons and is also the altitude of ionospheric intersection of the user line-of-sight to a tracked satellite [Mannucci *et al.*, 1995].

Using the first order approach to  $H$ , with the assumption of the ionosphere to be a thin-shell model, TEC values can be underestimated if a smaller height than actual height is used, or overestimated if a larger height than the actual height is used [Schaer *et al.*, 1995]. We conducted a sensitivity test to see if a change in  $H$  to 300 km would make a significant difference in VTEC. The daily overall percent difference was a 1.3% decrease in VTEC from 350 km to 300 km with the highest percent difference at 6.4%. Again, this points to the challenging conversion of VTEC.

Now that we have calculated VTEC, we can replot Figures 6.1 and 6.2 with STEC of  $\phi$  less than  $10^\circ$  and VTEC using the mapping function mentioned above. STEC of  $\phi$  less than  $10^\circ$  is shown in both Figures because a small  $\phi$  means it was close to being directly overhead of the receiver, so it should naturally be a true ionospheric electron density measurement. Figures 6.5 and 6.6 show the results for days 294 (quiet) and 297 (active), respectively.

In Figures 6.5 and 6.6, ISR TEC is represented by the black solid lines, GPS STEC by the black triangles, GPS STEC of  $\phi$  less than  $10^\circ$  by blue circles, GPS VTEC by pink circles, ISR topside contribution to total TEC by black squares, and ISR bottomside contribution to total TEC by black asterisks. Noticeably, daytime hours still show the

largest difference between GPS VTEC and ISR TEC, with GPS VTEC being slightly above ISR TEC.

The VTEC mapping technique works quite well for quiet reference day 294 shown in Figure 6.5 by smooth pink lines close to the ISR TEC black solid line. There is still a noticeable difference in GPS VTEC and ISR TEC during daytime hours by about 7 TECU. Nighttime hours for the same day are shown in Figure 6.7. GPS VTEC lies directly on and above the ISR TEC line with a few GPS VTEC lines dipping below. Notice the blue GPS STEC lines that overlay the pink lines and are within a few TECU of the ISR TEC line, especially between 9 and 10 UT for  $\phi$  less than  $10^\circ$ .

For active day 297, Figure 6.6 shows a GPS VTEC pink line particularly smooth during nighttime hours and turbulent during daytime hours smoothing out again just after sunset. There are definitely larger gaps in GPS VTEC and ISR TEC during daytime hours compared to nighttime hours, keeping consistent with previous results. Figure 6.8 shows day 297 during nighttime hours. GPS VTEC lines are not as smooth as day 294; however, they lie directly above the ISR TEC line, with no tracks directly on the ISR TEC line as shown in Figure 6.7 for day 294. There are also a few GPS VTEC lines dipping below as with the case for day 294. Blue GPS STEC lines are within a few TECU of the ISR TEC line, especially between 9 and 10 UT, again keeping consistent with day 294.

### **6.3. Ionosonde Methodology**

This section uses a similar technique described in section 6.2 to determine bottomside TEC using an ionosonde. The location of the ionosonde is that of the Millstone

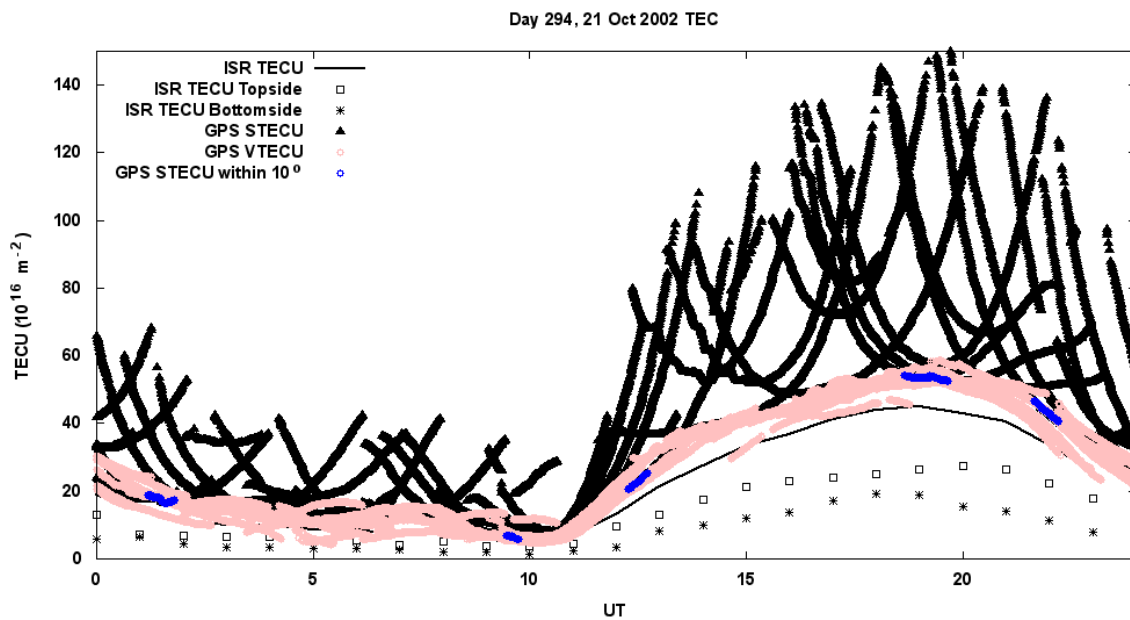


**Figure 6.5.** ISR TEC results compared to STEC and VTEC from GPS for quiet day 294.

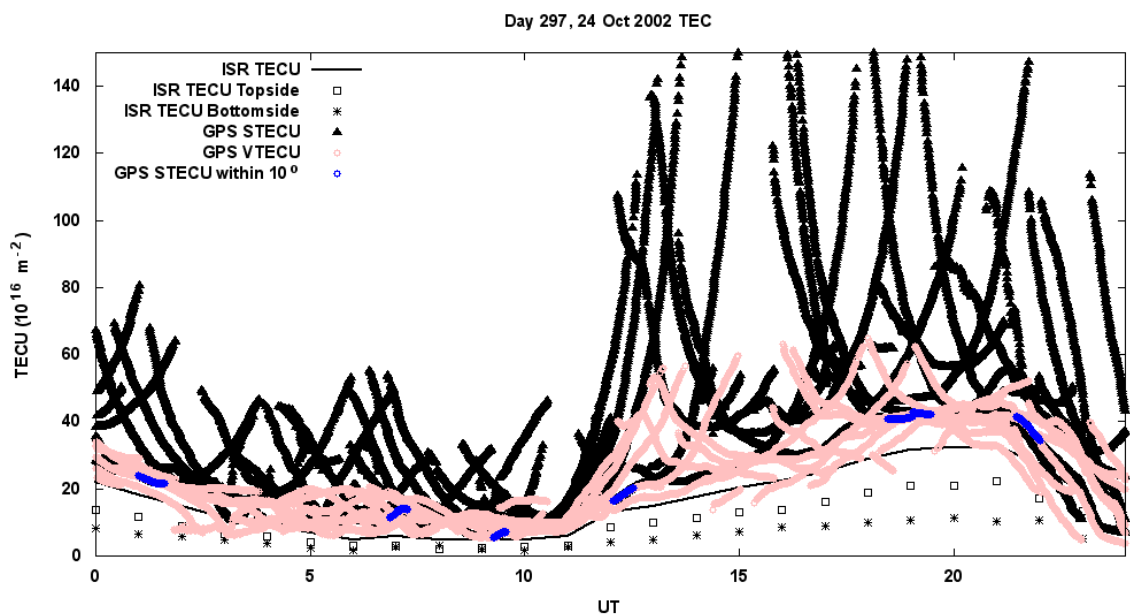


**Figure 6.6.** ISR TEC results compared to STEC and VTEC from GPS for active day 297.

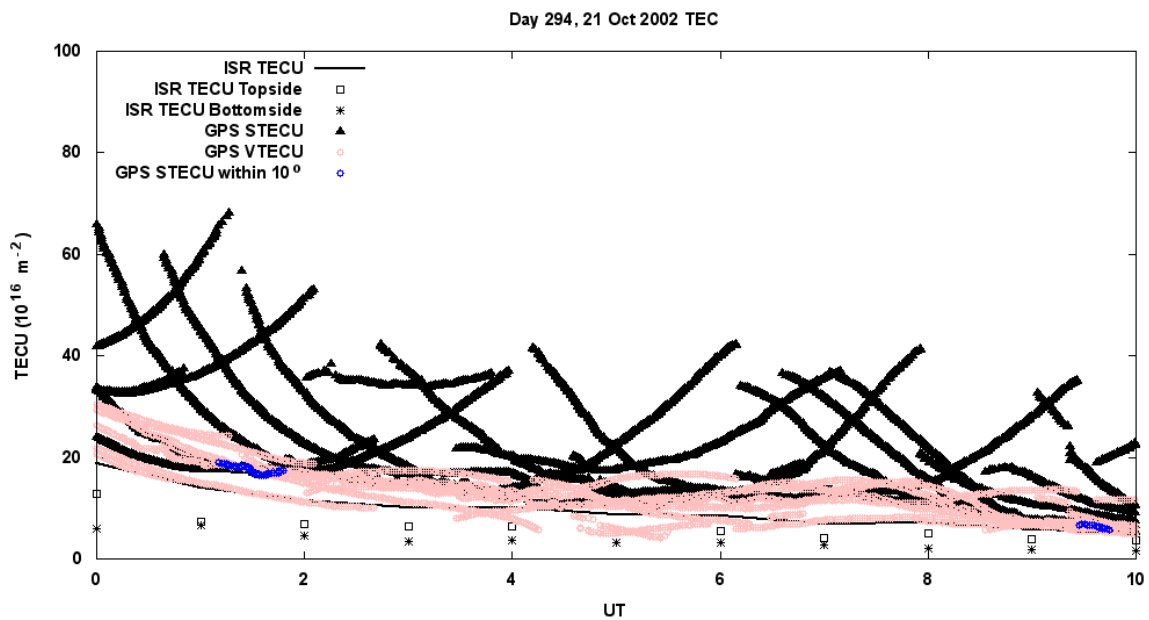


**Figure 6.7.** ISR TEC results compared to STEC and VTEC from GPS for quiet day 294 during nighttime hours 0 - 10 UT.

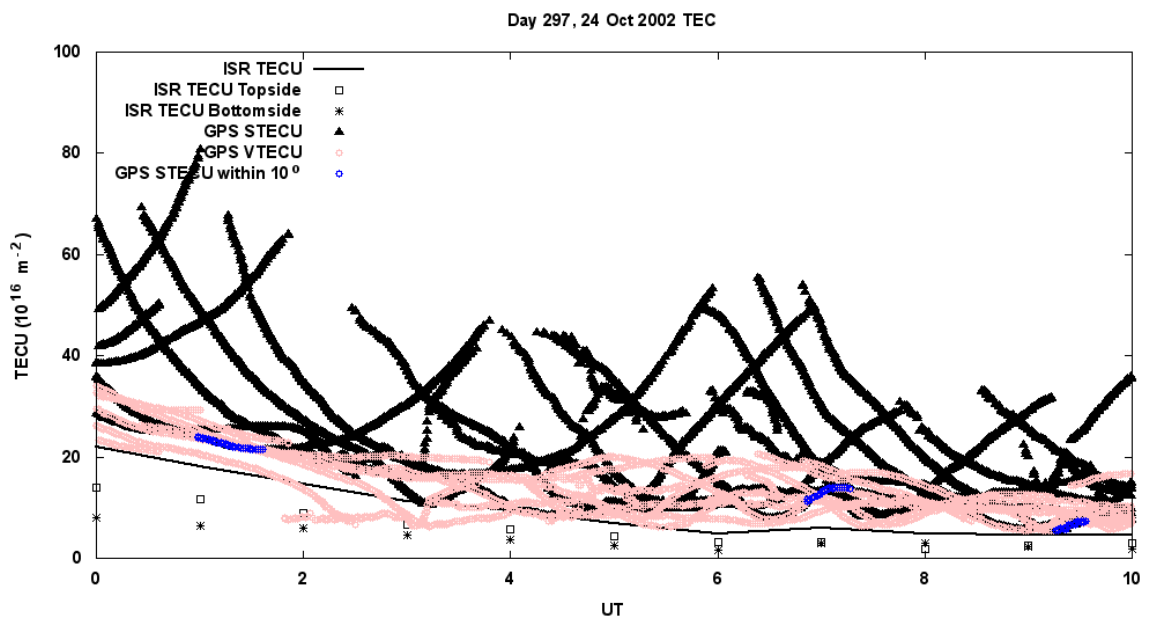


**Figure 6.8.** ISR TEC results compared to STEC and VTEC from GPS for active day 297 during nighttime hours 0 - 10 UT.



Hill ISR and is owned and operated by University of Massachusetts Lowell, Space Science Laboratory. Ionogram data were retrieved from the Lowell Global Ionospheric Radio Observatory Data Center (LGDC) with the Principal Investigator being Prof. B. W. Reinisch of the University of Massachusetts Lowell [*Reinisch and Galkin, 2011*].

An ionosonde is composed of a high-frequency transmitter that transmits short pulses, which are reflected at various layers of the ionosphere. The sounder sweeps from lower to higher frequencies, 1 MHz to as high as 40 MHz [*Lowell Digisonde International, 2015*], and their echoes are received by the receiver and analyzed with an end result displayed in the form of an ionogram, a graph of reflection height (actual time between transmission and reception of pulse) versus carrier frequency ( $f_oF_2$ ) [*NOAA National Centers for Environmental Information, 2016*]. Ionogram-derived characteristics, such as  $f_oF_2$ , are scaled, manually or by computer, typically every 15 minutes. An example of the ionograms used is shown in Figure 6.9.

Hourly ionogram data were collected for reference quiet day 294 and active day 297, keeping consistent with the previous section. If ionogram-derived characteristics were not available for a particular hour, the next or previous ionogram was used, which offsets our ISR data by about 15 minutes. The peak density height,  $h_mF_2$  (unit: km), and  $F_2$  layer critical frequency,  $f_oF_2$  (unit: MHz), are given by the ionograms and are used to determine the peak density,  $N_mF_2$  (unit:  $m^{-3}$ ) by:

$$N_mF_2 = (1.24 \times 10^{10}) \times (f_oF_2)^2 . \quad (6.8)$$

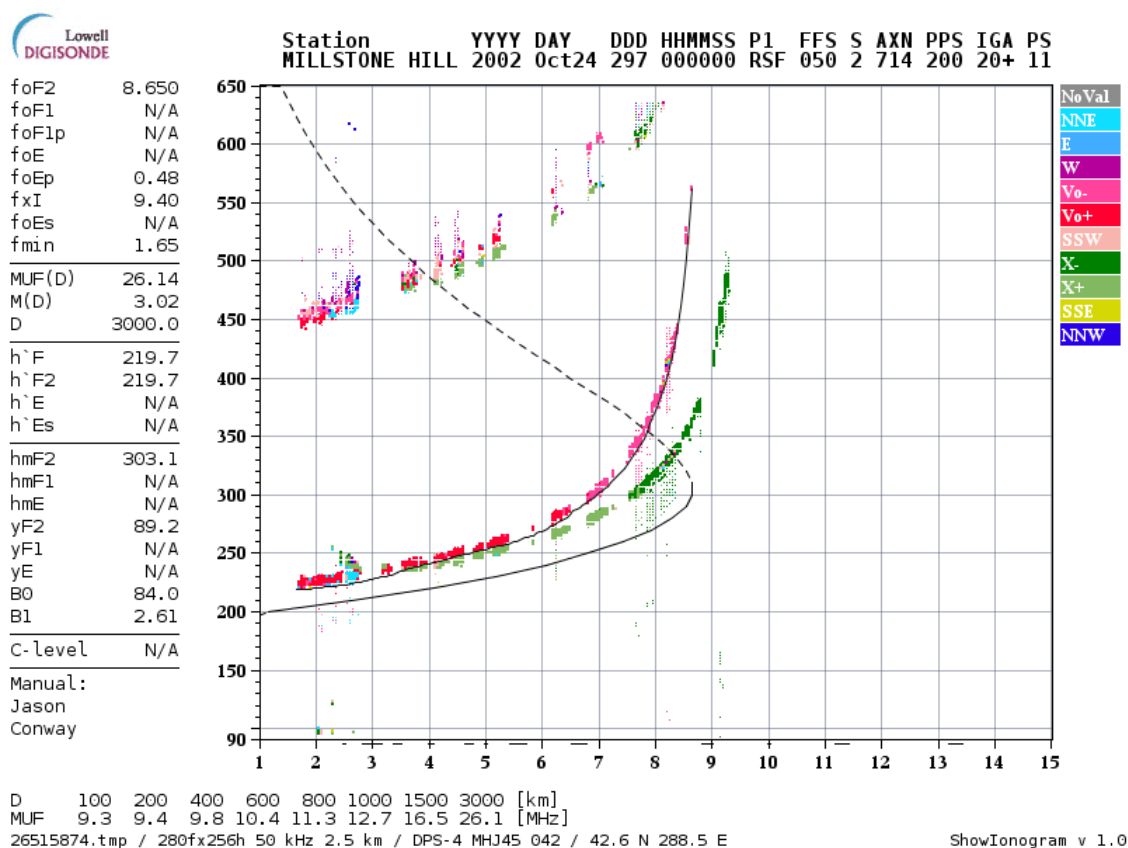


**Figure 6.9.** Ionogram from LGDC, Principal Investigator, Prof. B. W. Reinisch, of the University of Massachusetts Lowell. The solid line is the recorded ionosonde  $f_oF_2$  bottomside data and the dashed line is the inferred topside using ARTIST software, which scales the ionogram and calculates the vertical electron density profile.

Electron density was then hand calculated every 10 km from 100 km to  $h_mF_2$ , keeping consistent with the ISR data, and summed to give total bottomside TEC. The results were then compared to the ISR TEC bottomside calculations from the previous section and are shown in Figure 6.10 for quiet day 294 and Figure 6.11 for active day 297. For both figures, ISR TECU bottomside is represented by (\*) and ionosonde TECU bottomside by (x). The results for both figures are similar, as expected, because both instruments are co-located. Overall, the ionosonde and ISR measurements of bottomside

TEC were in very good agreement throughout the day for both days, with active day 297 having a better overall agreement between the instruments than quiet day 294.

The diurnal variations in TEC from the previous section is apparent in both Figures 6.10 and 6.11, with bottomside TEC having greater daytime values during quiet reference day 294, Figure 6.10, than active day 297, Figure 6.11. Nighttime bottomside TECU is, however, similar in value for both days 294 and 297.

For day 294, the daytime bottomside TEC peak occurs at 18 UT with an ISR value of 19.1 TECU and an ionosonde value of 17.2 TECU. For day 297, the daytime bottomside TEC peak occurs at 20 UT with an ISR value of 11.2 TECU and an ionosonde value of 11.7 TECU.

The largest discrepancies between the two different instrument results occur during nighttime hours 0 – 10 UT, with the most notable difference occurring on active day 297 between 05 – 10 UT. The discrepancies can be explained by the methodology of how the different instruments make electron density measurements. During nighttime, depletion of ionospheric electron density occurs, and so the critical frequency in the bottomside ionosphere may drop below the normal minimum scanning frequency of 1 MHz for ionosondes. The ionospheric critical frequency,  $f_oF_2$ , may drop low enough to the medium frequency range of AM radio broadcast bands, which extend up to 1.7 MHz according to the National Telecommunications and Information Administration's radio spectrum [2003] and can create noise signals in ionosondes.

The Lowell Digisonde International instrument description page [2015] describes how the physical parameters of the ionospheric plasma influence the way radio waves

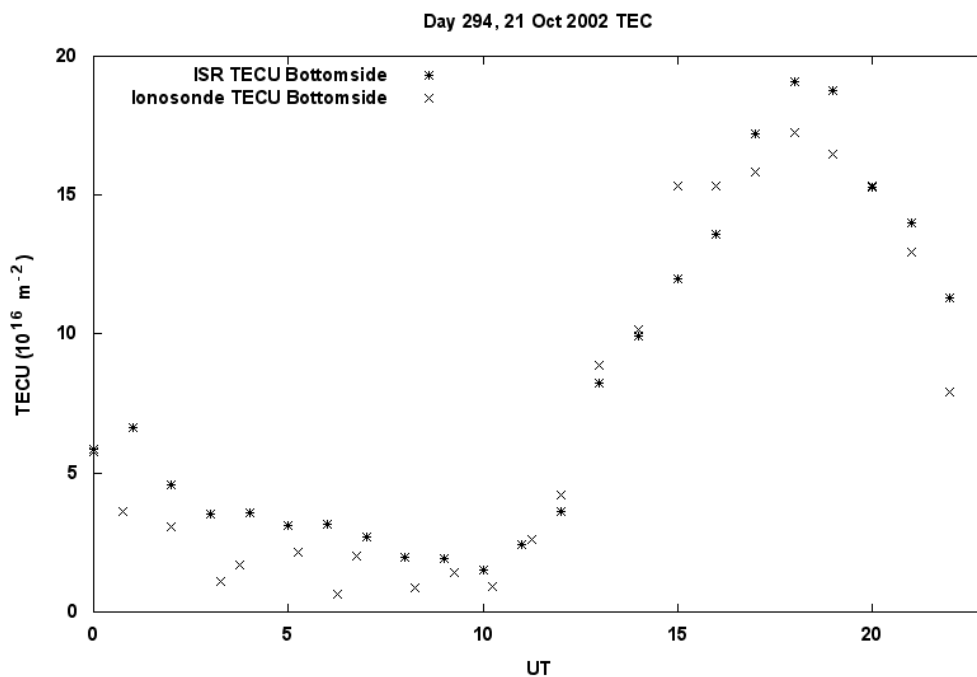


**Figure 6.10.** Quiet day 294 ionogram-derived bottomsides TECU versus ISR TECU bottomsides.

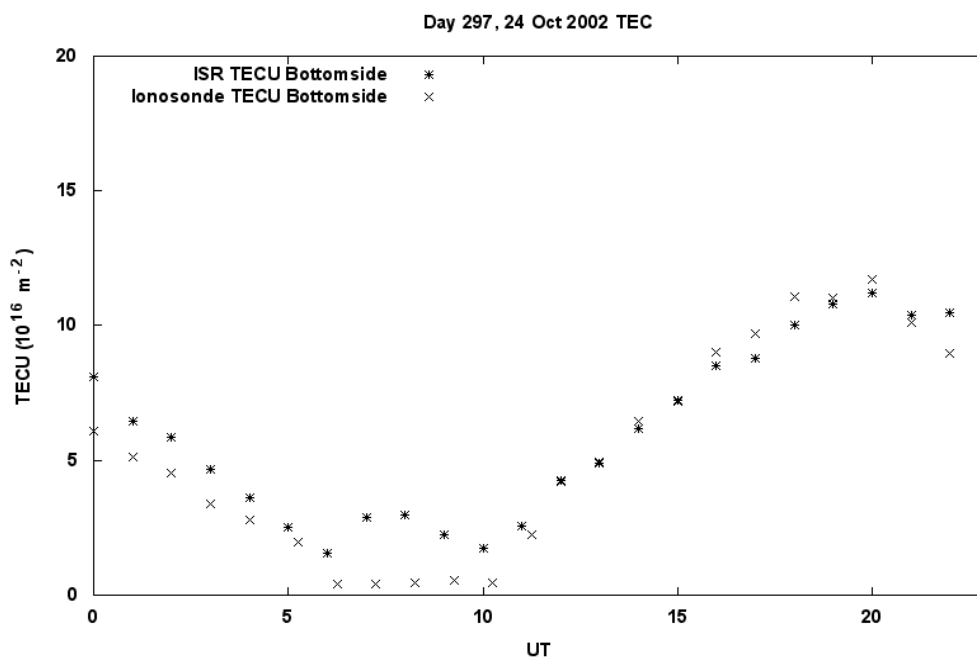


**Figure 6.11.** Active day 297 ionogram-derived bottomsides TECU versus ISR TECU bottomsides.

reflect from or pass through the ionosphere, with the only variable driving the relative refractive index of the ionospheric plasma being the density of the free electrons. Therefore, if the scanning radio frequency of the ionosonde is above the maximum plasma resonance frequency [McNamara *et al.*, 2011], the wave is never reflected and can penetrate the ionosphere and propagate into outer space. This would explain why the availability of ionogram data is sparse during nighttime hours. And may even explain the discrepancies between the ISR and ionosonde data.

Further, we investigated the major differences between ISR and ionosonde data for both days 294 and 297 by examining the peak density height,  $h_mF_2$ , shown in Figure 6.12. The left side of Figure 6.12, shown in green, is  $h_mF_2$  for quiet day 294 and the right side, shown in blue, is active day 297. The circles represent ionosonde determined  $h_mF_2$  and the triangles, ISR determined  $h_mF_2$ . At first glance the two measurements appear to track similarly for both days; with the notable exception of day 297 during hours 05 – 10 UT, which was noted above in Figure 6.11 and will be discussed in greater detail below. Overall, ISR reports a higher  $h_mF_2$  throughout the day compared to that of an ionosonde with the largest differences between the two measurements occurring during nighttime hours. For both days 294 and 297, the average difference between the two is between 30 – 40 km excluding the exception mentioned above.

Nighttime hours 05 – 10 UT on active day 297 show a remarkable difference between ISR and ionosonde data. Day 297 sees a strong ionospheric storm according to standard indices of geomagnetic activity, see criteria listed in Chapter 5, section 2 and defined in Appendix A, but it is not reflected in ionosonde data. Three-hour Kp values and

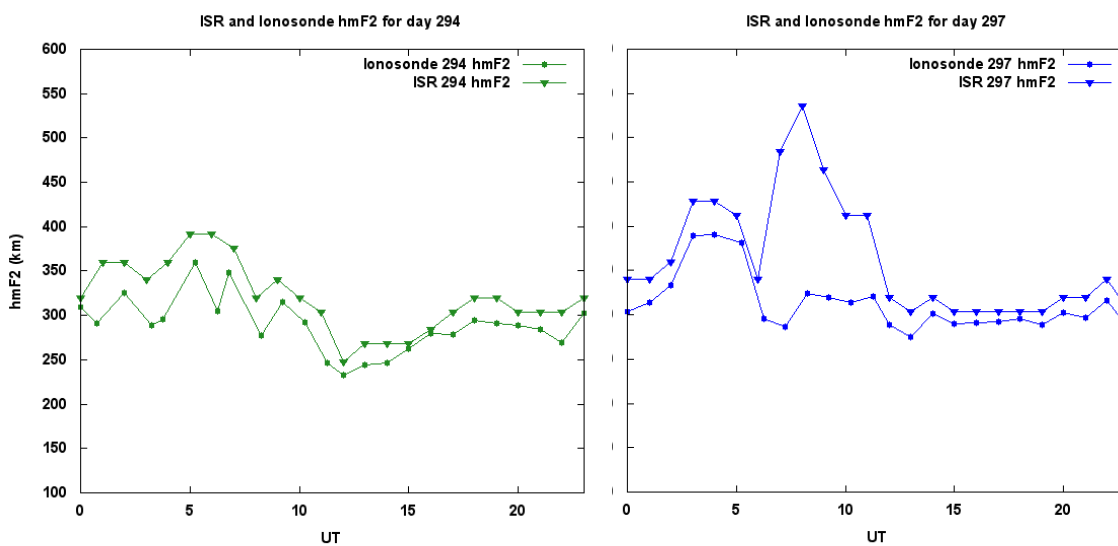


**Figure 6.12.**  $h_m F_2$  for quiet day 294 (green) and active day 297 (blue).

elevated PCN values indicate the storm began at 0 UT on day 297 with values reaching a G2 level (moderate geomagnetic storm according to NOAA Space Weather Scales) by 03 UT. PCN values nearly double by 11 UT. To see the ionospheric response to this magnetic storm, we examine the electron density for hours 05 – 10 UT. Figure 6.13 shows the results.

The profiles in Figure 6.13 show a relatively broad, flat peak that extends from 350 km to over 500 km with a constant value of peak density, especially for 08 and 09 UT. At 07 and 08 UT, the ISR analysis can find a peak anywhere in the altitude range, which is 500 and 550 km, respectively, and over 200 km higher than  $h_m F_2$  at 06 UT. The ionosonde, in contrast, has a scanning ability that works from the lower altitudes towards a peak; hence, at 09 UT, a reading at the 350 km altitude corresponds to a maximum density and the sounding frequency contains no further information from higher altitudes.

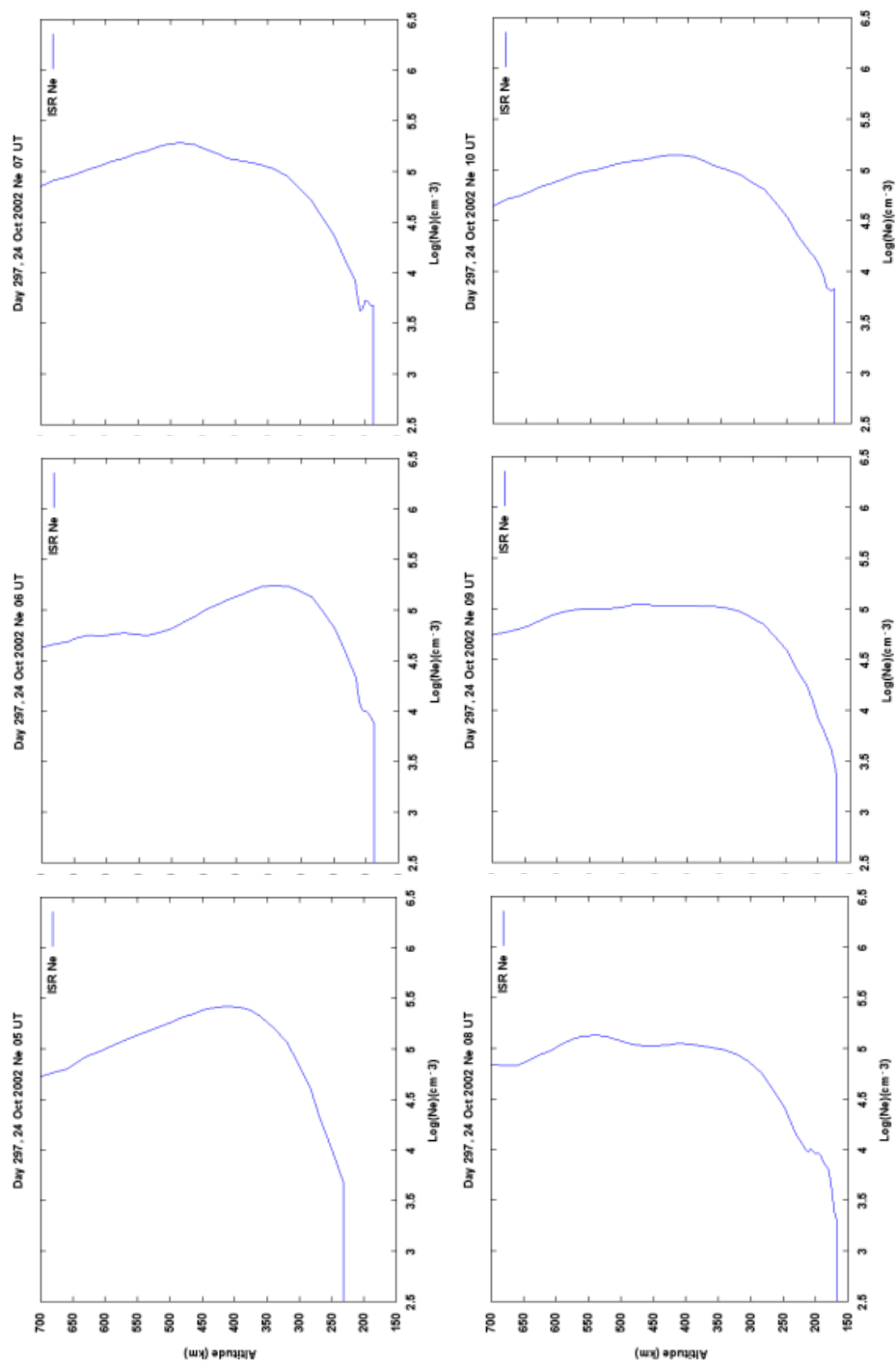


**Figure 6.13.** Electron density profiles for day 297, hours 05 – 10 UT in consecutive order from top left to bottom right.

Because the ionosondes only sound at discrete frequencies, the highest frequency returning an echo is considered to be  $f_oF_2$ , but it would always lie in a frequency range of the last (critical) frequency plus an additional extraordinary critical frequency. Being less than or equal to  $f_oF_2$  also implies the corresponding height will be less than or equal to  $h_mF_2$  as seen in Figure 6.12.

When a storm occurs in the ionosphere, it is due to the increased energy flow from the solar wind into the magnetosphere. Due to the enhanced magnetospheric electric field, particles are accelerated out of the ionospheric via flux tubes and into the equatorial plane [Kivelson and Russell, 1995]. This explains why we see an increased ionospheric slab thickness ( $\tau$ ) and subsequent increase in  $h_mF_2$  in Figure 6.13, which is discussed in great detail in section 6.4.3. With the increase in  $\tau$ , the electron density profiles become flat in shape with no real distinct  $F_2$  layer peak and may raise the question of determining the actual  $h_mF_2$  altitude, how ionosondes see a real problem with the fixed scanning frequencies, and how they are scaled via top and bottom traces of the  $F_2$  layer.

## **6.4. Our Unique Methodology**

This section combines what we've learned thus far with an attempt to devise a method of determining topside  $T_e$  that will allow us to reconstruct the topside ionospheric profile.

### **6.4.1. TEC Topside Percentage**

Section 6.1 gave insight of how much TEC can be allocated to the topside ionosphere by the results shown in Figures 6.1 and 6.2. For both days, quiet day 294 and



active day 297, TEC topside ( $TEC_t$ ) was greater than TEC bottomside ( $TEC_b$ ) for each hour during the entire duration of the day/night.

To find out whether or not this held true for all days in our data set, the percentage of  $TEC_t$  from TEC was determined hourly for each day then averaged over the entire day. The results are shown in Figure 6.14. The overall  $TEC_t$  average was found to be 65% of TEC and falls within one standard deviation of each day of our dataset with only nine out of 29 days slightly offset from the overall average line.

Figures 6.15 and 6.16 break down the daily  $TEC_t$  percent averages into solar noon and solar midnight hours with the associated daily standard deviation. Noon hours were from 13 – 18 UT, which are composed of the three hours prior to noon and three hours following noon. The same approach was done for midnight hours, 01 – 06 UT. The overall  $TEC_t$  average for noon hours and  $TEC_t$  average for midnight hours is designated by the red line in figures 6.15 and 6.16, respectively.

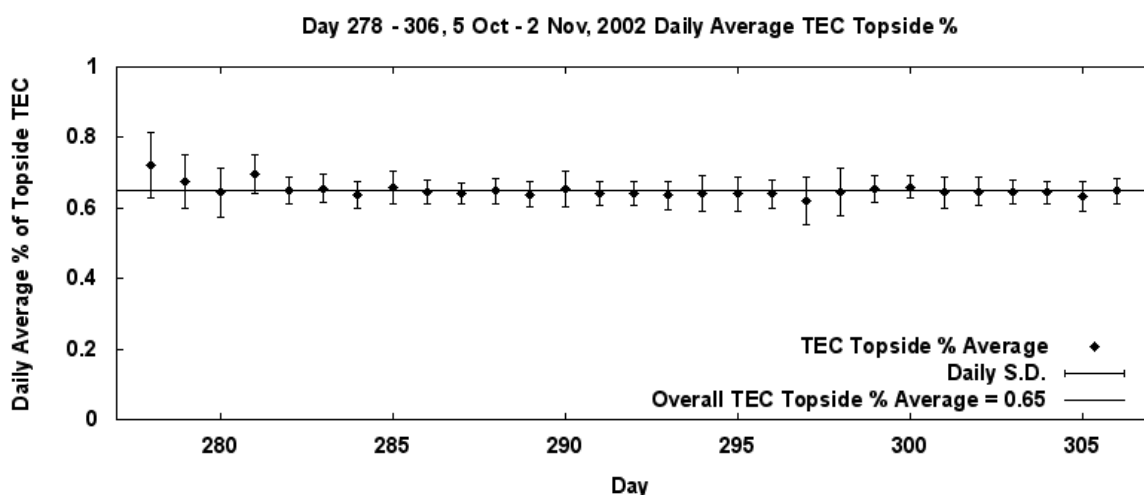


**Figure 6.14.** Daily average percentages of topside TEC and associated daily standard deviation for days 278 – 306.

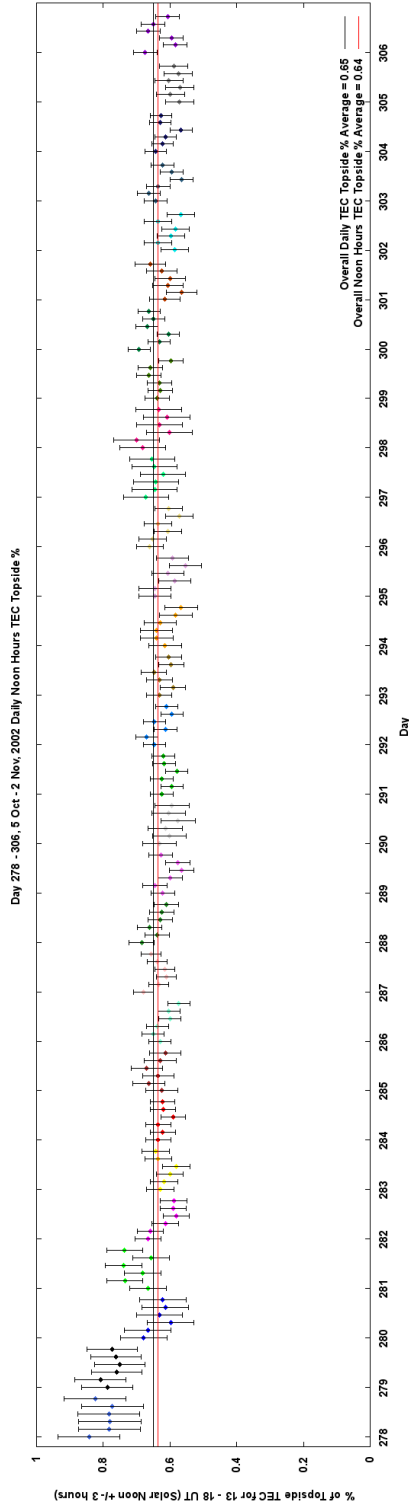


**Figure 6.15.** Daily average percentages of topside TEC for noontime hours 13 – 18 UT and associated daily noontime hours standard deviation for days 278 – 306.

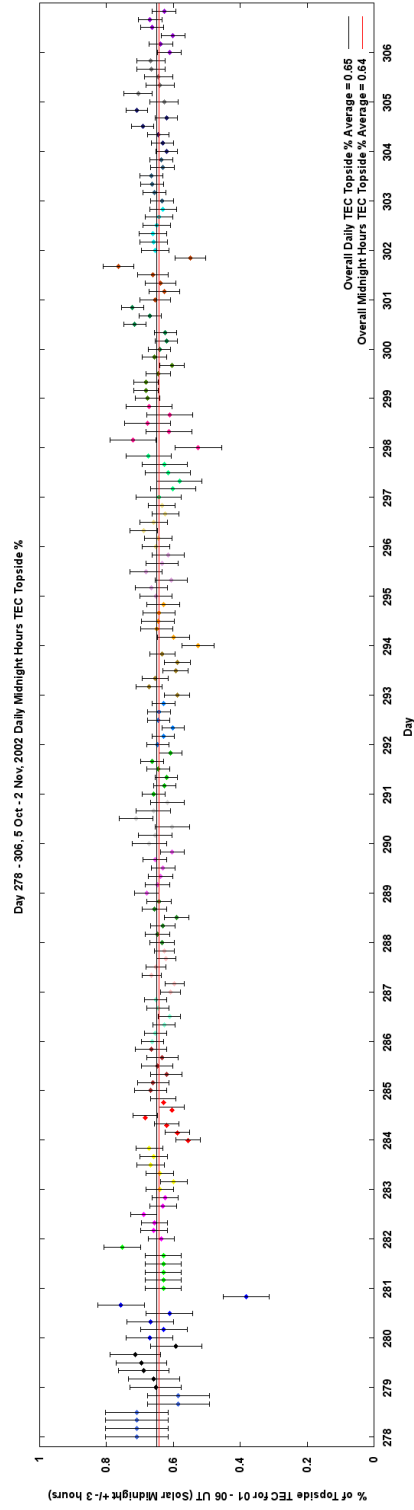


**Figure 6.16.** Daily average percentages of topside TEC for midnight hours 01 - 06 UT and associated daily midnight hours standard deviation for days 278 – 306.

Figure 6.15 shows an overall  $TEC_t$  of 63.6% for daily noontime hours compared to the overall daily  $TEC_t$  of 65% found in Figure 6.14. There are several outliers, with days 278 and 279 being most apparent to not fall within one standard deviation of the overall noontime hour average. Days 278 and 279 may offset the overall noontime average line with large discrepancies in percentage values compared to noontime hours for the following days in our dataset. The line might be better fit if these outliers were removed. Nevertheless, a majority of the data is contained within one standard deviation of the overall noontime hour average line and daily average line.

Midnight hours shown in Figure 6.16 had a better result with an overall  $TEC_t$  of 64.3% compared to the overall daily  $TEC_t$  of 65% found in Figure 6.14. There are not nearly as many outliers compared to noontime hours; however, there are several significant hours that did not fall within one standard deviation, namely day 280. Despite the outliers, the overall midnight hour average line and overall daily average line contain a majority of the data.

For both noontime and midnight hour cases, the daily average line for  $TEC_t$  can be considered a good fit for a simple model. Therefore, we can conclude that 65% of TEC is allocated to the topside ionosphere. If we know TEC we can solve for  $TEC_t$  by this simple relationship:

$$TEC_t = 0.65 \times TEC , \quad (6.9)$$

or, if we know  $TEC_b$  we can determine TEC:

$$TEC = \frac{TEC_b}{0.35} . \quad (6.10)$$

Knowing only  $TEC_b$  we can plug equation 6.10 into 6.9 and solve for  $TEC_t$ :

$$TEC_t = 0.65 \times \frac{TEC_b}{0.35} . \quad (6.11)$$

This relationship now lets us solve for either  $TEC$ ,  $TEC_t$ ,  $TEC_b$  given only one measurement by either GPS  $TEC$ , ISR  $TEC$ , or ionosonde  $TEC_b$  by the simple equation:

$$TEC = TEC_t + TEC_b . \quad (6.11)$$

#### **6.4.2. Determining Topside TEC from Ionosondes**

This section builds off the results from 6.3 using what we have found in 6.4.1. The previous section concluded with a simple equation to solve for  $TEC_t$  only knowing  $TEC$  or  $TEC_b$ .  $TEC_b$  can be determined from ionograms with the use of equation 6.11, we can now solve for  $TEC_t$  or use equation 6.10 to solve for  $TEC$ . Figures 6.10 and 6.11 are replotted using this new relationship to solve for  $TEC$ , which are compared to ISR. The results are shown in Figure 6.17 for day 294 and Figure 6.18 for day 297. The black solid line represents ISR determined  $TEC$ , ionosonde derived  $TEC$  by the blue line, ISR  $TEC$  bottomside by the black asterisks, and lastly, ionosonde bottomside  $TEC$  by blue Xs.

Interestingly, Figure 6.18 for active day 297 shows better results between ISR and ionosonde determination of  $TEC$  and  $TEC_b$  compared to quiet day 294, Figure 6.17. In Figure 6.17 there is a large discrepancy between ISR and ionosonde  $TEC$  between nighttime hours 2 – 8 UT and day time hours 15 – 18 UT and again around 22 UT. In Figure 6.18, there is one significant difference between the two during nighttime hours 6 – 10 UT.

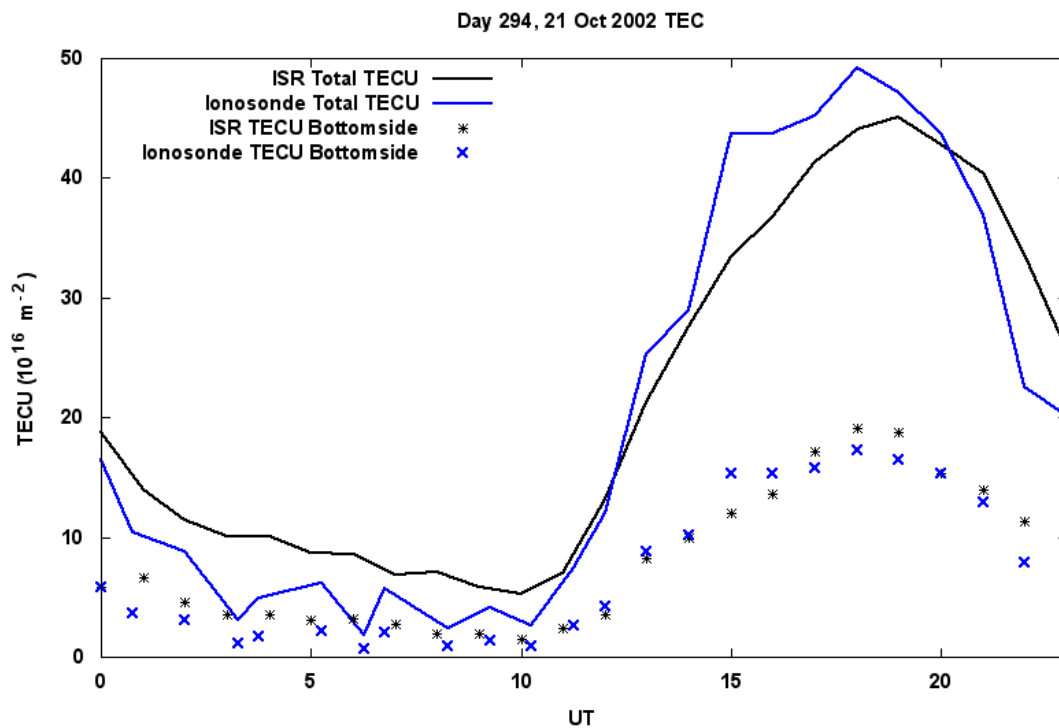


**Figure 6.17.** Quiet day 294 ionogram-derived TECU (blue) versus ISR TECU (black).

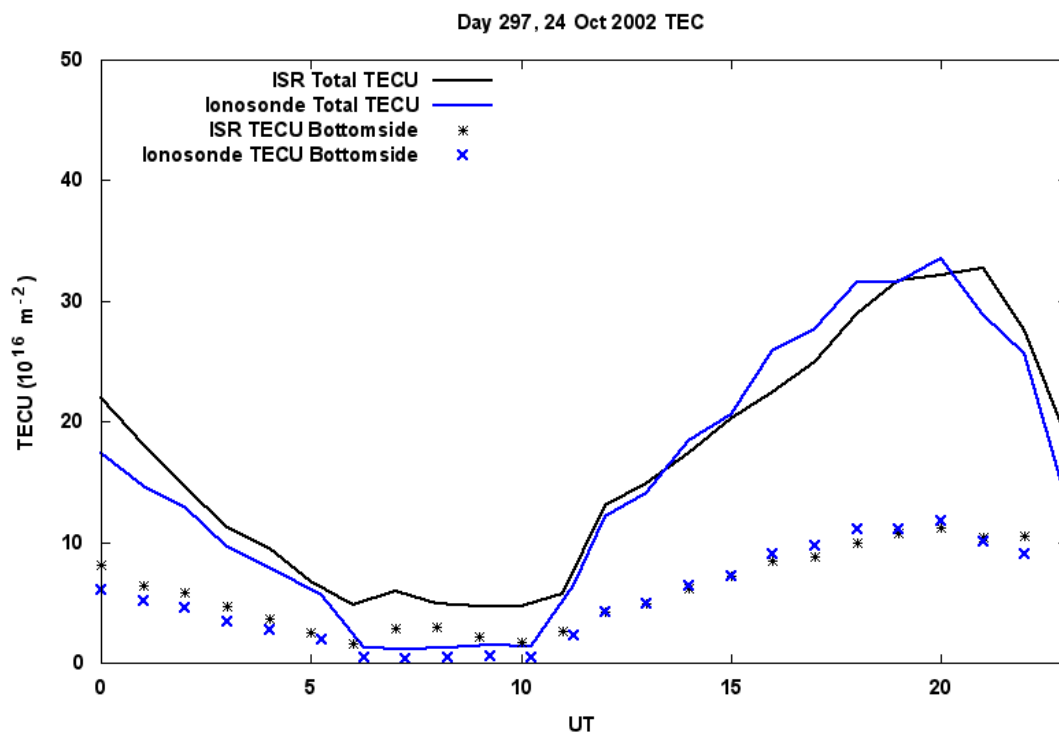


**Figure 6.18.** Active day 297 ionogram-derived TECU (blue) versus ISR TECU (black).

Overall, the comparisons between ISR and ionosonde TEC and  $TEC_b$  are in good agreement for days 294 and 297. Both days show similar behavior for either ionosonde or ISR methods with the alignment of the peaks and troughs in TEC and  $TEC_b$  occurring at the same UT, as well as their comparable TECU values.

### 6.4.3. Correlation between $h_mF_2$ and $\tau$

A new correlation has been found between peak density layer height,  $h_mF_2$  and slab thickness,  $\tau$ . Slab thickness was discussed in Chapter 2, section 5 as the ratio of TEC to the peak density value ( $N_mF_2$ ):

$$\tau = \frac{TEC}{N_mF_2}, \quad (6.12)$$

where  $\tau$  represents the equivalent thickness of the ionosphere having a constant uniform density equal to that of the  $F_2$  peak. It also describes the nature of the distribution of ionization at a specific location thickness and relates the shape of the electron density profile; the smaller  $\tau$  is, the sharper the profile [Amayenc *et al.*, 1971]. This means there is direct proportionality between slab thickness and scale height.

What we stumbled on was that  $h_mF_2$  and  $\tau$  show some sort of correlation. Day 294 is shown in Figure 6.19 and day 297, Figure 6.20. The black line represents  $h_mF_2$  and the gray line,  $\tau$ . Both figures show that when the  $h_mF_2$  increases,  $\tau$  increases and when  $h_mF_2$  decreases,  $\tau$  decreases. There is a large variation in  $h_mF_2$  on active day 297, Figure 6.20, with a rapid decrease at 6 UT followed by the sharp increase at 7 UT; however, it is not reflected well in  $\tau$ . Overall, there is a strong correlation between the two parameters throughout the day for both days.

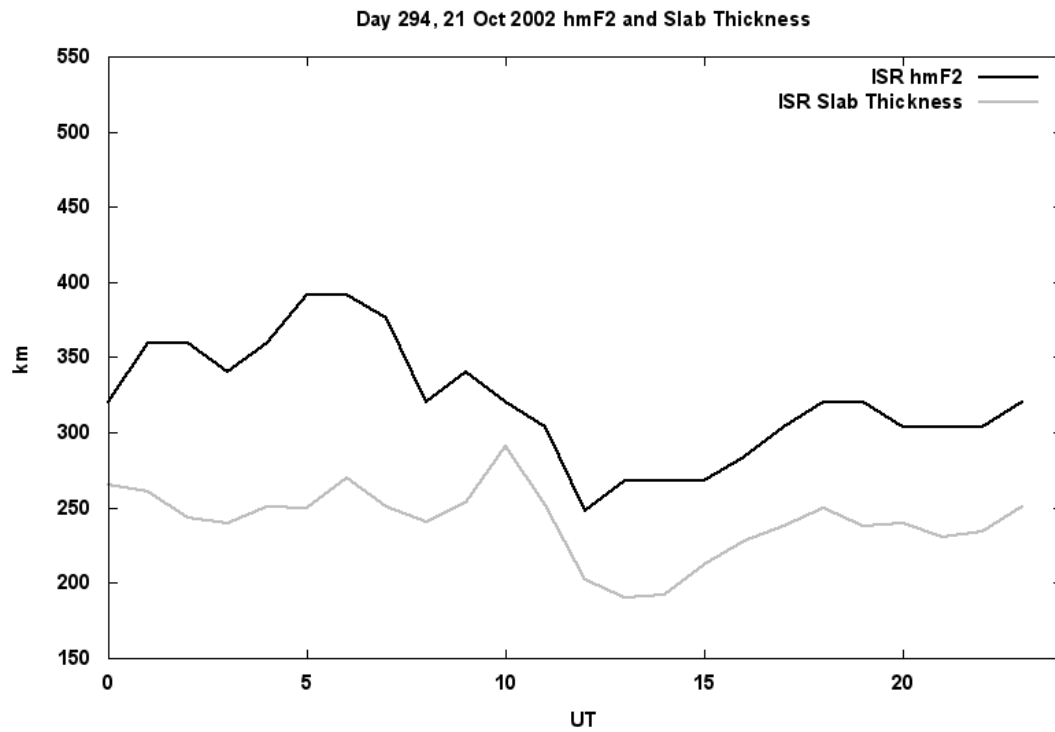


**Figure 6.19.** Quiet day 294 ISR relationship between  $h_mF_2$  and slab thickness.

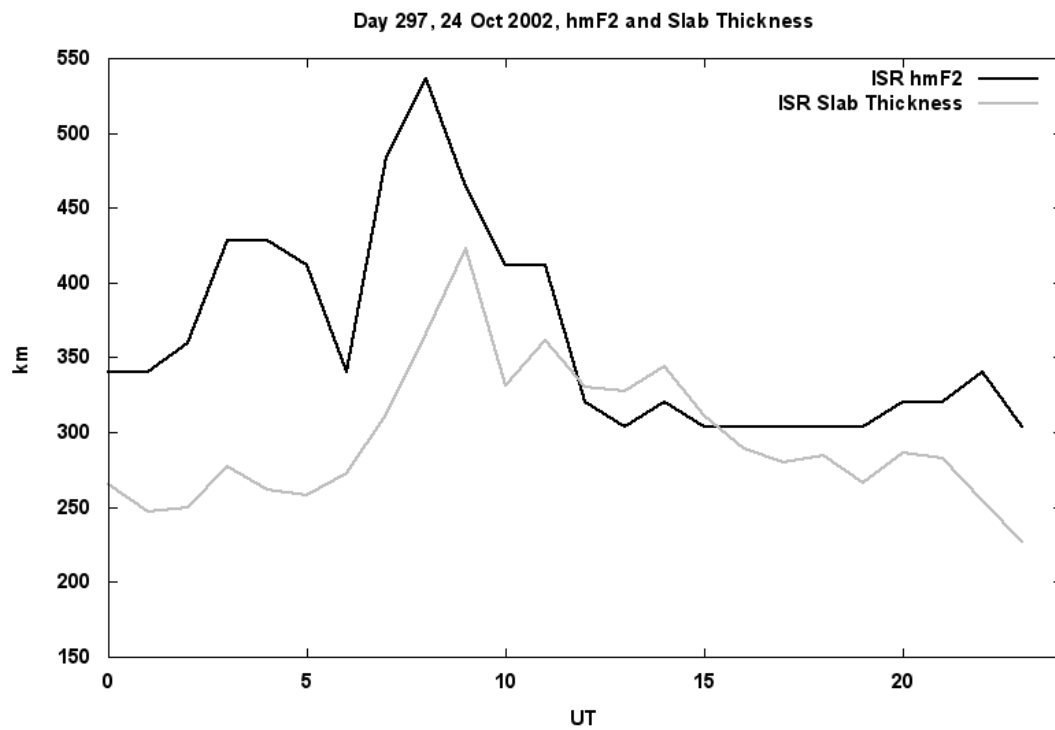


**Figure 6.20.** Active day 297 ISR relationship between  $h_mF_2$  and slab thickness.

As discussed in Chapter 2, there have been many studies done to understand the physical meaning behind  $\tau$ , which still remains unclear; however, this new correlation may provide new insight as to why the thickness of the ionosphere increases when the peak layer altitude increases. This new correlation of  $h_m F_2$  to  $\tau$ , will now be referred to as  $\kappa$ :

$$\kappa = \frac{h_m F_2}{\tau}, \quad (6.13)$$

and was thoroughly inspected throughout the data campaign and is shown in Figures 6.21, 6.22, and 6.23. Figure 6.21 shows the individual daily averages of  $\kappa$  and the overall dataset average to equal 1.28. This means that one can expect the peak density altitude ( $h_m F_2$ ) to be 28% greater than that of the thickness of the ionosphere ( $\tau$ ). All but 3 out of 29 days fall within one standard deviation of our overall average line.

Figures 6.22 and 6.23 separate daily  $\kappa$  ratio averages into solar noon and solar midnight hours with the associated daily standard deviation. Keeping consistent with

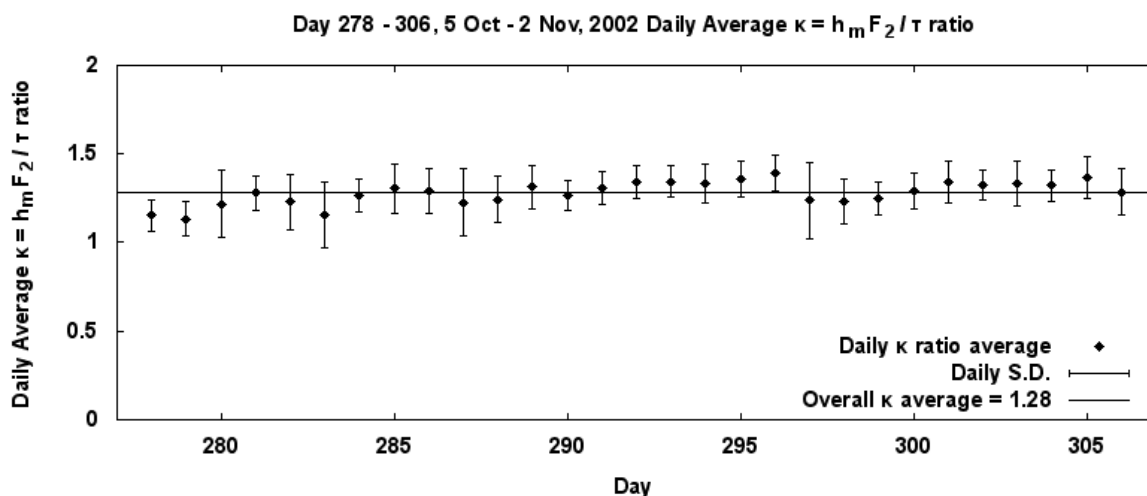


**Figure 6.21.** Daily average  $h_m F_2 / \tau$  ratio and associated daily standard deviation for days 278 – 306.



noontime hours and  $\kappa$  ratio average for midnight hours is designated by the red line in Figures 6.22 and 6.23, respectively. Because there were noticeable variations from the average lines, it was beneficial to see if ionospheric active and quiet periods were responsible. For this, consecutive quiet days (at least two or more) are highlighted in green, the reference active day, 297, in red, and remaining active days in black with the notable exception of quiet days 302 and 305, which did not meet the criteria for consecutive quiet periods shown in green. The results for the case of active days versus quiet days were very noticeable in both Figures 6.22 and 6.23.

Figure 6.22 has an overall  $\kappa$  ratio of 1.23 for daily noontime hours, a 0.4% decrease compared to the overall daily  $\kappa$  ratio of 1.28 found in Figure 6.21. There are several significant outliers that can explain the deviation from the overall average line, most of them being active days, especially reference active day 297. For active days, 65% of the noontime hours are within one standard deviation of either the daily noontime and/or overall daily average lines and 92% being the case for noontime hours during quiet days.

It seems as if during active days,  $\kappa$  ratio values approach one, meaning the peak density height is equal to the thickness of the ionosphere. Looking at Figure 6.20,  $\tau$  becomes greater than and equal to  $h_m F_2$  briefly during noontime hours, which is reflected here in Figure 6.22. This may be explained by the rapid increase in photoionization after sunrise coupled with an ionospheric storm and compositional changes, as well as a rapid decrease in  $h_m F_2$  as discussed in Chapter 3, section 3.1, and Chapter 4, section 4.2.

Midnight hours shown in Figure 6.23 had a larger deviation from the overall daily  $\kappa$  ratio of 1.28 than noontime hours with a  $\kappa$  ratio of 1.38, an 8% increase; however, more

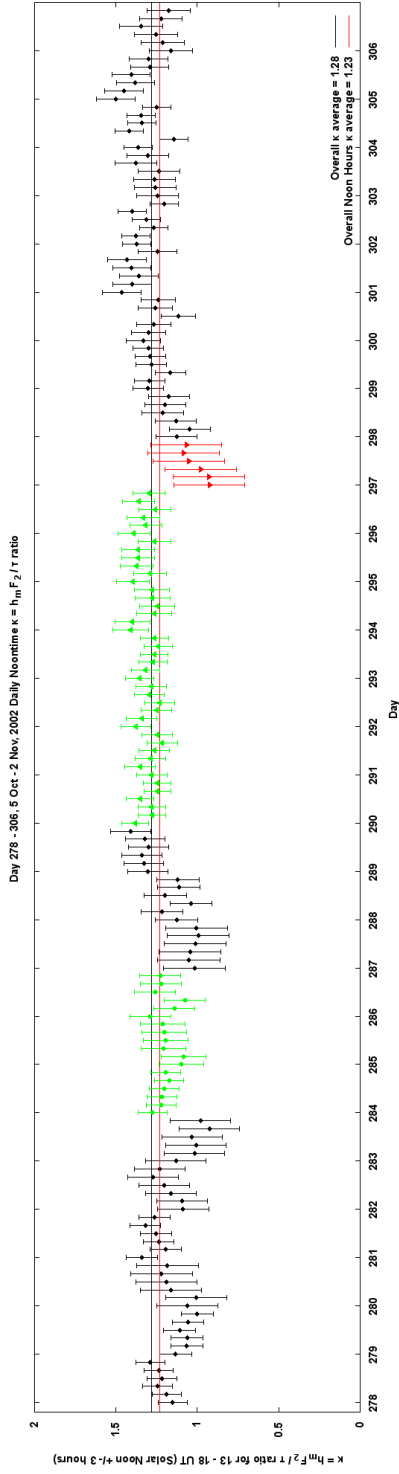


**Figure 6.22.** Daily average ratios of  $h_m F_2$ /Slab Thickness for noontime hours 13 – 18 UT and associated daily noontime hours standard deviation for days 278 – 306. Quiet consecutive quiet days (at least two or more) are highlighted in green, the reference active day, 297, in red, and remaining active days in black with the exception of quiet days 302 and 305.

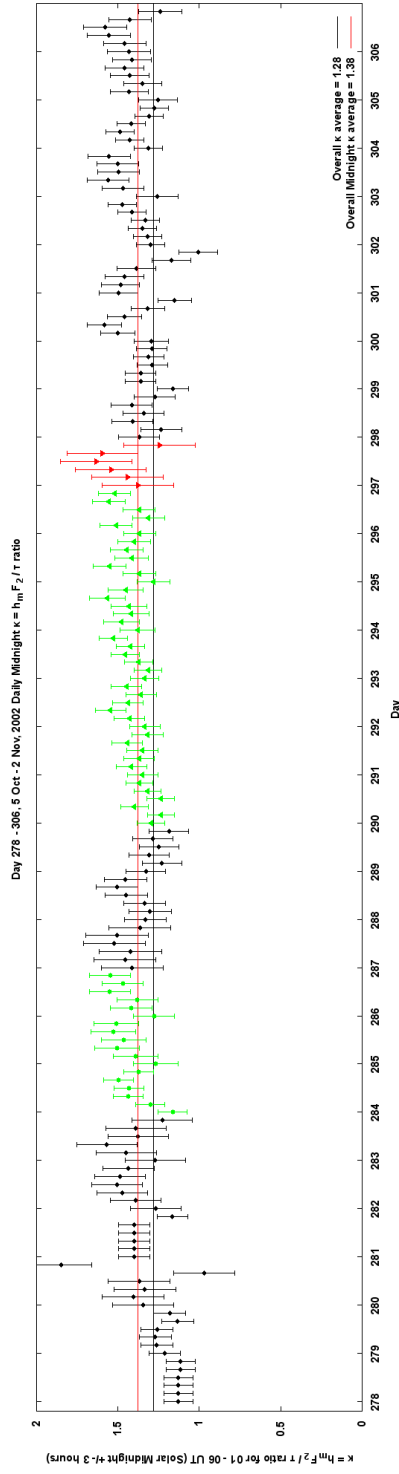


**Figure 6.23.** Daily average ratios of  $h_m F_2$ /Slab Thickness for midnight hours 01 - 06 UT and associated daily midnight hours standard deviation for days 278 – 306. Quiet consecutive quiet days (at least two or more) are highlighted in green, the reference active day, 297, in red, and remaining active days in black with the exception of quiet days 302 and 305.

active day midnight hours fell within one standard deviation of either the midnight hour average line and/or the overall daily average line at 79% compared to 65% for noontime hours. Only 82% of quiet day midnight hours fell within one standard deviation of either the midnight hour average line and/or the overall daily average, a 10% decrease compared to noontime hours. This might be expected as there is a larger discrepancy in the two different average lines than at noontime hours, so we can expect to see less hours fall within one standard deviation of the overall average line and more hours fall on the midnight hours  $\kappa$  ratio average line.

It is again interesting to point out that during midnight hours for both active and quiet days,  $\kappa$  ratio values approach 1.5 at times in Figure 6.23 when they approached one in Figure 6.22 for noontime hours. This may be explained by the well observed rise in  $h_m F_2$  during nighttime hours with the loss of daytime photoionization, but may suggest a lag in or subtle decrease of the ionospheric thickness. Signatures of this can be found in both Figures 6.19 and 6.20 with the largest differences in  $h_m F_2$  and  $\tau$  occurring during midnight hours 01 – 06 UT.

Still, a majority of the data is well contained within one standard deviation of the overall daily  $\kappa$  ratio average line, though, I would suggest proceeding with caution when specifically discussing noontime and midnight hours, especially during active and quiet days. The overall daily  $\kappa$  ratio average of  $h_m F_2 / \tau = 1.28$  can be considered a good fit for a simple model ionosphere and supports the undeniable correlation between  $h_m F_2$  and  $\tau$ , which is very clear in the results.

## 6.5. Discussion

This chapter outlines our topside reconstruction technique that will be applied to our data in Chapter 7. TEC data collected from a GNSS receiver located in Westford, Massachusetts had conclusive results compared to our ISR TEC data collected at Millstone Hill, especially using STEC when the GPS satellite had an inclination angle of  $10^\circ$  or less. This suggests the methodology of using TEC data from GPS could be a good representation of the topside TEC contribution to the topside ionosphere; however, the plasmaspheric contribution cannot be ignored.

Next, bottomside ionosonde data were collected from the Lowell GIRO Data Center [Reinisch and Galkin, 2011] for Millstone Hill and used to calculate TEC for the bottomside ionosphere. The new relationship found between TEC,  $TEC_t$ , and  $TEC_b$  was established in section 6.4.1 and applied to successfully determine TEC and  $TEC_t$  using only ionogram data. The initial results are promising; however, it must be noted that the unavailability of ionogram data during nighttime hours limits our study for comparison, especially during diffusive equilibrium conditions which is favorable for determining electron temperature trends.

For the first time, slab thickness, which is directly proportional to scale height, was found to be correlated to  $h_mF_2$  and introduced as a new index,  $\kappa$ . Ultimately,  $\kappa$  is a relationship between TEC,  $N_mF_2$  and  $h_mF_2$ , and can be a very useful tool for describing the topside ionosphere and subsequently, scale height.

Our unique methodology found in section 6.4 will be used in conjunction with a Chapman profile to recreate the topside ionosphere using ionosonde data and compared to

both GPS STEC of  $\phi$  less than  $10^\circ$  and ISR data. As discussed in section 6.2, GPS STEC of  $\phi$  less than  $10^\circ$  offers a true representation of TEC directly above Millstone Hill without needing to factor in the mapping function correction, which makes standard ionospheric assumptions, such as a constant ionospheric thickness of 350 km. And because GPS satellites take TEC measurements approximately 19,400 km higher than ISR measurements, this will also allow us to properly evaluate the plasmaspheric contribution. GPS TEC data will be used in conjunction with ionosonde data, which provides peak parameters not available from GPS VTEC:  $N_mF_2$  and  $h_mF_2$ . Also, the discrepancies found in ionosondes compared to ISR must be accounted for such as Figure 6.12, which suggests ionosondes continually underestimate  $h_mF_2$  values and must be adjusted for the purpose of this study.

## CHAPTER 7

### RECONSTRUCTED TOPSIDE ELECTRON DENSITY PROFILE

#### 7.1. Introduction

This chapter applies our scale height trend analysis results found in Chapter 5 and topside reconstruction technique outlined in Chapter 6. Our results thus far suggest scale height calculation techniques during nighttime hours and quiet geomagnetic activity should be in diffusive equilibrium allowing us to calculate an appropriate scale height using data only containing density information with the end goal of obtaining topside temperature trends.

This chapter will begin by discussing how ionogram data collected from the ionosonde used in this study was scaled to Millstone Hill's ISR. Next, the ionosonde bottomside TEC values calculated in Chapter 6 will be used for the reconstruction of the topside by using the relationship found between TEC,  $TEC_t$ , and  $TEC_b$  in Chapter 6 section 4.1 and a Chapman profile technique described in Chapter 2, sections 2 and 6. The results will then be analyzed and compared to ISR electron density profile measurements.

When the comparisons are complete and the correct Chapman profile is determined, the Chapman scale heights will then be calculated. This will lead into a determination of the topside ionospheric plasma temperature trends. For the first time, a possible relationship may be found between plasma temperature trends by only using knowledge of density parameters:  $N_mF_2$ ,  $h_mF_2$ , and TEC.

Finally, this chapter will ultimately evaluate whether or not the methodology of using ionosonde bottomside TEC combined with TEC calculated from ISR (or by GPS

TEC) could be a good representation of the topside ionosphere.

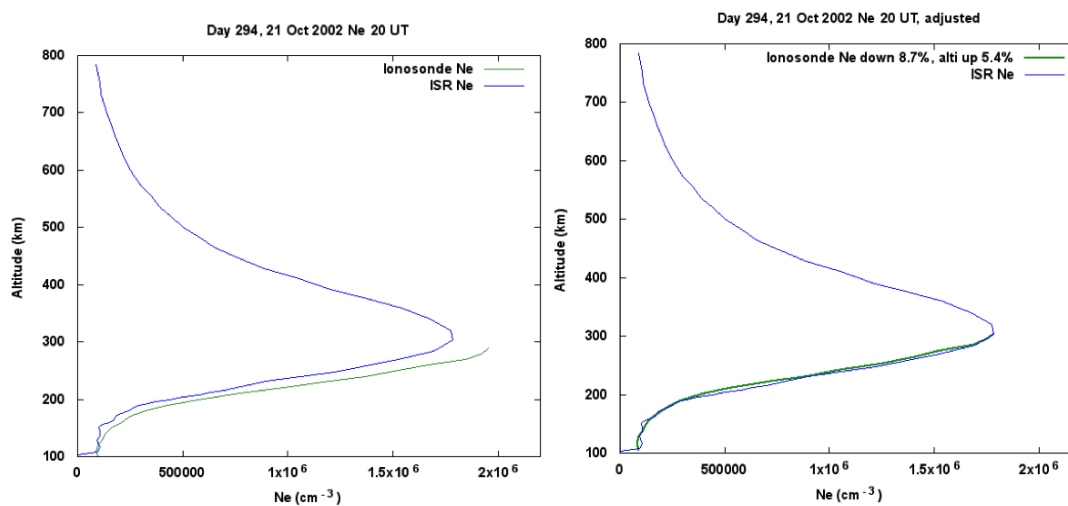
## 7.2. Ionosonde Scaling

Major differences were found between ISR and ionosonde bottomside data for both days 294 and 297 in Chapter 6, section 3 by the examination of the peak density height,  $h_mF_2$ , which was shown in Figure 6.12. The ISR data used in this study provides the full ionospheric electron density profile information against which the ionosonde bottomside results are compared. Because the goal of this study is to recreate the topside ionosphere using bottomside TEC data collected by an ionosonde, for the purpose of this study, the ionosonde data was scaled to fit the ISR data. This is alarming for the reasons mentioned in section 3.3: the stated calibration constant used in Millstone Hill's ISR is determined by direct comparison with the University of Massachusetts Lowell ionosonde measurements of peak electron density [Madrigal, 2017]. Appendix D shows the results of Chapter 7 when ISR is scaled to fit the ionosonde bottomside data.

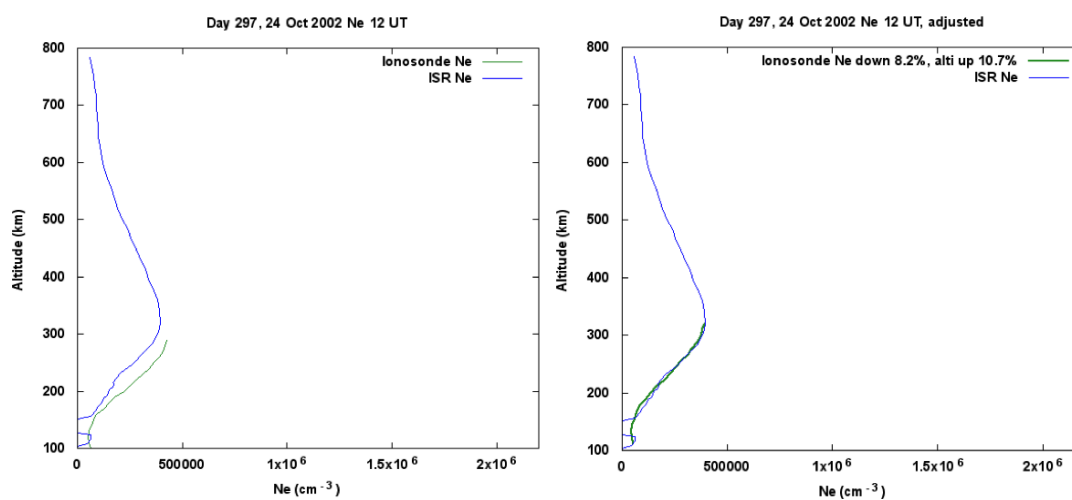
Compared to ISR, ionosondes routinely determine a lower altitude of peak density height,  $h_mF_2$ , and a higher peak density value,  $N_mF_2$ . Examples showing the adjustments made to the ionosonde bottomside density profiles are shown in Figures 7.1 and 7.2 where the blue line represents the ISR density profile and the green line, the ionosonde bottomside density profile.

Figure 7.1 shows the 20 UT density profile during quiet day 294. For this hour, the ionosonde adjustment was an 5.4 % increase in all altitude values and an 8.7 % decrease in all density values in order to match the ISR observed  $h_mF_2$  and  $N_mF_2$  values. The density profile during 12 UT on active day 297 is shown in Figure 7.2. The ionosonde data had the

following adjustments to match the ISR observed  $h_m F_2$  and  $N_m F_2$  values: a 10.7 % increase in all altitude values and an 8.2 % decrease in all density values.



**Figure 7.1.** Quiet day 294, 20 UT density profile ISR (blue) versus ionosonde (green). The right side shows the adjustments made to the raw ionosonde bottomside profile (left) to fit ISR.



**Figure 7.2.** Active day 297, 12 UT density profile ISR (blue) versus ionosonde (green). The right side shows the adjustments made to the raw ionosonde bottomside profile (left) to fit ISR.



Without the adjustments in both Figures 7.1 and 7.2 the peak density shape would not be captured correctly by the ionosonde data and subsequent topside reconstruction. It must be noted that the scaling was not consistent over the two days used for the topside analysis with some hours during the day requiring a scaling of over 20%, as shown in Table 7.1 for day 294 and Table 7.2 for day 297. For both days,  $N_mF_2$  needed significant ionosonde scaling compared to  $h_mF_2$  values. Quiet day 294 required the most ionosonde scaling for  $N_mF_2$  values during the hours of 12 and 14 UT at 20.7% and 23.7%, respectively. Day 294 also saw the largest and smallest  $h_mF_2$  ionosonde scaling at 13.1% during 22 UT and 1.5% at 16 UT. Overall, the daily average  $h_mF_2$  and  $N_mF_2$  ionosonde scaling values for day 294 was 7.3 % and 11.9 % compared to 6.9% and 9.9% for day 297. This raises a concern in our methodology to use ionosondes that are significantly different than ISR, but will not be investigated in this study.

### 7.3. $\alpha$ – Chapman Profile

Now that the ionosonde data has been scaled to fit the ISR data, we can move to the reconstruction of the topside ionosphere using the  $\alpha$  – Chapman profile [*Chapman, 1931; Rishbeth and Garriott, 1969; Reinisch and Huang, 2001*] outlined in Chapter 2, sections 2 and 6, reintroduced here. Again, the  $\alpha$  – Chapman profile is as follows:

$$N(h)_T = N_mF_2 \exp \left[ \frac{1}{2} (1 - z - e^{-z}) \right], \quad (7.1)$$

where

$$z = \frac{h - h_mF_2}{H(h)_C}, \quad (7.2)$$

and

**Table 7.1.** Day 294 Absolute Difference Between Ionosonde and ISR Data.

UT	$h_m F_2$ numerical difference (km)	$h_m F_2$ % error	$N_m F_2$ numerical difference ( $m^{-3}$ )	$N_m F_2$ % error
00	11.0	3.56	9.36E+10	11.6
02	34.8	10.7	3.86E+10	7.59
12	15.8	6.80	2.03E+11	23.7
13	23.3	9.52	2.58E+11	18.7
14	22.0	8.94	3.77E+11	20.7
15	6.00	2.29	1.85E+11	10.5
16	4.10	1.46	1.81E+11	10.1
17	25.1	9.00	1.68E+11	8.85
18	25.0	8.47	1.82E+11	9.37
19	28.7	9.85	1.84E+11	8.84
20	15.5	5.37	1.70E+11	8.69
21	20.0	7.04	1.97E+11	10.1
22	35.2	13.1	1.01E+11	6.56
23	17.0	5.61	1.24E+11	10.8

**Table 7.2.** Day 297 Absolute Difference Between Ionosonde and ISR Data.

UT	$h_m F_2$ numerical difference (km)	$h_m F_2$ % error	$N_m F_2$ numerical difference ( $m^{-3}$ )	$N_m F_2$ % error
00	36.9	12.2	9.70E+10	10.5
01	26.4	8.42	5.95E+10	7.50
02	26.3	7.88	7.43E+10	11.2
03	38.2	9.80	5.59E+10	12.1
04	37.1	9.49	3.48E+10	8.80
12	30.9	10.7	3.49E+10	8.15
13	28.5	10.3	5.53E+10	10.9
14	18.9	6.28	6.76E+10	11.8
15	14.4	4.97	6.61E+10	9.23
16	12.7	4.36	1.31E+11	14.4
17	12.1	4.15	1.31E+11	12.9
18	8.20	2.77	1.31E+11	11.4
19	14.9	5.15	1.39E+11	10.5
20	17.3	5.72	1.55E+11	12.1
21	23.1	7.78	1.16E+11	9.16
22	23.2	7.32	1.04E+11	8.72
23	19.6	6.89	8.19E+10	9.03

$$H(h)_C = \frac{k_B T_C}{m g_h}. \quad (7.3)$$

Again, equation 7.1 is dependent on  $N_m F_2$ ,  $h_m F_2$ , and  $H(h)_C$ , with  $H(h)_C$  dependent on gravity due to height ( $h$ ) and  $T_C$ , which will be referred to as the Chapman temperature. Several studies in the past such as [Titheridge, 1973] relate  $T_C$  to the neutral temperature,  $T_N$ . Because of this, we use a range of  $T_C$  equal to 800 K, 900 K, 1000 K, 1100 K, 1200 K, 1300 K, and 1400 K. The ionosonde  $N_m F_2$ ,  $h_m F_2$  values used are the ones adjusted as mentioned in section 7.2.

The Chapman temperature variations of the  $\alpha$  – Chapman profile was calculated hourly for quiet reference day, 294 and active reference day 297. Ionosonde data that were offset from the exact hour (a nighttime problem discussed in Chapter 6, section 3 as the scanning radio frequency of the ionosonde above the maximum plasma resonance frequency) was not used in this Chapter’s study, which unfortunately means a thorough evaluation of the topside ionosphere during diffusive conditions could not be conducted at this time. The hours available for comparison for day 294 are 00, 02, 12 – 23 UT and for day 297, hours 00 – 04 and 12 – 23 UT.

The ionosphere’s electron density profile is then recreated using the ionosonde-generated bottomside profile and  $h_m F_2$  and  $N_m F_2$  values scaled accordingly to ISR data, along with the  $\alpha$  – Chapman Profile described in this section.

### 7.3.1. $\alpha$ – Chapman Pseudo-Temperature

Once the  $\alpha$  – Chapman profiles were computed for each of the above-mentioned variations in Chapman temperature,  $TEC_t$  was found by calculating electron density every

20 km from  $h_mF_2$  to 800 km and summed, keeping consistent with the ISR data. The Chapman temperature, which produced the closest  $\alpha -$  Chapman profile  $TEC_t$  values to ISR  $TEC_t$ , was then selected to represent the topside ionosphere and referred to as the Chapman pseudo-temperature. This was important to determine because the Chapman pseudo-temperature significantly controls scale height values, which we will use for our comparison.

Figures 7.1 and 7.2 are recreated to show the results of the topside reconstruction in Figures 7.3 and 7.4, respectively. In both Figures 7.3 and 7.4, the ISR electron density profile is shown in bold-black and the bottomside ionosonde profile in bold-green. The remaining different colors represent the varying  $\alpha -$  Chapman profile dependent on the Chapman temperature used. The red-dashed line is equal to the Chapman pseudo-temperature or the Chapman temperature that produced the closest  $TEC_t$  values to ISR  $TEC_t$ . The right side in both Figures shows the adjustments made to the raw ionosonde bottomside profile, shown on the left side of each figure, to fit ISR as discussed in section 7.2.

A Chapman temperature of 1000 K produced the best fit  $\alpha -$  Chapman profile during 20 UT on quiet day 294 and is shown by the red-dashed line in Figure 7.3. On the adjusted side (right) of Figure 7.3, the ionosonde bottomside fit lies directly on the ISR profile with the peak captured nicely by the  $\alpha -$  Chapman profile. Overall, the  $\alpha -$  Chapman profile appears to be a good fit compared to the ISR density profile except between 400 – 600 km where the red-dashed line is slightly above ISR.

Impressive results were found for active day 297 during 12 UT, shown in Figure 7.4. The best fit  $\alpha$  – Chapman profile had a Chapman temperature of 1400 K and on the right side of Figure 7.4, the adjusted ionosonde data and red-dashed line lie directly on the ISR profile. Again, it was imperative the adjustments were made to the ionosonde data to correctly capture the peak shape and subsequent topside ionosphere. For the full set of the topside reconstruction results, see Appendix E.

Consistency was checked in the Chapman temperature ( $T_C$ ) results for quiet day 294 and active day 297 and are shown in Tables 7.3 and 7.4, respectively, as well as the corresponding  $TEC_t$  % errors when compared to ISR  $TEC_t$ . Overall, day 294 had 10 hours with a  $T_C$  value less than 1000 K compared to day 297, which only saw one  $T_C$  value less than 1000 K. For day 294, daytime hours 12 – 15 UT, just before solar noon, saw the lowest daily  $T_C$  values, while nighttime hours 00 and 23 UT saw the highest  $T_C$  values. Conversely, day 297 had higher  $T_C$  values occur just before solar noon during the hours of 12 – 14 UT, and lowest during nighttime hours 00 – 04 UT.

Surprisingly, in terms of  $TEC_t$  % errors, active day 297 had eight hours with an error less than 1% compared to quiet day 294, which only had one hour less than 1%. Day 294 also saw the largest  $TEC_t$  error at 8.9 % between the two days occurring at 13 UT. Consistency was not found in Tables 7.3 and 7.4 for the two days used in the study, in regards to the  $\alpha$  – Chapman profile results of  $T_C$  and  $TEC_t$  % error.

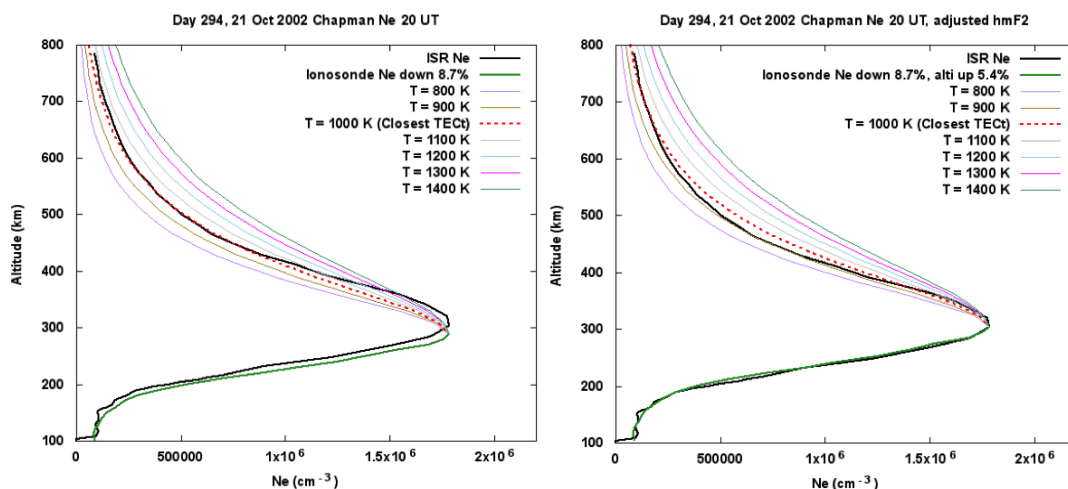


**Figure 7.3.** Quiet day 294, 20 UT density profile ISR (black) versus ionosonde (green). The different colors represent the  $\alpha$  – Chapman profile and Chapman temperature used. The red-dashed line is equal to the Chapman pseudo-temperature. The right side shows the adjustments made to the raw ionosonde bottomside profile (left) to fit ISR.

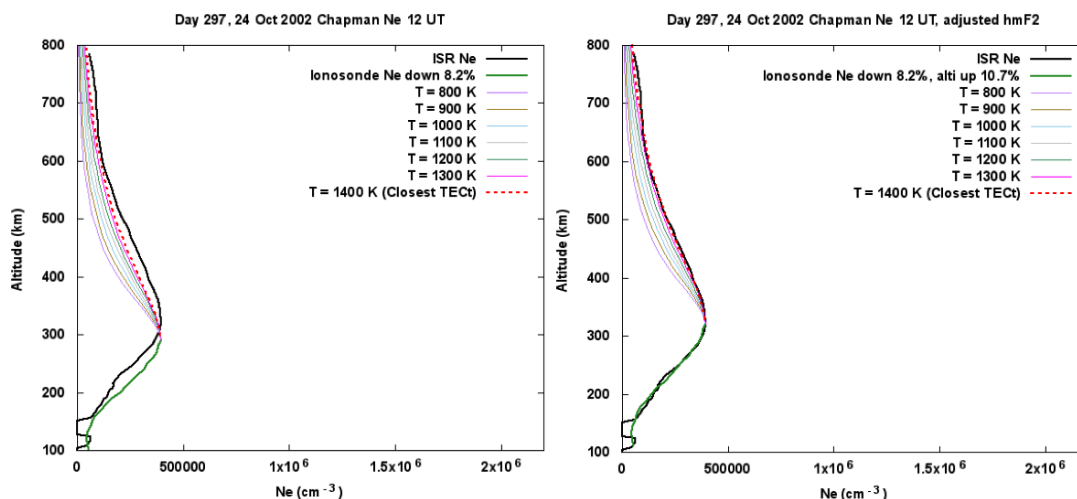


**Figure 7.4.** Active day 297, 12 UT density profile ISR (blue) versus ionosonde (green). The different colors represent the  $\alpha$  – Chapman profile and Chapman temperature used. The red-dashed line is equal to the Chapman pseudo-temperature. The right side shows the adjustments made to the raw ionosonde bottomside profile (left) to fit ISR.

**Table 7.3.** Day 294 Chapman Temperature and TEC<sub>t</sub> % Error

<b>UT</b>	<b>T<sub>C</sub> (K)</b>	<b>TEC<sub>t</sub> % Error</b>
00	1100	2.36
02	900	0.0859
12	900	1.86
13	800	8.94
14	800	3.78
15	800	6.30
16	900	1.06
17	900	4.58
18	900	2.61
19	900	4.92
20	1000	4.97
21	900	3.80
22	1000	4.34
23	1100	2.07

**Table 7.4.** Day 297 Chapman Temperature and TEC<sub>t</sub> % Error

<b>UT</b>	<b>T<sub>C</sub> (K)</b>	<b>TEC<sub>t</sub> % Error</b>
00	1000	3.35
01	1000	1.96
02	900	2.95
03	1000	0.584
04	1000	0.628
12	1400	0.649
13	1400	0.730
14	1400	0.690
15	1200	3.11
16	1100	0.835
17	1100	1.87
18	1200	3.86
19	1100	1.16
20	1200	3.70
21	1200	0.0452
22	1000	2.82
23	1000	0.355

### 7.3.2. $\alpha$ – Chapman Profile Scale Height

In order to recreate the topside ionosphere, a scale height must be calculated. Equation 7.1 uses a Chapman scale height ( $H_C$ ), equation 7.3, that is dominated by a temperature that has been postulated by previous literature to resemble the neutral temperature and not give any information about the plasma temperature. Using an  $\alpha$  – Chapman profile determined to be a good fit for the topside ionosphere; however, gives the density structure and allows one to extract density values at any given altitude. Because of this, vertical scale height (VSH), introduced in Chapter 5, equation 5.1 can be calculated. VSH determined from an  $\alpha$  – Chapman profile will be referred to as a Chapman VSH, or  $VSH_C$  for short, throughout the rest of this chapter.

The Chapman VSH was calculated for day 294 and day 297 and compared to the scale height results using the ISR methodology found in Chapter 5, section 3, and shown in Figure 7.5 for day 294, recreating Figure 5.1, and Figure 7.6 for day 297. Both Figures 7.5 and 7.6 show an hourly comparison between all scale heights: plasma scale height,  $H_p$ , using plasma temperature measurements from ISR (black lines); neutral scale heights,  $H_n$ , using ISR neutral temperatures (blue lines); calculated ISR VSH (red lines) using ISR density measurements; calculated Chapman VSH (green lines) using ionosonde  $\alpha$  – Chapman profile density determined values; and Chapman scale height,  $H_C$ , found by equation 7.3 (purple lines). Keeping consistent with previous results, there are two altitude comparisons, lower altitude at 428 km and upper altitude at 520 km, for each parameter. Both altitudes are located above the density layer peak,  $h_mF_2$ , representing the topside ionosphere.



The ISR hourly variations were discussed in Chapter 5, section 3, and will not be addressed here; rather, an analysis of how the Chapman scale heights  $VSH_C$  and  $H_C$  measured up to the ISR results will be discussed: for  $H_C$ , a comparison against ISR  $H_n$  and  $VSH_C$  against ISR VSH. Again, for day 294 only hours 00, 02, 12 – 23 UT are available for comparison and for day 297, hours 00 – 04 and 12 – 23 UT.

Quiet day 294  $H_C$ , shown in Figure 7.5, seems to track  $H_n$  well during 00, 02, 12, and 23 UT but a noticeable gap of about 20 - 25 km exists between the hours of 13 – 22 UT. For example, during 15 UT this small scale height difference translates to a 360 K difference in  $T_C$  and  $T_n$ . Active day 297 shown in Figure 7.6 shows  $H_C$  tracking  $H_n$  better overall compared to day 294 with a smaller gap in scale heights of about 10 km except for 22 and 23 UT in which the gap is slightly larger. In both figures, with the exception of day 297's hours of 12 – 14 UT,  $H_C$  under predicts  $H_n$ . It is because of the results found in Figures 7.5 and 7.6 for  $H_C$  that it cannot be concluded that  $H_C$  is a good representation of  $H_n$ .

The results for Chapman VSH were surprising. It was theorized that fitting an  $\alpha$  – Chapman profile for the topside ionosphere as shown in Figures 7.3 and 7.4 by the red-dashed line, and the density values determined from it would match ISR VSH since the red-dashed line overlays the bold-black ISR profile line; however, for both days, the overall results fall short.

Noticeable in both Figures 7.5 and 7.6 is the lack of separation in  $VSH_C$  values for the two altitudes that are very apparent in both ISR  $H_p$  and ISR VSH. The lower altitude Chapman VSH for quiet day 294, shown by green circles in Figure 7.5, shows

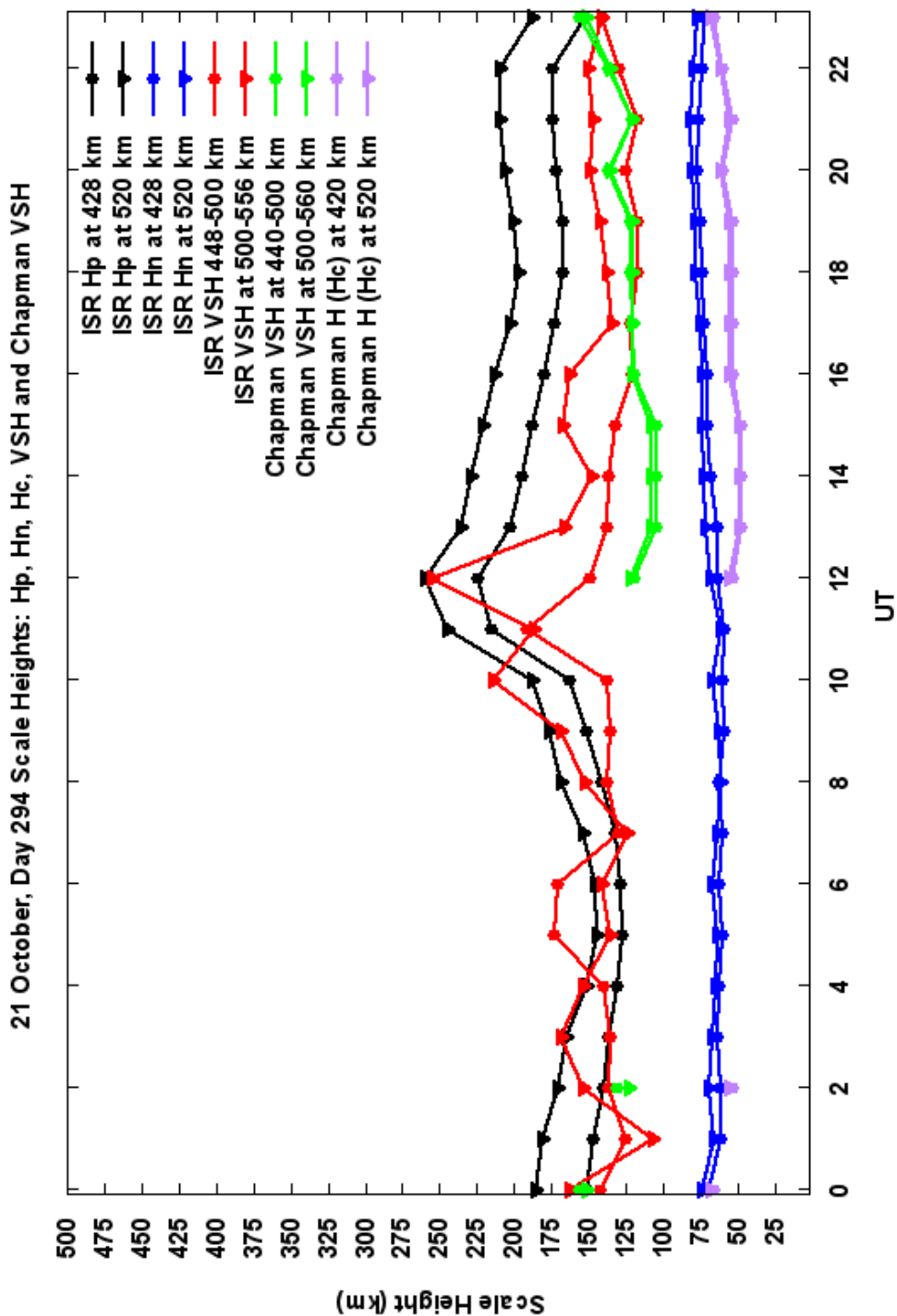


**Figure 7.5.** Scale height calculations for quiet day 294 at two altitudes above the peak density height. Shown are ISR plasma scale height,  $H_p$ , (black lines), ISR VSH (red lines), ISR neutral temperature scale height,  $H_n$ , (blue lines), Chapman VSH (green lines), Chapman scale height  $H_c$  (purple lines). The lower altitude is represented by circles and the upper altitude is represented by triangles.

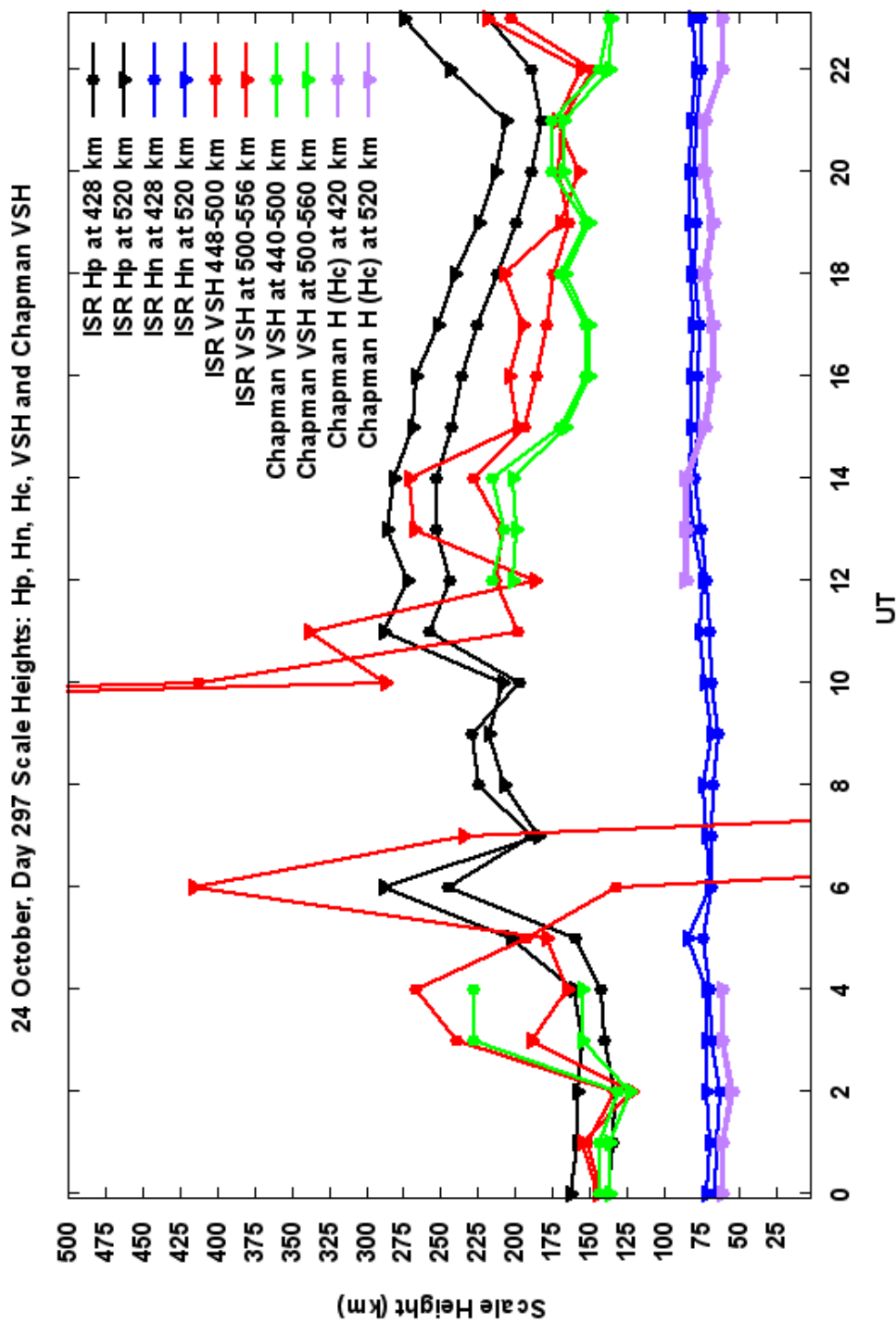


**Figure 7.6:** Scale height calculations for active day 297 at two altitudes above the peak density height. Shown are ISR plasma scale height,  $H_p$ , (black lines), ISR VSH (red lines), ISR neutral temperature scale height,  $H_n$ , (blue lines), Chapman VSH (green lines), Chapman scale height  $H_c$  (purple lines). The lower altitude is represented by circles and the upper altitude is represented by triangles.

promising results compared to ISR  $H_p$  (black circles) and ISR VSH (red circles) for nighttime hours 00, 02, 23 UT, which may be expected due to previous chapters suggesting diffusive conditions. For hours 12 – 15 UT, there is a significant difference in  $VSH_C$  and ISR VSH for both the upper and lower altitudes. But, the lower altitude  $VSH_C$  and ISR VSH track nicely during 16 – 22 UT.

The same diffusive conditions can be said for active day 297 during 00 – 02 UT before the ionosphere saw disruptions due to a moderate geomagnetic storm as discussed in Chapter 6, section 3. A large spike in both altitudes is seen in both  $VSH_C$  and ISR VSH methods at 03 UT and the lower altitude continues to match well between 12 – 14 UT. There are large discrepancies in the upper and lower altitude  $VSH_C$  and ISR VSH calculations during 13 – 18 UT and at 23 UT.

As expected, these results are consistent with the findings in Chapter 5, section 3.3 that the daytime topside ionosphere over Millstone Hill cannot be described by diffusive equilibrium; however, during nighttime hours 00 – 04 UT more than likely gave a diffusive profile shape; and from this, we expect to determine temperature structures from the Chapman VSH. Moving forward, we suspect we can quantify the consistent offset during daytime hours between VSH in order to yield plasma temperature information.

### **7.3.3. $\alpha$ – Chapman Profile-determined $T_e + T_i$**

Using density values determined from the fitted  $\alpha$  – Chapman profile in the Chapman VSH equation given by equation 5.1 and setting it equal to the plasma scale height,  $H_p$ , given by equation 5.2,  $T_e + T_i$  values are inferred by equation 7.4:

$$\frac{(-\Delta h)m_i g_h}{k_b \ln \left( \frac{N_e(h_2)}{N_e(h_1)} \right)} = T_i + T_e . \quad (7.4)$$

Given the results in 7.3.2, we expect the inferred  $T_e + T_i$  to not be a good measure during nondiffusive conditions; however, examining the offset and checking for consistency is beneficial. The results for quiet day 294 are shown in Figure 7.7 and active day in Figure 7.8 with the black line representing the Chapman inferred  $T_e + T_i$  and the observed ISR  $T_e + T_i$  by the blue line. The triangles symbolize the upper altitude, 520 km, and the circles, the lower altitude, 420 km. As expected, there are large discrepancies during daytime hours for both altitudes and both days. The largest occurring during daytime hours for quiet day 294.

The lower altitude for day 294, shown in Figure 7.7, had a fit within 7% error for 00, 02, and 23 UT. Interestingly, there appears to be a steady increase in Chapman inferred  $T_e + T_i$  from 12 – 23 UT while observed ISR  $T_e + T_i$  sees a steady decrease. In Figure 7.8, the lower altitude for active day 297 fit within 7% error during 00, 01, 02, 21 UT and sees an overall decrease in Chapman inferred  $T_e + T_i$  during 12 – 23 UT with the exception of 18, 20, and 21 UT compared to ISR observed  $T_e + T_i$  which decrease steadily between 12 – 21 UT then sees an increase at 22 UT. Also in Figure 7.8, the upper altitude had a fit within 3% errors for hours 03 and 04 UT.

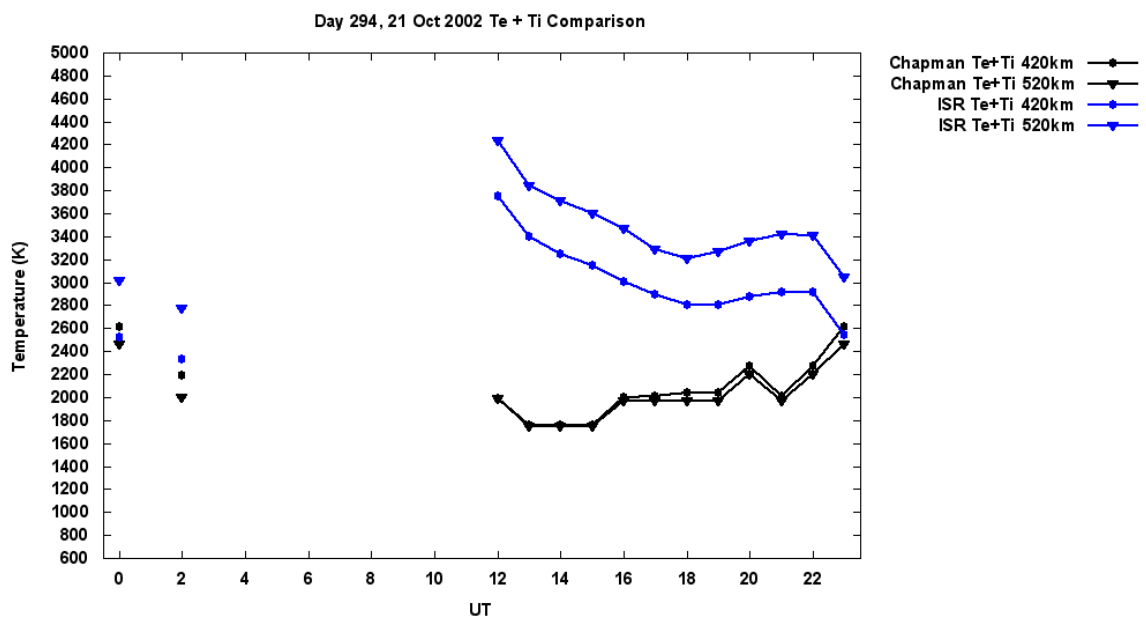


**Figure 7.7.** Chapman determined  $T_e + T_i$  compared to observed ISR measurements of  $T_e + T_i$  during quiet day 294.

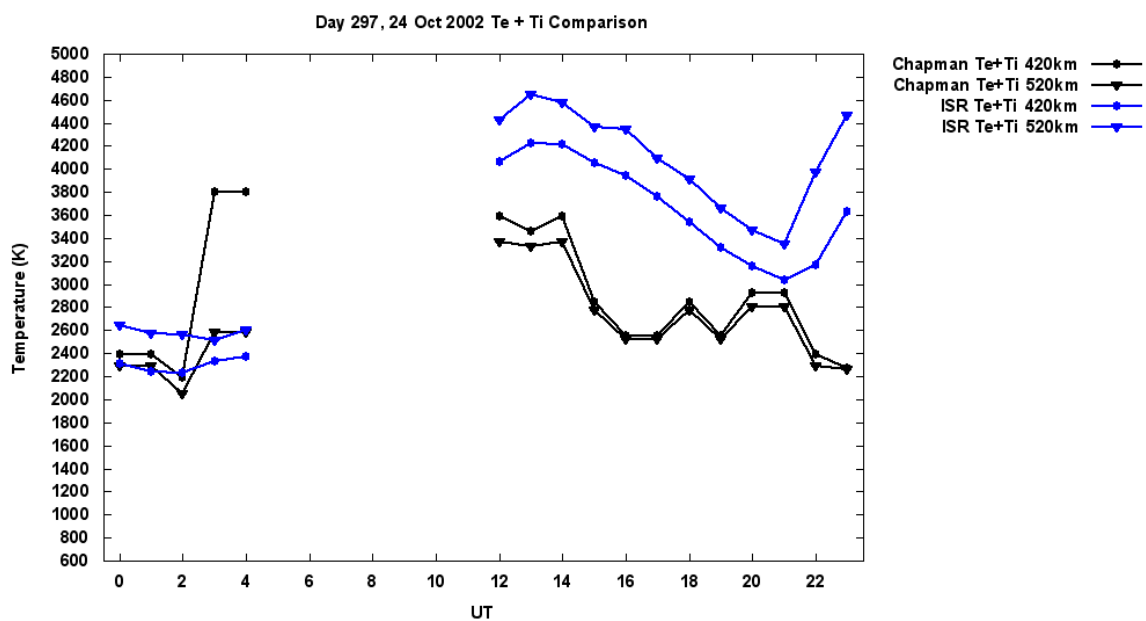


**Figure 7.8.** Chapman determined  $T_e + T_i$  compared to observed ISR measurements of  $T_e + T_i$  during active day 297.

### 7.3.4. $\alpha$ – Chapman Profile-determined $T_e + T_i$ and the Relationship to $\kappa$

Combining the results found in the previous section, 7.3.3, with the new relationship found in section 6.4.3 offers, for the first time, a possible relationship between plasma temperature trends by only using knowledge of density parameters:  $N_m F_2$ ,  $h_m F_2$ , and TEC. Equation 6.13 described a new correlation found between the peak density height,  $h_m F_2$ , and slab thickness,  $\tau$ , of the ionosphere, which was named  $\kappa$ . Slab thickness was given by equation 6.12 as the ratio of TEC to the peak density value,  $N_m F_2$ . Essentially then,

$$\kappa = \frac{h_m F_2 \times N_m F_2}{TEC} . \quad (7.5)$$

We postulate that knowing the density structure of the ionosphere will allude to insight of plasma temperature trends during nondiffusive conditions. We do this by optimizing equation 7.4 by including equation 7.5 raised to a power. We reintroduce equation 7.4 as equation 7.6 with this new relationship included in VSH<sub>C</sub>:

$$\kappa^2 \times \frac{(-\Delta h) m_i g_h}{k_b \ln \left( \frac{N_e(h_2)}{N_e(h_1)} \right)} = T_i + T_e . \quad (7.6)$$

Section 7.3.3 found the Chapman inferred  $T_e + T_i$  given by equation 7.4 to be a good fit for the lower altitude, 420 km, during nighttime hours 00, 02, and 23 UT for quiet day 294 and hours 00, 01, and 02 UT for active day 297. Equation 7.4 was also a good fit for the upper altitude, 520 km, during nighttime hours 03 and 04 UT on active day 297. Equation 7.6 was then used to determine  $T_e + T_i$  at 520 km for hours 12 – 22 UT on day 294 and hours 12 – 23 on day 297.

As discussed in Chapters 3 and 4, thermal equilibrium does not exist in the topside ionosphere; and therefore, the average altitudinal increase of temperature had to be calculated from 420 km to 520 km using ISR data to determine  $T_e + T_i$  at 420 km, knowing  $T_e + T_i$  at 520 km or vice versa. For day 294, the altitudinal increase had a daily average of 463.7 K from 420 km to 520 km (equation 7.7) and 386 K for day 297 (equation 7.8):

$$(T_e + T_i)_{520 \text{ km}} = (T_e + T_i)_{420 \text{ km}} + 463.7 \text{ K} , \quad (7.7)$$

$$(T_e + T_i)_{520 \text{ km}} = (T_e + T_i)_{420 \text{ km}} + 386 \text{ K} . \quad (7.8)$$

Knowing this altitudinal increase of temperature for both days will allow us to calculate  $T_e + T_i$  at either 420 km or 520 km given we know  $T_e + T_i$  at one of the altitudes.

Using the new relationships found in equations 7.6, 7.7, and 7.8, Figure 7.7 for day 294 and Figure 7.8 for day 297, from previous section 7.3.3, are recreated to determine  $T_e + T_i$  and are reflected below in Figures 7.9 and 7.10, respectively.

The results were surprising. Quiet day 294, shown in Figure 7.9, saw nine out of 14 hours produced a  $T_e + T_i$  result (black line) within 10% of the observed  $T_e + T_i$  given by ISR measurements (blue line) at the lower altitude of 420 km. Even better, 11 out of 14 hours at the upper altitude of 520 km produced a (modified) Chapman  $T_e + T_i$  result within 10% of the observed ISR  $T_e + T_i$ . The largest differences in  $T_e + T_i$  were found for hours 12 and 15 UT. Comparing both altitudes against ISR measurements, daytime hours 18 and 21 UT had the best results of less than 2% error.

Better results overall were found in Figure 7.10 for active day 297. At both upper and lower altitudes 14 out of 17 hours produced a (modified) Chapman  $T_e + T_i$  result within 10% of the observed ISR  $T_e + T_i$ ; however, hours that saw a  $\kappa$  value dip below 1.1 had



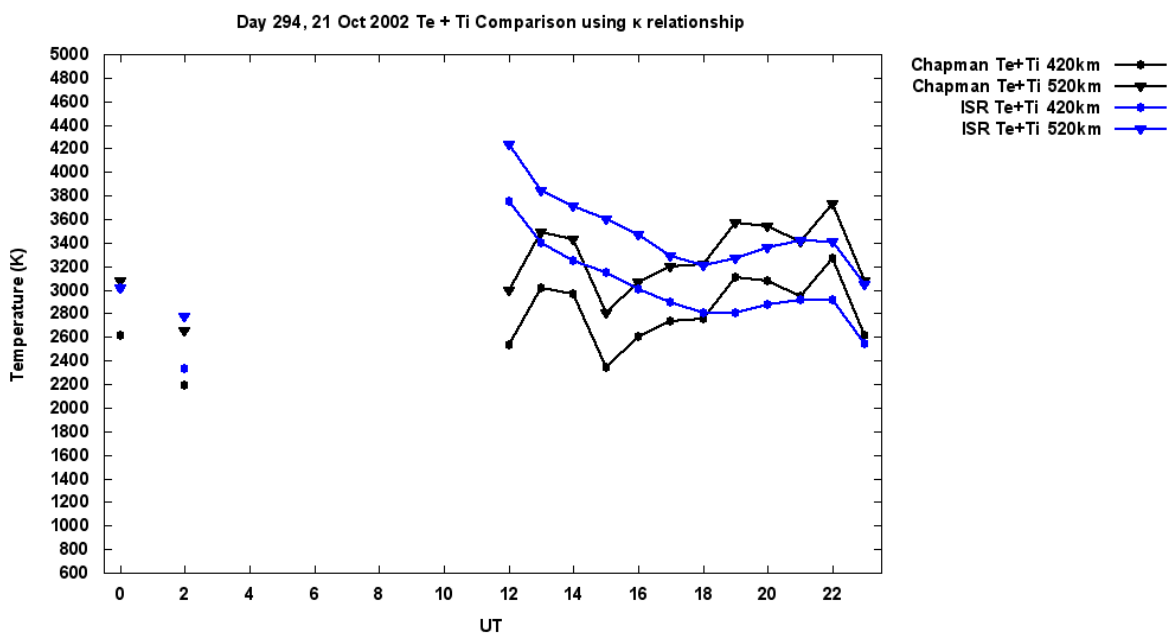


**Figure 7.9.** Chapman determined  $T_e + T_i$  with  $\kappa$  relationship factor compared to observed ISR measurements of  $T_e + T_i$  during quiet day 294.

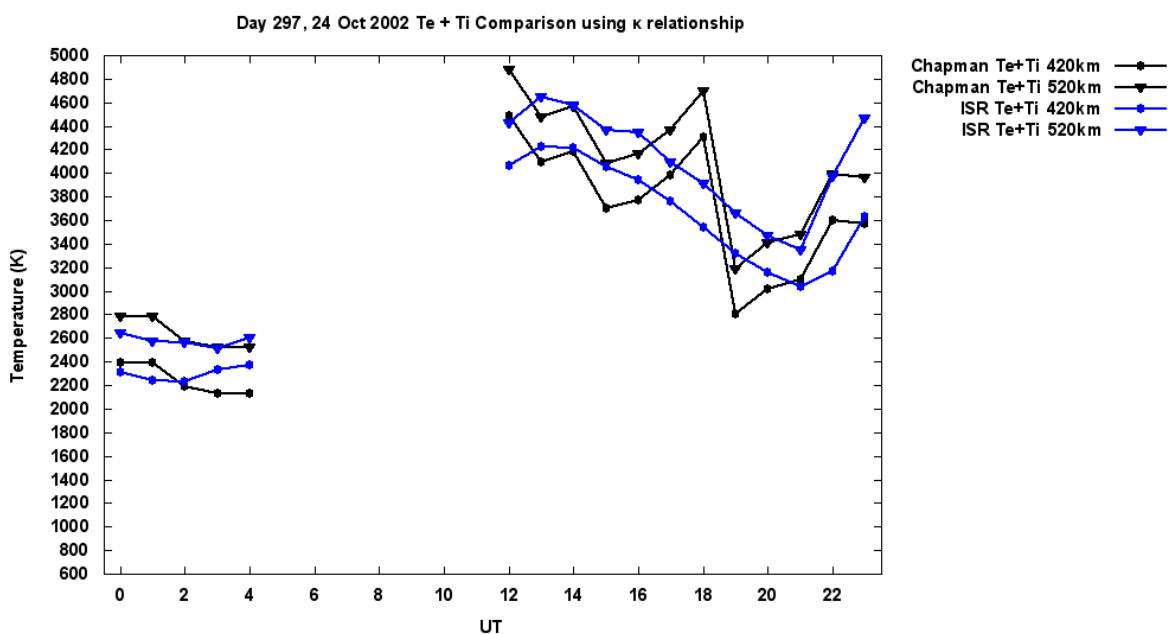


**Figure 7.10.** Chapman determined  $T_e + T_i$  with  $\kappa$  relationship factor compared to observed ISR measurements of  $T_e + T_i$  during active day 297.

a value of 0.25 added considering the results from Chapter 6, section 4.3, which found an overall daily average  $\kappa$  equal to 1.28. Hours 12 – 18 UT needed this adjustment and may be explained by the timing of the ionospheric storm and the electron density response. The largest discrepancies compared to ISR and found in both upper and lower altitudes, occurred during 18 and 19 UT. Hours 02, 14, 20, and 22 UT had the best results with an error of 2% or less.

#### 7.4. Discussion

Using our scale height calculation techniques during diffusive equilibrium conditions found on both quiet day 294 and active day 297 allowed us to calculate an appropriate scale height using data only containing density information. This was done by an  $\alpha$  – Chapman profile and an appropriately selected Chapman pseudo-temperature. With this, we are able to obtain topside temperature information,  $T_e + T_i$ , which gives the plasma temperature by:  $(T_e + T_i)/2$ .

For nondiffusive conditions, a  $\kappa$  relationship was included in the Chapman VSH calculation to determine  $T_e + T_i$  and upon a first impression, a relationship between plasma temperature trends by only using knowledge of density parameters:  $N_mF_2$ ,  $h_mF_2$ , and TEC that are collected by ionosonde bottomside data was found. This  $\kappa$  relationship does; however, come with limitations. It was only found to be a good fit for the upper altitude of 520 km and not 420 km. Also, when the  $\kappa$ -value fell below 1.1, there needed to be some sort of modification, such as  $\kappa + 0.25$ , though a thorough investigation is needed to detail such modifications and what this relationship between plasma temperature trends and density parameters truly means.

Finally, this chapter found using ionosonde bottomside TEC and an  $\alpha$  – Chapman profile with the appropriately selected Chapman pseudo-temperature that is fitted against  $TEC_t$  from ISR data, can be a good representation of the topside ionosphere.

## CHAPTER 8

### CONCLUSIONS AND FUTURE WORK

#### 8.1. Conclusions

A 29-day analysis of scale heights and the inference of the topside ionosphere over Millstone Hill during the 2002 Incoherent Scatter Radar campaign has been conducted. Normal ISR operations only allow data collection to span a few days; therefore, the long duration of this data campaign provided a unique opportunity to study the ionosphere over Millstone Hill. The data campaign used in this study also captured ionospheric variability during a time of both geomagnetically active and quiet periods. Millstone Hill Observatory is a subauroral mid-latitude site in North America and offers a wealth of available data from ground-based instruments including an incoherent scatter radar (ISR), an ionosonde, and a GPS receiver tracking several space-based GPS satellites of which were collectively used in this research.

Chapter 4 began the study by an analysis of the collected 696 hourly altitudinal profiles of electron density and electron, ion, and neutral temperatures observed by ISR. An appreciation was gained in regards to the daily variability of electron density parameters  $h_mF_2$  and  $N_mF_2$ , along with electron temperatures, by examining Figures 4.5, 4.6, 4.7, and 4.8. This chapter also addressed issues with previous studies that assessed data from the same Millstone Hill campaign and found inconclusive results on the behavior of the ionospheric scale heights. The two methods used to calculate scale heights by either density (VSH), or temperature ( $H_p$ ) information was adapted from *Liu et al.* [2007].

How much the two scale height methods differed was discussed in Chapter 5. The ISR data methodology was given and days were separated by their respective solar and geomagnetic conditions, classified as either a quiet or active day. Thermal diffusive equilibrium was found to be a main driver of scale height; however, scale height is also dependent on the dominate ion species, as well as other drivers during nondiffusive conditions.

Overall, the two methods of calculating scale heights were in good agreement between nighttime hours 0 – 10 UT, during quiet solar, and geomagnetic activity, so it was reasonable to assume diffusive equilibrium conditions. During said conditions, using equation 5.5 [*Whitten and Poppoff, 1971*], a measure of the electron density profile enabled a scale height to be inferred, which yielded temperature information. During daytime hours 12 – 22 UT, large discrepancies were found between the two scale height methods suggesting nondiffusive conditions for the topside ionosphere, keeping consistent with previous literature results.

Chapter 6 introduced data collected from a GPS receiver located in the same area as Millstone Hill's ISR. The GPS TEC methodology used was discussed, as well as the issues surrounding radio occultation inversion techniques. Converting slant TEC into ionospheric vertical TEC was shown to be geometrically challenging due in part by the constant changing of ionospheric pierce points and ionospheric conditions, which ultimately ends as an average TEC calculation versus what the GPS satellite actually sees. Figures 6.5 and 6.6 show the variations between ISR-determined TEC, slant, and vertical GPS TEC for quiet reference day 294 and active reference day 297. To properly evaluate

TEC from GPS satellites, it was determined only slant TEC could be used when a GPS satellite had an inclination angle ( $\phi$ ) of 10 degrees or less as discussed in Chapter 6, section 2.

A similar technique was used to determine bottomside TEC using ionosonde data collected from the Lowell GIRO Data Center [Reinisch and Galkin, 2011] for quiet reference day 294, Figure 6.10 and active reference day 297, Figure 6.11. A new relationship was established between TEC, TEC top ( $TEC_t$ ), and TEC bottom ( $TEC_b$ ) in section 6.4.1 and applied to successfully determine TEC and TEC top using ionosonde data only containing information, such as  $N_mF_2$ , and  $h_mF_2$ , to derive  $TEC_b$ .

For the first time, slab thickness, which is directly proportional to scale height, was found to be correlated to  $h_mF_2$  and introduced as a new index,  $\kappa$ . Ultimately,  $\kappa$  is a relationship between TEC,  $N_mF_2$  and  $h_mF_2$  and can be a very useful tool for describing the topside ionosphere and subsequently, scale height. Our initial results of  $\kappa$  found the peak density altitude ( $h_mF_2$ ) to be 28% greater than that of the thickness of the ionosphere ( $\tau$ ) with the value having slight changes due to diurnal variations.

Major issues surrounding the availability of ionogram data during nighttime hours greatly limited our study, especially during diffusive equilibrium conditions. Significant differences were also found between ISR and ionosonde-determined  $N_mF_2$  and  $h_mF_2$ . Chapter 7 made an attempt to adjust said differences; however, ionosondes routinely determined a lower  $h_mF_2$  and a higher  $N_mF_2$ . An example of the adjustments made to ionosonde bottomside density profiles was shown in Figures 7.1 and 7.2. This raised a concern in the methodology to use ionosondes that significantly differ from ISR

observations and question whether or not a proper self-consistent scaling of ionosondes is in place.

Scale height was then calculated using the adjusted ionosonde data that contained only bottomside density information in conjunction with an  $\alpha$  – Chapman profile and an appropriately selected Chapman pseudo-temperature. The Chapman pseudo-temperature can only be determined knowing TEC topside, which for this part of the study, ISR TEC topside was used; however, the TEC topside can be retrieved from a GPS receiver subtracting ionosonde bottomside TEC from GPS slant TEC, Figure 8.1 for quiet reference day 294 and Figure 8.2 for active day 297, when a GPS satellite has an inclination angle ( $\phi$ ) of 10 degrees or less.

Obvious altitude differences exist between ISR (from 100 km - 786 km) and GPS's medium-Earth orbit (surface of the Earth - 20,200 km) [National Coordination Office for Space-Based Positioning, Navigation, and Timing, 2016] so this study could set the stage needed for proper evaluation of the plasmaspheric contribution to TECU, which may explain the TECU differences in Figures 8.1 and 8.2.

During diffusive equilibrium conditions for both reference quiet day 294 and reference active day 297, an  $\alpha$  – Chapman profile determined Chapman VSH topside temperature information,  $T_e + T_i$ , was determined within 2% of observed ISR  $T_e + T_i$  which gives the plasma temperature by:  $(T_e + T_i)/2$ . A  $\kappa$  relationship was included in the Chapman VSH calculation for nondiffusive conditions to determine  $T_e + T_i$ , which means for the first time a relationship between plasma temperature trends by only using knowledge of density parameters:  $N_m F_2$ ,  $h_m F_2$ , and TEC collected by ionosonde bottomside data and

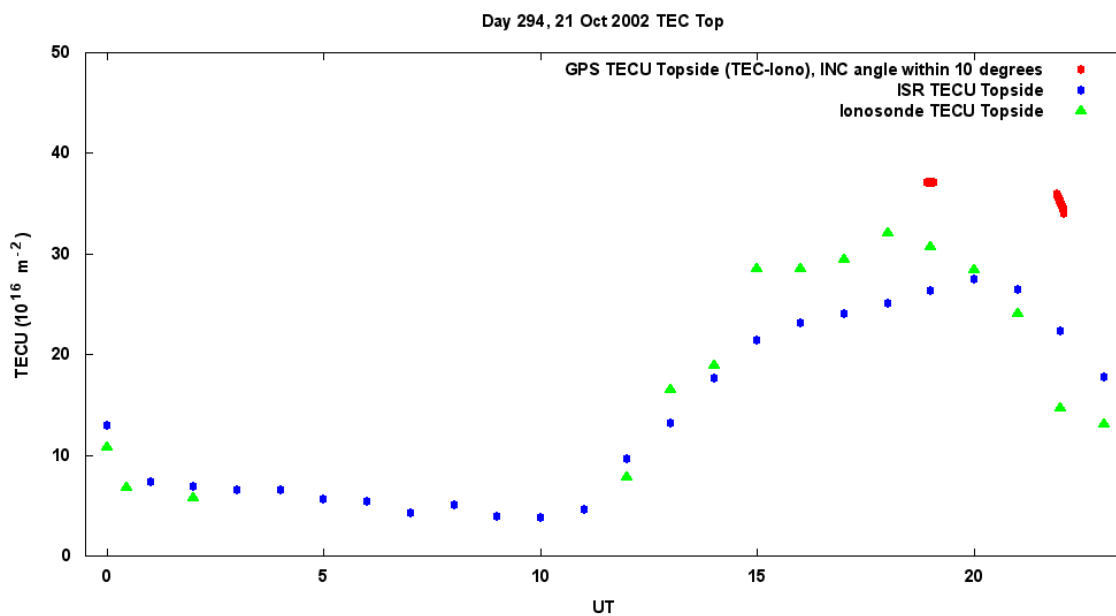


**Figure 8.1.** TEC topside comparison between ISR (blue), ionosonde (green), and GPS STEC (red) for quiet day 294.

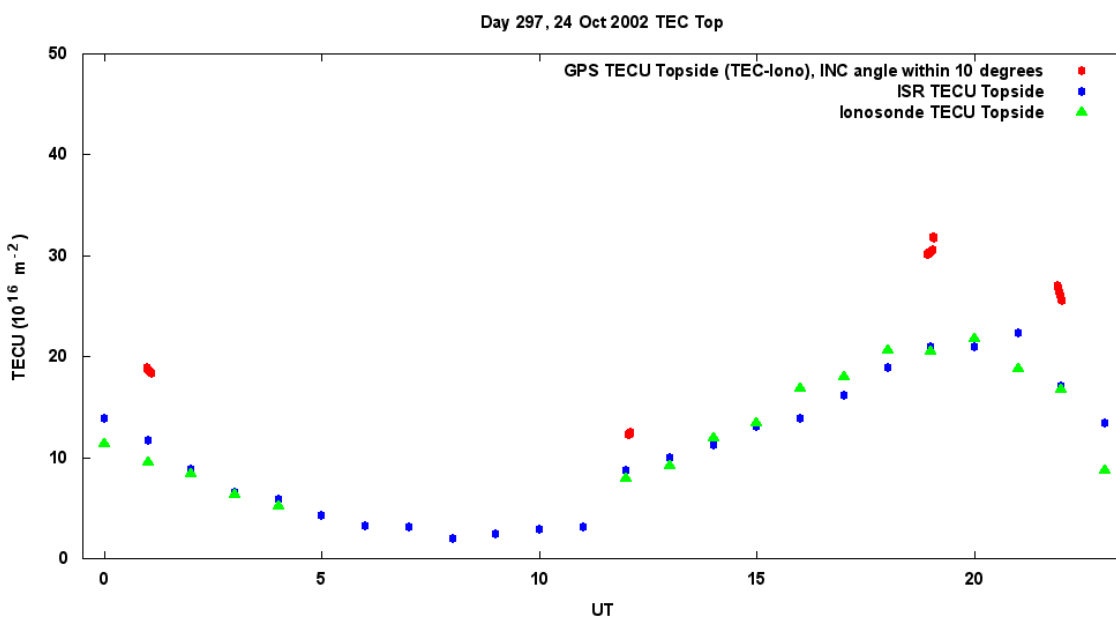


**Figure 8.2.** TEC topside comparison between ISR (blue), ionosonde (green), and GPS STEC (red) for active day 297.



compared against TEC topside data, was found.

Finally, the fundamental question of this study addressed whether or not the electron density altitude dependence in the topside ionosphere could be inferred over Millstone Hill during the 2002 ISR campaign. Ultimately, the methodology of using cost-effective, readily available ionosonde bottomside TEC combined with GPS TEC is capable of inferring of the topside ionosphere, as verified by ISR, though concerns raised in this study need careful consideration.

## **8.2. Future Work**

This dissertation opens the door for many areas of continued study. The very dynamic topside ionosphere undergoes significant changes in structure and composition rapidly throughout the day. The wealth of data from Millstone Hill's 2002 ISR campaign used in this study would allow a comprehensive study to be conducted at the 15-minute timescale (comparable to ionosonde data) to understand our results and new findings, as well as the physical implications. It would also allow for one to truly study the evolution of the topside ionosphere under changing solar and geomagnetic activity, as well as the diurnal effects. As presented in Chapter 4, previous statistical studies conducted using this same dataset have only used 24- and 12-hour timescales, whereas this dissertation used hourly data, yet it does not capture the timing of the rapid physical changes in the topside ionosphere. This study could perhaps investigate the timing a solar storm has on compositional changes in the ionosphere that are reflected in density and plasma temperature profiles at different times and how that may compare to ionosonde data.

An understanding of how ISR is calibrated to ionosonde data is needed. Chapters 6 and 7 raised a flag of concern in terms of major differences seen in electron density peak parameters between ISR and ionosonde data. An analysis matching the timeframe recommended above needs to be conducted between the differences seen in ISR data and ionosonde data, which can be extracted from the Lowell Global Ionospheric Radio Observatory Data Center (LGDC) with the Principal Investigator being Prof. B. W. Reinisch of the University of Massachusetts Lowell [*Reinisch and Galkin, 2011*]. This may also address the issues surrounding the availability of ionogram data during nighttime hours, which greatly limited our study, especially during diffusive equilibrium conditions.

Once the concerns raised in the prior two paragraphs have been addressed, a thorough analysis can be built upon the results found in this dissertation by the following:

- A new relationship found between  $TEC$ ,  $TEC_t$ , and  $TEC_b$  was established in section 6.4.1 with ISR data and applied to successfully determine  $TEC$  and  $TEC_t$  using only ionogram data of  $TEC_b$ . This was only confirmed for two days of our study. Further confirmation is needed with the rest of the dataset at the timescale mentioned above.
- A combination of the new relationship found between  $TEC$ ,  $TEC_t$ , and  $TEC_b$  and new  $\kappa$  index may be used to better understand and predict the topside ionosphere. An extensive dataset mentioned at the beginning of this section can confirm this and what, if any, implications solar and geomagnetic activity may have.

- Because the topside reconstruction requires TEC from GPS, GPS STEC of  $\phi$  less than  $10^\circ$  (Chapter 6, section 2) must be used initially to properly evaluate the plasmaspheric contribution to TEC (Figures 8.1 and 8.2). GPS STEC offers a true representation of electron density directly above Millstone Hill without needing to factor in a mapping function correction (VTEC), which makes standard ionospheric assumptions and averages.
- For nondiffusive conditions, the Chapman VSH with a  $\kappa$  relationship included (equation 7.6) was able to determine the plasma temperature at the upper altitude. This answered a long-running question of whether or not a relationship between plasma temperature trends and density parameters:  $N_m F_2$ ,  $h_m F_2$  and TEC, could be found. But the stipulations of  $\kappa$  are not well understood, such as why it works better at the upper altitude and not the lower altitude and why when  $\kappa < 1.1$  a modification of  $\kappa + 0.25$  was needed. A thorough investigation is needed to detail such criteria and modifications needed and what this relationship between plasma temperature trends and density parameters truly means.
- Finally, Chapter 5 tested equation 5.3 introduced by *Whitten and Poppoff* [1971] and found it to be a good measure of  $T_e$  when the topside ionosphere was in diffusive equilibrium. This equation will need to undergo further testing for verification using an  $\alpha$  – Chapman profile and Chapman scale height. To solve for  $C$  in equation 5.3, knowledge of  $T_n$  is needed and can be easily obtained by the Defense Meteorological Satellite Program (DMSP).

Interestingly, the simplification suggested in Chapter 5, section 4 for  $(C + 1)$  to equal a multiplier of 2 in equation 5.3 during nighttime diffusive conditions is equal to  $\kappa^2$  in equation 7.6 used during nondiffusive conditions, especially around local and solar noon hours. Understanding the physical meaning behind this may be worth investigating.

## REFERENCES

- Amayenc, P., F. Bertin, and J. Papet-Lepine (1971), An empirical relationship between ionospheric equivalent slab thickness and mean gradient of the electron temperature in the F-region, *Planet and Space Sci.*, *19*(10), 1313–1317.
- Aragon-Angel, A., M. Hernandez-Pajares, J. M. J. Zornoza, and J. S. Subirana (2009), Improving the Abel transform inversion using bending angles from FORMOSAT-3/COSMIC, *GPS solutions*, *14*(1), 23–33, doi:10.1029/2010RS004578.
- Banks, P. M., and G. Kockarts (1973b), *Aeronomy, Part B*, Elsevier, New York.
- Bauer, S. J. (1969), Diffusive equilibrium in the topside ionosphere, *Proceedings of the IEEE*, *57*(6), 1114–1118.
- Bauer, S. J. (1973), *Physics of Planetary Ionospheres*, Springer, New York.
- Bhonsle, R. V., A. V. Da Rosa, and O. K. Garriott (1965), Measurement of Total Electron Content and the Equivalent Slab Thickness of the Mid-latitude Ionosphere, *Radio Sci.*, *69D*, 7, 929.
- Bilitza, D. (1991), Electron and ion temperature data for ionospheric modeling, *Adv. Space Res.*, *11*(10), 139–148.
- Bilitza, D., B. W. Reinisch, S. M. Radicella, S. Pulnits, T. Gulyaeva, and L. Triskova (2006), Improvements of the International reference ionosphere model for the top-side electron density profile, *Radio Sci.*, *41*, RS5S15, doi:10.1029/2005RS003370.
- Booker, H. G. (1956), A theory of scattering by non-isotropic irregularities with applications to radar reflections from the aurora, *J. Atmos. Terr. Phys.*, *8*, 204.
- Bowles, K. L. (1958), Observation of vertical incidence scatter from the ionosphere at 41 Mc/s, *Phys. Rev. Lett.*, *1*, 454.
- Chapman, S. (1931), The absorption and dissociative or ionizing effect of monochromatic radiation in an atmosphere on a rotating earth, *Proc. Physical Society*, *43*(1), 26.
- Coster, A., and A. Komjathy (2008), Space Weather and Global Positioning System, *Space Weather*, *6*, S06D04, doi:10.1029/2008SW000400.
- Davies, K., and X. M. Liu (1991), Ionospheric slab thickness in middle and low-latitudes, *Radio Sci.*, *26*, 1997, doi:10.1029/91RS00831.

- Fjeldbo, G. (1964), Bistatic-radar methods for studying planetary ionospheres and surfaces, *Sci. Rpt.* No. 2, NsG-377, SU-SEL-64-025, Stanford Electronics Laboratories, Stanford, California.
- Foster, J. C., and H. B. Vo (2002), Average characteristics and activity dependence of the subauroral polarization stream, *J. Geophys. Res.*, *107*(A12), 1475, doi:10.1029/2002JA009409.
- Fox, M. W., M. Mendillo, and J. A. Klobuchar (1991), Ionospheric equivalent slab thickness and its modeling applications, *Radio Sci.*, *26*(2), 429–438, doi:10.1029/90RS02624.
- Furman, D. R., and S. S. Prasad (1973), Ionospheric Slab Thickness: Its Relation to Temperature and Dynamics, *J. Geophys. Res.*, *78* (25), 5837–5843.
- Gerson, N. C. (1951), *Rep. Progr. Phys.*, *14*, 316.
- Gonzalez, S. A., B. G. Fejer, R. A. Heelis and B. Hanson (1992), Ion composition of the topside equatorial ionosphere during solar minimum, *J. Geophys. Res.*, *97* (A4), 4299–4303.
- Greenwald, R. A. (1996), The role of coherent radars in ionospheric and magnetospheric research, H. Kohl, R. Rüster and K. Schlegel (eds.), *Modern Ionospheric Science*, European Geophysical Society, Katlenburg-Lindau, Germany.
- Hanson, W. B., and F. S. Johnson (1961), Electron temperatures in the ionosphere, *Mem. Soc. Roy. Sci. Liege*, *4*, 390–423.
- Haystack (2016), <http://www.haystack.mit.edu/atm/mho/instruments/isr/isTutorial.html>.
- Hernández-Pajares, M., J. M. Juan, J. Sanz, R. Orus, A. Garcia-Rigo, J. Feltens, A. Komjathy, S. C. Schaer, and A. Krankowski (2008), The IGS VTEC maps: a reliable source of ionospheric information since 1998, *Geodesy*, *83*(3–4), 263–275.
- Huang, Y. N. (1983), Some result of ionospheric slab thickness observations at Lunping, *J. Geophys. Res.*, *88*, 5517.
- Huang, X. and B. W. Reinisch (1996), Vertical electron profiles from the Digisonde network, *Adv. Space Res.*, *18*(6), 121–129.
- Huang, X., and B. W. Reinisch (2001), Vertical electron content from ionograms in real time, *Radio Sci.*, *36*(2), 335–342.

- Isham, B., C. A. Tepley, M. P. Sulzer, Q. H. Zhou, M. C. Kelley, J. S. Friedman, and S. A. Gonzalez (2000), Upper atmospheric observations at the Arecibo Observatory: Examples obtained using new capabilities, *J. Geophys. Res.*, *105*(A8), 18609–18637.
- Jayachandran, B., T. N. Krishnankutty, and T. L. Gulyaeva, (2004), Climatology of ionospheric slab thickness, *Ann. Geophys.*, *2*, 25–33.
- Johnson, C. Y. (1966), Ionospheric composition and density from 90 to 1200 kilometers at solar minimum, *J. Geophys. Res.*, *71*(1), 330–332.
- Jursa, A., (1985), *Handbook of Geophysics and the Space Environment*, Air Force Geophysics Laboratory, Springfield.
- Kelley, M. C., V. K. Wong, N. Aponte, C. Coker, A. J. Mannucci, and A. Komjathy (2009), Comparison of COSMIC occultation-based electron density profiles and TIP observations with Arecibo incoherent scatter radar data, *Radio Sci.*, *44*, RS4011, doi:10.1029/2008RS004087.
- Kersley, L. and H. H. Hosseinieh (1976), Dependence of ionospheric slab thickness on geomagnetic activity, *J. Atmos. Terr. Phys.*, *38*, 1357.
- Kivelson, M. G. and C. T. Russell (1995), *Introduction to Space Physics*, Cambridge University Press, London.
- Knipp, D. (2011), *Understanding Space Weather and the Physics Behind It*, McGraw Hill, New York.
- Kunches, J. (2007), GNSS and Space Weather, Making the Least Out of Solar Max, *Inside GNSS*.
- Lei, J., L. Liu, W. Wan, and S. R. Zhang (2005), Variations of electron density based on long-term incoherent scatter radar and ionosonde measurements over Millstone Hill, *Radio Sci.*, *40*(2).
- Lei, J., S. Syndergaard, A. G. Burns, S. C. Solomon, W. Wang, Z. Zeng, R. G. Roble, Q. Wu, Y. Kuo, J. M. Holt, S. Zhang, D. L. Hysell, F. S. Rodrigues, and C. H. Lin (2007), Comparison of COSMIC ionospheric measurements with ground-based observations and model predictions: Preliminary results, *J. Geophys. Res.*, *112*, A07308, doi:10.1029/2006JA012240.
- Liu, L., H. Huang, Y. Chen, H. Le, B. Ning, W. Wan, and H. Zhang (2014), Deriving the effective scale height in the topside ionosphere based on ionosonde and satellite in situ observations, *J. Geophys. Res. Space Phys.*, *119*, 8472–8482.

- Liu, L., W. Wan, M. L. Zhang, B. Ning, S. R. Zhang, and J. M. Holt (2007), Variations of topside ionospheric scale heights over Millstone Hill during the 30-day incoherent scatter radar experiment, *Ann. Geophys.*, Vol. 25, No. 9, 2019-2027. This paper is licensed under CC BY 3.0, [http://publications.copernicus.org/for\\_authors/license\\_and\\_copyright.html](http://publications.copernicus.org/for_authors/license_and_copyright.html).
- Leitinger, R. (1996), Tomography, H. Kohl, R. Rüster, and K. Schlegel (eds.), *Modern Ionospheric Science*, European Geophysical Society, Katlenburg-Lindau, Germany, 346–370.
- Lowell Digisonde International (LDI) (2015), Instrument Description, <http://digisonde.com/instrument-description.html>.
- MacDoran, P. F. (1979), SERIES: Satellite emission range inferred Earth surveying, SERIES-GPS geodetic system, *Bull. Geod.*, 53, 11.
- Madrigal (2017), Overview of the Millstone Hill Incoherent Scatter Radar for Madrigal users, [http://madrigal.haystack.mit.edu/madrigal/siteSpecific/MLH\\_description.pdf](http://madrigal.haystack.mit.edu/madrigal/siteSpecific/MLH_description.pdf).
- Mannucci, A. J., B. D. Wilson, D. N. Yuan, U. J. Lindqwister, and T. F. Runge (1995), Global Monitoring of Ionospheric Total Electron Content Using the IGS Network, *IGS SPECIAL TOPICS AND NEW DIRECTIONS, Workshop proceedings*, 49.
- McNamara, L. F., G. J. Bishop, and J. A. Welsh (2011), Assimilation of ionosonde profiles into a global ionospheric model, *Radio Sci.*, 46(2), doi:10.1029/2010RS004457.
- Meehan, J., G. Fisher and W. Murtagh (2010), Understanding space weather customers in GPS-reliant industries, *Space Weather*, 8(6), doi:10.1029/2009SW000556.
- National Coordination Office for Space-Based Positioning, Navigation, and Timing (2016), <http://www.gps.gov/systems/gps/space/>.
- National Telecommunications and Information Administration (2003), United States Frequency Allocations: The Radio Spectrum, <https://www.ntia.doc.gov/files/ntia/publications/2003-allochrt.pdf>.
- NOAA Space Weather Scales (2016), <http://www.swpc.noaa.gov/noaa-scales-explanation>.
- NOAA National Centers for Environmental Information (2016), Vertical Incidence Soundings (Ionograms), <https://www.ngdc.noaa.gov/stp/IONO/ionogram.html>.



- Oliver, W. L. (1979), Incoherent scatter radar studies of the daytime middle thermosphere, *Ann. Geophys.*, *35*, 121–139.
- Reinisch, B. W., and I. A. Galkin (2011), Global ionospheric radio observatory (GIRO), *Earth, Planets, and Space*, *63*, 377–381, doi:10.5047/eps.2011.03.001.
- Reinisch, B. W., X. Huang, A. Belehaki, J. Shi, M. Zhang, and R. Ilma (2004), Modeling the IRI topside profile using scale height from ground-based ionosonde measurements, *Adv. Space Res.*, *34*, 2026–2031.
- Reinisch, B. W., and X. Huang (2001), Deducing topside profiles and total electron content from bottomside ionograms, *Adv. Space Res.*, *27*(1).
- Rishbeth, H., and O. K. Garriott (1969), *Introduction to ionospheric physics*, Elsevier, New York.
- Royal Observatory of Belgium GNSS Research Group (2014), *Ionosphere Tutorial*, [http://gnss.be/ionosphere\\_tutorial.php](http://gnss.be/ionosphere_tutorial.php).
- Schaer, S. (1999), Mapping and Predicting the Earth's Ionosphere Using the Global Positioning System, *Ph.D. Dissertation, Astronomical Institute, University of Berne, Berne, Switzerland*.
- Schaer, S., G. Beutler, L. Mervart, M. Rothacher and U. Wild (1995), Global and Regional Ionosphere Models Using the GPS Double Difference Phase Observable, *IGS SPECIAL TOPICS AND NEW DIRECTIONS*, Workshop Proc, 77.
- Schreiner, W. S., S. V. Sokolovskiy, C. Rocken, and D. C. Hunt (1999), Analysis and validation of GPS/MET radio occultation data in the ionosphere, *Radio Sci.*, *34*(4), 949–966.
- Schunk, R., and A. Nagy (2009), *Ionospheres: Physics, Plasma Physics, and Chemistry*, Cambridge University Press, London.
- Sethi, N. K., V. K. Pandey, and K. K. Mahajan (2003), Seasonal and solar activity changes of electron temperature in the F-region and topside ionosphere, *Adv. Space Res.*, *33*(6), 970–974.
- Sharma, D. K., et al. (2008), Solar activity on ionospheric temperatures in F2 region, *Ind. J. Radio Space Phys.*, *37*, 319–325.
- Stankov, S. M. and N. Jakowski (2006a), Topside plasma scale height retrieved from radio occultation measurements, *Adv. Space Res.*, *37*, 958–962.

- Stankov, S. M. and N. Jakowski (2006b), Topside ionospheric scale height analysis and modeling based on radio occultation measurements, *J. Atmos. Sol. Terr. Phys.*, *68*, 134–162.
- Stankov, S. M., N. Jakowski, S. Heise, P. Muhtarov, I. Kutiev, & R. Warnant (2003), A new method for reconstruction of the vertical electron density distribution in the upper ionosphere and plasmasphere. *J. Geophys. Res. Space Phys.*, *108*(A5), 1978–2012.
- Stankov, S. M. and R. Warnant (2009), Ionospheric slab thickness–analysis, modeling and monitoring, *Adv. Space Res.*, *44*(11), 1295–1303.
- Stauning, P. (2013), Power grid disturbances and polar cap index during geomagnetic storms, *J. Space Weather Space Clim.*, *3*, A22.
- Tepley, C. A. (1997), Current developments at Arecibo for research in the atmospheric sciences at low latitudes, *J. Atmos. Sol. Terr. Phys.*, *59*(13), 1679–1686.
- Titheridge, J. E. (1968), The maintenance of the night ionosphere, *J. Atmos. Sol. Terr. Phys.*, *30*(11), 1857–1875.
- Titheridge, J. E. (1973), The slab thickness of the mid-latitude ionosphere, *Planet Space Sci.*, *21*(10), 1775–1793.
- Thomson, J. J. (1906), *Conduction of Electricity Through Gases*, Cambridge University Press, London, UK.
- Tulasi Ram, S., S. Y. Su, C. H. Liu, B. W. Reinisch, and L. A. McKinnell (2009), Topside ionospheric effective scale heights (HT) derived with ROCSAT-1 and ground-based ionosonde observations at equatorial and midlatitude stations, *J. Geophys. Res. Space Phys.*, *114*(A10).
- Ware, R., C. Rocken, F. Solheim, M. Exner, W. Schreiner, R. Anthes, D. Feng, B. Herman, M. Gorbunov, S. Sokolovskiy, and K. Hardy (1996), GPS sounding of the atmosphere from low Earth orbit: Preliminary results, *Bulletin of the American Meteorological Society*, *77*(1), 19–40.
- Whitten, R. C. and I. G. Poppoff (1971), *Fundamentals of Aeronomy*, John Wiley & Sons, New York.
- Yue, X., W. S. Schreiner, J. Lei, S. V. Sokolovskiy, C. Rocken, D. C. Hunt, and Y. H. Kuo (2010), Error analysis of Abel retrieved electron density profiles from radio occultation measurements, *Ann. Geophys.*, *28*(1), 217.

- Yunck, T. P., L. Chao-Han, and R. Ware (2000), A history of GPS sounding, *Terr. Atmos. and Oceanic Sci.*, *11*(1), 1–20.
- Zhang, S. R., J. M. Holt, A. M. Zalucha, and C. Amory-Mazaudier (2004), Midlatitude ionospheric plasma temperature climatology and empirical model based on Saint Santin incoherent scatter radar data from 1966 to 1987, *J. Geophys. Res.*, *109*, A11311, doi:10.1029/2004JA010709.
- Zhang, S. R., J. M. Holt, P. J. Erickson, F. D. Lind, J. C. Foster, A. P. van Eyken, Y. Zhang, L. J. Paxton, W. C. Rideout, L. P. Goncharenko, and G. R. Campbell (2005), October 2002 30-day incoherent scatter radar experiments at Millstone Hill and Svalbard and simultaneous GUVI/TIMED observations, *Geophys. Res. Lett.*, *32*, L01108, doi:10.1029/2004GL020732.
- Zolesi, B. and L. R. Cander (2014), *Ionospheric prediction and forecasting*, Springer, Berlin.

**APPENDICES**

## APPENDIX A


### SOLAR AND GEOMAGNETIC INDICES

#### A.1. Explanation of Indices


- K-index is represented by disturbances in the horizontal component of Earth's magnetic field and is an integer ranging from 0 – 9, 0 classified as a period of quiet geomagnetic activity and 9 for highly disturbed geomagnetic conditions. The K-index is derived from fluctuations observed on a magnetometer for three hours from 13 geomagnetic observatories between 44 degrees and 60 degrees northern or southern geomagnetic latitude. Kp is from NOAA's National Geophysical Data Center. These fluctuations are driven by storm time geomagnetic enhancements.
- Dst-index is a classification of storm strength and possible because the strength of the surface magnetic field at low latitudes responds to the magnetospheric storm time ring current. The index is inversely proportional to the energy content of the ring current, which increases during geomagnetic storms. Values are obtained from the World Data Center for Geomagnetism and operated by the Data Analysis Center at Kyoto University.
- The solar radio flux at 10.7 cm (2800 MHz) is one of the longest running records of solar activity. The F10.7 radio emissions originate high in the chromosphere and low in the corona of the solar atmosphere. The F10.7 correlates well with the sunspot number, as well as a number of UltraViolet (UV) and visible solar irradiance records.
- The north polar cap index (PCN) monitors magnetic activity from a single near-pole station, Thule, Greenland. Magnetic activity responds to solar wind parameters as

the southward component of the interplanetary magnetic field (IMF), the azimuthal component of the IMF ( $B_y$ ), and the solar wind velocity ( $v$ ). It is a 15-minute index averaged hourly by the World Data Center for Geomagnetism and managed by the National Space Institute, Copenhagen, Denmark.

## A.2. NOAA Space Weather Prediction Center's Space Weather Scales



### NOAA Space Weather Scales



Category		Effect	Physical measure	Average Frequency (1 cycle = 11 years)
Scale	Descriptor	Duration of event will influence severity of effects		
<b>Geomagnetic Storms</b>				
G 5	Extreme	<b>Power systems:</b> widespread voltage control problems and protective system problems can occur, some grid systems may experience complete collapse or blackouts. Transformers may experience damage. <b>Spacecraft operations:</b> may experience extensive surface charging, problems with orientation, uplink/downlink and tracking satellites.	Kp values* determined every 3 hours Kp=9	Number of storm events when Kp level was met; (number of storm days) 4 per cycle (4 days per cycle)
		<b>Power systems:</b> possible widespread voltage control problems and some protective systems will mistakenly trip out key assets from the grid. <b>Spacecraft operations:</b> may experience surface charging and tracking problems, corrections may be needed for orientation problems. <b>Other systems:</b> induced pipeline currents affect preventive measures, HF radio propagation sporadic, satellite navigation degraded for hours, low-frequency radio navigation disrupted, and aurora has been seen as low as Alabama and northern California (typically 45° geomagnetic lat.)**	Kp=8	100 per cycle (60 days per cycle)
G 3	Strong	<b>Power systems:</b> voltage corrections may be required, false alarms triggered on some protection devices. <b>Spacecraft operations:</b> surface charging may occur on satellite components, drag may increase on low-Earth-orbit satellites, and corrections may be needed for orientation problems. <b>Other systems:</b> intermittent satellite navigation and low-frequency radio navigation problems may occur, HF radio may be intermittent, and aurora has been seen as low as Illinois and Oregon (typically 50° geomagnetic lat.)**	Kp=7	200 per cycle (130 days per cycle)
G 2	Moderate	<b>Power systems:</b> high-latitude power systems may experience voltage alarms, long-duration storms may cause transformer damage. <b>Spacecraft operations:</b> corrective actions to orientation may be required by ground control; possible changes in drag affect orbit predictions. <b>Other systems:</b> HF radio propagation can fade at higher latitudes, and aurora has been seen as low as New York and Idaho (typically 55° geomagnetic lat.)**	Kp=6	600 per cycle (360 days per cycle)
G 1	Minor	<b>Power systems:</b> weak power grid fluctuations can occur. <b>Spacecraft operations:</b> minor impact on satellite operations possible. <b>Other systems:</b> migratory animals are affected at this and higher levels; aurora is commonly visible at high latitudes (northern Michigan and Maine)**	Kp=5	1700 per cycle (900 days per cycle)
* Based on this measure, but other physical measures are also considered. ** For specific locations around the globe, use geomagnetic latitude to determine likely sightings (see <a href="http://www.swpc.noaa.gov/Aurora">www.swpc.noaa.gov/Aurora</a> )				
<b>Solar Radiation Storms</b>				
S 5	Extreme	<b>Biological:</b> unavoidable high radiation hazard to astronauts on EVA (extra-vehicular activity), passengers and crew in high-flying aircraft at high latitudes may be exposed to radiation risk. *** <b>Satellite operations:</b> satellites may be rendered useless, memory impacts can cause loss of control, may cause serious noise in image data, star-trackers may be unable to locate sources; permanent damage to solar panels possible. <b>Other systems:</b> complete blackout of HF (high frequency) communications possible through the polar regions, and position errors make navigation operations extremely difficult.	Flux level of ≥ 10 MeV particles (ions)* 10 <sup>7</sup>	Number of events when flux level was met** Fewer than 1 per cycle
		<b>Biological:</b> unavoidable radiation hazard to astronauts on EVA; passengers and crew in high-flying aircraft at high latitudes may be exposed to radiation risk.*** <b>Satellite operations:</b> memory device problems and noise on imaging systems; star-tracker problems may cause orientation problems, and solar panel efficiency can be degraded. <b>Other systems:</b> blackout of HF radio communications through the polar regions and increased navigation errors over several days are likely.	10 <sup>6</sup>	3 per cycle
S 3	Strong	<b>Biological:</b> radiation hazard avoidance recommended for astronauts on EVA; passengers and crew in high-flying aircraft at high latitudes may be exposed to radiation risk.*** <b>Satellite operations:</b> single-event upsets, noise in imaging systems, and slight reduction of efficiency in solar panel are likely. <b>Other systems:</b> degraded HF radio propagation through the polar regions and navigation position errors likely.	10 <sup>5</sup>	10 per cycle
S 2	Moderate	<b>Biological:</b> passengers and crew in high-flying aircraft at high latitudes may be exposed to elevated radiation risk.*** <b>Satellite operations:</b> infrequent single-event upsets possible. <b>Other systems:</b> effects on HF propagation through the polar regions, and navigation at polar cap locations possibly affected.	10 <sup>4</sup>	25 per cycle
S 1	Minor	<b>Biological:</b> none. <b>Satellite operations:</b> none. <b>Other systems:</b> minor impacts on HF radio in the polar regions.	10	50 per cycle
* Flux levels are 5 minute averages. Flux in particles*ster*cm <sup>-2</sup> Based on this measure, but other physical measures are also considered. ** These events can last more than one day. *** High energy particle (>100 MeV) are a better indicator of radiation risk to passenger and crews. Pregnant women are particularly susceptible.				
<b>Radio Blackouts</b>				
R 5	Extreme	<b>HF Radio:</b> Complete HF (high frequency)** radio blackout on the entire sunlit side of the Earth lasting for a number of hours. This results in no HF radio contact with mariners and en route aviators in this sector. <b>Navigation:</b> Low-frequency navigation signals used by maritime and general aviation systems experience outages on the sunlit side of the Earth for many hours, causing loss in positioning. Increased satellite navigation errors in positioning for several hours on the sunlit side of Earth, which may spread into the night side.	GOES X-ray peak brightness by class and by flux* X20 (2x10 <sup>-5</sup> )	Number of events when flux level was met; (number of storm days) Fewer than 1 per cycle
R 4	Severe	<b>HF Radio:</b> HF radio communication blackout on most of the sunlit side of Earth for one to two hours. HF radio contact lost during this time. <b>Navigation:</b> Outages of low-frequency navigation signals cause increased error in positioning for one to two hours. Minor disruptions of satellite navigation possible on the sunlit side of Earth.	X10 (10 <sup>-5</sup> )	8 per cycle (8 days per cycle)
R 3	Strong	<b>HF Radio:</b> Wide area blackout of HF radio communication, loss of radio contact for about an hour on sunlit side of Earth. <b>Navigation:</b> Low-frequency navigation signals degraded for about an hour.	X1 (10 <sup>-6</sup> )	175 per cycle (140 days per cycle)
R 2	Moderate	<b>HF Radio:</b> Limited blackout of HF radio communication on sunlit side of the Earth, loss of radio contact for tens of minutes. <b>Navigation:</b> Degradation of low-frequency navigation signals for tens of minutes.	M5 (5x10 <sup>-7</sup> )	350 per cycle (300 days per cycle)
R 1	Minor	<b>HF Radio:</b> Weak or minor degradation of HF radio communication on sunlit side of the Earth, occasional loss of radio contact. <b>Navigation:</b> Low-frequency navigation signals degraded for brief intervals.	M1 (10 <sup>-7</sup> )	2000 per cycle (950 days per cycle)
* Flux, measured in the 0.1-0.8 nm range, in W m <sup>-2</sup> . Based on this measure, but other physical measures are also considered. ** Other frequencies may also be affected by these conditions. URL: <a href="http://www.swpc.noaa.gov/NOAA_scales">www.swpc.noaa.gov/NOAA_scales</a>				

April 7, 2011

Figure A.1. NOAA Space Weather Prediction Center's Space Weather Scales.

## APPENDIX B

### SCALE HEIGHT DERIVATIONS

#### B.1. Hydrostatic Scale Height, H

At any height in the atmosphere, the air pressure is due to the force per unit area exerted by the weight of all air above it. Net upward force acting on a thin slab of air due to the decrease in atmospheric pressure with height is in balance with the net downward force due to gravity:

$$\frac{dP}{dh} = -g\rho, \quad (B.1)$$

where  $g$  is gravity and  $\rho$  is density of a gas.  $\rho$  is also equal to the number density,  $N$ , multiplied by the mean molecular mass,  $m$ . Equation B.1 can be rewritten as

$$\frac{dP}{dh} = -gNm. \quad (B.2)$$

From the ideal gas law

$$P = Nk_bT, \quad (B.3)$$

where  $P$  is the pressure,  $k_b$  is the Boltzmann's constant and  $T$  is temperature. Equation B.2 can be written as

$$\frac{d(Nk_bT)}{dh} = -gNm. \quad (B.4)$$

With respect to how density,  $N$ , varies with height,  $h$ , equation B.4 becomes

$$\frac{dN}{dh}k_bT = -gNm. \quad (B.5)$$

Solving for  $N$ ,



$$\frac{dN}{dh} = \frac{-gNm}{k_b T}, \quad (B.6)$$

and

$$\frac{dN}{N} = \frac{-gm}{k_b T} dh, \quad (B.7)$$

and finally

$$\int_{N_o}^N \frac{dN}{N} = \int_{h_o}^h \frac{-gm}{k_b T} dh. \quad (B.8)$$

If scale height,  $H = \frac{k_b T}{gm}$ ,

$$\ln \frac{N}{N_o} = \frac{-(h - h_o)}{H}, \quad (B.9)$$

$$N = N_o \exp \left[ \frac{-(h - h_o)}{H} \right]. \quad (B.10)$$

## B.2. The $\alpha$ – Chapman Layer from First Principles

Again, the ideal gas law describes particle interactions due to the dependent variables of pressure, density and temperature:

$$P = Nk_b T, \quad (B.11)$$

where  $P$  is the pressure,  $N$  is number density,  $k_b$  is the Boltzmann's constant and  $T$  is temperature. Atmospheric pressure can only vary by height,  $h$ , which the gradient  $\frac{dP}{dh}$  is equal to the weight of the atmosphere above:

$$\frac{dP}{dh} = -gNm, \quad (B.12)$$

where  $g$  is gravity and  $m$  the mean molar mass. The first order differential solution for  $N$  is

$$N = N_0 \exp\left(\frac{-h}{H}\right), \quad (B.13)$$

as shown by equation B.10 where  $H$  is the scale height and given by

$$H = \frac{k_b T}{gm}. \quad (B.14)$$

In order to superimpose an ionosphere of very little pressure, Chapman [1931] proposed  $H$  be treated as a unit from a reference height,  $h_o$ . The change in  $H$  due to  $h$  at and near  $h_o$  will be assumed small and neglected. Therefore,

$$z = \frac{(h - h_o)}{H}. \quad (B.15)$$

Plugging equation B.15 into B.13 gives

$$N = N_0 \exp(-z). \quad (B.16)$$

Equation B.16 assumes both temperature,  $T$ , and scale height,  $H$ , are independent of altitude.

The distribution of charged particles, electrons and ions, in the ionosphere are governed by the equation of continuity:

$$\frac{dN}{dt} = P - L, \quad (B.17)$$

where  $P$  is the production of positive ions and free electrons due to intensity of radiation,  $I$ .  $I$  is given by

$$I(h, \chi) = I_o \exp[1 - z - \sec \chi \exp(-z)], \quad (B.18)$$

and describes the number of species produced by absorption of radiation per unit area as you change in height,  $h$ , and solar zenith,  $\chi$ .  $L$  in equation B.17 is the loss rate due to recombination and is given by Bauer [1973] as

$$L = a_e NN_e + a_- NN_- , \quad (B.19)$$

where  $a$  is the coefficient for recombination. Because pressure in the topside ionosphere is low, coefficients of recombination for the electrons and ions are equal, therefore equation (B.19) reduces to

$$L = aN^2 . \quad (B.20)$$

In a steady-state ionosphere, the time-derivative term in equation B.17 is negligible.

Plugging equation B.18 and B.20 into B.17 gives

$$0 = I(h, \chi) - aN^2 . \quad (B.21)$$

At reference height,  $h_o$ ,  $\chi = 0^\circ$  and equation B.21 becomes

$$I_o = aN_o^2 , \quad (B.22)$$

or

$$N_o = \left( \frac{I_o}{a} \right)^{\frac{1}{2}} . \quad (B.23)$$

Solving for equation B.21 at all other heights and zenith angles,

$$0 = I_o \exp[1 - z - \sec \chi \exp(-z)] - aN^2 , \quad (B.24)$$

$$aN^2 = I_o \exp[1 - z - \sec \chi \exp(-z)] , \quad (B.25)$$

$$N^2 = \left( \frac{I_o}{a} \right) \exp[1 - z - \sec \chi \exp(-z)] , \quad (B.26)$$

$$N = \left( \frac{I_o}{a} \right)^{1/2} \exp \left[ \frac{1}{2} (1 - z - \sec \chi \exp(-z)) \right] , \quad (B.27)$$

plugging equation B.23 into B.27

$$N = N_o \exp \left[ \frac{1}{2} (1 - z - \sec \chi \exp(-z)) \right] . \quad (B.28)$$

When  $\chi = 0^\circ$ ,  $\frac{N}{N_o} = \text{maximum values}$  and  $\sec \chi = 1$ . Equation B.28 becomes the  $\alpha -$  Chapman layer:

$$N = N_o \exp \left[ \frac{1}{2} (1 - z - \exp(-z)) \right]. \quad (\text{B. 29})$$

### B.3. Plasma Scale Height, $H_p$ , in which Ambi-Polar Diffusion Plays a Significant Role

The upper ionosphere is characterized by the transfer of charged particles in a plasma by ambi-polar diffusion, thermospheric winds, and ionospheric-magnetospheric interactions. The height distribution of electron density in the topside ionospheric is governed by the plasma scale height:

$$H_p = \frac{2k_b \frac{(T_i + T_e)}{2}}{m_i g}, \quad (\text{B. 30})$$

or

$$H_p = \frac{k_b (T_i + T_e)}{m_i g}, \quad (\text{B. 31})$$

where  $k_b$  is the Boltzmann's constant,  $m_i$  the mass of an ion,  $g$ , gravity,  $T_i$  the ion temperature, and  $T_e$  the electron temperature.

Ambi-polar diffusion allows no net electrical current to flow in the plasma and ions and electrons diffuse at the same rate. In a simple model of plasma transport for steady-state conditions, the ion equation of continuity can be combined with the momentum equation, as given by *Banks and Kockarts* [1973]:

$$\frac{d^2 N_e}{dh^2} + \left[ \frac{1}{H_p} + \frac{1}{D_a} \frac{dD_a}{dh} - \frac{\omega_D}{D_a \sin^2 I} \right] \frac{dN_e}{dh} + \left[ \frac{1}{D_a H_p} \frac{dD_a}{dh} - \frac{1}{D_a \sin^2 I} \frac{d\omega_D}{dh} \right] N_e =$$

$$= \frac{L_i - P_i}{D_a \sin^2 I}, \quad (\text{B.32})$$

where  $D_a$  is the ambi-polar diffusion coefficient

$$D_a = \left(1 + \frac{T_e}{T_i}\right) D_{in}, \quad (\text{B.33})$$

and  $D_{in}$  is the ion-neutral coefficient:

$$D_{in} = \left(\frac{k_b T}{m_i}\right) \frac{1}{\nu_{in}}, \quad (\text{B.34})$$

where  $\nu_{in}$  is the velocity term for ion-neutrals. For the motion of plasma having one ion species,  $N_e = N_i$  and  $\nu_{in}$  is proportional to  $N_n$ . Equation B.33 becomes

$$D_a = \left(1 + \frac{T_e}{T_i}\right) \left(\frac{k_b T}{m_i}\right) \frac{1}{\nu_{in}} = \left(\frac{k_b}{m_i}\right) \frac{(T_i + T_e)}{\nu_{in}}. \quad (\text{B.35})$$

At high altitudes, the neutral density decreases exponentially and drift, production and loss terms become negligible. Also,  $D_a$  increases exponentially because  $D_a \propto \frac{1}{N_n}$ , where  $\nu_{in} \propto$

$N_n$ . Equation B.32 becomes

$$\frac{d^2 N_e}{dh^2} + \frac{1}{H_p} \frac{dN_e}{dh} = 0. \quad (\text{B.36})$$

Let  $\frac{d^2 N_e}{dh^2} = y''$ ,  $\frac{1}{H_p} \frac{dN_e}{dh} = y'$ ,  $N_e = y$ , and  $x = h$ .

If  $y = e^{rx}$ , then  $y' = r e^{rx}$ , and  $y'' = r^2 e^{rx}$ .

Equation B.36 becomes

$$r^2 e^{rx} + \frac{1}{H_p} r e^{rx} = 0 \quad \Rightarrow \quad e^{rx} \left( r^2 + \frac{1}{H_p} r \right) = 0. \quad (\text{B.37})$$

Solving for r,

$$r^2 + \frac{1}{H_p} r = 0, \quad (B.38)$$

$$r = -\frac{1}{H_p}. \quad (B.39)$$

Therefore, the linear solution to the second-order differential equation B.36 is

$$N_e(h) = C_1 \exp\left(\frac{-h}{H_p}\right). \quad (B.40)$$

For a reference height,  $h_o$ ,  $C_1 = N_{e_o}$ . Equation B.40 then becomes

$$N_e(h) = N_{e_o} \exp\left(\frac{-(h - h_o)}{H_p}\right). \quad (B.41)$$

## APPENDIX C

### ISR ERRORS

#### C.1. Overview of ISR Errors

The Madrigal-distributed database interface is hosted online for open access to Millstone Hill's ISR and other instrumentation data as discussed in Chapter 4. The original campaign data files were reobtained from the Madrigal website including the statistical error in the following parameters used in this dissertation: uncorrected electron density ( $N_e$ ), corrected electron density ( $N_e$ ), electron ( $T_e$ ), and ion ( $T_i$ ) temperatures.

In the Madrigal Parameter Documentation (MPD) file found at [http://madrigal.haystack.mit.edu/madrigal/parmDesc.html#HMAX\\_MODEL](http://madrigal.haystack.mit.edu/madrigal/parmDesc.html#HMAX_MODEL), it details selected Madrigal parameters. For the uncorrected electron density parameter (POPL) and associated error in uncorrected electron density (DPOPL) a statistical uncertainty of the fit autocorrelation function (ACF) at zero lag is used. The report titled, Overview of the Millstone Hill Incoherent Scatter Radar for Madrigal users states that the Millstone Hill ISR uses INSCAL for standard fitting [*Madrigal*, 2017]. Ionospheric plasma parameters are determined by the way INSCAL analyzes incoherent scatter ACFs, which are formed from the measured lag-products using a trapezoidal summation rule [*Madrigal*, 2017]. A multidimensional nonlinear least squares fit to each ACF is then performed to compute estimates of the plasma parameters, and parameter error bars are computed by assuming that chi square is 1.0 [*Madrigal*, 2017].

In the MPD file, under the DPOPL description there is a disclaimer, “the statistical uncertainty is normally much smaller than the larger uncertainty in the density calibration, which is ~20%.”

The electron density ( $N_e$ ) and associated errors are shown in Figures C.1 and C.2 below for reference quiet day 294 during the hours of 02 and 15 UT, respectively. The Figures use both the previous Madrigal data and the newly obtained Madrigal single pulse data. Each Figure shows the previously used  $N_e$  values (red line), single pulse corrected  $N_e$  values (purple line) with associated errors, single pulse uncorrected  $N_e$  (orange line) with associated errors, the madrigal given ionosonde  $N_mF_2$  value (bright green dot), and the madrigal given ISR  $N_mF_2$  value (dark green dot). For comparison, Figures C.3 and C.4 show example plots of what 10% error looks like for 11 UT and 18 UT on quiet day 294.

The same procedure mentioned above for reference quiet day 294 was conducted for reference active day 297 and are shown in Figures C.5 and C.6 below. In all figures for both days, the errors in  $N_e$  are minimal and do not offer up an explanation of why there are large differences in the ionosonde and ISR found  $N_e$  values. These results will not change the results found in this dissertation.

From the data plots it is clear, in general, the final ISR densities (after correction) increase the density towards the ionosonde values, as expected. The fact they do not produce a one-to-one match at the peak probably reflects upon how calibration is done. For example, if only noon times are chosen to adjust the calibration, then all day a hard-wired multiplier is introduced. The question that arises is whether there is an expectation of ISR  $N_mF_2$  to track exactly to the ionosonde  $N_mF_2$ ? This is not expected; hence, diurnal



variability of this calibration would exist. Even worse if the noon calibration was done once per week. We do not have access to these old log book records, and it's unclear if they exist. The text above states "...than the larger uncertainty in the density calibration, which is ~20%," this is most certainly consistent with what we found. Our analysis by comparing ISR with ionosonde at selected times suggests the uncertainty is more like 10% - 20%.

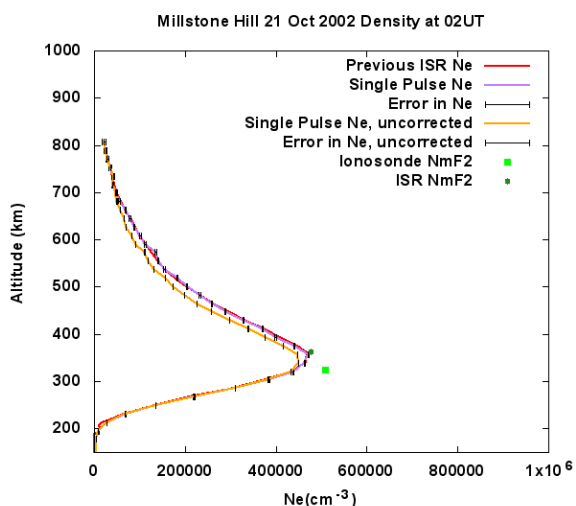


**Figure C.1.**  $N_e$  results with errors for nighttime hour 02 UT on quiet day 294.

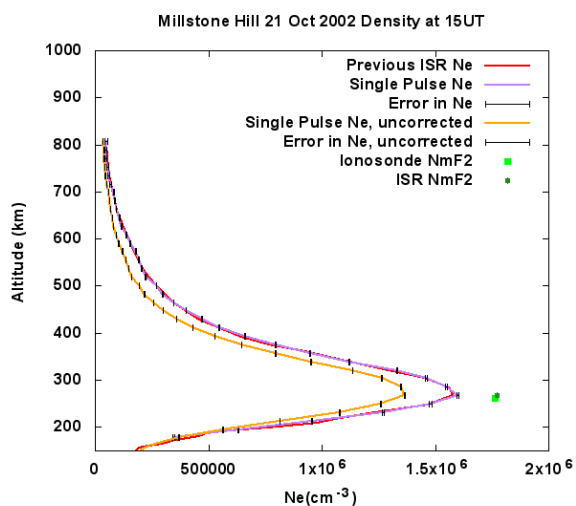


**Figure C.2.**  $N_e$  results with errors for daytime hour 15 UT on quiet day 294.

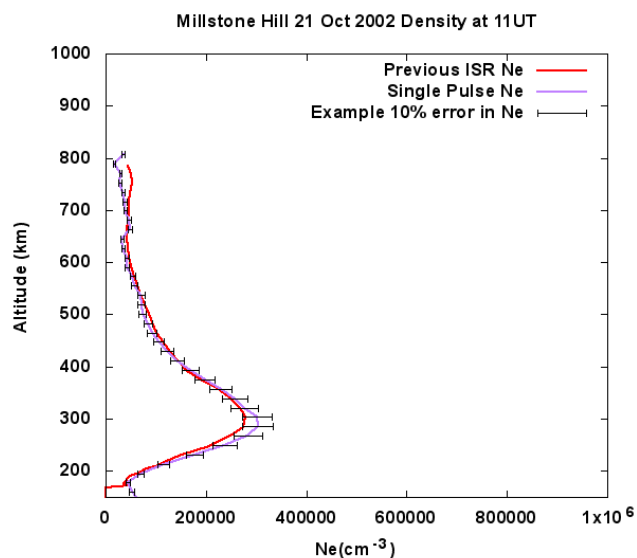


**Figure C.3.**  $N_e$  results with an example error of 10% for daytime hour 11 UT for quiet day 294.

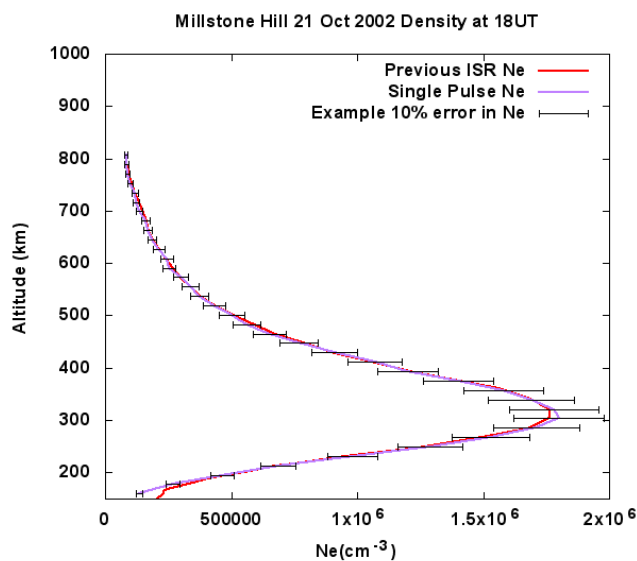


**Figure C.4.**  $N_e$  results with an example error of 10% on daytime hour 18 UT for quiet day 294.

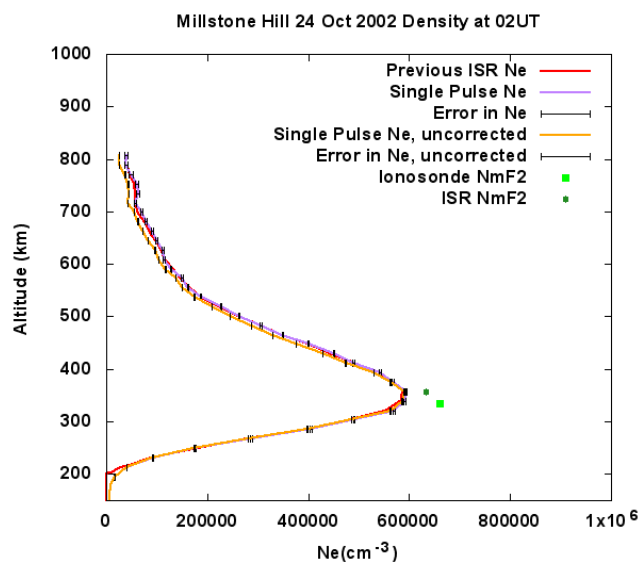


**Figure C.5.**  $N_e$  results with errors for nighttime hour 02 UT on active day 297.

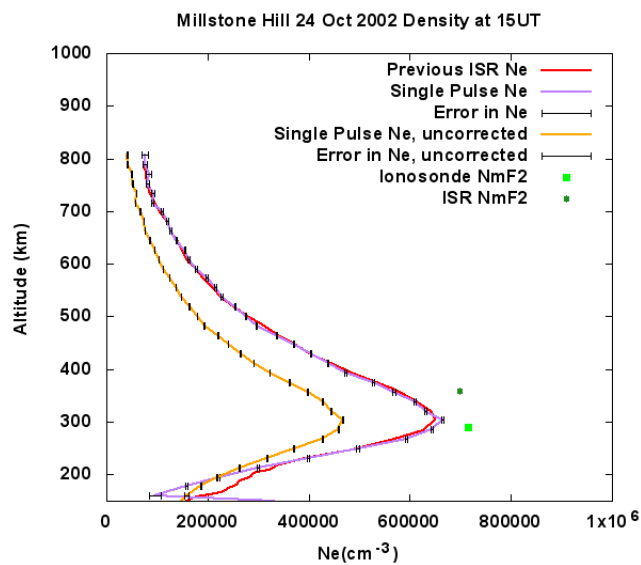


**Figure C.6.**  $N_e$  results with errors for daytime hour 15 UT on active day 297.

The electron temperature ( $T_e$ ), ion temperature ( $T_i$ ), and associated errors are shown in Figures C.7 and C.8 for reference quiet day 294 during the hours of 02, and 12 UT, respectively. The Figures use both the previous Madrigal data and the newly obtained Madrigal single pulse data. Each figure shows the previously used  $T_e$  values (black line) and  $T_i$  values (red line), as well as the single pulse corrected  $T_e$  values (purple line) with associated error bars and single pulse corrected  $T_i$  values (orange line) and associated error bars. The same procedure was done for reference active day 297 and are shown in Figures C.9 and C.10.

For comparison, Figure C.11 shows an example plot of what 10% error looks like for 18 UT for active day 297. In all figures for both the reference quiet and active days, the errors in  $T_e$  and  $T_i$  are minimal, especially the region used to calculate scale heights in the topside ionosphere (428 km – 520 km) and will not change the results found in this dissertation.

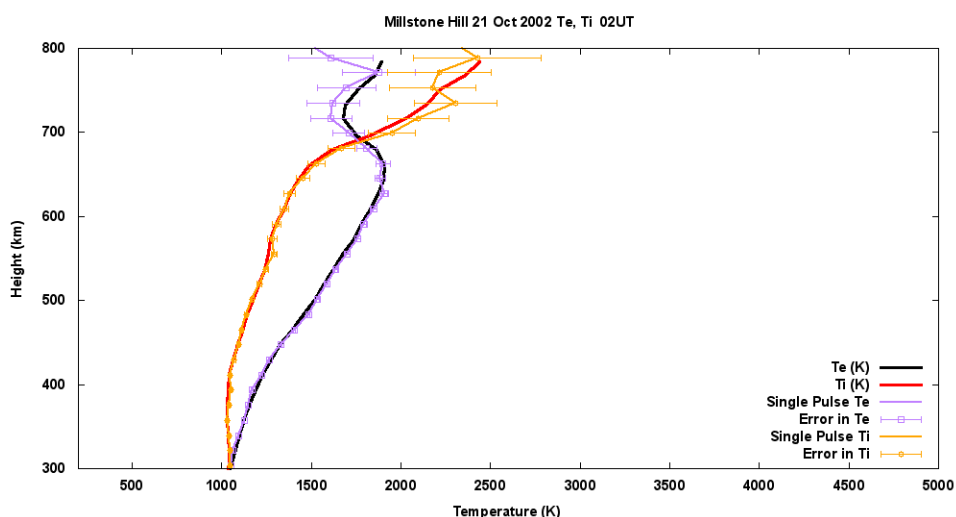


**Figure C.7.**  $T_e$  and  $T_i$  results with associated errors for nighttime hour 02 UT on quiet day 294.

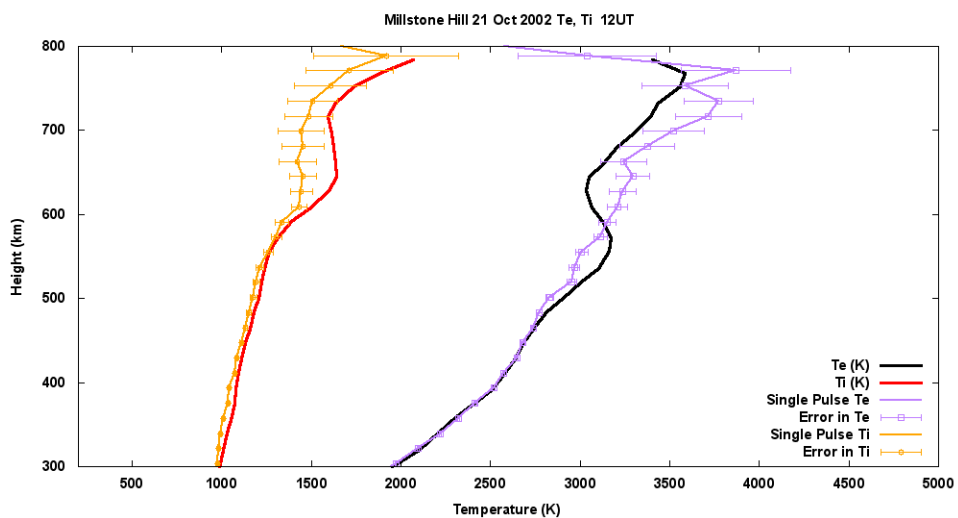


**Figure C.8.**  $T_e$  and  $T_i$  results with associated errors for daytime hour 12 UT on quiet day 294.

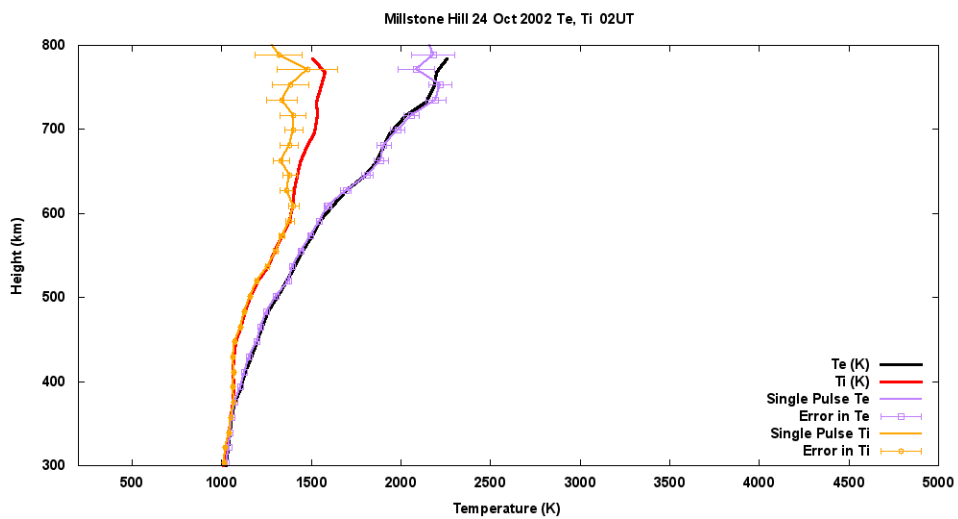


**Figure C.9.**  $T_e$  and  $T_i$  results with associated errors for nighttime hour 02 UT on active day 297.

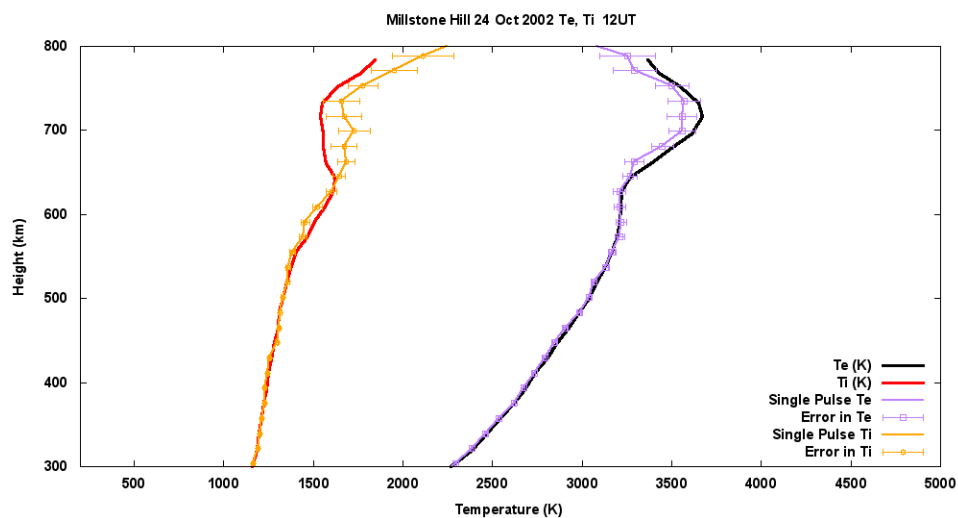


**Figure C.10.**  $T_e$  and  $T_i$  results with associated errors for daytime hour 12 UT on active day 297.

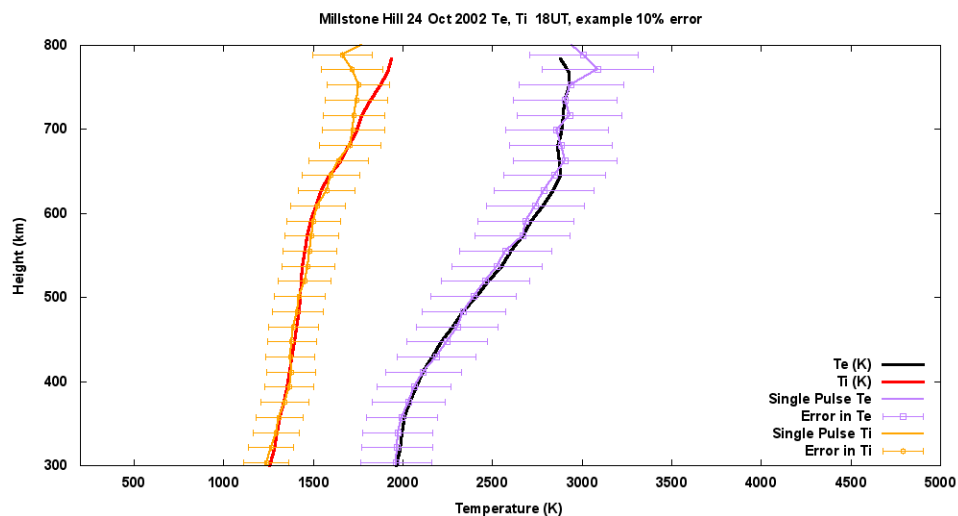


**Figure C.11.**  $T_e$  and  $T_i$  results with an example error of 10% for daytime hour 18 UT on active day 294.

## APPENDIX D

### ISR SCALED TO IONOSONDE RESULTS

#### D.1. When ISR is scaled to an ionosonde, how does TEC change?

Section 7.2 of the dissertation found ionosondes routinely determined a lower altitude of peak density height,  $h_mF_2$ , and a higher peak density value,  $N_mF_2$  when compared to ISR. The question was raised to scale ISR data to match the ionosonde bottomside  $N_e$  profiles to see how that would affect total electron content (TEC). Tables 7.1 and 7.2 were used to scale ISR  $N_e$  values to match that of the ionosonde values. Figure D.1 shows the results for reference quiet day 294 and Figure D.2 for reference active day 297. In both Figures D.1 and D.2, ISR TEC is represented by the black solid lines, adjusted ISR TEC (green lines) GPS STEC by the black triangles, GPS STEC of  $\phi$  less than  $10^\circ$  by blue circles, and GPS VTEC of  $\phi$  less than  $30^\circ$  by pink circles. The TEC increases between 3-5 TECU maximum for both reference quiet day 294 (Figure D.1) and reference active day 297 (Figure D.2) when ISR is adjusted to match ionosondes, making very minimal changes in our results.

Figures 8.1 and 8.2 from the dissertation are recreated in Figures D.3 and D.4 to show the TEC topside comparison between ISR (black), adjusted ISR to ionosonde (blue), GPS STEC (red) when a GPS satellite has an inclination angle of 10 degrees or less, and GPS VTEC (pink) when a GPS satellite has an inclination angle of 30 degrees or less for quiet day 294 and active day 297, respectively. In the dissertation, it is discussed how the TEC topside can be retrieved from a GPS receiver subtracting ionosonde bottomside TEC.

In both Figures D.3 and D.4, the change of TEC topside for the adjusted ISR is between 1-3 TECU, making very minimal changes in our results.

By increasing the ISR  $N_mF_2$  to match the ionosonde  $N_mF_2$ , the TEC associated with the ISR profile is increased. Proceeding to determine topside TEC from the revised ISR electron density profiles moves the topside TEC closer to the GPS value. This effectively reduces the difference that might be attributed to the plasmaspheric contribution. Note: the reduced value of 2 to 5 TECU is more probable to be responsible for the plasmasphere than was the 3 to 10 TECU difference for day 294. Also, due to the limited availability of ionosonde data at night, Figure D.3 shows only two periods when TEC topside could be calculated from GPS STEC – Ionosonde bottomside TEC on day 294 when Figure D.1 shows five GPS STEC periods throughout the day. The same issue occurred for day 297, Figures D.2 and D.4.



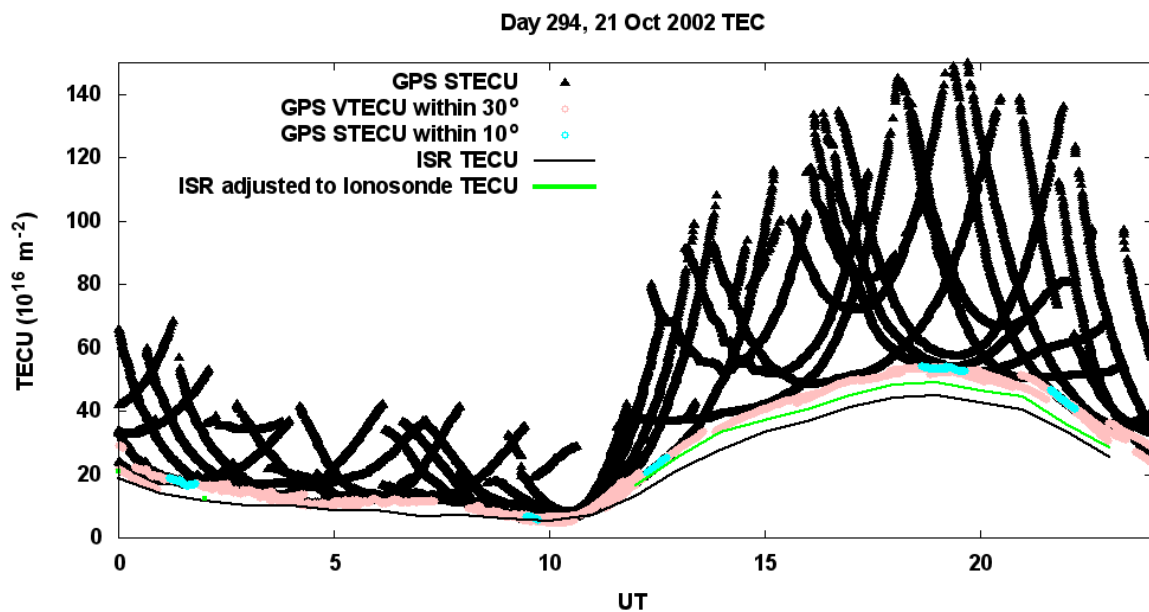


**Figure D.1.** Adjusted ISR to fit ionosonde bottomside Ne data versus GPS TEC results on quiet day 294.

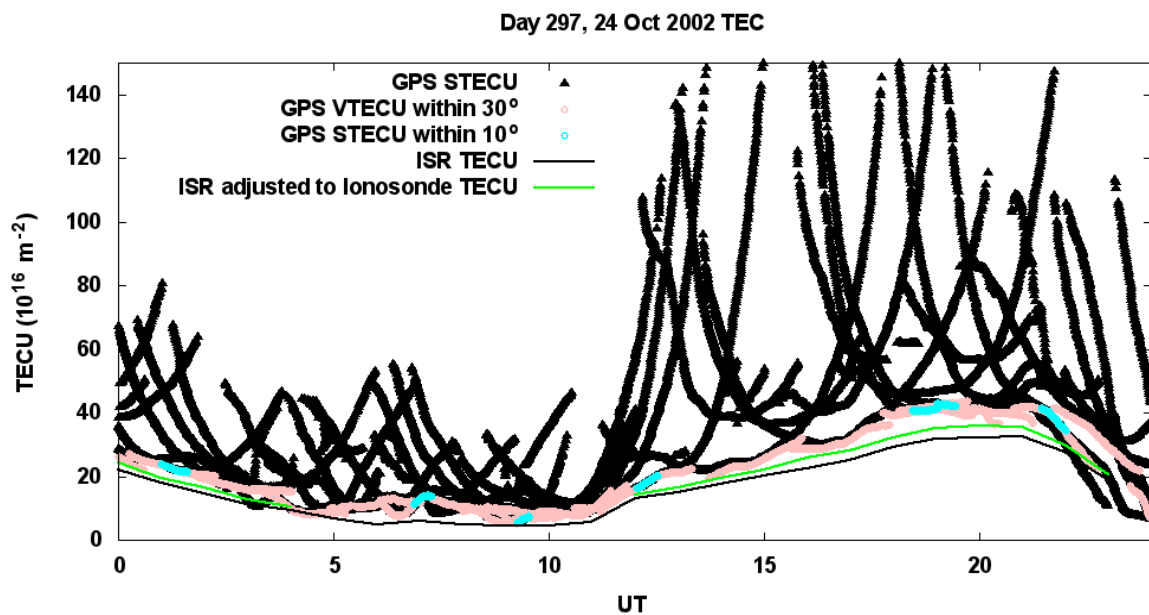


**Figure D.2.** Adjusted ISR to fit ionosonde bottomside Ne data versus GPS TEC results on active day 297.

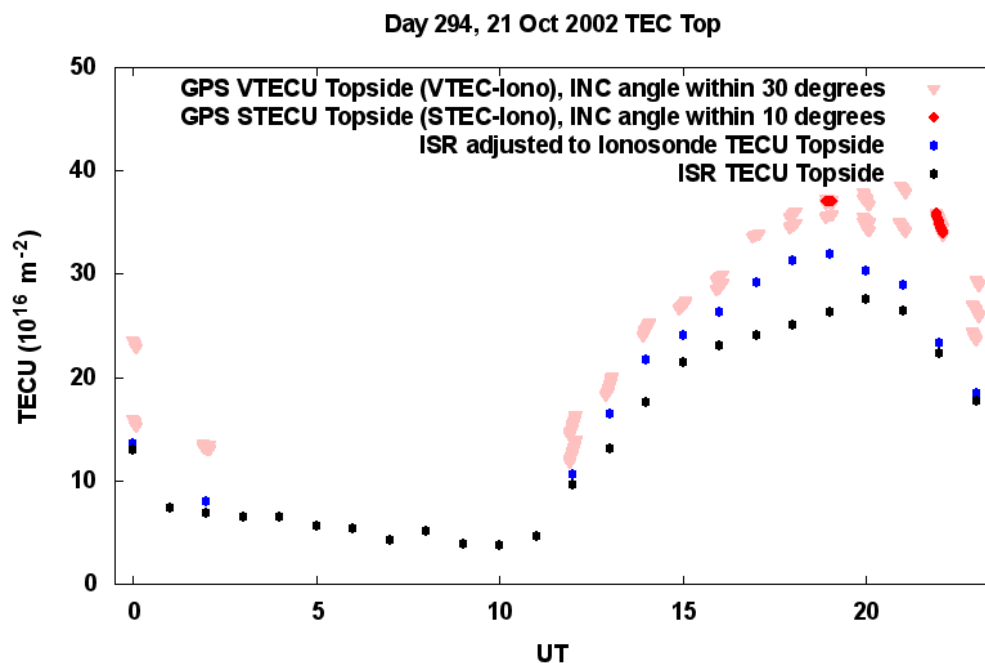


**Figure D.3.** TEC topside comparison between ISR (black), adjusted ISR to ionosonde (blue), GPS STEC (red), and GPS VTEC (pink) for quiet day 294.

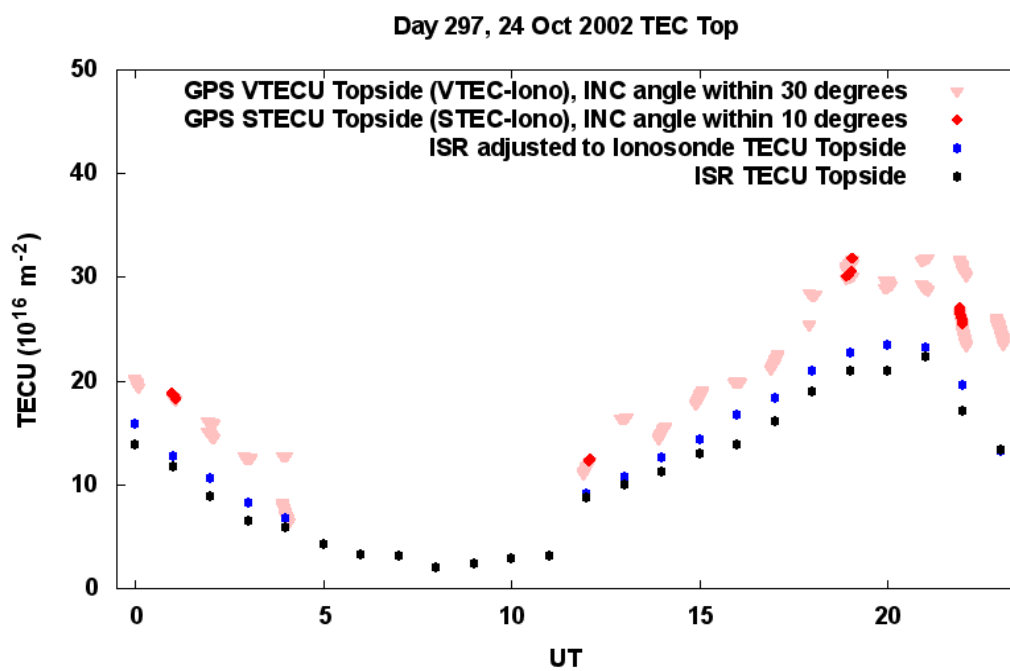


**Figure D.4.** TEC topside comparison between ISR (black), adjusted ISR to ionosonde (blue), GPS STEC (red), and GPS VTEC (pink) for active day 297.

## APPENDIX E

## IONOSPHERE TOPSIDE RECONSTRUCTION RESULTS

## E.1. Hourly Topside Reconstruction Results for Quiet Reference Day 294

Each figure contains an ISR density profile (black) versus an ionosonde profile (green). The different colors represent the  $\alpha$  – Chapman profile and Chapman temperature used. The red-dashed line is equal to the Chapman pseudo-temperature. The right side shows the adjustments made to the raw ionosonde bottomside profile (left) to fit ISR.

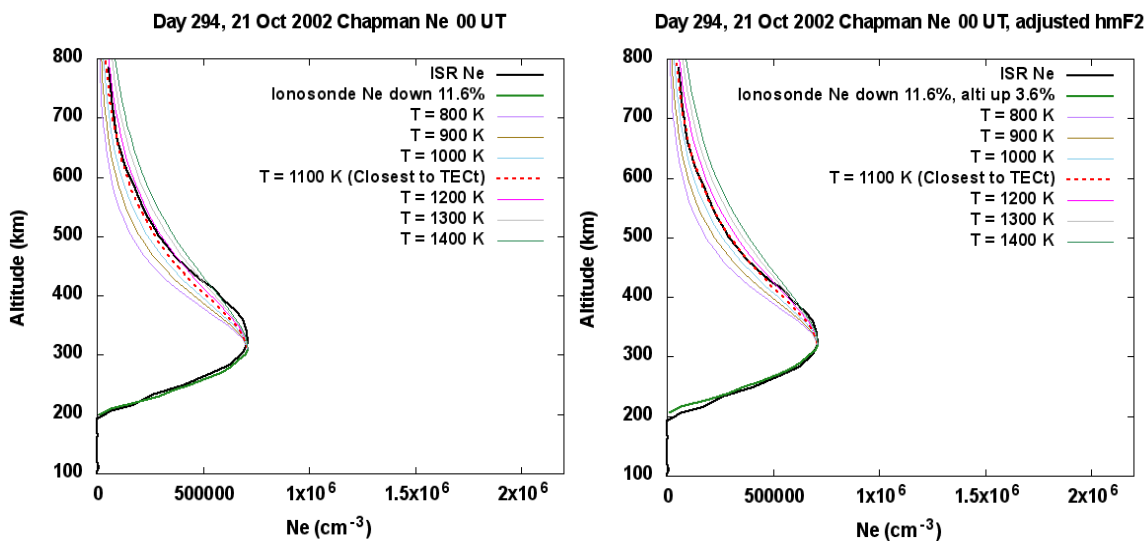


**Figure E.1.** Quiet day 294, 00 UT density profile ISR (black) versus ionosonde (green). The different colors represent the  $\alpha$  – Chapman profile and Chapman temperature used. The red-dashed line is equal to the Chapman pseudo-temperature. The right side shows the adjustments made to the raw ionosonde bottomside profile (left) to fit ISR.

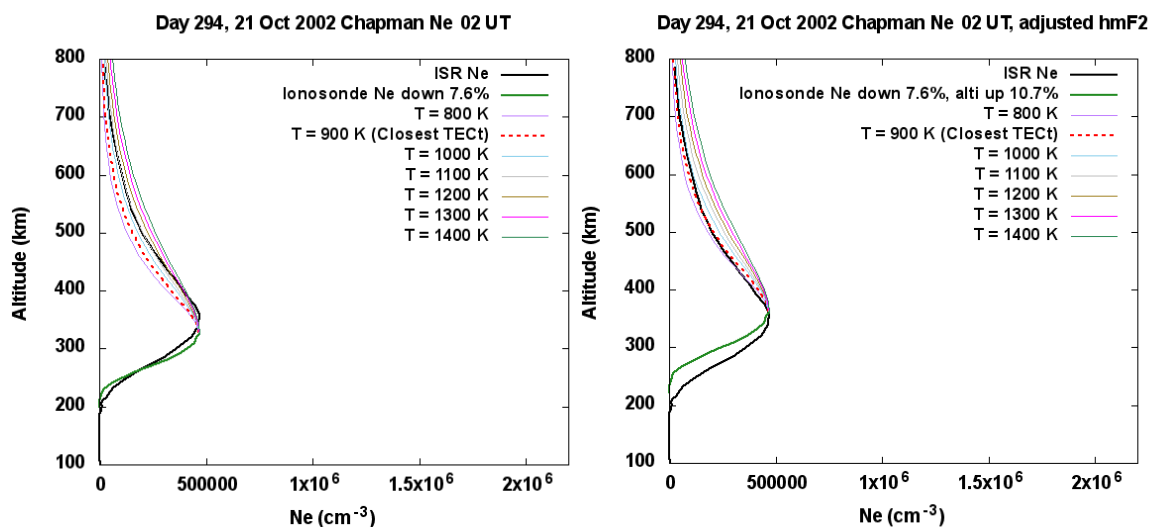


**Figure E.2.** Quiet day 294, 02 UT density profile ISR (black) versus ionosonde (green). The different colors represent the  $\alpha$  – Chapman profile and Chapman temperature used. The red-dashed line is equal to the Chapman pseudo-temperature. The right side shows the adjustments made to the raw ionosonde bottomside profile (left) to fit ISR.

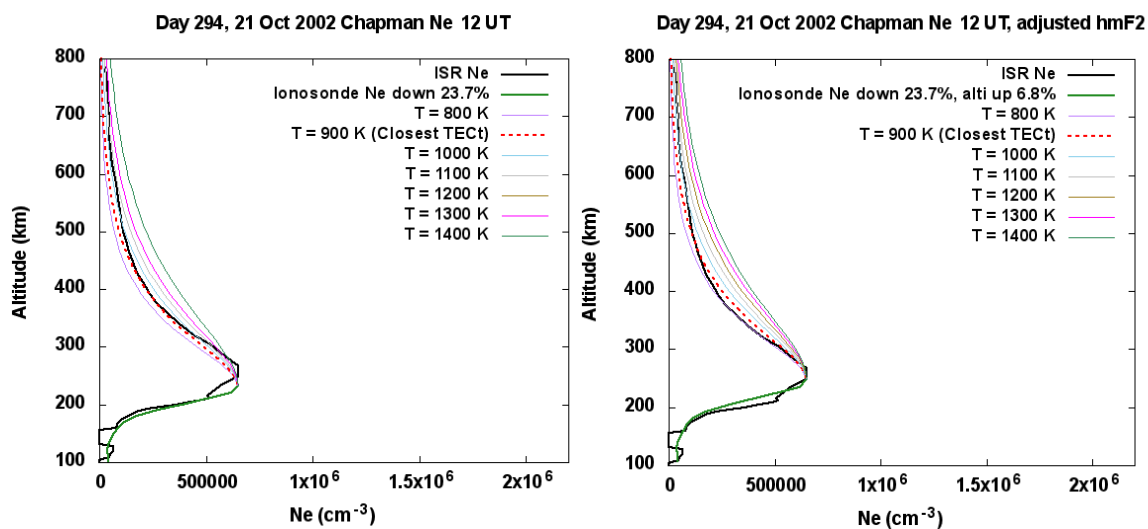


**Figure E.3.** Quiet day 294, 12 UT density profile ISR (black) versus ionosonde (green). The different colors represent the  $\alpha$  – Chapman profile and Chapman temperature used. The red-dashed line is equal to the Chapman pseudo-temperature. The right side shows the adjustments made to the raw ionosonde bottomside profile (left) to fit ISR.

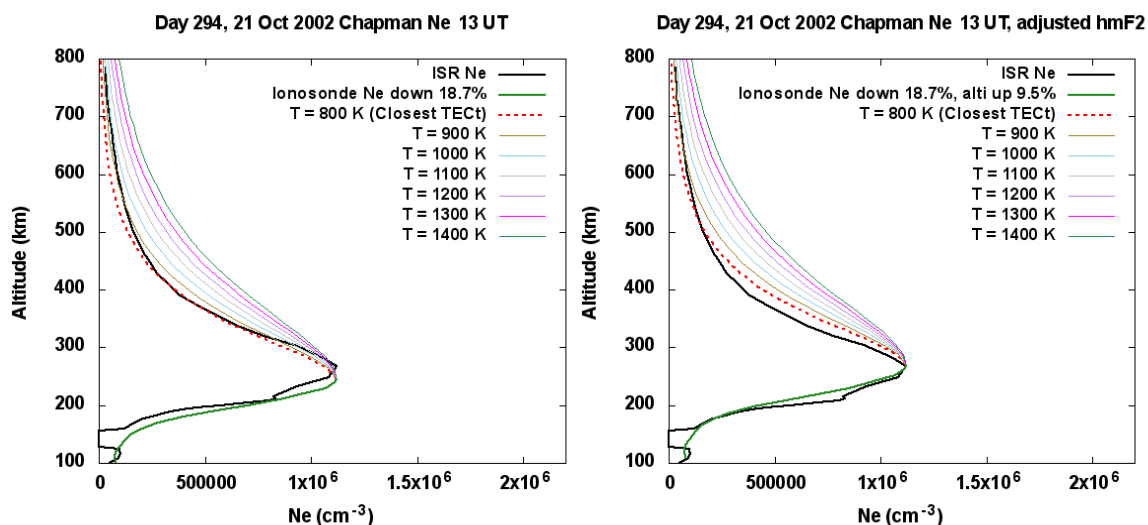


**Figure E.4.** Quiet day 294, 13 UT density profile ISR (black) versus ionosonde (green). The different colors represent the  $\alpha$  – Chapman profile and Chapman temperature used. The red-dashed line is equal to the Chapman pseudo-temperature. The right side shows the adjustments made to the raw ionosonde bottomside profile (left) to fit ISR.

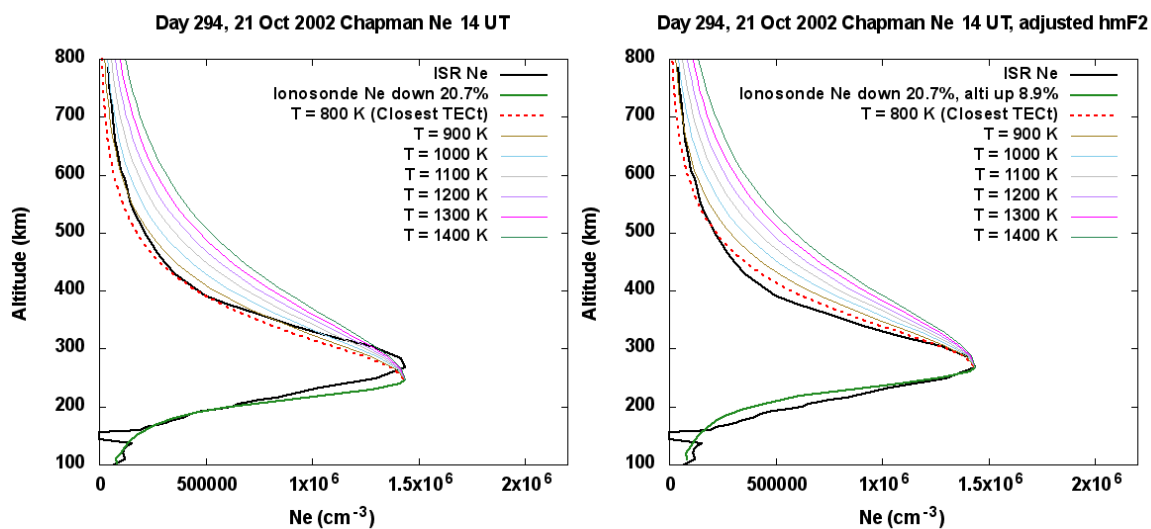


**Figure E.5.** Quiet day 294, 14 UT density profile ISR (black) versus ionosonde (green). The different colors represent the  $\alpha$  – Chapman profile and Chapman temperature used. The red-dashed line is equal to the Chapman pseudo-temperature. The right side shows the adjustments made to the raw ionosonde bottomside profile (left) to fit ISR.

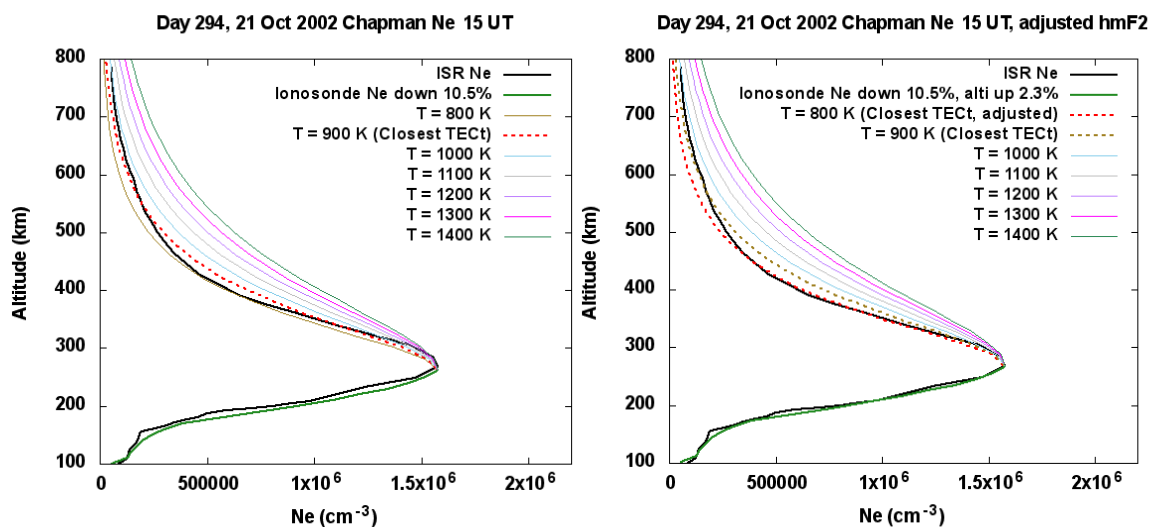


**Figure E.6.** Quiet day 294, 15 UT density profile ISR (black) versus ionosonde (green). The different colors represent the  $\alpha$  – Chapman profile and Chapman temperature used. The red-dashed line is equal to the Chapman pseudo-temperature. The right side shows the adjustments made to the raw ionosonde bottomside profile (left) to fit ISR.

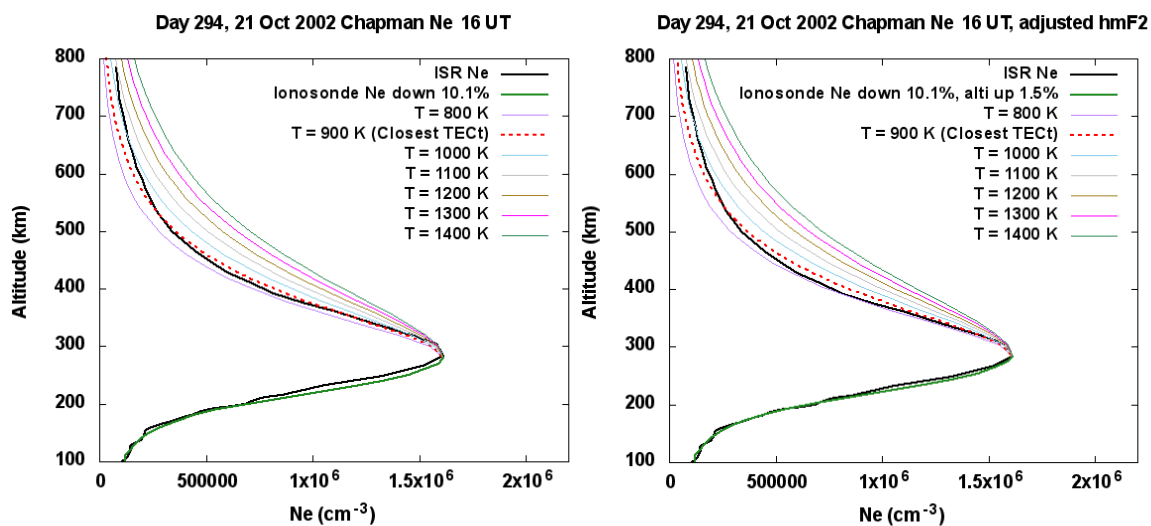


**Figure E.7.** Quiet day 294, 16 UT density profile ISR (black) versus ionosonde (green). The different colors represent the  $\alpha$  – Chapman profile and Chapman temperature used. The red-dashed line is equal to the Chapman pseudo-temperature. The right side shows the adjustments made to the raw ionosonde bottomside profile (left) to fit ISR.

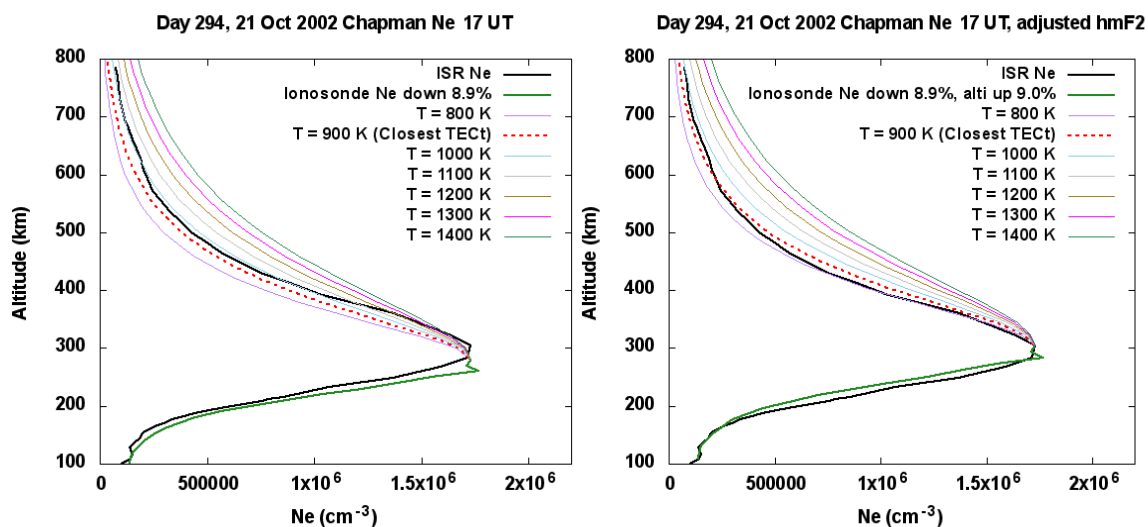


**Figure E.8.** Quiet day 294, 17 UT density profile ISR (black) versus ionosonde (green). The different colors represent the  $\alpha$  – Chapman profile and Chapman temperature used. The red-dashed line is equal to the Chapman pseudo-temperature. The right side shows the adjustments made to the raw ionosonde bottomside profile (left) to fit ISR.

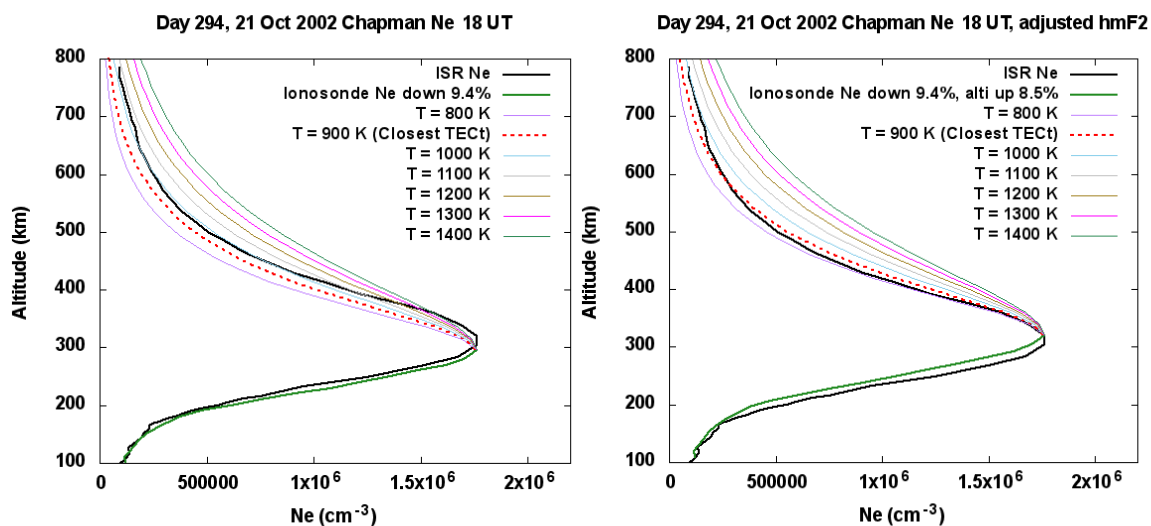


**Figure E.9.** Quiet day 294, 18 UT density profile ISR (black) versus ionosonde (green). The different colors represent the  $\alpha$  – Chapman profile and Chapman temperature used. The red-dashed line is equal to the Chapman pseudo-temperature. The right side shows the adjustments made to the raw ionosonde bottomside profile (left) to fit ISR.

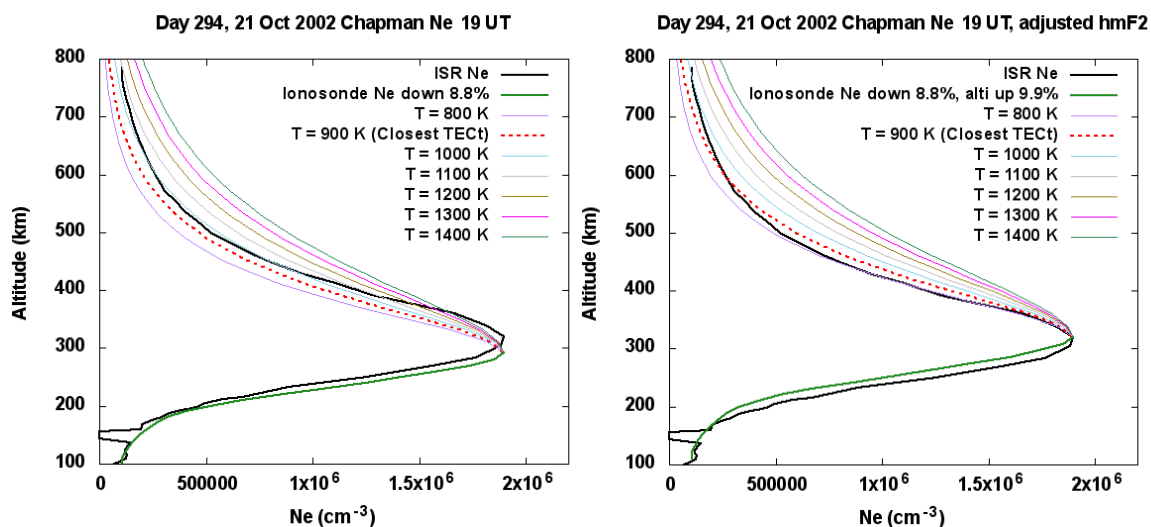


**Figure E.10.** Quiet day 294, 19 UT density profile ISR (black) versus ionosonde (green). The different colors represent the  $\alpha$  – Chapman profile and Chapman temperature used. The red-dashed line is equal to the Chapman pseudo-temperature. The right side shows the adjustments made to the raw ionosonde bottomside profile (left) to fit ISR.

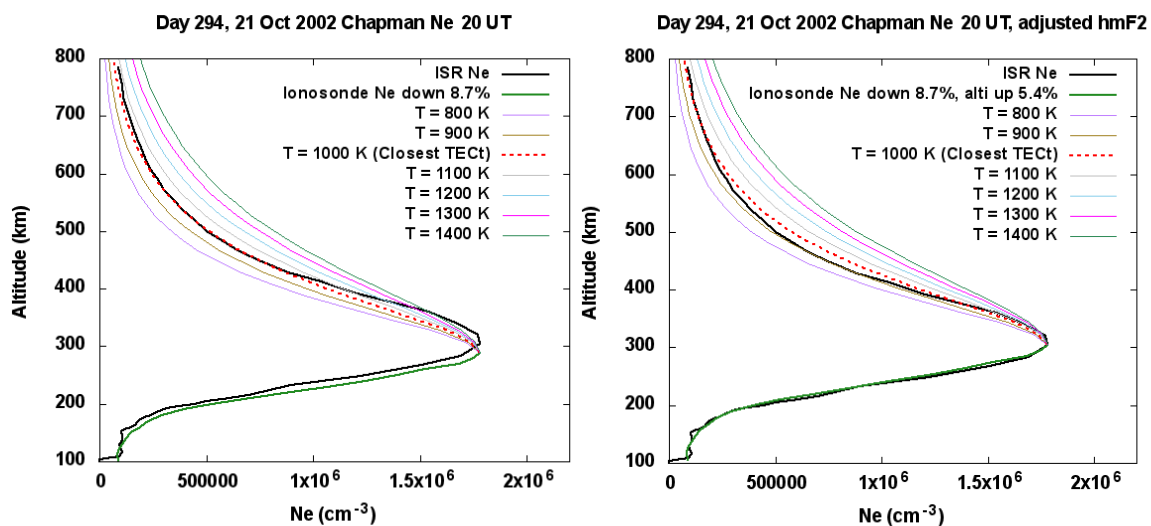


**Figure E.11.** Quiet day 294, 20 UT density profile ISR (black) versus ionosonde (green). The different colors represent the  $\alpha$  – Chapman profile and Chapman temperature used. The red-dashed line is equal to the Chapman pseudo-temperature. The right side shows the adjustments made to the raw ionosonde bottomside profile (left) to fit ISR.



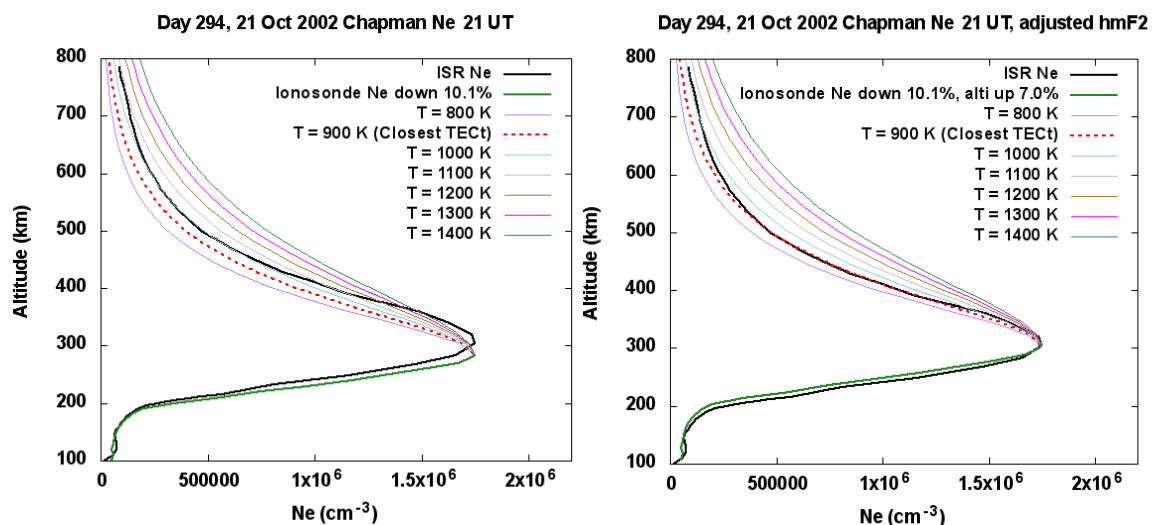


**Figure E.12.** Quiet day 294, 21 UT density profile ISR (black) versus ionosonde (green). The different colors represent the  $\alpha$  – Chapman profile and Chapman temperature used. The red-dashed line is equal to the Chapman pseudo-temperature. The right side shows the adjustments made to the raw ionosonde bottomside profile (left) to fit ISR.

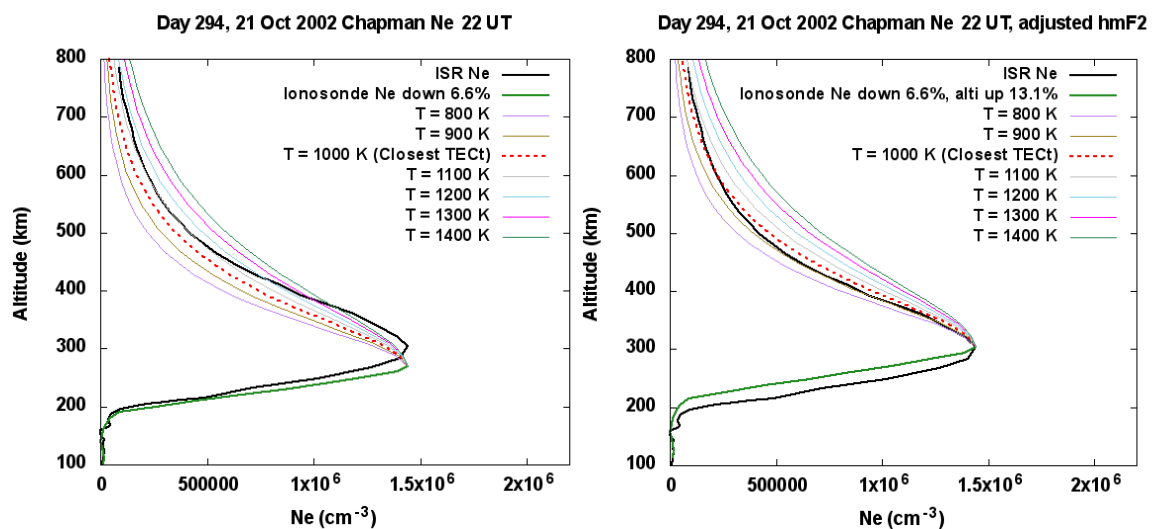


**Figure E.13.** Quiet day 294, 22 UT density profile ISR (black) versus ionosonde (green). The different colors represent the  $\alpha$  – Chapman profile and Chapman temperature used. The red-dashed line is equal to the Chapman pseudo-temperature. The right side shows the adjustments made to the raw ionosonde bottomside profile (left) to fit ISR.

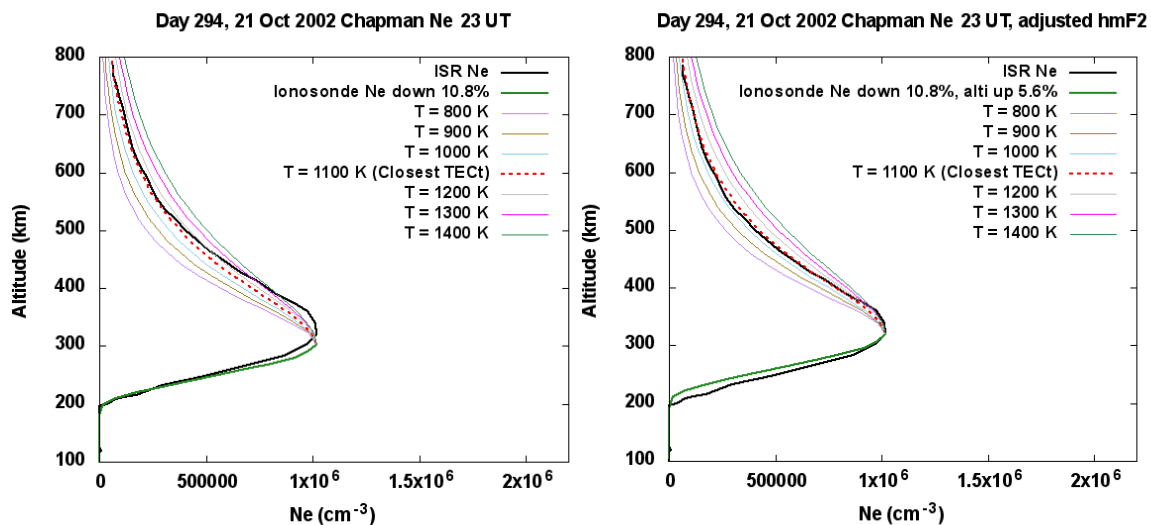


**Figure E.14.** Quiet day 294, 23 UT density profile ISR (black) versus ionosonde (green). The different colors represent the  $\alpha$  – Chapman profile and Chapman temperature used. The red-dashed line is equal to the Chapman pseudo-temperature. The right side shows the adjustments made to the raw ionosonde bottomside profile (left) to fit ISR.

## E.2. Hourly Topside Reconstruction Results for Active Reference Day 297

- Each figure contains an ISR density profile (black) versus an ionosonde profile (green). The different colors represent the  $\alpha$  – Chapman profile and Chapman temperature used. The red-dashed line is equal to the Chapman pseudo-temperature. The right side shows the adjustments made to the raw ionosonde bottomside profile (left) to fit ISR.

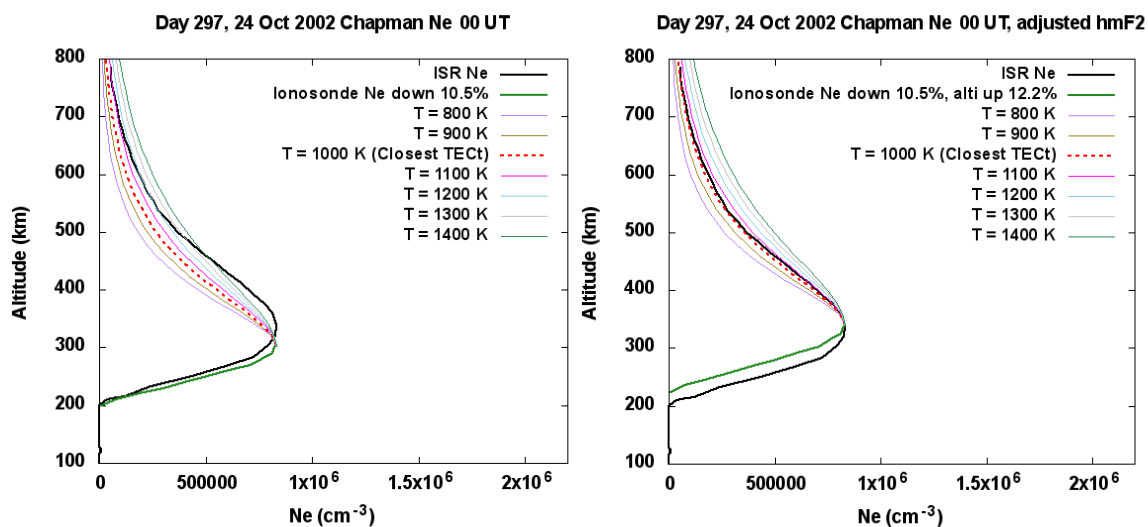


**Figure E.15.** Active day 297, 00 UT density profile ISR (black) versus ionosonde (green). The different colors represent the  $\alpha$  – Chapman profile and Chapman temperature used. The red-dashed line is equal to the Chapman pseudo-temperature. The right side shows the adjustments made to the raw ionosonde bottomside profile (left) to fit ISR.

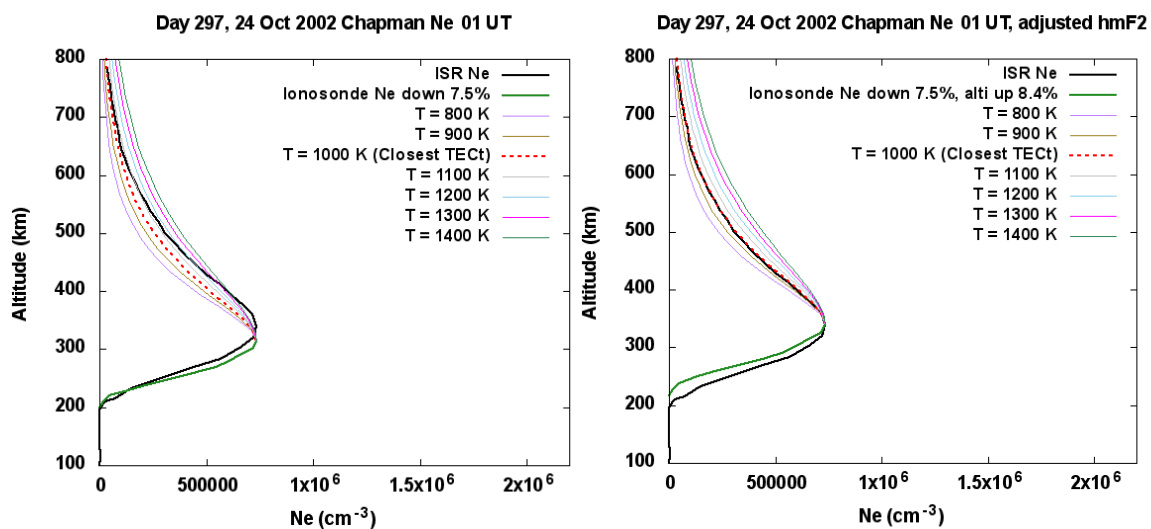


**Figure E.16.** Active day 297, 01 UT density profile ISR (black) versus ionosonde (green). The different colors represent the  $\alpha$  – Chapman profile and Chapman temperature used. The red-dashed line is equal to the Chapman pseudo-temperature. The right side shows the adjustments made to the raw ionosonde bottomside profile (left) to fit ISR.

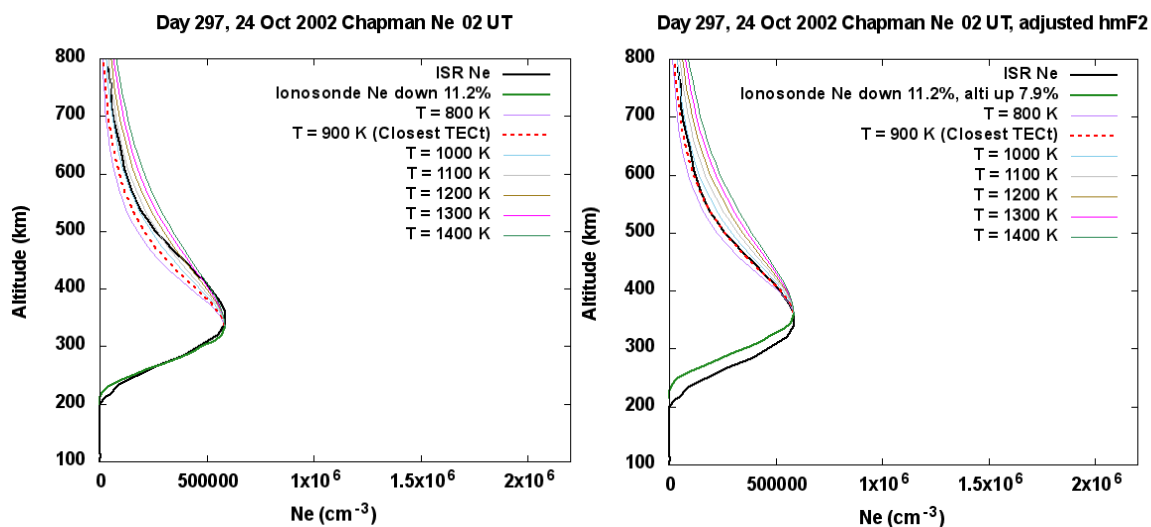


**Figure E.17.** Active day 297, 02 UT density profile ISR (black) versus ionosonde (green). The different colors represent the  $\alpha$  – Chapman profile and Chapman temperature used. The red-dashed line is equal to the Chapman pseudo-temperature. The right side shows the adjustments made to the raw ionosonde bottomside profile (left) to fit ISR.

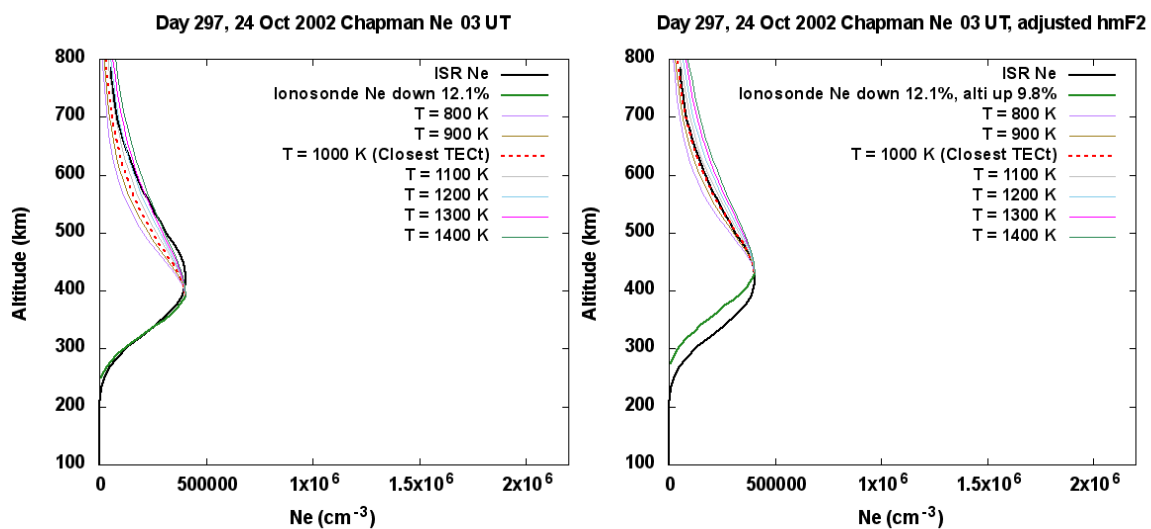


**Figure E.18.** Active day 297, 03 UT density profile ISR (black) versus ionosonde (green). The different colors represent the  $\alpha$  – Chapman profile and Chapman temperature used. The red-dashed line is equal to the Chapman pseudo-temperature. The right side shows the adjustments made to the raw ionosonde bottomside profile (left) to fit ISR.

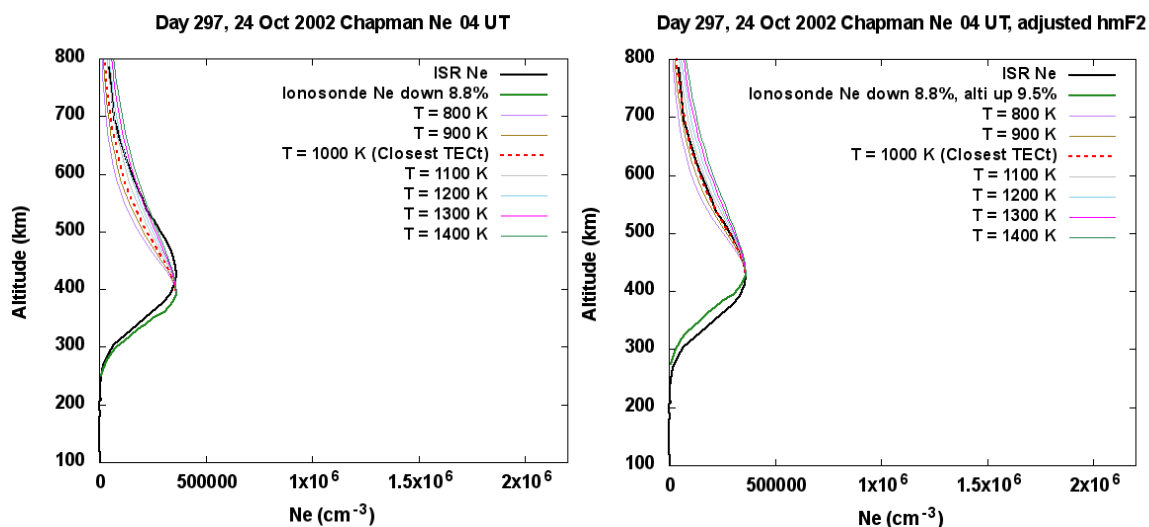


**Figure E.19.** Active day 297, 04 UT density profile ISR (black) versus ionosonde (green). The different colors represent the  $\alpha$  – Chapman profile and Chapman temperature used. The red-dashed line is equal to the Chapman pseudo-temperature. The right side shows the adjustments made to the raw ionosonde bottomside profile (left) to fit ISR.

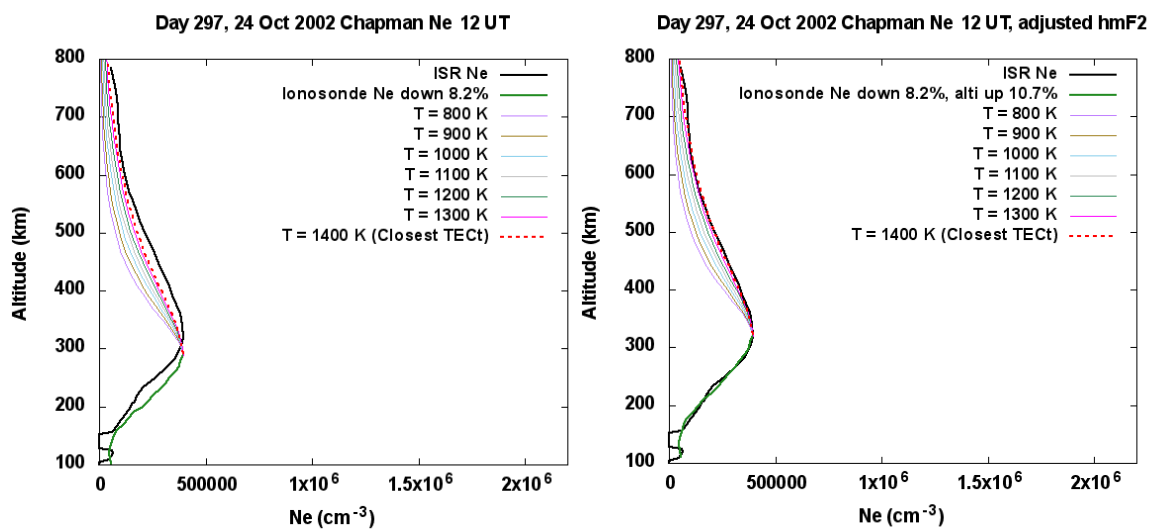


**Figure E.20.** Active day 297, 12 UT density profile ISR (black) versus ionosonde (green). The different colors represent the  $\alpha$  – Chapman profile and Chapman temperature used. The red-dashed line is equal to the Chapman pseudo-temperature. The right side shows the adjustments made to the raw ionosonde bottomside profile (left) to fit ISR.

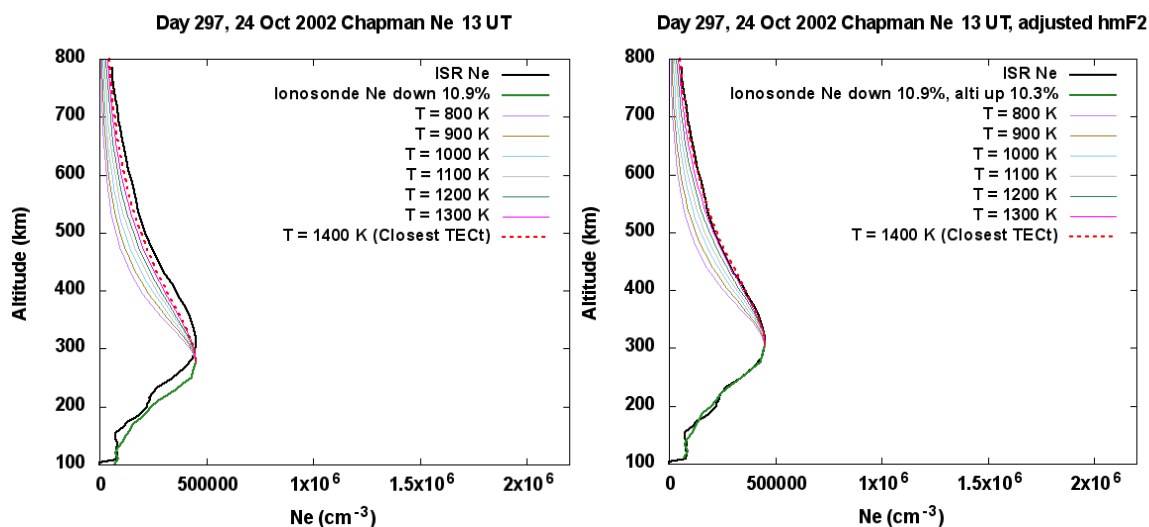


**Figure E.21.** Active day 297, 13 UT density profile ISR (black) versus ionosonde (green). The different colors represent the  $\alpha$  – Chapman profile and Chapman temperature used. The red-dashed line is equal to the Chapman pseudo-temperature. The right side shows the adjustments made to the raw ionosonde bottomside profile (left) to fit ISR.

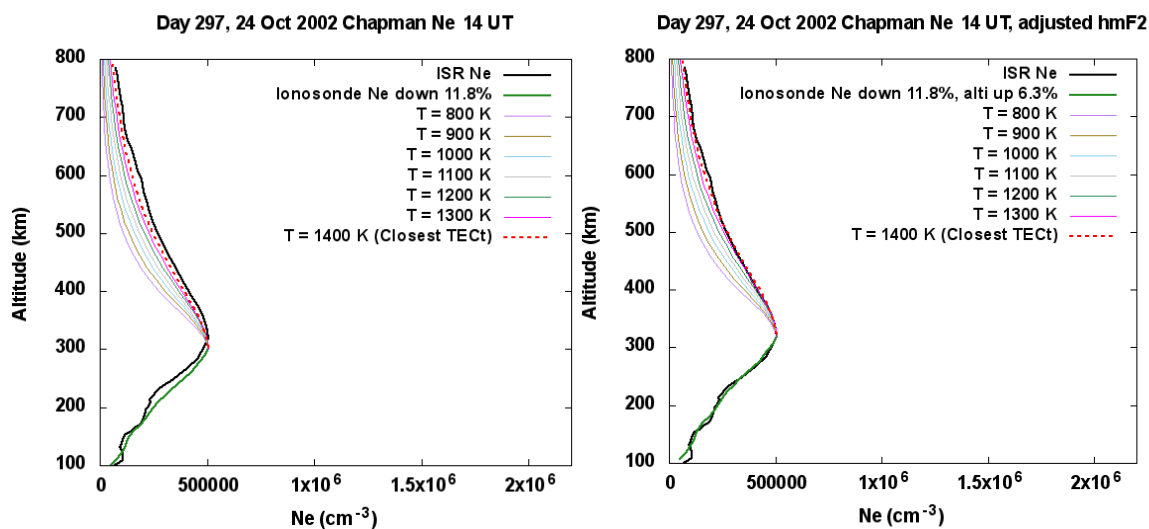


**Figure E.22.** Active day 297, 14 UT density profile ISR (black) versus ionosonde (green). The different colors represent the  $\alpha$  – Chapman profile and Chapman temperature used. The red-dashed line is equal to the Chapman pseudo-temperature. The right side shows the adjustments made to the raw ionosonde bottomside profile (left) to fit ISR.

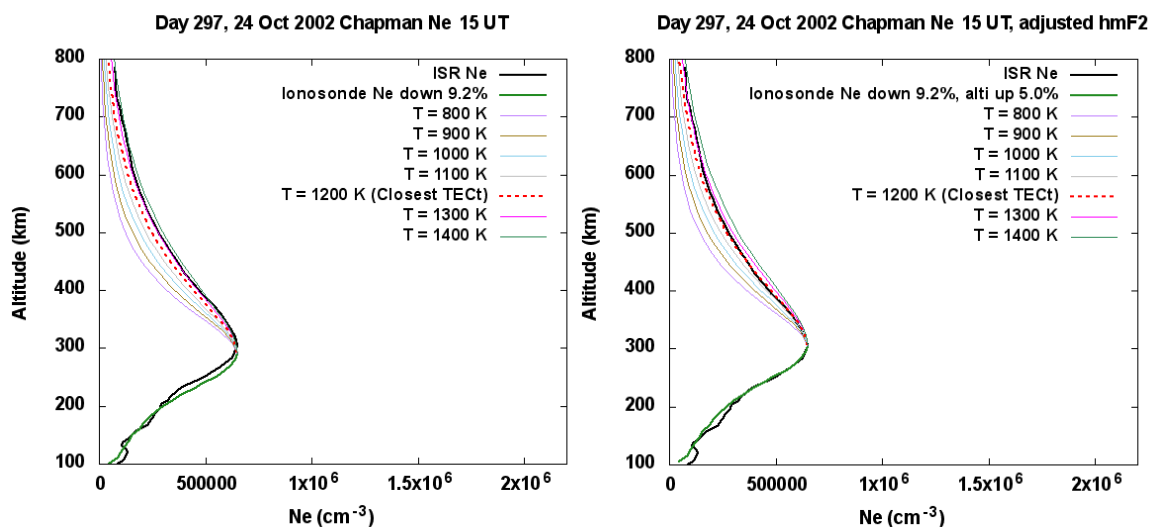


**Figure E.23.** Active day 297, 15 UT density profile ISR (black) versus ionosonde (green). The different colors represent the  $\alpha$  – Chapman profile and Chapman temperature used. The red-dashed line is equal to the Chapman pseudo-temperature. The right side shows the adjustments made to the raw ionosonde bottomsides profile (left) to fit ISR.

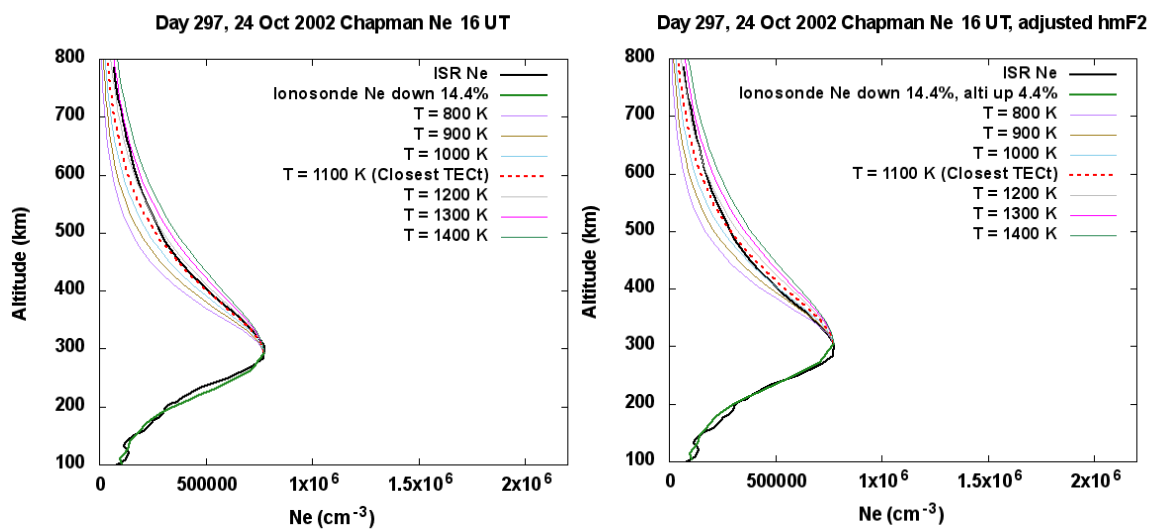


**Figure E.24.** Active day 297, 16 UT density profile ISR (black) versus ionosonde (green). The different colors represent the  $\alpha$  – Chapman profile and Chapman temperature used. The red-dashed line is equal to the Chapman pseudo-temperature. The right side shows the adjustments made to the raw ionosonde bottomsides profile (left) to fit ISR.

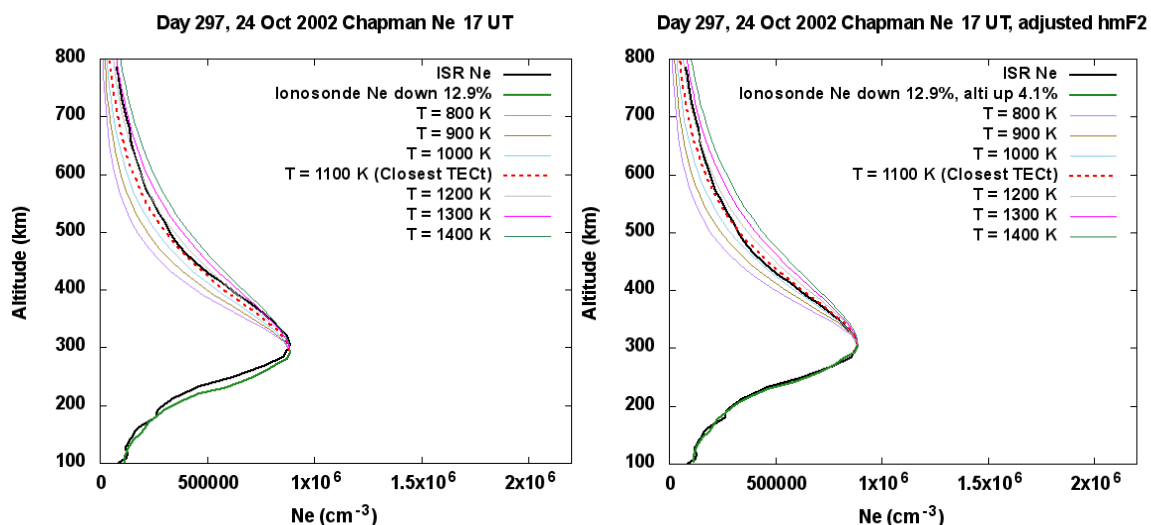


**Figure E.25.** Active day 297, 17 UT density profile ISR (black) versus ionosonde (green). The different colors represent the  $\alpha$  – Chapman profile and Chapman temperature used. The red-dashed line is equal to the Chapman pseudo-temperature. The right side shows the adjustments made to the raw ionosonde bottomside profile (left) to fit ISR.

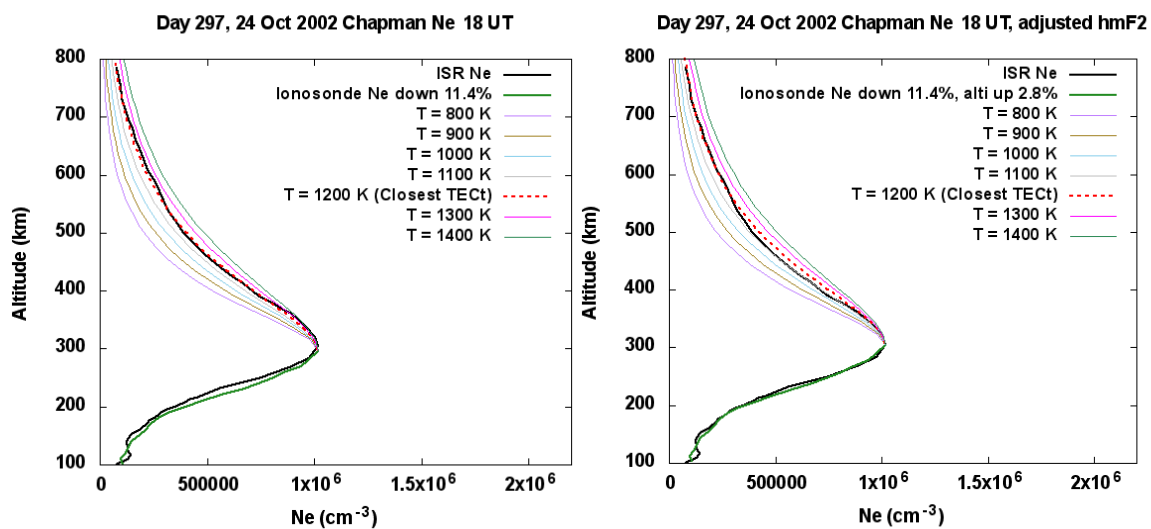


**Figure E.26.** Active day 297, 18 UT density profile ISR (black) versus ionosonde (green). The different colors represent the  $\alpha$  – Chapman profile and Chapman temperature used. The red-dashed line is equal to the Chapman pseudo-temperature. The right side shows the adjustments made to the raw ionosonde bottomside profile (left) to fit ISR.



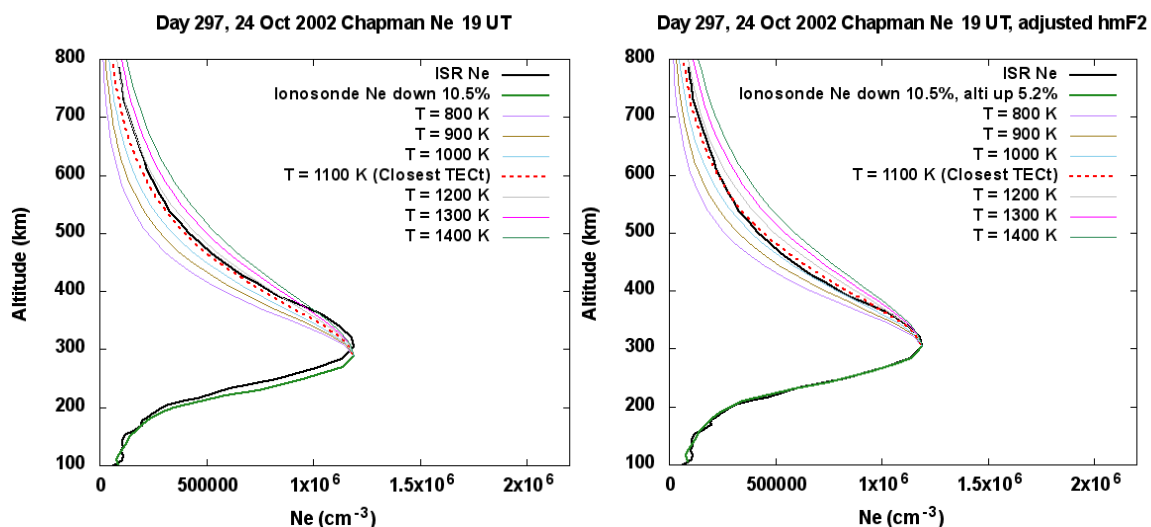


**Figure E.27.** Active day 297, 19 UT density profile ISR (black) versus ionosonde (green). The different colors represent the  $\alpha$  – Chapman profile and Chapman temperature used. The red-dashed line is equal to the Chapman pseudo-temperature. The right side shows the adjustments made to the raw ionosonde bottomside profile (left) to fit ISR.

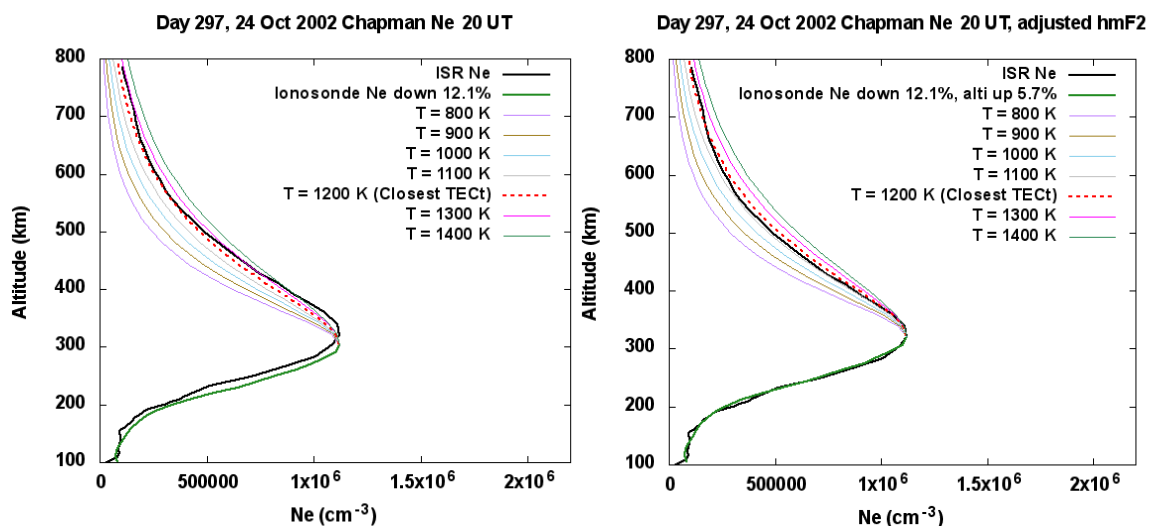


**Figure E.28.** Active day 297, 20 UT density profile ISR (black) versus ionosonde (green). The different colors represent the  $\alpha$  – Chapman profile and Chapman temperature used. The red-dashed line is equal to the Chapman pseudo-temperature. The right side shows the adjustments made to the raw ionosonde bottomside profile (left) to fit ISR.

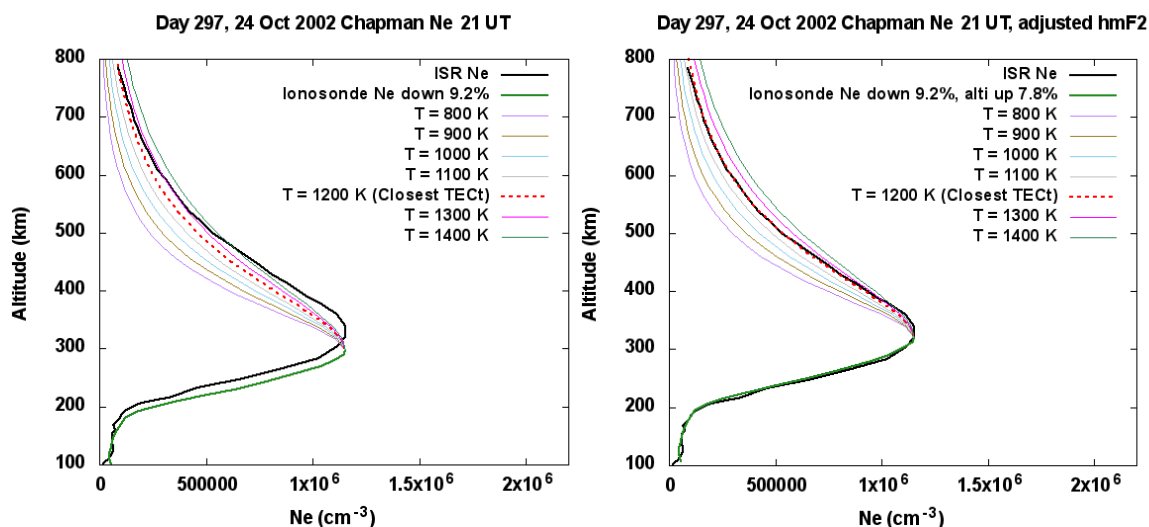


**Figure E.29.** Active day 297, 21 UT density profile ISR (black) versus ionosonde (green). The different colors represent the  $\alpha$  – Chapman profile and Chapman temperature used. The red-dashed line is equal to the Chapman pseudo-temperature. The right side shows the adjustments made to the raw ionosonde bottomside profile (left) to fit ISR.

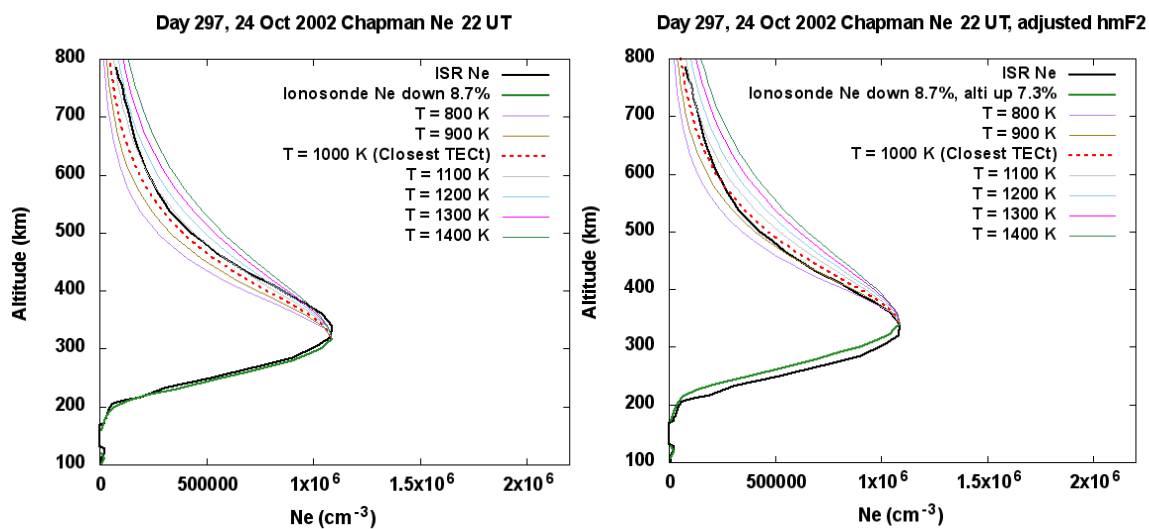


**Figure E.30.** Active day 297, 22 UT density profile ISR (black) versus ionosonde (green). The different colors represent the  $\alpha$  – Chapman profile and Chapman temperature used. The red-dashed line is equal to the Chapman pseudo-temperature. The right side shows the adjustments made to the raw ionosonde bottomside profile (left) to fit ISR.

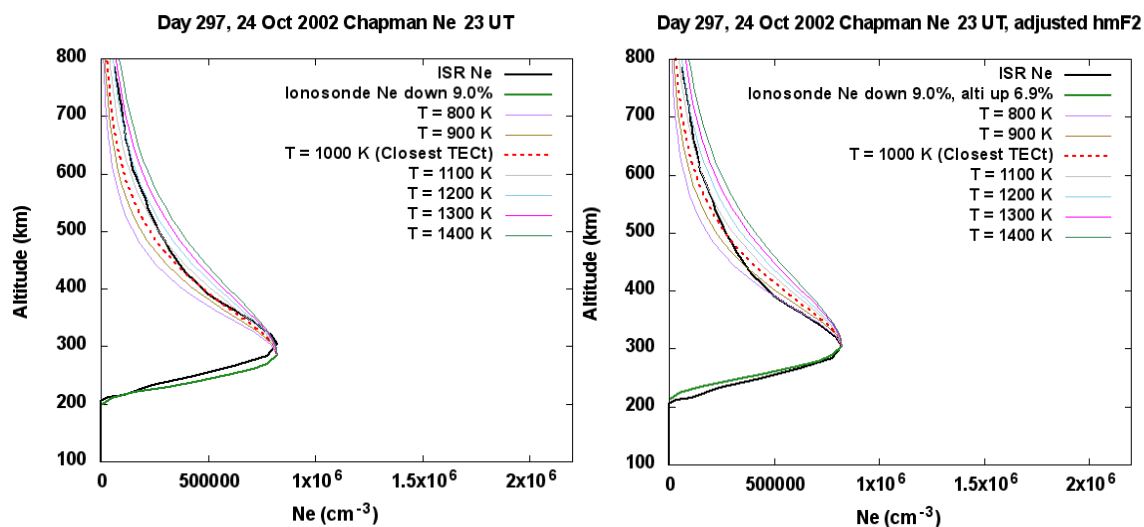


**Figure E.31.** Active day 297, 23 UT density profile ISR (black) versus ionosonde (green). The different colors represent the  $\alpha$  – Chapman profile and Chapman temperature used. The red-dashed line is equal to the Chapman pseudo-temperature. The right side shows the adjustments made to the raw ionosonde bottomside profile (left) to fit ISR.

## **APPENDIX F**

### **COPYRIGHT PERMISSIONS**

Eleven Figures from Chapters 1, 3, and 4 of this dissertation required copyright permissions from their original sources. As outlined in the Publication Guide for Graduate Students, the copyright licenses were obtained and the copies are provided in the subsequent pages. It must be noted, Figure 4.3 from *Liu et al.* [2007] operates under an open access, Creative Commons Attribution 3.0 License and does not require copyright permission.



### **PARTIES:**

1. **John Wiley & Sons Limited** (Company number – 00641132) (Licensor); and
2. **Jennifer Meehan** (Licensee).

Thank you for your recent permission request. Some permission requests for use of material published by the Licensor, such as this one, are now being facilitated by PLSclear.

Set out in this licence cover sheet (the **Licence Cover Sheet**) are the principal terms under which Licensor has agreed to license certain Licensed Material (as defined below) to Licensee. The terms in this Licence Cover Sheet are subject to the attached General Terms and Conditions, which together with this Licence Cover Sheet constitute the licence agreement (the **Licence**) between Licensor and Licensee as regards the Licensed Material. The terms set out in this Licence Cover Sheet take precedence over any conflicting provision in the General Terms and Conditions.

### **Free Of Charge Licence Terms**

Licence Date: 26/06/2017  
 PLSclear Ref No: 3184

### **The Licensor**

Company name: John Wiley & Sons Limited  
 Address: The Atrium  
 Southern Gate  
 Chichester  
 PO19 8SQ  
 United Kingdom

### **The Licensee**

Licensee Contact Name: Jennifer Meehan  
 Licensee Address: 4405 Old Main Hill  
 Department of Physics  
 84322  
 United States

### **Licensed Material**

title: FUNDAMENTALS OF AERONOMY  
 ISBN: 9780471941200  
 publisher: John Wiley & Sons Limited

figure number & title / caption	Figure 1.4: Schematic representation of layer formation
Are you the author of the work you are requesting?	I am NOT the author
page number	16

#### For Use In Licensee's Publication(s)

usage type	Book, Journal, Magazine or Academic Paper...-Thesis
estimated publication date	July 2017
number of pages	200
publication title	29 Day Analysis of Scale Heights and the Inference of the Topside Ionosphere over Millstone Hill during the 2002 Incoherent Scatter Radar Campaign
type of document	Ph.D. Dissertation

#### Rights Granted

Exclusivity:	Non-Exclusive
Format:	Thesis
Language:	English
Territory:	
Duration:	Lifetime of Licensee's Edition
Maximum Circulation:	0

**Figure F.1.** Copyright permission received for [*Whitten and Poppoff*, 1971]. Permission is for use of Figure 1.1.

6/23/2017

RightsLink - Your Account

## ELSEVIER LICENSE TERMS AND CONDITIONS

Jun 23, 2017

This Agreement between Utah State University -- Jennifer Meehan ("You") and Elsevier ("Elsevier") consists of your license details and the terms and conditions provided by Elsevier and Copyright Clearance Center.

License Number	4134930516338
License date	Jun 23, 2017
Licensed Content Publisher	Elsevier
Licensed Content Publication	Advances in Space Research
Licensed Content Title	Ionospheric slab thickness – Analysis, modelling and monitoring
Licensed Content Author	S.M. Stankov,R. Warnant
Licensed Content Date	Dec 1, 2009
Licensed Content Volume	44
Licensed Content Issue	11
Licensed Content Pages	9
Start Page	1295
End Page	1303
Type of Use	reuse in a thesis/dissertation
Portion	figures/tables/illustrations
Number of figures/tables/illustrations	1
Format	both print and electronic
Are you the author of this Elsevier article?	No
Will you be translating?	No
Order reference number	
Original figure numbers	Figure 1
Title of your thesis/dissertation	29 Day Analysis of Scale Heights and the Inference of the Topside Ionosphere over Millstone Hill during the 2002 Incoherent Scatter Radar Campaign
Expected completion date	Jul 2017
Estimated size (number of pages)	200
Elsevier VAT number	GB 494 6272 12
Requestor Location	Utah State University 84 W 400 S  Logan, UT 84321 United States Attn: Utah State University
Publisher Tax ID	98-0397604
Total	<b>0.00 USD</b>
Terms and Conditions	

### INTRODUCTION

1. The publisher for this copyrighted material is Elsevier. By clicking "accept" in connection with completing this licensing transaction, you agree that the following terms and conditions apply to this transaction (along with the Billing and Payment terms and conditions

<https://s100.copyright.com/MyAccount/web/jsp/viewprintablelicensefrommyorders.jsp?ref=2a2b64e8-7566-4bac-a14c-09f16d5f10b1&email=>

1/4

**Figure F.2.** Copyright permission received for *Stankov and Warnant* [2009]. Permission is for use of Figure 1.2.

7/7/2017

RightsLink - Your Account

## ELSEVIER LICENSE TERMS AND CONDITIONS

Jul 07, 2017

This Agreement between Utah State University -- Jennifer Meehan ("You") and Elsevier ("Elsevier") consists of your license details and the terms and conditions provided by Elsevier and Copyright Clearance Center.

License Number	4143671180683
License date	Jul 07, 2017
Licensed Content Publisher	Elsevier
Licensed Content Publication	Elsevier Books
Licensed Content Title	Aeronomy
Licensed Content Author	P.M. Banks,G. Kockarts
Licensed Content Date	Jan 1, 1973
Licensed Content Volume	n/a
Licensed Content Issue	n/a
Licensed Content Pages	49
Start Page	238
End Page	286
Type of Use	reuse in a thesis/dissertation
Intended publisher of new work	other
Portion	figures/tables/illustrations
Number of figures/tables/illustrations	1
Format	both print and electronic
Are you the author of this Elsevier chapter?	No
Will you be translating?	No
Order reference number	
Original figure numbers	22.2
Title of your thesis/dissertation	29 Day Analysis of Scale Heights and the Inference of the Topside Ionosphere over Millstone Hill during the 2002 Incoherent Scatter Radar Campaign
Expected completion date	Jul 2017
Estimated size (number of pages)	200
Elsevier VAT number	GB 494 6272 12
Requestor Location	Utah State University 84 W 400 S  Logan, UT 84321 United States Attn: Utah State University
Publisher Tax ID	98-0397604
Billing Type	Invoice
Billing Address	Utah State University 84 W 400 S  Logan, UT 84321 United States Attn: Jennifer Meehan
Total	<b>0.00 USD</b>
Terms and Conditions	

**Figure F.3.** Copyright permission received for *Banks and Kockarts* [1973]. Permission is for use of Figures 3.1.



## ELSEVIER LICENSE TERMS AND CONDITIONS

Jun 23, 2017

This Agreement between Utah State University -- Jennifer Meehan ("You") and Elsevier ("Elsevier") consists of your license details and the terms and conditions provided by Elsevier and Copyright Clearance Center.

License Number	4134951051922
License date	Jun 23, 2017
Licensed Content Publisher	Elsevier
Licensed Content Publication	Advances in Space Research
Licensed Content Title	Seasonal and solar activity changes of electron temperature in the F-region and topside ionosphere
Licensed Content Author	N.K Sethi,V.K Pandey,K.K Mahajan
Licensed Content Date	Jan 1, 2004
Licensed Content Volume	33
Licensed Content Issue	6
Licensed Content Pages	5
Start Page	970
End Page	974
Type of Use	reuse in a thesis/dissertation
Intended publisher of new work	other
Portion	figures/tables/illustrations
Number of figures/tables/illustrations	2
Format	both print and electronic
Are you the author of this Elsevier article?	No
Will you be translating?	No
Order reference number	
Original figure numbers	figures 1, 2
Title of your thesis/dissertation	29 Day Analysis of Scale Heights and the Inference of the Topside Ionosphere over Millstone Hill during the 2002 Incoherent Scatter Radar Campaign
Expected completion date	Jul 2017
Estimated size (number of pages)	200
Elsevier VAT number	GB 494 6272 12
Requestor Location	Utah State University 84 W 400 S  Logan, UT 84321 United States Attn: Jennifer Meehan
Total	<b>0.00 USD</b>
Terms and Conditions	

**Figure F.4.** Copyright permission received for *Sethi et al.* [2003]. Permission is for use of Figures 3.2 and 3.3.

## JOHN WILEY AND SONS LICENSE TERMS AND CONDITIONS

Jun 23, 2017

This Agreement between Utah State University -- Jennifer Meehan ("You") and John Wiley and Sons ("John Wiley and Sons") consists of your license details and the terms and conditions provided by John Wiley and Sons and Copyright Clearance Center.

License Number	4134960122850
License date	Jun 23, 2017
Licensed Content Publisher	John Wiley and Sons
Licensed Content Publication	Journal of Geophysical Research: Space Physics
Licensed Content Title	Midlatitude ionospheric plasma temperature climatology and empirical model based on Saint Santin incoherent scatter radar data from 1966 to 1987
Licensed Content Author	Shun-Rong Zhang,John M. Holt,Angela M. Zaluca,Christine Amory-Mazaudier
Licensed Content Date	Nov 23, 2004
Licensed Content Pages	1
Type of Use	Dissertation/Thesis
Requestor type	University/Academic
Format	Print and electronic
Portion	Figure/table
Number of figures/tables	1
Original Wiley figure/table number(s)	Figure 6
Will you be translating?	No
Title of your thesis / dissertation	29 Day Analysis of Scale Heights and the Inference of the Topside Ionosphere over Millstone Hill during the 2002 Incoherent Scatter Radar Campaign
Expected completion date	Jul 2017
Expected size (number of pages)	200
Requestor Location	Utah State University 84 W 400 S  Logan, UT 84321 United States Attn: Utah State University
Publisher Tax ID	EU826007151
Billing Type	Invoice
Billing Address	Utah State University 84 W 400 S  Logan, UT 84321 United States Attn: Jennifer Meehan
Total	<b>0.00 USD</b>
Terms and Conditions	

**Figure F.5.** Copyright permission received for *Zhang et al.* [2004]. Permission is for use of Figure 3.4.

## JOHN WILEY AND SONS LICENSE TERMS AND CONDITIONS

Jun 23, 2017

This Agreement between Utah State University -- Jennifer Meehan ("You") and John Wiley and Sons ("John Wiley and Sons") consists of your license details and the terms and conditions provided by John Wiley and Sons and Copyright Clearance Center.

License Number	4134960696875
License date	Jun 23, 2017
Licensed Content Publisher	John Wiley and Sons
Licensed Content Publication	Journal of Geophysical Research
Licensed Content Title	Ionospheric composition and density from 90 to 1200 kilometers at solar minimum
Licensed Content Author	Charles Y. Johnson
Licensed Content Date	Dec 6, 2012
Licensed Content Pages	3
Type of Use	Dissertation/Thesis
Requestor type	University/Academic
Format	Print and electronic
Portion	Figure/table
Number of figures/tables	1
Original Wiley figure/table number(s)	Figure 1
Will you be translating?	No
Title of your thesis / dissertation	29 Day Analysis of Scale Heights and the Inference of the Topside Ionosphere over Millstone Hill during the 2002 Incoherent Scatter Radar Campaign
Expected completion date	Jul 2017
Expected size (number of pages)	200
Requestor Location	Utah State University 84 W 400 S  Logan, UT 84321 United States Attn: Utah State University
Publisher Tax ID	EU826007151
Billing Type	Invoice
Billing Address	Utah State University 84 W 400 S  Logan, UT 84321 United States Attn: Jennifer Meehan
Total	<b>0.00 USD</b>
Terms and Conditions	

**Figure F.6.** Copyright permission received for *Johnson* [1966]. Permission is for use of Figure 3.5.

## JOHN WILEY AND SONS LICENSE TERMS AND CONDITIONS

Jun 23, 2017

This Agreement between Utah State University -- Jennifer Meehan ("You") and John Wiley and Sons ("John Wiley and Sons") consists of your license details and the terms and conditions provided by John Wiley and Sons and Copyright Clearance Center.

License Number	4134970012086
License date	Jun 23, 2017
Licensed Content Publisher	John Wiley and Sons
Licensed Content Publication	Journal of Geophysical Research: Space Physics
Licensed Content Title	Ion composition of the topside equatorial ionosphere during solar minimum
Licensed Content Author	
Licensed Content Date	Apr 1, 1992
Licensed Content Pages	5
Type of Use	Dissertation/Thesis
Requestor type	University/Academic
Format	Print and electronic
Portion	Figure/table
Number of figures/tables	1
Original Wiley figure/table number(s)	Figure 3
Will you be translating?	No
Title of your thesis / dissertation	29 Day Analysis of Scale Heights and the Inference of the Topside Ionosphere over Millstone Hill during the 2002 Incoherent Scatter Radar Campaign
Expected completion date	Jul 2017
Expected size (number of pages)	200
Requestor Location	Utah State University 84 W 400 S  Logan, UT 84321 United States Attn: Utah State University
Publisher Tax ID	EU826007151
Billing Type	Invoice
Billing Address	Utah State University 84 W 400 S  Logan, UT 84321 United States Attn: Jennifer Meehan
Total	<b>0.00 USD</b>
Terms and Conditions	

**Figure F.7.** Copyright permission received for *Gonzalez et al.* [1992]. Permission is for use of Figure 3.6.

## JOHN WILEY AND SONS LICENSE TERMS AND CONDITIONS

Jun 23, 2017

This Agreement between Utah State University -- Jennifer Meehan ("You") and John Wiley and Sons ("John Wiley and Sons") consists of your license details and the terms and conditions provided by John Wiley and Sons and Copyright Clearance Center.

License Number	4134970468161
License date	Jun 23, 2017
Licensed Content Publisher	John Wiley and Sons
Licensed Content Publication	Radio Science
Licensed Content Title	Comparison of COSMIC occultation-based electron density profiles and TIP observations with Arecibo incoherent scatter radar data
Licensed Content Author	M. C. Kelley,V. K. Wong,Nestor Aponte,Clayton Coker,A. J. Mannucci,A. Komjathy
Licensed Content Date	Aug 8, 2009
Licensed Content Pages	1
Type of Use	Dissertation/Thesis
Requestor type	University/Academic
Format	Print and electronic
Portion	Figure/table
Number of figures/tables	2
Original Wiley figure/table number(s)	Figures 7 and 9
Will you be translating?	No
Title of your thesis / dissertation	29 Day Analysis of Scale Heights and the Inference of the Topside Ionosphere over Millstone Hill during the 2002 Incoherent Scatter Radar Campaign
Expected completion date	Jul 2017
Expected size (number of pages)	200
Requestor Location	Utah State University 84 W 400 S  Logan, UT 84321 United States Attn: Utah State University
Publisher Tax ID	EU826007151
Billing Type	Invoice
Billing Address	Utah State University 84 W 400 S  Logan, UT 84321 United States Attn: Jennifer Meehan
Total	<b>0.00 USD</b>
Terms and Conditions	

**Figure F.8.** Copyright permission received for *Kelley et al.* [2009]. Permission is for use of Figures 3.7 and 3.8.

## JOHN WILEY AND SONS LICENSE TERMS AND CONDITIONS

Jun 23, 2017

This Agreement between Utah State University -- Jennifer Meehan ("You") and John Wiley and Sons ("John Wiley and Sons") consists of your license details and the terms and conditions provided by John Wiley and Sons and Copyright Clearance Center.

License Number	4134970824914
License date	Jun 23, 2017
Licensed Content Publisher	John Wiley and Sons
Licensed Content Publication	Journal of Geophysical Research: Space Physics
Licensed Content Title	Comparison of COSMIC ionospheric measurements with ground-based observations and model predictions: Preliminary results
Licensed Content Author	Jiuhou Lei, Stig Syndergaard, Alan G. Burns, Stanley C. Solomon, Wenbin Wang, Zhen Zeng, Raymond G. Roble, Qian Wu, Ying-Hwa Kuo, John M. Holt, Shun-Rong Zhang, David L. Hysell, Fabiano S. Rodrigues, Chien H. Lin
Licensed Content Date	Jul 25, 2007
Licensed Content Pages	1
Type of Use	Dissertation/Thesis
Requestor type	University/Academic
Format	Print and electronic
Portion	Figure/table
Number of figures/tables	1
Original Wiley figure/table number(s)	Figure 3
Will you be translating?	
Title of your thesis / dissertation	29 Day Analysis of Scale Heights and the Inference of the Topside Ionosphere over Millstone Hill during the 2002 Incoherent Scatter Radar Campaign
Expected completion date	Jul 2017
Expected size (number of pages)	200
Requestor Location	Utah State University 84 W 400 S  Logan, UT 84321 United States Attn: Utah State University
Publisher Tax ID	EU826007151
Billing Type	Invoice
Billing Address	Utah State University 84 W 400 S  Logan, UT 84321 United States Attn: Jennifer Meehan
Total	<b>0.00 USD</b>

**Figure F.9.** Copyright permission received for *Lei et al.* [2007]. Permission is for use of Figure 3.9.

## JOHN WILEY AND SONS LICENSE TERMS AND CONDITIONS

Jun 23, 2017

This Agreement between Utah State University -- Jennifer Meehan ("You") and John Wiley and Sons ("John Wiley and Sons") consists of your license details and the terms and conditions provided by John Wiley and Sons and Copyright Clearance Center.

License Number	4134971234743
License date	Jun 23, 2017
Licensed Content Publisher	John Wiley and Sons
Licensed Content Publication	Geophysical Research Letters
Licensed Content Title	October 2002 30-day incoherent scatter radar experiments at Millstone Hill and Svalbard and simultaneous GUVI/TIMED observations
Licensed Content Author	Shun-Rong Zhang, John M. Holt, Phil J. Erickson, Frank D. Lind, John C. Foster, Anthony P. van Eyken, Yongliang Zhang, Larry J. Paxton, William C. Rideout, Larisa P. Goncharenko, Glenn R. Campbell
Licensed Content Date	Jan 15, 2005
Licensed Content Pages	1
Type of Use	Dissertation/Thesis
Requestor type	University/Academic
Format	Print and electronic
Portion	Figure/table
Number of figures/tables	1
Original Wiley figure/table number(s)	Figure 1
Will you be translating?	No
Title of your thesis / dissertation	29 Day Analysis of Scale Heights and the Inference of the Topside Ionosphere over Millstone Hill during the 2002 Incoherent Scatter Radar Campaign
Expected completion date	Jul 2017
Expected size (number of pages)	200
Requestor Location	Utah State University 84 W 400 S  Logan, UT 84321 United States Attn: Utah State University
Publisher Tax ID	EU826007151
Billing Type	Invoice
Billing Address	Utah State University 84 W 400 S  Logan, UT 84321 United States Attn: Jennifer Meehan
<b>Total</b>	<b>0.00 USD</b>

**Figure F.10.** Copyright permission received for *Zhang et al.* [2005]. Permission is for use of Figure 4.1.

## JOHN WILEY AND SONS LICENSE TERMS AND CONDITIONS

Jun 23, 2017

This Agreement between Utah State University -- Jennifer Meehan ("You") and John Wiley and Sons ("John Wiley and Sons") consists of your license details and the terms and conditions provided by John Wiley and Sons and Copyright Clearance Center.

License Number	4134980013344
License date	Jun 23, 2017
Licensed Content Publisher	John Wiley and Sons
Licensed Content Publication	Radio Science
Licensed Content Title	Variations of electron density based on long-term incoherent scatter radar and ionosonde measurements over Millstone Hill
Licensed Content Author	Jiuhou Lei, Libo Liu, Weixing Wan, Shun-Rong Zhang
Licensed Content Date	Apr 30, 2005
Licensed Content Pages	1
Type of Use	Dissertation/Thesis
Requestor type	University/Academic
Format	Print and electronic
Portion	Figure/table
Number of figures/tables	1
Original Wiley figure/table number(s)	Figure 7
Will you be translating?	No
Title of your thesis / dissertation	29 Day Analysis of Scale Heights and the Inference of the Topside Ionosphere over Millstone Hill during the 2002 Incoherent Scatter Radar Campaign
Expected completion date	Jul 2017
Expected size (number of pages)	200
Requestor Location	Utah State University 84 W 400 S  Logan, UT 84321 United States Attn: Utah State University
Publisher Tax ID	EU826007151
Billing Type	Invoice
Billing Address	Utah State University 84 W 400 S  Logan, UT 84321 United States Attn: Jennifer Meehan
Total	<b>0.00 USD</b>

**Figure F.11.** Copyright permission received for *Lei et al.* [2005]. Permission is for use of Figure 4.2.



## CURRICULUM VITAE

### JENNIFER “JINNI” L. MEEHAN

Contact: 704.773.1263 / jinni.meehan@gmail.com

---

#### SUMMARY STATEMENT

Possesses an extensive background in STEM education with leadership and public relations experience through several science organizations. Strong skills in promoting informed and thoughtful decision making through analysis, communication, innovative problem solving, and research. Very passionate and motivated.

#### EDUCATION

- |              |  |
|--------------|--|
| 2011-present | <p><b>Utah State University, Logan, UT</b><br/>         Ph.D., Physics, Department of Physics, Defended February 2017<br/>         Advisor: Dr. Jan J. Sojka</p>   |
| 2009-2010    | <p><b>Hampton University, Hampton, VA</b><br/>         M.S. candidate, Department of Atmospheric and Planetary<br/>         Sciences, transferred<br/>         Advisor: Dr. William R. Paterson</p>          |
| 2004-2008    | <p><b>University of North Carolina at Charlotte, Charlotte, NC</b><br/><br/>         B.S., Meteorology<br/>         Advisor: Dr. Matthew D. Eastin<br/> <i>Cum Laude, Dean's List, Chancellor's List</i></p> |

#### HONORS & AWARDS

- |              |  |
|--------------|--|
| 2016         | Utah State University Keith Taylor Scholarship           |
| 2014, 2015   | Utah State University Howard L. Blood Scholarship        |
| 2012-2013    | Associated Students of Utah State University Scholarship |
| 2012         | Utah State University Adams Scholarship                  |
| 2011-Present | Sigma Pi Sigma National Physics Honor Society            |
| 2008-Present | Omicron Delta Kappa National Leadership Honor Society    |
| 2008-Present | National Scholars Honor Society                          |
| 2008-Present | Chi Epsilon Pi National Meteorology Honor Society        |

## PROFESSIONAL EXPERIENCE

### Research and Teaching Experience

- 07/2016-Present      **Legislative Policy Fellow**  
*Institute of Government & Politics, Federal & State Relations, Utah State University, Logan, UT*
- Fellowship advisor: Dr. Neil Abercrombie
  - Research focus: Impacts legislation has on the University at the federal, state, and local levels.
  - Reach goal: To understand the important role government plays in legislation at all levels at USU and in the state of Utah. Currently writing a series of white papers showcasing the fundamental research conducted in each individual college on the USU campus. This is done in part by translating very complex scientific abstracts and painting the bigger economic picture and the benefits to the State of Utah.
- 01/2011-Present      **Graduate Research Assistant**  
*Department of Physics, Utah State University, Logan, UT*
- Research focus: Ionospheric irregularities and Global Positioning System satellite corrections.
- 01/2011-05/2016      **Graduate Instructor**  
*Department of Physics, Utah State University, Logan, UT*
- Course: PHYS 2200/2210 - Physics for Scientists and Engineers Lab I. Responsible for teaching lab material and assisting students with lab equipment.
  - Course: PHYS 2225 - Physics for Scientists and Engineers Lab II. Official instructor, in charge of preparing and teaching lab material, grading lab reports, assisting students with lab equipment.
  - Course: USU 1010 – University Connections. Official instructor in charge of administering assignments and activities that develop critical college study skills, time-management techniques, and test-taking strategies, as well as promoting an awareness of the campus and community to incoming freshmen.
  - Tutor for Physics Learning Center.
- 09/2013-12/2013      **Lloyd V. Berkner Space Policy Intern**  
*Space Studies Board, National Research Council, Washington, DC*
- The Space Studies Board (SSB) is the principal advisory group providing independent scientific and programmatic advice to

NASA and other government agencies on all aspects of civil space research and associated ground-based activities.

- Attended several Division of Engineering and Physical Science committee meetings and ad hoc task group meetings and provided meeting recaps for members. Also, attended House meeting for the committee on science space and technology.
- Assisted with the NRC Assessment of NASA Science Mission Directorate 2014 Science Plan providing a report in brief.

09/2009-12/2010

**Graduate Research Assistant**

*Department of Atmospheric and Planetary Sciences, Hampton University, Hampton, VA*

- Research focus: Observational studies of space weather in the Earth-Moon system using Geotail satellite data.

01/2010-12/2010

**Graduate Teaching Assistant**

*Department of Atmospheric and Planetary Sciences, Hampton University, Hampton, VA*

- Course: SCI 104 - Physical Science Lab. Responsible for preparing and teaching material for each lab, as well as assisting the students with equipment.
- Course: SEA 105 - Astronomy. Responsible for grading homework and tests and assisting the professor with all extra credit opportunities.

06/2009-08/2009

**Student Fellow**

*American Meteorological Society Policy Program, Washington, DC*

- Participated in the 2009 AMS Summer Policy Colloquium.
- Investigated how space weather impacts various GPS industries by interacting with government, industry, and academic representatives of the space weather and meteorological communities.

9/2006-12/2006

**Undergraduate Meteorological Student Researcher**

*School of Ocean and Earth Science and Technology (SOEST), University of Hawaii at Manoa, Honolulu, HI*

- Assisted Ph.D. candidate, Ryan Ellis with his work titled, The Distribution of Kinetic Energy of the Near-Surface Winds in Pacific Typhoons: An Analysis of WSR-88D Radar and Anemometer Data. Presented as a poster presentation at the 2006 AGU Fall meeting.
- Responsible for processing WSR-88D radar data for Typhoons Dale (1996) and Keith (1997). Analyzed evidence of rolls in the hurricane boundary layer that could further the intensity.

## Leadership Experience

- 04/2013-04/2014      **Member, Graduate Faculty Task Force**  
*Utah State University, School of Graduate Studies, Logan, UT*
- Selected by Mark McLellan, Vice President for Research and Dean of the School of Graduate Studies, to serve as the graduate student representative in the revamp of policies and procedures of hiring Graduate Faculty.
- 04/2012-04/2013      **Member, Student Health Advisory Committee**  
*Utah State University, Logan, UT*
- 04/2012-04/2013      **Director of Graduate Research**  
*Associated Students of Utah State University, Utah State University, Logan, UT*
- Selected to represent the graduate student body at Utah State University.
  - Role serves the graduate student body by enhancing the quality of student life through academics, student concerns, public relations and service events and is accomplished by college, extension and legislative student representation.
  - Involved in the organizing and planning the 2013 Graduate Research Symposium.
- 04/2012-04/2013      **Chair, Research and Project Grants Committee**  
*Utah State University, Logan, UT*
- Budget of \$12,000 for graduate student awards.
- 04/2012-04/2013      **Chair, Graduate Student Interview Committee**  
*Utah State University, Logan, UT*
- Assisted the Selection Committee Chair in the hiring of a new associate vice president for research and associate dean of the School of Graduate Students.
- 01/2013                  **Academia Member, Organizing Committee**  
*NOAA Space Weather Week, Boulder, CO*
- 04/2012-04/2013      **Member, Enhancement Award Review Committee**  
*Utah State University, Logan, UT*
- Budget of \$80,000 for graduate student awards.
- 04/2012-04/2013      **Member, Graduate Council**  
*Utah State University, Logan, UT*

- 04/2012-04/2013      **Member, Research Council**  
*Utah State University, Logan, UT*
- 04/2012-04/2013      **Member, Library Advisory Committee**  
*Utah State University, Logan, UT*
- 04/2012-04/2013      **Member, Graduate Robins Award Selection Committee**  
*Utah State University, Logan, UT*
- Selected Utah State University's graduate student researcher of the year and graduate student teaching assistant of the year.
- 01/2013                  **Academia Member, Organizing Committee**  
*NOAA Space Weather Week, Boulder, CO*

### **Service Experience**

- 04/2015                  **Rapporteur**  
*NOAA Space Weather Week, Boulder, CO*
- Assisted with the Office of Science and Technology Policy session titled, "Space Weather National Strategy." Responsible for documenting session for a follow up report.
- 04/2012                  **Rapporteur**  
*NOAA Space Weather Week, Boulder, CO*
- Assisted with the workshop titled, "Aviation Workshop." Responsible for documenting meeting for a follow up report.
- 04/2011                  **Rapporteur**  
*NOAA Space Weather Week, Boulder, CO*
- Assisted with the workshop titled, "To Define Geomagnetic Storm Products in Support of the Electric Utilities." Responsible for documenting meeting for a follow up report.
- 10/2010                  **Student Assistant, Rapporteur**  
*American Meteorological Society (AMS), Washington, DC*
- Assisted with the Policy Program workshop titled, "Satellite Navigation & Space Weather: Understanding the Vulnerability & Building Resilience." Responsible for planning, set up, organization, and documenting meeting for a workshop report.
- 5/2010                   **Student Assistant**  
*Office of the Federal Coordinator for Meteorology, Washington, DC*

- Selected volunteer to assist the OFCM staff during the Space Weather Enterprise Forum. Helped with the registration table and made sure each attendee had the appropriate materials for the conference. Also assisted session chairs with panel discussion questions.

10/2009

**Student Assistant***American Meteorological Society (AMS), Williamsburg, VA*

- Volunteered to assist the AMS staff during the 34th *Conference on Radar Meteorology*. Responsible for uploading speaker presentations in meeting rooms and assisting the session chair with each presentation.

4/2009

**Student Assistant***University Corporation for Atmospheric Research/National Oceanic and Atmospheric Administration, Boulder, CO*

- Selected to assist the Space Weather Prediction Center staff during the Annual Space Weather Workshop. Responsible for uploading each speaker presentations, as well as assisting with each presentation.

1/2008

**Student Assistant***American Meteorological Society (AMS), New Orleans, LA*

- Selected volunteer to assist the AMS staff during the 88<sup>th</sup> Annual Meeting. Responsible for the organization of the registration desk and checking in over 2000 society members.

8/2007-5/2008

**Niner Weather Forecaster***UNC Charlotte University Times Campus Newspaper, Charlotte, NC*

- Volunteer. Provided a detailed weather forecast each week, including three-day forecast for the University area, Tuesday's national temperature map, and Tuesday's North and South Carolina major city high and low temperature projections.

8/2007-5/2008

**Weather Wall Forecaster***UNC Charlotte Department of Geography and Earth Sciences, Charlotte, NC*

- Volunteer. Place fronts and precipitation on US Weather Map, post two-day and weekend detailed forecasts.

## TECHNICAL SKILLS

Computer Languages – IDL, Fortran, MATLAB, Maple, Gnuplot

## SCIENTIFIC PUBLICATIONS & PRESENTATIONS

Meehan, J., “An Update on the project: 29-day Analysis of Scale Heights and the Inference of the Topside Ionosphere Over Millstone Hill during the 2002 Incoherent Scatter Radar Campaign,” oral presentation, *Utah State University Colloquium Series*, Logan, UT, October, 2016.

Meehan, J., J. Sojka, and M. David, "How to Utilize Scale Heights to Infer Information about the Topside Ionosphere," poster presentation, *NOAA Space Weather Workshop*, Boulder, CO, April 2016.

Meehan, J., “29-day Analysis of Scale Heights and the Inference of the Topside Ionosphere Over Millstone Hill during the 2002 Incoherent Scatter Radar Campaign,” oral presentation, *Utah State University Colloquium Series*, Logan, UT, October, 2015.

Meehan, J., J. Sojka, and M. David, "Ionospheric Scale Height and its Relationship to Upper Atmospheric Neutral and Plasma Temperatures," poster presentation, *NOAA Space Weather Workshop*, Boulder, CO, April 2015.

Meehan, J., “Ionospheric Scale Height and its Relationship to Ionospheric Plasma Temperature,” oral presentation, *Utah State University Colloquium Series*, Logan, UT, November, 2014.

Meehan, J., et al., "Comprehensive Comparison of an Ionospheric Data Assimilation Model and the International Reference Ionosphere," poster presentation, *SM-Large-Scale Ionospheric Dynamics and M-I Coupling at Midlatitudes I*, AGU Fall Meeting, San Francisco, CA, December 2012.

Meehan, J., and J. Kunches, 2012: “Workshop Addresses Aviation Community,” *Space Weather*, 10, S08011, doi:10.1029/2012SW000828.

Meehan, J., J. Fulgham, and W. K. Tobiska, 2012: “The Second Annual Space Weather Community Operations Workshop: Advancing Operations Into the Next Decade,” *Space Weather*, 10, S07005, doi:10.1029/2012SW000817.

Meehan, J., et al., “Improvements to GPS and Communication Technology at USU SWC,” poster presentation, *NOAA Space Weather Workshop*, Boulder, CO, April 2012.

Meehan, J., et al., "New Space Weather Data Sources and Products for Communication and Navigation Systems," poster presentation, *9<sup>th</sup> Conference on Space Weather*, AMS Annual Meeting, New Orleans, LA, January 2012.

Meehan, J., J. Sojka, et al., "Substitution of Ionosonde Data for GPS TEC Data in GAIM-GM: A Regional Study," poster presentation, *SPA-Aeronomy General Contributions II*, AGU Fall Meeting, San Francisco, CA, December 2011.

Fulgham, J., J. Meehan, and W. K. Tobiska, 2011: "Space Weather Community Operations Workshop: Planning for the Next Decade," *Space Weather*, 9, S08002, doi:10.1029/2011SW000691.

Meehan, J., et al., "New Space Weather Products for HF Radio, GPS Navigation, and Aviation," poster presentation, *NOAA Space Weather Workshop*, Boulder, CO, April 2011.

Meehan, J., G. Fisher, W. Murtagh, "Space Weather and Technological Impacts," poster presentation, *8<sup>th</sup> Conference on Space Weather*, AMS Annual Meeting, Seattle, WA, January 2011.

Meehan, J., G. Fisher, W. Murtagh, 2010: "Understanding Space Weather Customers in GPS-Reliant Industries," *Space Weather*, 8, S06003, doi:10.1029/2009SW000556.

Meehan, J., G. Fisher, W. Murtagh, "Space Weather & GPS Reliant Industries," poster presentation, *Hampton University Research Day*, Hampton, VA, February 2010. Poster received graduate student honorable mention.

Meehan, J., G. Fisher, W. Murtagh, "Space Weather & GPS Reliant Industries," poster presentation, *7<sup>th</sup> Symposium on Space Weather*, AMS Annual Meeting, Atlanta, GA, January 2010.

## INVITED TALKS

Meehan, J., et al., "Substitution of Ionosonde Data in GAIM-GM: A Regional Case Study," oral presentation, *Advances in Space Weather Operations - III (University/Commercial) 2nd annual Space Weather Community Operations Workshop*, Park City, UT, March 2012.

Meehan, J., "Space Weather and Societal Impacts," oral presentation, *AMS Utah Chapter Meeting*, Salt Lake City, UT, February 2012.



## PROFESSIONAL DEVELOPMENT

- 2016-2017 Participant, Women's Leadership Institute's Political Development Series
- 2011-2016 Selected Utah State University Department of Physics Graduate Student Representative to the faculty
- 2012 Selected Participant, Heliophysics Summer School: Heliophysical Exploration, sponsored by NASA *Living With a Star*, Boulder, CO
- 2012 Session Co-Chair, NOAA Space Weather Workshop Annual Meeting, Boulder, CO
- 2012 Session Chair, 2nd annual Space Weather Community Operations Workshop, Park City, UT
- 2012 Selected for funding, AMS Short Course on Space Weather: Space Weather: What is it and who needs to know about it? American Meteorological Society Annual Meeting, New Orleans, LA
- 2011 Session Co-Chair, NOAA Space Weather Workshop Annual Meeting, Boulder, CO
- 2011 Session Co-Chair, American Meteorological Society Annual Meeting, 8<sup>th</sup> Conference on Space Weather, Seattle, WA
- 2010-2011 Selected Inaugural Student Member, American Meteorological Society's Scientific and Technological Activities Commission Committee on Space Weather
- 2010 Selected Participant, Boston University's CISM Summer School on Space Weather Phenomena, Consequences, and Modeling, Boston, MA
- 2009 Selected Participant, AMS Summer Policy Colloquium, Washington, DC

## PROFESSIONAL ORGANIZATIONS

- 2016-present Student member, Association for Women Geoscientist
- 2016-present Student member, American Physical Society
- 2011-present AMS, Utah chapter
- 2009-present Student member, American Geophysical Union
- 2005-present Student member, American Meteorological Society
- 2009-2010 AMS, Hampton University student chapter

2007-2009	CoCoRahS volunteer
2007-2009	Trained Storm Spotter for the National Weather Service
2007-2008	AMS, UNCC Student Organization of Meteorology student chapter